UNIVERSITY OF OKLAHOMA

GRADUATE COLLEGE

RHEOLOGICAL AND FLOW CHARACTERISTICS OF DRAG REDUCING SURFACTANT SOLUTIONS IN STRAIGHT PIPES AND ANNULAR DUCTS

A DISSERTATION

SUBMITTED TO THE GRADUATE FACULTY

in partial fulfillment of the requirements for the

Degree of

DOCTOR OF PHILOSOPHY

By

IDOWU T DOSUNMU
Norman, Oklahoma
2014

RHEOLOGICAL AND FLOW CHARACTERISTICS OF DRAG REDUCING SURFACTANT SOLUTIONS IN STRAIGHT PIPES AND ANNULAR DUCTS

A DISSERTATION APPROVED FOR THE
MEWBOURNE SCHOOL OF PETROLEUM AND GEOLOGICAL
ENGINEERING

BY

____
Dr. Subhash N. Shah, Chair

____
Dr. John Pigott

____
Dr. Ramadan Ahmed

____
Dr. Bor-Jier Shiau

____
Dr. Maysam Pournik

To my Family

ACKNOWLEGDEMENTS

This work would not have been possible without the support of many people. My sincere appreciation goes to my advisor, Dr. Subhash N. Shah, for his support, guidance, wise counsel, and belief in me throughout my studies at The University of Oklahoma. I would like to thank and acknowledge members of my doctoral committee, Dr. John Pigott, Dr. Ramadan Ahmed, Dr. Ben Shiau, and Dr. Maysam Pournik, for their time and input in this work. I am grateful to Dr. Samuel Osisanya for his academic support and encouragement.

I would like to express my gratitude to the research team at the Well Construction Technology Center (WCTC). Special thanks go to Joe Flenniken, Jeff McCaskill, and my colleagues and friends for their help during every phase of my time as a graduate student. I would like to thank the staff of Mewbourne School of Petroleum and Geological Engineering for their help and support.

I am indeed grateful to my host family, Ron and Diana Wallace, for their hospitality and support throughout my stay in Norman. Thanks to Prof. and Mrs. Chukwu for their support and encouragement over the past five years; they are greatly appreciated.

I am deeply and profoundly grateful for the overwhelming love and support of my parents and siblings. They have always been there for me, and this work would not have been possible without their unwavering belief and encouragement.

TABLE OF CONTENTS

LIST OF TABLES

LIST OF FIGURES

ABSTRACT

Surfactants are well-known as effective drag reducers and viscosifying agents. The macroscopic properties of surfactants are dictated by the surfactant type and the condition of the solvent in which the surfactant is dissolved. In an aqueous medium, surfactants tend to aggregate, forming micelles that can vary in size and shape depending on several factors.

Scare information is available on the rheological and drag reduction characteristics of surfactant fluids particularly for oilfield operations. The objective of this research is to elucidate the rheological and drag reducing behavior of non-Newtonian surfactant fluid systems (Aromox® APA-T and APA-TW). In this work, the flow behavior of surfactants is studied in the context of pseudoplastic fluids. The rheological properties are measured using the Couette-type viscometer and rheometer. Flow behavior and drag reduction are investigated in straight pipes and annular ducts of different diameters in recirculation mode.

The rheological properties of test solutions (in fresh water, 2% KCl and 2% $CaCl_2$) at various concentrations are studied using steady shear and dynamic testing. The results showed that the solutions exhibit non-Newtonian behavior at all concentrations, with their rheological character influenced by the temperature and ionic content of the base fluid. Temperature is observed to have a significant effect on viscosity and dynamic data. The apparent viscosity at different temperatures could be reduced to a single master curve using horizontal and vertical shift factors. However, satisfactory scaling could not be attained for the dynamic or viscoelastic data. Molecular scaling using characteristic time for data at different concentrations proved unsuccessful due to the strong non-Newtonian character of surfactant solutions. Scaling relations between rheological parameters and concentration indicated the presence of long micelles in APA-T solutions. APA-TW solutions, on the other hand, contained branched micelles.

The laminar flow of surfactant solutions is studied using the Carreau and modified power-law (MPL)–Cross rheological models. These models are used to develop generalized Reynolds number expressions. The new definitions are shown to be comparable and in some cases more accurate than the generalized Reynolds number for power law fluids. In addition, a new flow rate - pressure drop equation, is derived for both models, overcoming the limitation imposed by the implicit nature of the Carreau and MPL-Cross models. This equation provided improved pressure loss prediction for non-Newtonian fluid flow.

Turbulent flow behavior of test solutions is investigated by measuring pressure drop across a straight pipe at various flow rates. The drag reduction character of surfactant solutions is observed to be affected by concentration, pipe diameter, pipe roughness, and solvent type. Higher percent drag reduction occurred at higher concentrations in larger pipes with minimal surface roughness. Surfactant solutions with a monovalent salt had increased drag reduction due to the presence of longer micelles. In addition, an analytical

Fanning friction factor equation is derived for non-drag reducing fluids. Good agreement is observed between predicted and measured data with the new equation.

The problem of axial annular flow of non-Newtonian power law fluids under laminar and turbulent flow is examined. By utilizing the modified-slot analogy, Fanning friction factor - generalized Reynolds number relationships for a power law fluid are developed and presented. Good agreement over the entire range of flow regimes is obtained between model predictions and experimental data. The advantage of the proposed approach is that it eliminates the need to determine the dimensionless radial position of zero shear stress required to solve flow equations. The relationships reported provide an effective means of determining friction pressures of non-Newtonian fluids in eccentric annuli.

Chapter 1

INTRODUCTION AND SCOPE OF RESEARCH

1.1 Introduction

Surfactants are surface-active agents that alter interactions at the interface between two immiscible phases (Rosen 2004). These surface-active agents reduce the amount of work by decreasing the surface tension required to create an interface. They are widely used in fluid circulation as flow improvers or drag reducing agents because they provide as much as 80% drag reduction (Kamel and Shah 2010). The molecular structure of any surfactant can be divided into the hydrophilic head and hydrophobic tail. When in solution, the hydrophobic (tail) group distorts the structure of the surrounding water molecules. Conversely, the hydrophilic (head) group is water soluble and forms hydrogen bonds (Bewersdoff 1996). The action of the hydrophobic group leads to its orientation toward a nonpolar medium, reducing the free energy at the water interface (Rosen 2004).

Rheology plays an important role in the characterization of surfactants. Many surfactants form viscoelastic solutions in aqueous media, which can result in shear thinning over a particular shear rate range. Several constitutive equations have been used to describe the steady shear behavior of surfactants. These models range from simple two-parameter models, such as the power law model, to complicated models that contain five or more parameters. For the dynamic shear data, the Maxwell model (Heinz 2003) has been shown to describe the fluid behavior. When compared to polymers, surfactants can reconstitute their structure once the applied shear is removed. Simply put, they are not susceptible to permanent mechanical breakdown under shearing action. The structure (ascertained from rheological measurements and flow visualization techniques) of surfactants and polymers makes them effective drag reducing agents under turbulent flow.

The phenomenon of drag reduction has been the subject of many studies. Toms (1948) observed this phenomenon experimentally, albeit accidentally, under turbulent flow of linear macromolecules. His experimental setup was designed to study the mechanical degradation of dilute solutions of high-molecular-weight poly (methyl methacrylate) in monochlorobenzene. The results showed that in turbulent flow, the flow rate at constant pressure drop increased with polymer addition. This phenomenon was originally referred to as the "Toms effect" but is now generally called drag reduction.

In 1949, Oldroyd attributed this phenomenon to the "wall effect" or the "wall slip effect" (Toms 1977). Central to this concept is that an absence of polymer molecules at the wall leads to lower viscosities; thus, slip occurs. However, this mechanism has since been discounted because it does not provide a fundamental engineering basis for drag reduction (Shenoy 1984) and because of more robust experimental findings that proved otherwise (Kostic 1994; Singh 2010). Other explanations for drag reduction include but are not limited to viscoelasticity and normal stress, viscosity anisotropy, presence of an absorbed layer, and turbulence suppression.

The knowledge of drag reduction was improved upon in the late 1950s. The simultaneous works of Dodge and Metzner (1959) and Shaver and Merrill (1959) gave credence to Toms' original findings in 1948. Dodge and Metzner (1959) observed low friction factors using aqueous carboxymethyl celluose (polymer). Similarly, Shaver and Merill (1959) presented experimental findings of a decrease in friction factors for several pseudoplastic fluids. Even with all the contributions made thus far, drag reduction (DR) is still not fully comprehended because of complexities in the areas of turbulence and mechanisms dictating mass transfer (Kostic 1994).

Polymers and surfactants are known to be very effective when used at relatively small concentrations. The use of drag reducing agents extends over a wide range of industrial applications. Some industrial applications of these additives are in firefighting, sewage transport (Sellin and Ollis 1983), paper/pulp industry, pipe line transport of crude oil (Burger et al. 1982), district heating and cooling (Gasjelvic 1995) and the oil and gas industry for drilling and fracturing operations (Savins 1964; 1967). Surfactants (which generally exhibit non-Newtonian behavior) used for hydraulic fracturing operations will be considered in this study.

Numerous researchers have published excellent review articles describing various aspects of drag reduction (Lumley 1969; Hoyt 1972; Shenoy 1984; Morgan and McCormick 1990; Matthys 1991; Kostic 1994; Brostow 2008; and Singh 2010). However, many of these reviews focused on drag reduction of polymer solutions. With the growth of hydraulic fracturing using surfactant-based fluids, it is important to understand the complex behavior of these fluids.

Although the rheological and flow behavior of non-Newtonian drag reducing surfactant solutions have been investigated for many years, there are still areas that require further and improved understanding in order to fully exploit the industrial applications of surfactant fluids. This poor understanding can be attributed to the complex nature of surfactant solutions coupled with limited knowledge of their flow behavior under turbulent conditions in complex geometries. With the expanded use of surfactant solutions in many industries, further investigation is needed to ensure proper design of operations that deal with the flow of surfactant solutions.

The present study will provide a fundamental understanding of the complex rheological behavior of surfactant solutions and show how these rheological properties affect its drag reducing characteristics. The results will be useful in fluid dynamics studies (e.g. pressure loss predictions for drilling and hydraulic fracturing operations) and will elucidate the relationship between micellar structures on the rheological behavior of surfactants. Also, the outcome will have a direct application to industries that deal with recirculation flows of drag reducing fluids.

1.2 Objective and Scope of Research

Fluid systems account for a significant percent of any industrial operation from an economic standpoint. For drilling and hydraulic fracturing jobs, accurate friction pressure estimation is required for pump type and size selection to ensure safe and economic operations. The implications of poor job design can be costly as well as dire.

The present research seeks to elucidate the rheological and drag reducing behavior of non-Newtonian fluid systems. Special emphasis is placed on surfactant solutions at several concentrations in various solvent environments. The steady shear and dynamic properties are investigated to provide an understanding of the influence of different factors on surfactant molecular (micellar) interaction. In addition to researching rheological properties, it is necessary to assess the flow behavior (in straight pipes and annular ducts) and drag reducing characteristics of these systems for a better understanding of the hydrodynamics of surfactant solutions. In this work, the flow behavior of surfactants is studied in the context of pseudoplastic fluids.

This dissertation is divided into nine chapters. The fundamentals of rheology and drag reducing properties of non-Newtonian fluids are presented in Chapter 2. Chapter 3 provides a description of the experimental apparatus used in this study. Chapters 4 and 5 present data on the rheological characterization of surfactant solutions and the effects of concentration, temperature, and salts on steady shear and dynamic properties. Chapter 6 presents new generalized Reynolds number definitions for non-Newtonian fluids in laminar flow. In this chapter, modeling is performed to develop flow rate - pressure drop expressions that give higher accuracy at low shear rates for commonly used non-Newtonian fluids. Chapter 7 presents turbulent flow measurements in terms of flow rate and pressure drop, assessing the effects of concentration, conduit size, and salts on drag reduction characteristics of surfactant solutions in great detail. In this chapter, a Fanning friction factor analytical expression for non-drag reducing pseudoplastic fluids is developed. The axial annular flow behavior of pseudoplastic fluids is presented in Chapter 8. Chapter 8 focuses on laminar flow of pseudoplastic fluids and Fanning friction factor – generalized Reynolds number expressions for power law fluids are presented. In this chapter, an empirical Fanning friction factor correlation is developed for turbulent flow of drag reducing power law fluids. Conclusions and recommendations from this investigation are listed in Chapter 9.

Chapter 2

LITERATURE REVIEW

2.1 Introduction

This chapter presents a detailed review of surfactants. Surfactants are known to exhibit remarkable and unique macroscopic properties when in solution. These unique properties are the result of interactions that occur on a microscopic scale. The subjects covered in this review include fundamentals of surfactant microstructure, rheological properties, and drag reduction characteristics of surfactants and polymeric fluids. In addition, the review presents applications of surfactants in the oil and gas industry.

2.2 Microstructures of Surfactants

Surfactants are surface-active agents composed of two parts covalently bonded together—a hydrophilic (head or water-loving) group and a hydrophobic (tail or oil-loving) group. Classification of surfactants is based on the charge of the head group. In general, surfactants can be ionic or nonionic. Ionic surfactants, or ionics, can be negatively charged, as in the case of anionic surfactants, or positively charged, as with cationic surfactants. Another group of surfactants, zwitterionics has both positive and negative charges.

The addition of surfactant to a polar solvent leads to the head group remaining in the solvent while the tail group is adsorbed at the air-solvent interface. Thermodynamically, an increase in surfactant concentration increases the free energy of the system (Raoul

2005). A concentration is reached at which the hydrophobic tails tend to come together or “self-assemble” to minimize the free energy. This concentration is referred to as the critical micelle concentration (CMC). The CMC is determined by a break in the plot of certain physiochemical properties (electrical conductivity and surface tension) against concentration. For example, surface tension decreases with increasing surfactant concentration until a certain point beyond which the surface tension remains fairly constant (Rosen 2004). The CMC depends on the hydrophilic species and the condition of the solvent (Moroi 1992).

Two critical concentrations (CMC and CMC_{II}) are of significance in the study of surfactants. Temperature dependence is greater for CMC_{II} than for CMC. Figure 2.1 is an illustration of the concentration-temperature relationship for a typical cationic surfactant. The Krafft point in this figure is the point at which the CMC is equal to the saturation solubility (Moroi 1992). At temperatures below the Krafft point, the system displays gel-like characteristics. Temperatures higher than the Krafft point with a corresponding concentration increase above the CMC favor the formation of spherical micelles. Further increase in concentration leads to the transition from spherical to rod-like micelles. More complex structures (vesicles and lamellar) are formed at even higher concentrations.

Some surfactants display certain characteristics such as the formation of shear induced structures (SIS) under the action of shear. Such structures can lead to an increase in apparent viscosities by a factor of 20-50 (Soltero et al. 2007). These structures (SIS) are unstable and disappear with the addition of more shear (Wang et al. 2011). The exact mechanism for this phenomenon still eludes researchers but is believed to be a contributing factor to the drag reduction characteristics of surfactant solutions. Surfactant microstructures can be visualized using cyro-Transmission electron microscopy (cyro-TEM), flow birefringence studies, nuclear magnetic resonance (NMR), and small-angle scattering (SAS) techniques.

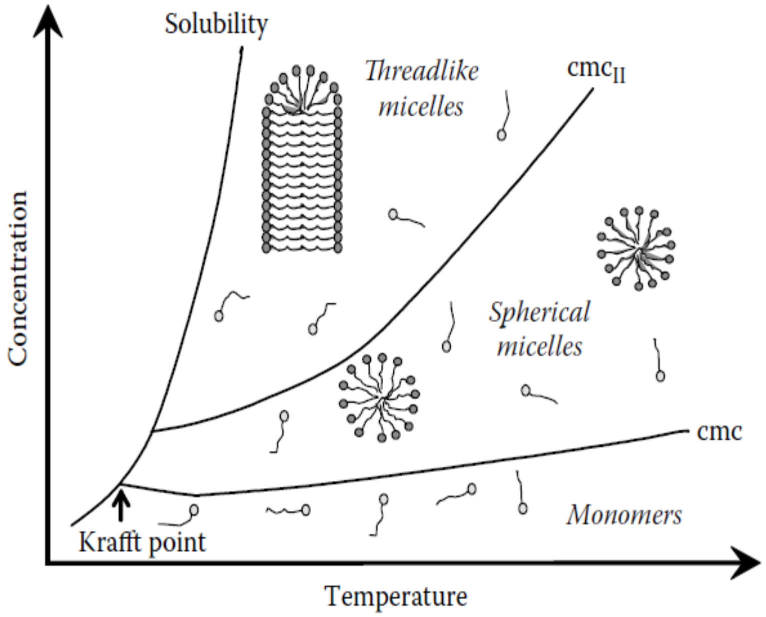

Figure 2.1: Phase Diagram Schematic for Cationic Surfactants (Chou 1991)

2.2.1 Dynamics of Micellar Solutions

The reversible scission mechanism, derived by Cates and Caudau (1990), provides a theoretical explanation for stress relaxation in micellar solutions. Stress relaxation can occur in two ways: reptation or micellar kinetics (Heinz 2005). The first mechanism, reptation (used in polymer dynamics), is due to the movement of a confined chain within a tube formed by the presence of surrounding chains. In reptation, diffusion takes place along the contour length of the chain. It is characterized by the reptation time (τ_{rep}). The second mechanism occurs through the breaking and reforming (micellar kinetics) of bonds, characterized by the breaking time, τ_b. The breaking time is the time required for a micelle of length (L) to break into two smaller chains. Alternatively, it represents the lifetime of a micellar end before recombination (Ezrahi et al. 2006). Equation (2.1) is an expression for τ_b assuming unimolar scission reaction:

$$\tau_b \sim \frac{1}{(K_I L)} \tag{2.1}$$

where, K_I is the rate constant for breakage.

Two possible scenarios can occur with both characteristic times: $\tau_{rep} >> \tau_b$ or $\tau_b >> \tau_{rep}$. For $\tau_{rep} >> \tau_b$, the breaking and reforming of bonds occurs regularly before the chain leaves its tube. The shear stress relaxation is expressed as an exponential function:

$$\sigma(t,\dot{\gamma}) = \sigma_o(\dot{\gamma}) exp\left(-\frac{t}{\tau_R}\right) \tag{2.2}$$

where, σ_o is the shear stress at time zero.

The relaxation time, τ_R, is associated with chain breakage at a point close enough to a given tube segment for reptation to occur before a new chain is lost by recombination (Ezrahi et al. 2006). It is expressed as follows:

$$\tau_R = \left(\tau_b \tau_{rep}\right)^{0.5} \tag{2.3}$$

Such a behavior ($\tau_{rep} >> \tau_b$) is adequately described by the single relaxation time Maxwell model (Eq. 2.4). By fitting the Maxwell model equations to experimental data, the plateau modulus (G_o) and τ_R can be determined:

$$G'(\omega) = G_o \frac{\omega^2 \tau_R^2}{1+\omega^2 \tau_R^2} \tag{2.4a}$$

$$G''(\omega) = G_o \frac{\omega \tau_R}{1+\omega^2 \tau_R^2} \tag{2.4b}$$

where, G_o is the plateau modulus extrapolated to time zero; ω is the angular frequency and τ_R is the relaxation time; $G'(\omega)$ is the elastic modulus; and $G''(\omega)$ is the viscous modulus.

From a plot of $G''(\omega)$ against $G'(\omega)$, Maxwellian-type behavior is represented by a semicircle that matches the experimental data in the low- to intermediate-frequency range. At higher frequencies, a deviation may occur due to small-scale processes such as Rouse-like breathing modes. An upturn becomes evident in the Cole-Cole plot signaling a deviation from Maxwell behavior. For viscoelastic solutions displaying Maxwell behavior, the zero shear viscosity (μ_o) is related to G_o and τ_R as follows:

$$\mu_o = G_o \tau_R \tag{2.5}$$

The G_o is proportional to the surfactant volume fraction as expressed below.

$$G_o \sim k_B T \emptyset^{\frac{9}{4}} \sim \emptyset^{\frac{9}{4}} \tag{2.6}$$

The relaxation time is expressed as follows:

$$\tau_R \sim L \emptyset^{\frac{3}{4}} \sim \emptyset^{\frac{5}{4}} \tag{2.7}$$

Also, the reptation time for polymer-like micelles of length L is expressed as:

$$\tau_{rep} = \emptyset^{\frac{3}{2}} L^3 \tag{2.8}$$

The zero shear viscosity becomes:

$$\mu_o \sim L \emptyset^3 \sim \emptyset^{3.5} \tag{2.9}$$

where, μ_o and τ_R are functions of concentration, temperature, salinity, surfactant type, and chain length (Ezrahi et al. 2006).

The second possible scenario for stress relaxation is when $\tau_b >> \tau_{rep}$. Here, relaxation due to reptation is dominant because no scission occurs before the chain diffuses from its tube. The micelles essentially behave like polymer chains. The relaxation time, which is equal to τ_{rep}, is expressed as follows:

$$\sigma(t, \dot{\gamma}) = \sigma_o(\dot{\gamma}) exp\left[-\frac{t}{\tau_{rep}}\right]^{\frac{1}{4}} \tag{2.10}$$

The zero shear viscosity is expressed as:

$$\mu_o \sim \emptyset^{\frac{15}{4}} L^3 \sim \emptyset^{5.25} \tag{2.11}$$

In the high-frequency region, Maxwell relations cannot be applied because short time scale processes are dominant. The characteristic time is expressed as:

$$\tau_R \sim \left(\frac{l_e}{L}\right) \tau_{rep} \tag{2.12}$$

where, l_e is the entanglement length.

The size of the mean contour length is estimated from Eq. (2.13).

$$\frac{G''_{min}}{G_o} \sim \frac{l_e}{L} \tag{2.13}$$

where, G''_{min} is the minimum value of G'' (when plotted against ω). The above equation is valid provided that $l_e/L << 1$.

The entanglement length is determined from G_o

$$G_o \sim \frac{k_B T}{\xi^3} \sim \frac{k_B T}{l_e^{\frac{9}{5}} l_p^{\frac{6}{5}}} \tag{2.14}$$

where, ξ is the mesh size (correlation length), or the distance between entanglements, and l_p is the persistence length (the length over which micelles are rigid).

2.3 Rheology of Micellar Solutions

2.3.1 Steady Shear and Viscoelastic Behavior of Surfactant Solutions

Micelles are dynamic structures in which intermicellar interactions occur. Micellar solutions generally display viscous and elastic properties, as in the case of entangled rod-like micelles (Hoffman and Ulbricht 2001). These entanglements are similar to polymers;

hence the name “living polymers” is often used for surfactants. In the dilute regime, the viscosity of the solution is close to that of the solvent. Above the CMC, worm-like micelles form transient entanglements of broad exponential length distribution (Dreiss 2007) with the length predicted using the mean field theory (Aït Ali and Makhloufi 1997). The viscosity of entangled network of rod-like micelles in the low shear rate range can be six orders of magnitude greater than that of the solvent. Such high viscosities can aid in the transport of solids during oilfield operations such as drilling and hydraulic fracturing.

The formation of WLMs is a prerequisite for the remarkable viscoelastic properties of such solutions. These WLMs become flexible when the micelle size is greater than the persistence length. Viscoelasticity is the outcome of the formation, growth, and entanglement of WLMs.

The viscoelastic properties provide information on the structure and dynamics of solutions. The mechanical spectra data ($G'(\omega)$ and $G''(\omega)$) are important for complete characterization of surfactant solutions. Generally, $G'(\omega)$ obtained from small amplitude oscillatory shear (SAOS) experiments is used to make inferences on the structure of solutions and is more reliable than steady shear measurements. Viscoelastic data may be described by the single time Maxwell model (Martin 2007) or the generalized Maxwell model (Heinz 2003), depending on the measured responses.

Usually, these viscoelastic fluids exhibit no yield stress (in most cases), and certain scaling laws have been developed based on measurable quantities such as the zero shear viscosity (μ_o), structural relaxation time (τ_R), and plateau/shear modulus (G_o) as presented in Sect. 2.2.1. The relaxation time and plateau modulus describe the disentanglement time and volume fraction of surfactant solutions, respectively (Hashizaki et al. 2009). Thus, the overall viscoelastic behavior is dictated by the plateau modulus (structure) and the relaxation time (dynamics).

2.3.2 Factors Affecting Rheological Characteristics of Surfactant Solutions

The structure and dynamics of micellar solutions have significant effects on the bulk rheological properties. Rheological behavior is influenced by surfactant type and concentration, counterions, temperature, and salts. Changes in any of these factors can affect the size and shape of micelles and, as an extension, affect rheology.

Surfactant and counterion concentration: The geometrical shape of microstructures is known based on the packing parameter. Transitions from one shape to another depend on the concentration of surfactants. It is expected that an increase in surfactant concentration causes an increase in the length of micelles. This in turn promotes micellar associations. Ionic surfactants have stabilizers (counterions) that promote micellization and higher viscosity. The effect of concentration should be considered in connection with the type of counterions and the counterion/surfactant molar ratio. From an experimental study on the behavior of cetylpridinium chloride (CPyCl) with sodium salicylate (NaSal) at different concentrations, Hoffman and Ulbricht (2001) observed that at a constant surfactant concentration with increasing NaSal, the zero shear viscosity goes through a maximum, minimum, and final maximum. The authors attributed this to the dependence of the solution's relaxation time on the NaSal concentration. Lin et al. (2001) noted a decrease in zero shear rate viscosity, with decreasing counterion/surfactant ratio for surfactant concentrations below 100mM. They provided three possible reasons for this observation: (1) branches formed in micellar networks, (2) micelles moving independently at high concentration, and (3) saturation of network structure.

Temperature: The contour length of micelles decreases exponentially with temperature (Raghavan and Kaler 2000), hindering intermicellar interactions. Smaller chain lengths limit network formation by entanglements and as such reduce drag reduction effectiveness (Jacques et al. 2007). Furthermore, other rheological parameters such as the zero shear viscosity, relaxation time, and normal stresses also decrease with temperature.

Surfactant type: The size and geometry of surfactants are affected by the chain length, head group, number of carbon atoms in chain, and saturation state of chain. Any change in any of these parameters will alter the rheological state of surfactant solutions. Surfactants with longer chain lengths are more sensitive to temperature and concentration changes (Wang et al. 2011). Interactions between head groups and the alkyl chain affect micelle size (Raoul 2005). The alkyl chain length affects the upper and lower temperature limits. Longer chains increase both temperature limits for cationic solutions; the increase in temperature limits is undesirable because of a decrease in surfactant solubility (Jacques et al. 2007). The presence of double bonds on the alkyl tail reduces the lower temperature limit. In addition, an odd number of carbon atoms on the chain results in a decrease in both the Krafft temperature and lower temperature limit (Lin et al. 2000). Li et al. (2012) stated that below a particular carbon number, solutions display Newtonian behavior. The packing of surfactant species increases with smaller head groups within the same chain group (Jacques et al. 2007).

Ionic strength: The increase in ionic strength with the addition of salts screens electrostatic repulsions between head groups. Correspondingly, the head group area is reduced, aggregation of micelles is increased, and WLM formation is favored.

2.4 Drag Reduction Fundamentals

Two definitions of drag reduction are used in literature and are provided here in chronological order. Savins (1964) defined drag reduction as an increase in the pumpability of a fluid *under turbulent flow* due to the introduction of certain high molecular weight polymers. Similarly, Lumley (1969) defined drag reduction as the reduction of skin friction in *turbulent flow* below that of the solvent. It becomes clear from both definitions that drag reduction is a phenomenon associated with turbulent flow.

Drag reduction can be achieved in two ways—active and passive drag reduction (Singh 2010). The difference between the two is that energy input is required for passive drag reduction (for example, riblets) and the level of drag reduction is small. Active techniques, on the other hand, involve the use of substances such as high molecular weight polymers and surfactants for drag reduction. Increased drag reduction with additives (as much as 70% with polymers and 80% with surfactants) has been reported.

Mathematically, percent drag reduction is expressed as follows:

$$DR(\%) = \left(\frac{\Delta P_s - \Delta P_a}{\Delta P_s}\right) 100 \text{ (at constant flow rate)} \quad (2.15a)$$

$$DR(\%) = \left(\frac{f_s - f_a}{f_s}\right) 100 \text{ (at constant Reynolds number)} \quad (2.15b)$$

where, ΔP_s is the pressure loss without additives (i.e., solvent alone), ΔP_a is the pressure loss with additives, f_s is the Fanning friction factor without additives, and f_a is the Fanning friction factor with additives. Equation (2.15) is valid based on the assumption of density remaining unchanged with additives in solution.

The Reynolds number, N_{Re} (or generalized Reynolds number, N_{Reg}), is used to designate flow regimes—laminar or turbulent. Below a Reynolds number of 2100, laminar flow condition exists and the Hagen-Poiseuille equation (Eq. 2.16) is used to calculate the Fanning friction factor for both Newtonian and non-Newtonian fluids flowing through a circular pipe.

$$f = \frac{16}{N_{Reg}} \quad (2.16)$$

$$N_{Reg} = \frac{\rho v d}{\mu_a}$$

where, ρ is the fluid density, v is the fluid velocity, d is the internal pipe diameter, and μ_a is the fluid viscosity (apparent viscosity for non-Newtonian fluids).

Under turbulent flow of Newtonian fluids, several expressions for Fanning friction factor have been reported, the variations depending on whether the flow conduit is smooth or rough. For smooth pipes, the Blasius-type expression (Eq. 2.17) and the Drew correlation (Drew et al. 1932) (Eq. 2.18) are frequently used. When pipe roughness is considered, the Chen correlation (Chen 1979) is applicable (presented in Chapter 7).

$$f = 0.079 N_{Re}^{-0.25} \tag{2.17}$$

$$f = 0.0014 + \frac{0.125}{N_{Re}^{0.32}} \tag{2.18}$$

The Drew correlation is valid for $2{,}100 < N_{Re} < 3 \times 10^6$.

Fluids (used for hydraulic fracturing) that exhibit drag reduction are mostly non-Newtonian with viscoelastic properties. As a result, the above correlations are not suitable for non-Newtonian fluids as they overestimate the Fanning friction factor. Moreover, unlike Newtonian fluids in which Fanning friction factor calculations are independent of the pipe size, non-Newtonian fluids are dependent on N_{Reg} and pipe diameter (diameter effect). Several empirical expressions have been reported for non-Newtonian drag reducing fluids with and without pipe roughness (Shah 1984; 1990).

Figure 2.2 is an illustration of the flow behavior of Newtonian, polymeric, and surfactant fluids to explain drag reduction. Curve A represents laminar flow, and the Fanning friction factor is determined using Eq. (2.16). Curve B represents the path followed by a Newtonian fluid in which the Fanning friction factor is calculated using Eq. (2.18). The Virk's maximum drag reduction asymptote (MDRA) is curve C. As the name implies, this expression was empirically developed for maximum drag reduction attainable by polymeric fluids (Virk 1975). Typically, Fanning friction factor data for polymers should be contained within the B-C envelope. Surfactants, however, can exhibit drag reduction at higher levels than polymers are able to exhibit. Zakin et al. (1996) empirically determined the corresponding asymptote for non-polymeric (surfactant) fluids (curve D). The MDRA for polymers and surfactants will be discussed in detail in later sections.

As stated in the introduction, drag reduction additives are not limited to polymers and surfactants; solids, fibers, and other additives are also known to be drag reducing agents. In this review, polymers and surfactants will be considered because of their appeal and common use in the oil and gas industry.

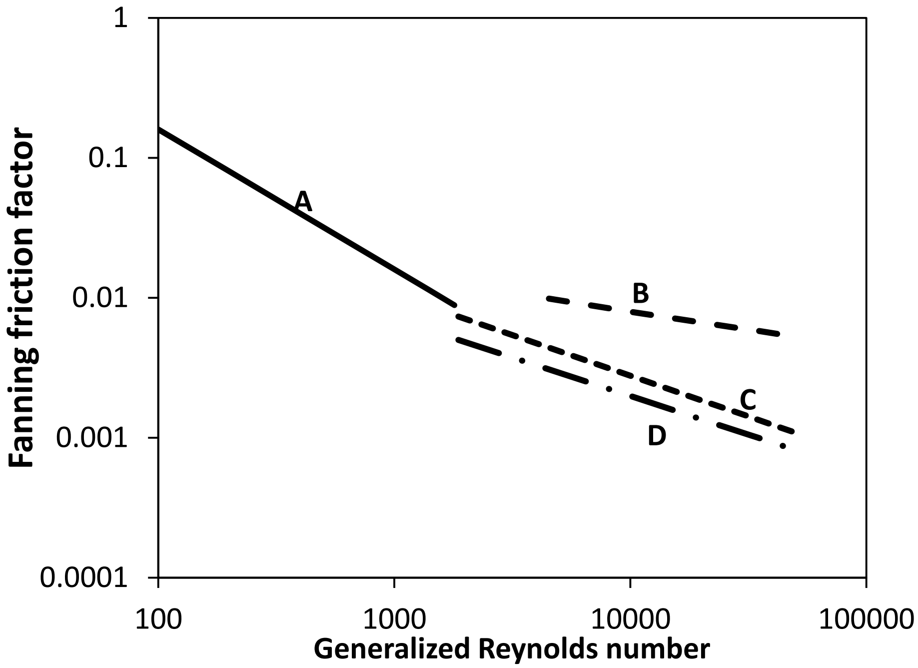

Figure 2.2: Maximum Drag Reduction Asymptotes for Polymers and Surfactants

2.4.1 Proposed Mechanisms of Drag Reduction

A number of researchers have proposed various mechanisms responsible for drag reduction. This review discusses a few of them in no particular order with the aim of examining the merits and demerits of each mechanism. Some mechanisms are viscoelasticity, molecular stretching, decreased turbulence production, and viscosity anisotropy.

In 1949, Oldroyd attributed drag reduction to slip at the wall, or the so-called wall effect (Toms 1977). According to him, the absence of polymer molecules at the wall leads to lower viscosities and the resulting slip effect at the wall. Several researchers have highlighted the shortcomings of this mechanism because of its lack of engineering foundation (Shenoy 1984). Toms (1977) attributed drag reduction to shear thinning near the wall, which causes lower friction factors when compared to only the solvent (Shenoy 1984). However, Walsh (1967) showed that some shear thickening solutions exhibit drag reduction.

Anisotropy in viscosity was proposed to explain the drag reduction phenomenon (as cited in Kostic 1994). In this theory, viscosity in the flow direction is low but is high in other directions to dampen or suppress turbulent fluctuations (Shenoy 1984). This mechanism takes advantage of the shear-rate dependency of typical drag reducing fluids (Kostic 1994).

Another explanation was based on viscoelasticity and normal stresses of drag reducing solutions (Kostic 1994). Although plausible for highly concentrated solutions of polymers and surfactants, it falls short for dilute solutions that do not display measurable viscoelasticity but are effective drag reducers. Furthermore, data by Lu (1997) suggest that viscoelasticity is not required for drag reduction to occur. This should not discount the fact that viscoelasticity might be an accompanying characteristic of many surfactant drag reducers that have rod-like micelles (Kostic 1994). Recent experimental and numerical work by Li et al. (2012) demonstrates that indeed viscoelasticity is important and should be considered for surfactant drag reduction.

Molecular stretching was postulated as being responsible for drag reduction. According to this explanation, added macromolecules tend to increase the resistance to elongational flow. This effect is referred to as “shear hardening” (as cited in Truong 2001), which hinders turbulent bursts close to the wall. Tulin (1966) claimed that greater turbulence dissipation was related to an increase in the laminar sublayer thickness, which is responsible for drag reduction (Shenoy 1984). However, this mechanism still lacks consensus in the scientific community as it fails to explain drag reduction in dilute solutions (Kostic 1994).

Turbulence production interference and turbulence dissipation have been put forward as possible causes of drag reduction. Pfenniger (1967) suggested that polymer molecules interfere with and possibly reduce turbulence disturbances (as cited in Shenoy 1984). It is believed that the process of energy transfer from large to small scale eddies (energy cascade) is significantly hindered by macromolecules. As such, turbulence is suppressed (Morgan and McCormick 1990), leading to more favorable flow in the streamwise direction (Kostic 1994).

Singh (2010) summarized the findings of drag reduction over many years from his studies as well as other researchers. He considered experimental and theoretical findings from several researchers in his discussion of drag reduction mechanism in terms of changes in flow and turbulence structures. This review presents a select list of the main points from Singh’s work.

- The position of the peak intensity of the streamwise component of velocity is shifted farther away from the wall.
- The velocity of the wall normal component is suppressed. Its peak position is moved away from the wall. The Reynolds shear stress, which is a measure of turbulence transport, attains its maximum at the center and zero at the wall.
- Drag reduction additives cause an increase in the non-dimensional streak spacing. This spacing increases with drag reduction.
- Bursting events are more energetic and less frequent with drag reduction increase.

It is plausible that more than one mechanism can be the cause of drag reduction. The above discussion is an attempt to review the existing models and possible mechanisms. Each represents an observation or a rationalization that may or may not be responsible for drag reduction. This is a testament to the varied opinions on the complex nature of turbulence coupled with drag reducing polymers and surfactants.

2.4.2 Drag Reduction with Polymers

The ability for small quantities of polymers, dissolved in various solvents, to reduce friction pressure has been utilized for more than 60 years. These substances (polymers) are the most studied and commercially attractive method of active drag reduction. Examples of drag reducing polymers include guar gum, polyethylene oxide, and polyacrylamide. Successful applications have been reported for the pipeline transport of crude oil (Burger et al. 1982). Studies on polymeric drag reduction are divided into the onset phenomenon, maximum drag reduction asymptote, and factors affecting drag reduction. These topics apply to both polymers and surfactants.

Onset phenomenon: The point at which the Fanning friction factor with polymer additive becomes less than that of the solvent is termed the "onset" of drag reduction. Onset is attributed to the stretching of polymeric units outside the viscous layer. Generally, two types of drag reduction based on the onset point have been identified—Type A and Type B (Virk and Wagger 1989). The difference between both relates to where drag reduction begins. Drag reduction for Type A applies to random coil polymers and starts in the fully turbulent regime, while Type B (fully extended polyelectroytes) starts in the extended laminar regime. The onset point is moved to lower N_{Reg} values at higher polymer concentrations (Morgan and McCormick 1990).

The onset phenomenon is explained using various models of length, time, and energy. Virk and Merril (1969) introduced the length scale (as cited in Virk 1975). Using the polymer radius of gyration, they defined a dimensionless constant, Γ, which is the ratio of length scale of the polymer to that of turbulence (Eq. 2.19). Drag reduction starts when Γ is equal to 0.015.

$$\Gamma = \left[\frac{2R_g}{\mu}\right]\left[\frac{\tau_w^*}{\rho}\right] \tag{2.19}$$

where, R_g is the radius of gyration of the polymer molecule, τ_w^* is the onset wall shear stress, μ is the solution viscosity, and ρ is the solution density.

The time scale or criterion states that the time scale for turbulence has to be comparable with that of the polymer relaxation time (Lumley 1969; Sreenivasan and White 2000). Lumley et al. (1969) posited that fluctuating strain rates in the near-wall region imposed on the polymer molecules result in higher extensional viscosities (stretching of molecules). With higher viscosities, smaller eddies are suppressed or dampened, decreasing momentum transport; thus inducing drag reduction (Morgan and McCormick 1990; Sreenivasan and White 2000). New numerical simulations have given credence to the concept of increased extensional viscosities close to the wall (Dimitropoulos et al. 1998). Sreenivasan and White (2000) noted that matches between simulations and experimental data were the result of higher elasticity values introduced in simulation models. Ryskin (1987) presented a model ("yo-yo") similar to that of Lumley et al. (1969). However, Morgan and McCormick (1990) pointed out an obvious limitation of Ryskin's model, highlighting the uncertainty in determining α, a parameter used in this model.

Tabor and de Gennes (1986) offered an alternative explanation for the onset of drag reduction. Their main criticism of the higher extensional viscosities approach is that fluctuating strain rates are inadequate to provide any substantial increase in viscosity. They proposed that the energy stored by polymer molecules has to be equivalent to the turbulence energy for drag reduction to occur. This alters the transfer of energy from large- to small-scale eddies and results in an increase in the elastic layer thickness resulting in drag reduction (Sreenivasan and White 2000). Based on the energy criterion, Walsh (1967) presented a dimensionless parameter, H, which is the ratio of energy stored by the polymer to the turbulence energy (Morgan and McCormick 1990). According to Walsh (1967), drag reduction starts when H is approximately equal to 0.01.

$$H = \frac{8cM[\mu]^2\tau_w^*}{R_gT} \tag{2.20}$$

where, M is the polymer molecular weight, R_g is the gas constant, T is the absolute temperature, and c is the concentration in g/ml.

Kohn (1973) proved the inadequacies in all three models mentioned above. He stated that the polymer molecules acted as "energy sinks." These molecules store energy in deformation for the balance of the viscous sublayer. The removal of stress causes the molecules to relax, release stored energy, and become available again for deformation. Drag reduction occurs by virtue of polymer molecules reducing turbulence mixing. Kohn proposed an energy theory based on mathematical theory of polymer behavior (Kohn 1973). In his model, drag reduction is a function of energy stored rather than decreased turbulence generation; it is not a function of rate of convection as proposed by Walsh (1967). The average amount of energy stored or strain energy density is expressed as follows:

$$W = \left(\frac{cRT}{2M}\right)\sum_i^N \ln[1 + (\dot{\gamma}\tau_i)^2] \tag{2.21}$$

where, N is the number of statistical segments per polymer, $\dot{\gamma}$ is the shear rate, and τ_i is the relaxation time of the i^{th} deformation calculated from Eq. (2.22).

$$\tau_i = \frac{b^2 f}{6kT\lambda_i} \tag{2.22}$$

where, parameters b and f are the root mean square (rms) segment length and segment friction, respectively, k is the Boltzmann's constant, and λ_i is the eigenvalues calculated using Pyun and Fixman's (1965) approximations. These parameters are obtained using optimization schemes, minimizing the rms with experimental data.

Kohn's results compared reasonably with experimental data for the onset of drag reduction, supporting his proposition that energy storage is the mechanism responsible for drag reduction (Kohn 1974). However, according to Morgan and McCormick (1990), Kohn's theory is difficult to verify because of difficulties in determining the molecular parameters.

Maximum drag reduction asymptote: Virk (1970) experimentally determined the MDRA for polymers (as cited in Virk 1975). Other asymptotes have been reported (Castro and Squire 1968; Giles and Pettit 1967), but Virk's MDRA is the most accepted expression. Drag reduction increases proportionally with concentration up to a particular concentration, at which point no further increase occurs. This implies an increase in the elastic sublayer. The MDRA is reached when the elastic layer extends across the pipe section. The same analogy for drag reduction with concentration applies to drag reduction with the generalized Reynolds number. Virk (1970) stated that the MDRA is independent of polymer species, molecular weight, and concentration. The expression of the MDRA in the Prandtl-Karman coordinates is:

$$f^{\frac{1}{2}} = 19 \log\left(N_{Reg} f^{\frac{1}{2}}\right) - 32.4 \tag{2.23}$$

Or explicitly,

$$f = 0.58N_{Reg}^{-0.58} \quad (4000 < N_{Reg} < 40{,}000)$$

The regime below the MDRA is given as follows:

$$f^{\frac{1}{2}} = [4.0 + \delta] \log\left(N_{Reg} f^{\frac{1}{2}}\right) - 4.0 - \delta \log\left(\sqrt{2}d\right)\omega \qquad (2.24)$$

where, d is the internal pipe diameter, δ and ω are polymer solution parameters.

Virk (1975) proposed the idea of a three-layer velocity profile. The velocity profile consists of the viscous sublayer (close to the wall), the buffer layer, and the logarithmic layer.

$$u^+ = y^+ (0 < y^+ < 5) \text{ (viscous sublayer)} \qquad (2.25)$$

$$u^+ = y^+ (0 < y^+ \leq 30) \text{ (buffer layer)}$$

$$u^+ = 2.5 \ln y^+ + 5.5\ (y^+ > 30) \text{ (logarithmic layer)}$$

where, $u^+ = \frac{u}{u_T}$ and $y^+ = \frac{y u_T}{v}$ are dimensionless velocity and distance, respectively.

For drag reducing polymers, the velocity profile for the logarithmic layer is parallel to the Newtonian profile, separated by a factor ΔB (see Fig. 2.3). The expression for the logarithmic layer is given below:

$$u^+ = 2.5 \ln y^+ + 5.5 + \Delta B \qquad (2.26)$$

where, ΔB depends on the polymer characteristics and on pipe flow conditions (Singh 2010). Virk's MDRA, in terms of dimensionless velocity and distance, is expressed as follows:

$$u^+ = 11.7 \ln y^+ - 17 \qquad (2.27)$$

The region between the laminar sublayer and the Newtonian turbulent core was termed the “elastic sublayer.” This elastic sublayer is described as important for drag reduction, with the viscous layer playing only a passive role (Gadd 2000; Tiederman et al. 1985).

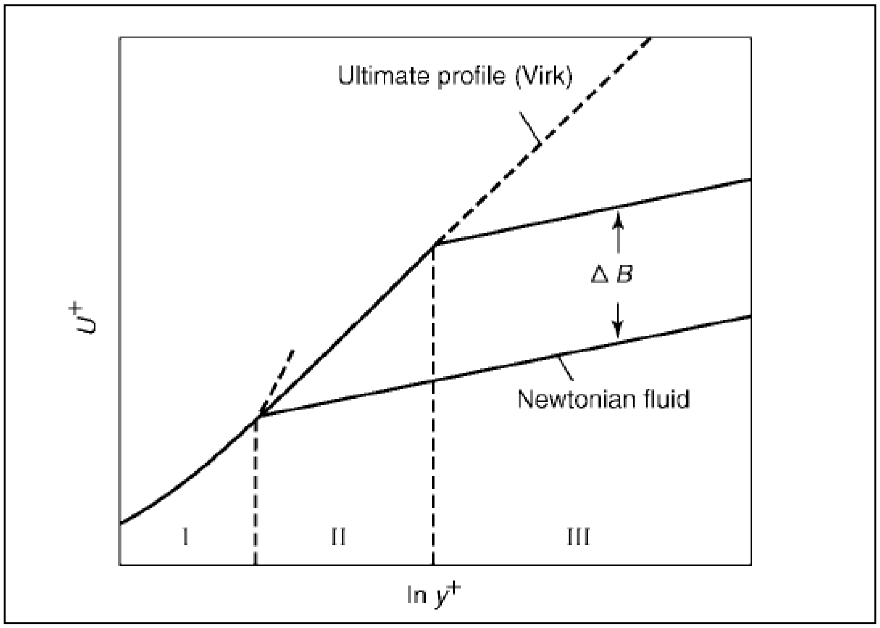

Figure 2.3: Virk's Three-Layer Model (Singh 2010)

Factors affecting polymer drag reduction: The effectiveness of polymers as drag reducers is a function of molecular weight, polymer flexibility, and the presence of electrolytes (Bewersdorff 1996). It has been confirmed experimentally that the higher the molecular weight (in the range of 10^6 Daltons), the greater the polymer flexibility and the better the drag reducing ability at a given concentration and Reynolds number (Truong 2001). The reverse holds true for lower molecular weight polymers. An increase in polymer concentration causes an increase in drag reduction up to a certain concentration (corresponding to the MDRA), above which the drag reduction remains constant.

A major advantage of polymers is that drag reduction is achieved with only a few parts per million (ppm) in aqueous and organic solvents (Shenoy 1984). However, susceptibility to permanent degradation—especially for high-molecular-weight and relatively low-concentration polymers (Cowan 2000)—limits their use in operations that require recirculation (Gasljevic 1995).

2.4.3 Drag Reduction with Surfactants

As described earlier, surfactants are surface-active agents that possess both a hydrophilic head and a hydrophobic tail. An increase in surfactant concentration favors self-association or micellization. Such an association results in the formation of various geometrical structures (spherical and rod-like). Drag reduction is exhibited when the rod-like structure is formed.

A common feature of drag reducing surfactants is the critical/threshold wall shear stress. This shear stress corresponds to the point of maximum drag reduction (Savins 1967). An increase in shear stress beyond this threshold value causes a drop in drag reduction. Further shear results in the pressure loss being the same as that of the solvent. However, unlike with polymers, the loss of drag reduction is temporary for surfactants (Gasljevic 1995). Savins (1967) explained the loss of DR as the disentanglement of the network structure due to higher levels of turbulence. A decrease in shear stress below the critical shear stress leads to restructuring or reconstitution of the micellar structure needed for effective drag reduction.

Zakin et al. (2007) classified drag reducing surfactants into three categories with reference to their microstructure and correlation with drag reduction. These categories include the following:

1. Surfactant systems that form micelles in the quiescent state with high zero shear viscosity, shear thinning, formation of SIS, high viscoelasticity, and large first normal stress.
2. Surfactant systems that form WLMs with branching points (smaller unbranched WLMs) exhibiting lower drag reduction. Fluids in this category have smaller critical shear stress, complex rheological properties, low zero shear viscosities, low viscoelasticity and zero first normal stress, and high extensional viscosities.
3. Systems with vesicles that form WLMs at high shear stress in excess of the critical shear stress.

According to Zakin et al. (2007), high viscoelasticity does not always correlate to drag reduction. On the other hand, high ratios of extensional viscosities to shear viscosities (~ 100) have been shown to correlate with surfactant drag reduction (Zhang 2005).

The factors that affect the rheological characteristics influence drag reduction. Concentration and molecular structure, salts, temperature, pH, and cosolvents, are all factors that should be considered. Longer micelles improve drag reduction effectiveness. Drag reduction effectiveness depends on the maximum drag reduction ability, the effective temperature range (upper and lower limits), and the critical wall shear stress (Jacques et al. 2007).

Maximum drag reduction asymptote with surfactants: From several experimental studies, it was discovered that the Fanning friction factors measured for surfactants were below those predicted by Virk's MDRA. Zakin et al. (1996) attributed this observation to morphological differences and possibly different mechanisms of drag reduction. They stated that morphological differences marked by the formation of SIS in surfactants are better in altering turbulence production and eddy generation as compared to structures in polymers. It should be noted that the mechanisms for drag reduction are widely believed to be similar for polymers and surfactants (Li et al. 2012).

The Zakin et al. (1996) surfactant MDRA is expressed as follows:

$$f \approx 0.32 R_e^{0.55} \quad (4{,}000 < N_{Reg} < 130{,}000) \tag{2.28}$$

The mean velocity profile was found to be steeper than that predicted by Virk's MDRA and is given as follows:

$$u^+ = 53.9 \log_{10} y^+ - 65 \quad (y^+ > 15) \tag{2.29}$$

2.5 Diameter Effect

The pressure loss for turbulent flow of Newtonian fluids through smooth pipes is a function of the Reynolds number. For Newtonian fluid flow in rough pipes, it is a function of the Reynolds number and pipe roughness. Pressure loss for non-Newtonian fluids, on the other hand, depends on N_{Reg} and pipe size (in the case of rough pipes, pipe roughness). Simply put, the same fluid at a certain N_{Reg}, will have different Fanning friction factor values in different pipes. This presents another level of complexity, incorporating more parameters to the already complex nature of drag reduction turbulent flow mechanics (Gasljevic et al. 1999; 2001).

The diameter effect has more of an impact on surfactant fluid flow than on the flow of polymers. Gasljevic et al. (2001) found out that the entrance length (x/D) ratio of 100 for polymer solutions is not suitable for surfactants. In other studies (Suzuki et al. 2004) it appears that the x/D ratio should be higher for surfactant solutions. The critical wall shear stress that precludes degradation occurs at a lower N_{Reg} in smaller pipes. Moussa and Tiu (1994) accounted for this as due to greater extensional strain at the same N_{Reg} in small pipes. For non-asymptotic flow situations, the diameter effect is clearly evident in the region between onset and degradation. In this region, drag reduction is a strong function of pipe size. At flow conditions for asymptotic conditions (MDRA), the Fanning friction factor is independent of pipe size (Gasljevic et al. 1999).

The diameter effect presents discrepancies between laboratory data and actual field results. Although the diameter effect has been the subject of many research efforts, a firm understanding is still lacking. Empirical models from robust testing have been developed. These models can be described as “scale-up correlations” or “scale-up techniques.” Admittedly, these correlations are limited theoretically but are often a practical tool for many applications (Gasljevic et al. 1999). Some of these scale-up approaches are described below.

2.5.1 Diameter Scale-up Techniques

Whitshitt et al. (1968) suggested a correlation technique using drag reduction and solution friction velocity ($u_p^* = \sqrt{\tau/\rho}$). The reason behind this approach was that the friction factor showed a dependence on the wall shear stress. With this method, they obtained an accuracy of $\pm 15\%$ regardless of the pipe size. An obvious limitation with this approach lies in the determination of the wall shear stress (Gasljevic et al. 1999). Other investigators (Savins and Seyer 1977) have recommended using the solvent friction velocity (u_s^*) in place of u_p^*. The former was an improvement over the latter but its (solvent friction velocity) validity was brought into question by Gasljevic et al. (1999) for its inapplicability to drag reducing flows.

Gasljevic et al. (2001) evaluated three different scaling approaches in literature. These are (1) drag reduction vs. u_s^* (or wall shear stress, τ_w), (2) τ_w vs. bulk velocity (V), and (3) drag reduction vs. V. The correlation approaches were applied to experimental data for two surfactants (Ethoquad/NaSal and a nonionic surfactant) and two polymers (xanthan gum and partially degraded polyacrylamide). Some pertinent conclusions can be drawn from the study of Gasljevic et al. (2001). First, two procedures (drag reduction vs. V and τ_w vs. V) were the most successful for samples tested. Second, solutions that have strong diameter effect were scaled better with τ_w vs. V. Gasljevic et al. (2001) noted that different techniques apply to different solutions, but typically fluids that follow the three-layer profile proposed by Virk (see Virk 1975) scale well with drag reduction vs. V.

Sood and Rhodes (1998) developed a scale-up model based on Prandtl's mixing length; which was adapted for drag reducing fluids. Results using this approach compared favorably with experimental data and data from the Trans-Alaska Pipeline. The model, however, is an iterative-based approach for pipe scale-up. Hoyt (2003) proposed a promising analytical expression for scale-up of drag reducing fluids. Considering the mean velocity profile for drag reduction ($u^+ = 2.5 \ln y^+ + 5.5 + \Delta B$), the scale-up expression is the following:

$$N_{Re2} = \left[\frac{\sqrt{f_1}}{\sqrt{f_2}}\right]\left[\frac{D_2}{D_1}\right] N_{Re1} \tag{2.30a}$$

The above equation can be corrected for temperature differences by the kinematic viscosities (υ).

$$N_{Re2} = \left[\frac{\sqrt{f_1}}{\sqrt{f_2}}\right]\left[\frac{D_2}{D_1}\right]\left[\frac{\upsilon_1}{\upsilon_2}\right] N_{Re1} \tag{2.30b}$$

The model was developed with the assumption that ΔB is the same for equal shear stress in both the small and large pipes. Hoyt (2003) found satisfactory agreement with Eq. (2.30) and gathered data. Hoyt's approach was evaluated for surfactants used in district heating application by Ma et al. (2011). Satisfactory predictions were obtained for this application.

The discussions above highlight several scale-up correlations with their applicability and, in some cases, shortcomings. What is clear is that diameter effect is important and has to be accounted for in drag reducing flows. Based on current knowledge, no single scale-up law can be applied to all fluids at different conditions primarily because of the complicated nature of drag reducing fluids combined with the mechanics of turbulent flow.

2.6 Surfactants in the Oil and Gas Industry

The application of surfactants in the petroleum industry is varied and diverse. Surfactants are used in a myriad of roles within the oil and gas industry. In drilling operations, surfactants can act as thinners, lubricants, and emulsifiers. Examples of some surfactants are lignosulfonates and sulfonated asphalt, which function as thinners and emulsifiers, respectively (Nelson 1982). For cementing operations, surfactants are used as spacer fluids that condition the wellbore in preparation for pumping cement. They act as viscosifiers when added to completion brines. For enhanced oil recovery operations, surfactants are used for interfacial tension reduction. Other applications include the following: matrix diversion, filter cake removal, and wellbore cleanouts (Samuel et al. 2000).

More recently, surfactants have been developed for hydraulic fracturing operations. Exploration and exploitation of less permeable reservoirs encouraged research into the development of viscous fluids for stimulation. Polymer fluids, introduced in the 1960s, were observed to cause formation damage and thereby hinder production (Kefi et al. 2004). This is because the relatively large size of polymer molecules has a greater tendency to plug pore throats. Thus, it became important for researchers and the industry to develop fluids that not only are sufficiently viscous to initiate and propagate fractures but also are non-damaging to the formation. This led to the development of polymer-free viscoelastic surfactant (VES) fluids.

Viscoelastic surfactants contain molecules that are smaller (5,000 times smaller) than guar molecules (Samuel et al. 2000). Moreover, they satisfy other criteria for their widespread use. These criteria are low pressure drop in pipes, ability to transport and place proppants, and flow back with little or no formation damage (Samuel et al. 2000). The role of surfactants has been expanded to operations in low and high temperature reservoirs as well as to unconventional plays such as coalbed methane reservoirs (Kefi et al. 2004). For coalbed methane applications, viscoelastic surfactants have proved effective at minimizing formation damage, which ultimately results in greater production.

Chapter 3

EXPERIMENTAL SETUP AND ANALYSIS

This chapter is divided into two sections. The first section reviews information on the surfactants studied and provides a detailed description of the experimental apparatus for steady shear and dynamic oscillatory measurements. The second section provides a detailed description of the experimental loop used for flow measurements.

3.1 Surfactant Samples

The test fluid for this study is tallowalkylamidopropyldimetylamine oxide, which is commercially marketed as Aromox® APA-T—and more recently as Aromox® APA-TW by Akzo Nobel Chemical Inc (Chicago, Illinois). It consists of 50–65 wt% active surfactant, 25–40 wt% propylene (solvent) and 5–10 wt% water (solvent). The structure of this surfactant is shown in Fig. 3.1.The chain is composed of carbon atoms in the range of C_{14}–C_{18}. Aromox® APA-T (APA-TW) is stable in the temperature range of 40 to 155 °F and can form viscoelastic gels. In oil and gas operations, it is used as a gelling agent for hydraulic fracturing to initiate fractures and aid in proppant transport.

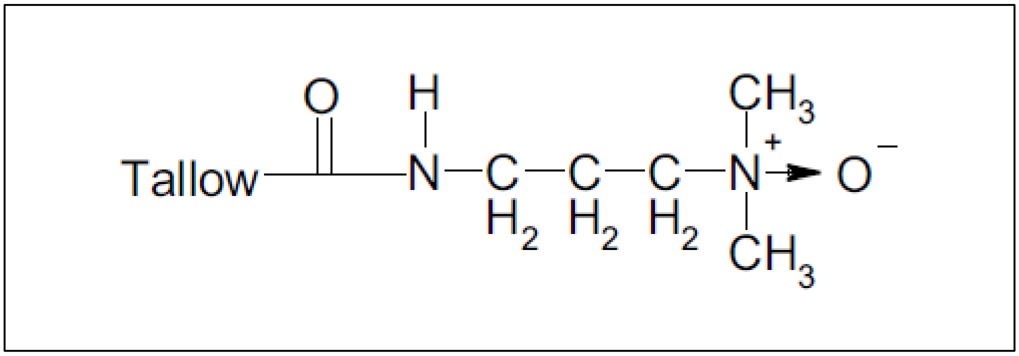

Figure 3.1: Tallow Amine Oxide

Aromox® APA-T has been classified as zwitterionic (Ge 2008) but can be cationic in acid solutions and nonionic in neutral or alkaline media (Akzo Nobel Chemical Inc. 2001). The gels formed are shear dependent with high viscosity in the low shear rate and decreasing viscosity with increasing shear. They are known to be highly elastic and have good solids-carrying capacity under high and low shear (Akzo Nobel Chemical Inc. 2001). Table 3.1 shows the physical properties of this surfactant.

Table 3-1: Physical Properties of Aromox® APA-T

Quantity	**Property**
color	Clear golden liquid
Freezing point	39–48 °F
Sp. gr	0.99 at 77 °F
pH	6–9

Concentrations for rheological characterization are presented in Tables 3.2 and 3.3. These concentrations are based on actual field application of Aromox® APA-T and APA-TW.

Table 3.2: Fluids Tested for Rheological Characterization (APA-T)

Surfactant	Conc., % vol.	Salinity
		2% KCl
APA-T	1.5	✓
	2	✓
	3	✓
	4	✓

Table 3.3: Fluids Tested for Rheological Characterization (APA-TW)

Surfactant	Conc., % vol.	Salinity	
		2% KCl	2 % $CaCl_2$
APA-TW	1.5	✓	✓
	2	✓	✓
	3	✓	✓
	4	✓	✓
	5	✓	✓
	6	✓	✓

3.1.1 Test Fluid Preparation

Aromox® APA-T and APA-TW are supplied in liquid form, making solution preparation straightforward. The same mixing procedure was followed for rheology and flow measurements. A test solution was prepared by adding the required volume of surfactant to a given volume of water.

For laboratory rheology tests, 1 liter of water was used as the basis to which an appropriate amount of surfactant was added. The resulting solution was continuously mixed in a blender, initially at moderate speed and then at higher speeds to ensure proper mixing. The solution was left for 24 hours to hydrate and build structure. To investigate the effect of salts on rheology, 2% KCl or 2% $CaCl_2$ was added to the water before the introduction of the surfactant.

For flow tests, a scaled-up volume of surfactant was added to water in a 50-barrel mixing tank. The hydraulically-driven paddle of the mixing tank was set at a desired moderate speed. The mixer was left for approximately two hours to obtain a homogeneous solution. This homogeneous solution was left to hydrate for 24 hours before any test was conducted.

As defined in the scope of this study, two salts were considered (2% KCl and 2% $CaCl_2$). The same mixing procedure was followed, but this time a required amount of salt was added to a prepared surfactant solution. The surfactant-salt solution was thoroughly stirred for 1 hour. The solution was left for another hour to build viscosity. Hydration was confirmed by rheology measurements.

3.2 Rheology Instruments

Rheometers and viscometers are devices used to measure data for the characterization of fluid systems. The difference between both relates to equipment configuration and measurement capabilities. Viscometers are relatively simpler setups that yield limited data such as shear viscosity. Rheometers, on the other hand, are versatile, sophisticated devices that offer flexibility with greater measurement capabilities that preclude viscometers. Measuring devices can be grouped into two categories:

1. Flow through capillary or tube viscometers
2. Flow in rotational rheometers/viscometers (concentric cylinders, cone and plate, and parallel plate)

Two rheological instruments were used in this investigation. These are the model 35 Fann viscometer and the controlled stress Bohlin CS-50 rheometer. The bob-and-cup geometry was selected for rheology measurements.

These are devices in which one part moves while the other part is fixed. Viscoelastic measurements are conveniently done either in the controlled-stress or controlled-strain modes. For controlled-stress rheometers, stress is imposed and the resulting rate is measured, while the controlled-strain involves stress measurements under imposed shear rate. The assumptions with rotational devices include steady state laminar flow, isothermal conditions, and negligible gravity and end effects.

Concentric cylinder: In concentric cylinders, flow is in the gap between two cylinders, with the inner cylinder called the *bob* and the outer the *cup*. Either the bob or cup can be rotated relative to the other. Fluid placed in between both cylinders is sheared, and torque is generated on the stationary cylinder because of the viscosity of the fluid. With the torque, shear stress resulting from the applied rate is calculated. The advantages of couette rheometers are (1) they are ideal for viscosity measurements in the intermediate shear rate range, (2) they are good for low viscosity fluids (less than 100 Pa.s), and (3) they can be used for high shear rate applications. The major limitation is that the couette device is unable to measure the normal stress.

The working equations for couette rheometers are the following (Macosko, 1994):

Shear stress:

$$\tau_{r\theta} = \frac{M_i}{2\pi R_i^2 L} \tag{3.1}$$

Shear rate:

$$\dot{\gamma}(R_i) = \dot{\gamma}(R_o) = \frac{\Omega_i \bar{R}}{R_o - R_i} \text{ (for } R_i/R_o \geq 0.99\text{)} \tag{3.2}$$

For $0.5 < R_i/R_o < 0.99$

$$\dot{\gamma}(R_i) = \frac{2\Omega_i}{n\left(1 - \left(\frac{R_i}{R_o}\right)^{\frac{2}{n}}\right)} \tag{3.3}$$

$$\dot{\gamma}(R_o) = \frac{-2\Omega_i}{n\left(1 - \left(\frac{R_i}{R_o}\right)^{\frac{2}{n}}\right)} \tag{3.4}$$

$$n = \frac{d \ln M_i}{d \ln \Omega_i}$$

Normal stress:

$$T_{11} - T_{22} = \frac{[\tau_{rr}(R_i) - \tau_{rr}(R_o)]}{R_o - R_i} \bar{R} \tag{3.5}$$

$$\bar{R} = \frac{(R_o + R_i)}{2}$$

3.2.1 Fann 35 Viscometer

The model 35 Fann viscometer (Fig. 3.2) is the workhorse of the oil and gas industry and has been the mainstay in many research and industry laboratories. It is particularly suited for measurements in the moderate shear rate range (5–1022 s^{-1}). The equipment specifications for the model 35 Fann viscometer are given in Table 3.4.

Figure 3.2: Model 35 Fann Viscometer

Table 3.4: Specifications of Model 35 Fann Viscometer

Instrument	**Geometry**	**Dimensions, mm**	**Shear Rate Range, s^{-1}**
Fann 35 Viscometer	Diameter of Bob	D_b = 34.49	5.1 - 1022
	Diameter of Cup	D_c = 36.83	
	Ratio (β)	D_b / D_c = 0.9365	

3.2.2 Bohlin CS-50 Rheometer

The Bohlin CS-50 rheometer (see Fig. 3.3) is a much more versatile instrument. Its applicability spans both steady shear and dynamic oscillatory measurements. Further, it encompasses the functionality of the Fann 35 viscometer by providing an automated system for data acquisition in the low to moderate shear rate range. Complete rheological characterization requires measuring the steady as well as dynamic shear properties of test samples. The steady shear data provides the apparent viscosity data, which is vital for drag reduction calculations. The dynamic data provides viscoelastic properties [$G'(\omega)$ and $G''(\omega)$] for inferences about fluid structure. Amplitude sweep tests are run to obtain the minimum strain value in the linear viscoelastic region (LVR). Such a test is referred to as small amplitude oscillatory shear (SAOS). The SAOS mode is used to ensure the sample structure is left intact during each test.

The Bohlin CS-50 has three geometries: bob and cup, cone and plate, and parallel plate. Bob and cup geometry is used here, with the dimensions shown in Table 3.5. With this apparatus, torque is applied to the test sample, and by means of an optical angular position transducer, the resulting displacement is measured. Added test functionality for high temperature (284 °F) and pressure conditions (600 psi) are included in the hardware for this rheometer. For studying the effect of temperature, a water bath is used to supply or remove heat by oil circulation.

Figure 3.3: Bohlin CS-50 Rheometer

Table 3.5: Specifications of Bohlin CS-50 Rheometer

Geometry	**R_b, in.**	**R_c, in.**	**R_b/R_c**	**L_b**	**Shear rate range, s^{-1}**
bob and cup	0.492	0.541	0.926	1.476	0.648–1944

Tests were conducted using a required quantity of test fluid. A 13-ml syringe was used to load the sample. Measurements at ambient conditions were performed initially in the dynamic oscillatory mode to gather viscoelastic data. Steady shear data were acquired in the shear rate range specified in Table 3.5. Each test required a time period of 2 hours. After each test, this instrument was thoroughly cleaned before the next experiment.

3.3 Experimental Flow Loop

Figure 3.4 shows the field scale experimental flow loop at the Well Construction Technology Center (WCTC). The loop consists of straight pipes and fully eccentric annular sections. Straight pipes that cover the range of field scale diameter are used for this study. These are the 1½-in. (200 ft long, 1.188-in. ID) and 2⅞-in. (199.3 ft long, 2.441-in. ID) pipe sections. In addition, friction pressure data from other pipe sizes (½-in. and 2⅜-in.) at WCTC are included to add robustness to data evaluation. The various annular section dimensions are shown in Table 3.6.

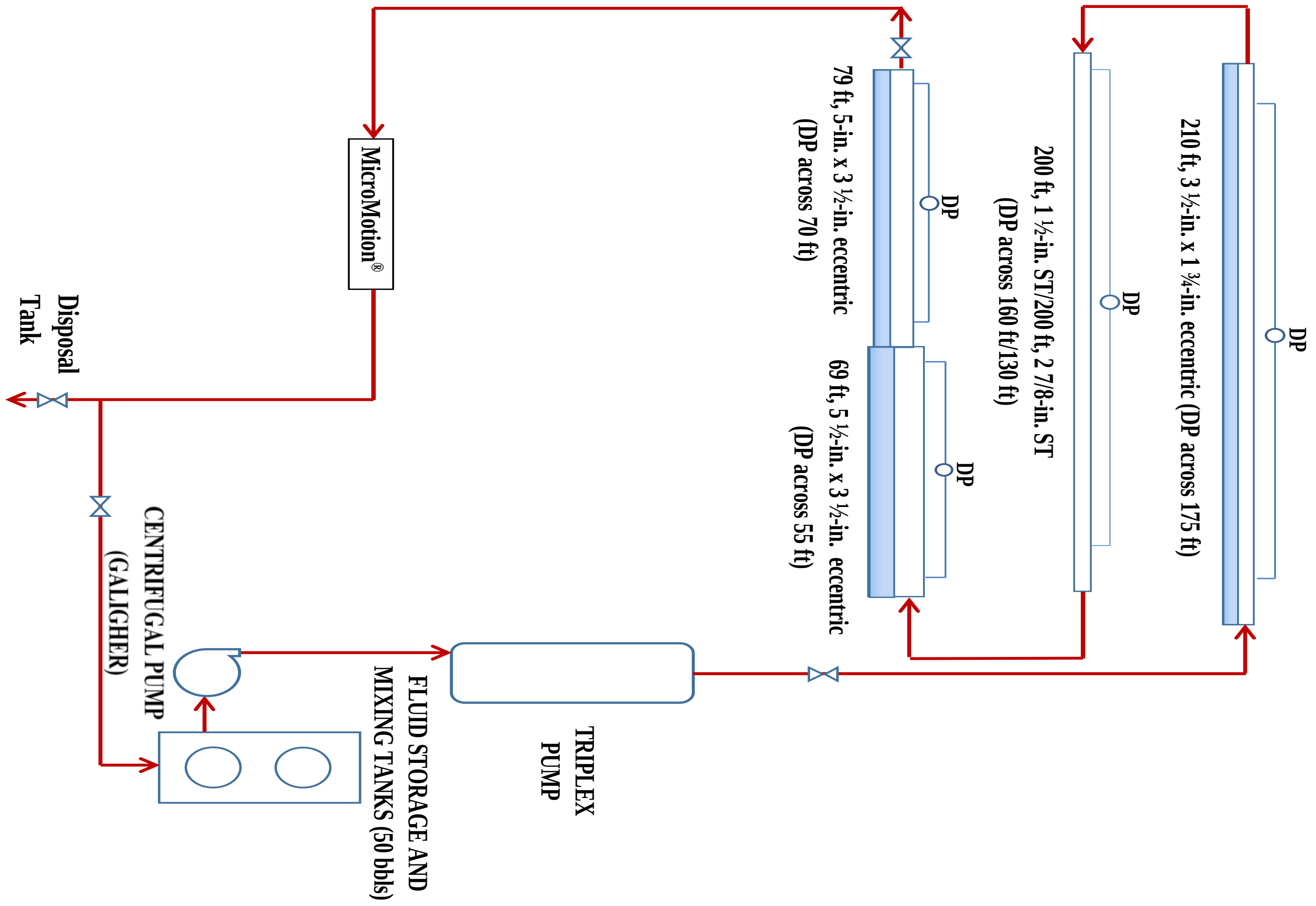

Figure 3.4: Schematic of Experimental Setup

Table 3.6: Dimensions of Eccentric Annular Sections in Flow Loop

Tubing Type	Diameter, d_2 and d_1 (in.)	Equivalent Diameter ($d_2 - d_1$) (in.)	Length between Pressure Ports (ft)
Eccentric Annulus (1)	3 ½ x 1 ¾	1.000	175
Eccentric Annulus (2)	5 ½ x 4	0.892	55
Eccentric Annulus (3)	5 x 3 ½	0.776	70

3.3.1 Fluid Preparation and Pumping

Test solutions were mixed and stored in two 50-barrel holding tanks mounted on a trailer unit (see Fig. 3.5). The solutions are mixed in one tank, as described in Sect. 3.1.1, while the second tank is used for water storage (for system calibration and flushing). Series of connecting pipes are used to transport fluid to the pumps and into the test section.

Figure 3.5: Fluid Mixing and Storage Tanks

Two pumps connected in series provide the means to circulate fluid through the entire flow loop. These are the Galigher centrifugal and Schlumberger B804 high pressure triplex pumps (max. pressure of 10,000 psi at a rate of 290 gpm). The former is used to ensure constant supply of fluid for optimum running of the latter. Figures 3.6 and 3.7 show the centrifugal and triplex pumps.

Figure 3.6: Galigher Centrifugal Pump

Figure 3.7: Schlumberger B804 Triplex Plunger Pump

3.3.2 Instrumentation

In addition to pressure data, other parameters are monitored and recorded to aid in data analysis. The instrumentation consists of differential pressure transducers (Honeywell) and a MicroMotion$^{®}$ flow meter. The MicroMotion$^{®}$ flow meter is used to acquire flow rate, fluid density, and temperature in real time. The specifications for the pressure transducers and MicroMotion$^{®}$ flow meters are listed in Tables 3.7 and 3.8.

Table 3.7: Specifications of MicroMotion$^{®}$ Flow Meters

No.	Quantity	Model	Span, psi		Rating, psi	Accuracy*
			Max.	Min.		
1	2	STD170V	0–3,000	0–100	6,000	±0.15%
2	1	STD170G	0–3,000	0–100	3,000	±0.15%
3	2	(1) STD130V	0–100	0–5	6,000	±0.75%
		(2) YSTD130G				
4	4	(1) STD130G	0–100	0–5	6,000	±0.075%
		(2) STD 130V				
5	2	STG98LC	0–6,000	0–500	9,000	±0.1%

* Expressed in terms of percentage of calibration span

Table 3.8: Specifications of Pressure Transducers

Item	Flowmeter 1	Flowmeter 2
Model	DL200 S228SU	DS300 S157SU
S/N	154891	251696
Flow rate range, gal/min	0 - 420	0 - 840
Flow rate accuracy, %	±0.15	±0.15
Temperature accuracy, °C	±0.1	±0.1
Density accuracy, g/cm^3	±0.0005	±0.0005
Operating pressure, psi	740	740

3.3.3 Data Monitoring and Acquisition

Completing the hardware is the data monitoring and acquisition system. With this system, a wireless data logger is the medium through which data is acquired and transmitted. These data include friction pressure loss, flow rate, temperature, and fluid density. The wireless logger system consists of two Fluke Hydra systems (model 2625A) with different channels, each representing a recorded parameter.

As the name implies, data are transmitted through a wireless connection to a computer in the data acquisition room. The computer is equipped with software that displays graphs showing trends of all measured parameters with time. This display makes it easy to assess steady state reference points. Measured parameters are monitored to observe changes as each test progresses and to record data for subsequent interpretation.

3.3.4 Flow Loop Operation

The test sample was prepared in the mixing tank at ambient conditions. Prior to each test, calibration fluid (water) was pumped from the storage tank at different flow rates (turbulent regime) through the test section to (1) ensure that the system is free of debris and (2) acquire baseline data for subsequent analysis. Water calibration plots for straight pipe and annular sections can be found in Chapter 7 and Appendix II, respectively. Upon completion of the water test, a valve was actuated to allow the flow of the test solution in recirculation mode. The flow rate, being the control variable, was increased at specified intervals to cover both laminar and turbulent flow conditions (30 to 250 gpm). As flow rate was changed, the resulting pressure loss was measured and recorded. A period of 2–3 minutes of flow was required to achieve steady state. Fluid samples were collected and sampled before, during, and after each test as a means of quality control (to rule out possible fluid degradation). At the end of testing, water was pumped to flush the test section in preparation for future experiments.

3.4 Analysis of Flow Data

Rheological and flow data were analyzed using the equations presented in this section.

3.4.1 Rheological Data Analysis

Steady shear data for the 35 Fann Model was recorded in the form of dial reading and rotor speed using the standard R1-B1 geometry. These quantities were converted to wall shear stress and wall shear rate using the following equations:

$$\tau_w = 0.01066 \times S \times \theta_i \tag{3.6}$$

$$\dot{\gamma}_w = 1.703 \times N \tag{3.7}$$

where, τ_w = wall shear stress (lb_f/ft^2); S = spring number (1 and 0.2 for the no. 1 and $^1/_5$th spring); θi = dial reading; $\dot{\gamma}_w$= wall shear rate (s^{-1}); and N = rotor speed (rpm).

For power law fluids ($\tau_w = K_v(\dot{\gamma}_w)^n$), parameters n and K_v for each solution were determined by least squares regression from log-log plots of wall shear stress–wall shear rate. The viscometer consistency index can be converted to pipe consistency index (K_p) or annular consistency index:

$$K_p = K_v \left[\frac{(3n+1)\left(1-\beta^{\frac{2}{n}}\right)}{4(1-\beta^2)} \right]^n \tag{3.8a}$$

$$K_a = \frac{K_p}{\left[\frac{9n+3}{8n+4}\right]^n} \tag{3.8b}$$

where, β is the ratio of bob-to-cup radius; n is the flow behavior index; K_p and K_a are the pipe consistency index ($lb_f\ s^n/ft^2$) and annular consistency index ($lb_f\ s^n/ft^2$), respectively.

The power law parameters for test solutions under investigation are reported in Tables 3.9 and 3.10 for APA-T and APA-TW, respectively.

Table 3.9: Rheological properties of APA-T Solutions

Test Fluid	n	K_v ($lb_f\ s^n/ft^2$)	K_p ($lb_f\ s^n/ft^2$)
1.5% Aromox APA-T in fresh water	0.569	0.0036	0.0039
4% Aromox APA-T in fresh water	0.248	0.0450	0.0540

Table 3.10: Rheological properties of APA-TW Solutions

Test Fluid	n	K_v ($lb_f\ s^n/ft^2$)	K_a ($lb_f\ s^n/ft^2$)
5% Aromox APA-TW in fresh water	0.387	1.78×10^{-2}	3.34×10^{-2}
5% Aromox APA-TW in 2% KCl	0.269	4.17×10^{-2}	4.74×10^{-2}
5% Aromox APA-TW in 2% $CaCl_2$	0.298	3.22×10^{-2}	3.66×10^{-2}

3.4.2 Flow Data Analysis

Flow rate (q) and pressure drop (Δp) were converted to the generalized Reynolds number (N_{Reg}) and Fanning friction factor (f), respectively. The pressure gradient is related to the Fanning friction factor as expressed below:

$$\frac{\Delta p}{l} = \frac{f \rho u^2}{25.8d} \tag{3.9}$$

where, ρ = fluid density (ppg); u = fluid velocity (ft/s); d = internal diameter (in.).

The fluid velocity is calculated from flow rate (q) as expressed below:

$$u = \frac{q}{2.448d^2} \tag{3.10}$$

The Reynolds number and generalized Reynolds number for pseudoplastic fluids are defined as follows:

$$N_{Re} = \frac{\rho u d}{\mu} \tag{3.11}$$

$$N_{Reg} = \frac{\rho u d}{K_p \left(\frac{8u}{d}\right)^n} \tag{3.12}$$

Equations (3.11) and (3.12) are in consistent units.

For a power law fluid, the generalized Reynolds number is expressed as follows:

$$N_{Reg} = \left(\frac{1}{12}\right)^n \frac{7.48}{32.17 \times 8^{n-1}} \frac{d^n u^{2-n} \rho}{K_p} \tag{3.13}$$

For annular flow, the pipe diameter (d) is replaced with the hydraulic diameter ($d_2 - d_1$). where, d_2 is the inner diameter of outer pipe and d_1 is the outer diameter of inner pipe.

Chapter 4

RHEOLOGICAL CHARACTERIZATION OF SURFACTANT SOLUTIONS

4.1 Introduction

Viscoelastic surfactants are widely used in the oil and gas industry for hydraulic fracturing operations. These surfactants have the ability to impart high viscosity at low shear rates, display shear thinning characteristics, and exhibit drag reducing characteristics. As described in Chapter 2, shear degradation with surfactants is temporary when compared to permanent degradation with polymers. They are non-damaging to hydrocarbon formations because they leave no residue in pore spaces. A drawback of surfactants is loss of functionality at elevated temperatures.

Many industrial applications, especially in the chemical and petroleum industries, involve solids transport by means of a non-Newtonian carrier fluid. The fluid viscosity at 100 s^{-1} is often used to assess the solids transport capability of a fluid. However, rheological and atomic force microscopy (AFM) tests on crosslinked guar polymer solutions by Goel et al. (2001) highlighted the inadequacies with viscosity (at 100 s^{-1}) as a significant transport criterion. They observed that solids transport is qualitatively related to the fluid structure as marked by an increase in the storage modulus. From a comprehensive literature review, it can be stated that limited information exists on the rheological character of surfactant solutions (at concentrations used for industrial operations) as it relates to solids transport capability. The intent of this chapter is to address this issue by providing a systematic and detailed investigation of the rheological behavior of surfactant solutions as inferred from steady shear and dynamic oscillatory tests.

Surfactant solution rheology is influenced by several factors, including shear rate, concentration, temperature, type and concentration of counterion, and solvent type. This chapter examines and characterizes surfactant solutions. Steady shear and dynamic oscillatory measurements are reported to elucidate the effect of concentration and temperature on the rheological behavior of surfactant solutions used for oilfield operations.

4.2 Steady Shear Behavior

4.2.1 Concentration Dependence

Figures 4.1 and 4.2 show the apparent viscosity as a function of shear rate at 75 °F for the surfactant solutions under consideration. Two regions (I and II) can be identified in both figures. These are the lower Newtonian and shear thinning regions at low and high shear rates, respectively. In the lower Newtonian region, the viscosity (referred to as zero shear rate viscosity, μ_o) is unaffected by shear rate and remains constant. At a certain shear rate value (critical shear rate), a transition from I to II occurs. In Region II, the apparent viscosity decreases, with shear rate displaying the shear thinning behavior that is common to many WLM solutions. The shear thinning region covers approximately four decades of shear rate. As shown in both figures, the shape of the apparent viscosity–shear rate curves is dependent on surfactant concentration.

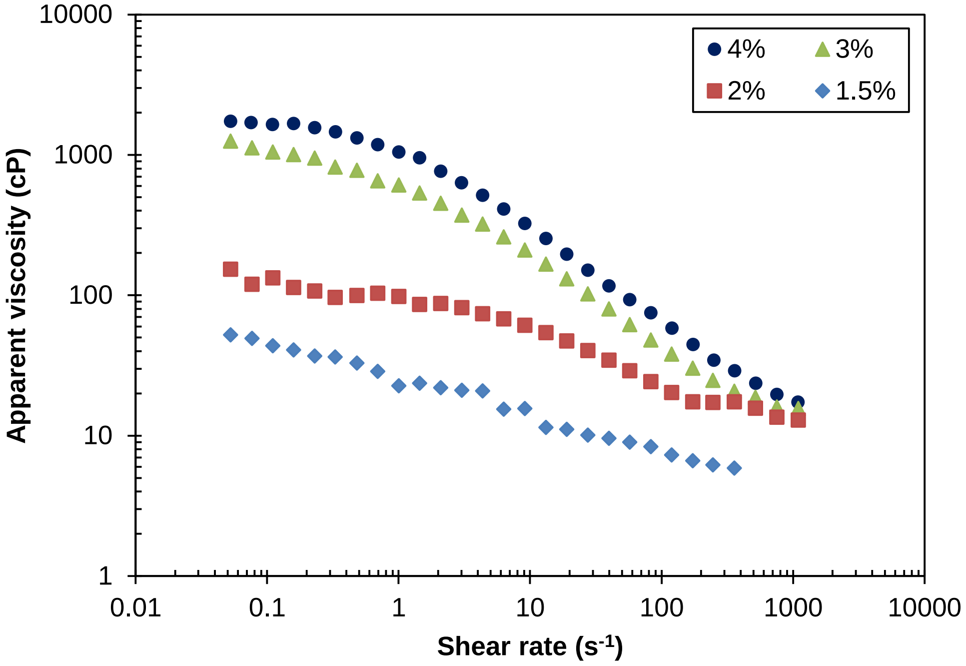

Figure 4.1: Apparent Viscosity for APA-T Solutions

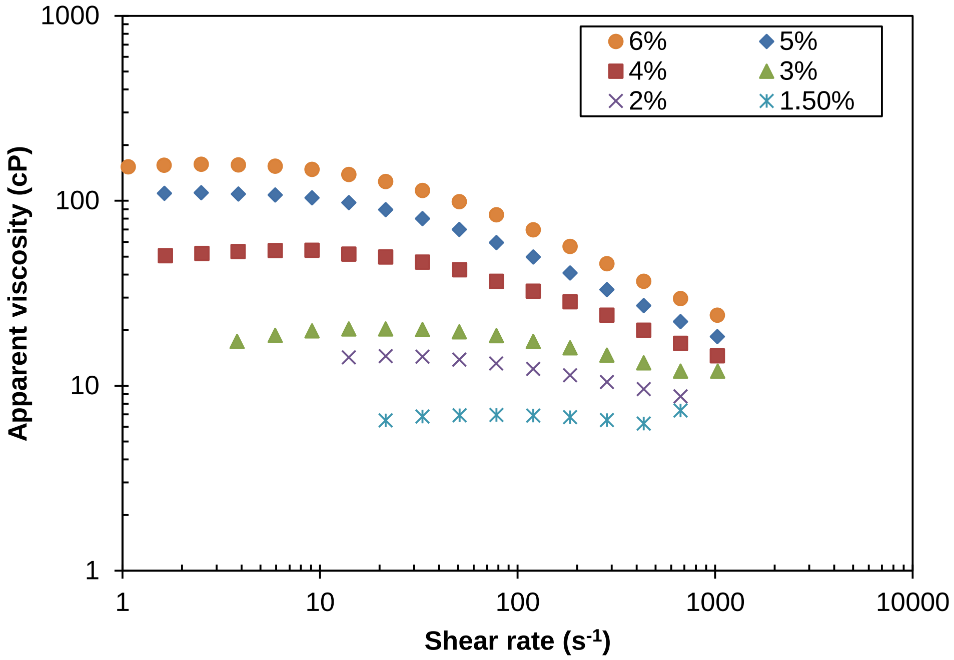

Figure 4.2: Apparent Viscosity for APA-TW Solutions

The μ_o is a parameter frequently employed in characterizing non-Newtonian fluids. In the drilling industry, it is used as an indicator of solids-carrying capacity of fluids. It is believed that the higher the μ_o, the better the solids-suspension properties of a fluid system. Figures 4.3 and 4.4 show μ_o plotted against concentration for APA-T and APA-TW samples. The magnitude of μ_o increases with concentration, as represented by the slope of these curves. As observed from both figures, μ_o for both surfactants vary at the same concentration even though the equivalent mass is the same for the samples. APA-T solutions have consistently higher μ_o values than the APA-TW samples.

An increase in surfactant concentration promotes one-dimensional micellar growth due to increasing aggregation number and number density of aggregates (Acharya et al.

2006). The power-law scaling exponent for APA-T samples is close to the Cates' theoretical value (Cates and Candau 1990) for neutral micelles ($\mu_o \sim c^{3.5}$). For APA-TW samples, the scaling exponent is lower than the theoretical value. The lower value suggests the presence and reptation of branched micelles (Lequeux 1992) as the system has end-caps and intermicellar connections (Oelschlaeger and Willenbacher 2011). The scaling relationship for the APA-T fluid is indicative of long micelles in which micellar kinetics (breaking and recombination) occurs several times while reptating out of the cylindrical tube (i.e., $\tau_b << \tau_{rep}$) (Shashkina et al. 2005).

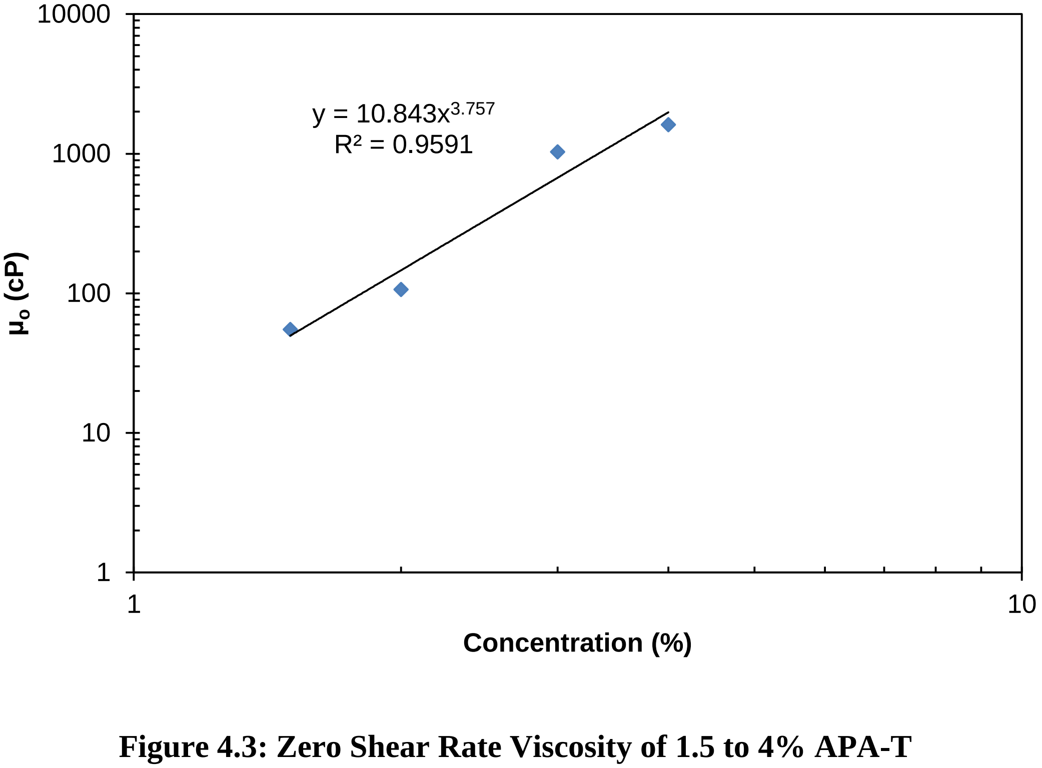

Figure 4.3: Zero Shear Rate Viscosity of 1.5 to 4% APA-T

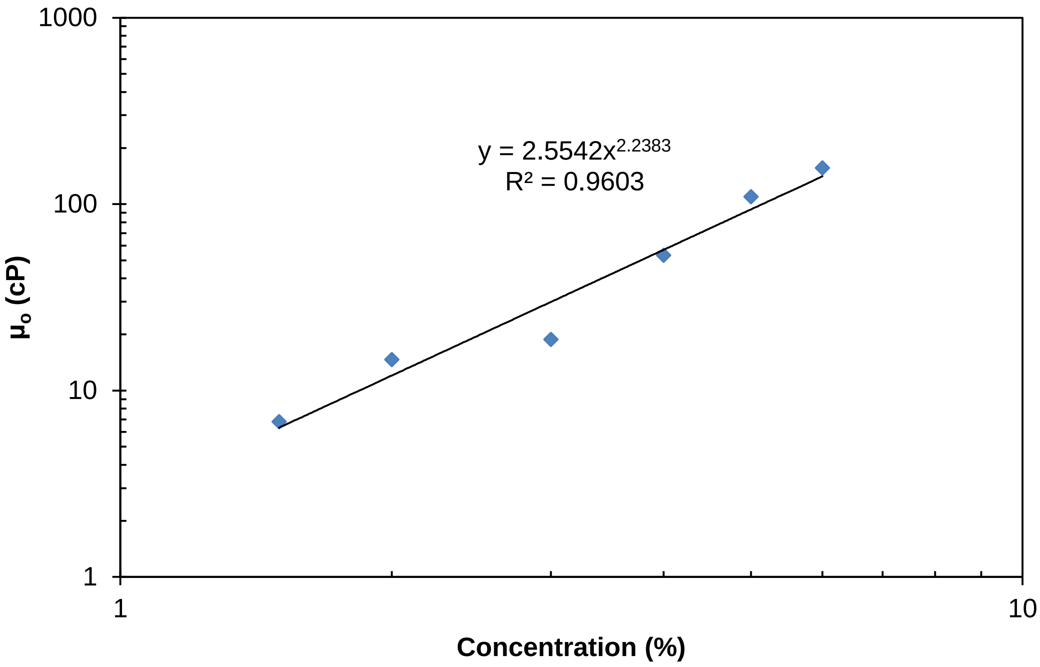

Figure 4.4: Zero Shear Rate Viscosity of 1.5 to 6% APA-TW

4.2.2 Rheological Model Predictions of Steady Shear Properties

Many fluids used for industrial applications are classified as pseudoplastics. These fluids are known to be structurally complex with viscosity dependence on shear rate. Viscosity varies with shear between the upper Newtonian plateau (low rates of shear) and the limiting lower Newtonian plateau. Several fluid rheological models are available in the literature to describe the shear rate dependence of viscosity.

For this work, the Carreau (1972) and the extended power-law (referred to as the modified power law–Cross, or MPL-Cross) are chosen because these models provide complete characterization of samples in the measured shear rate range studied. The Carreau and MPL-Cross models represent the typical structural behavior exhibited by many engineering fluid systems. The power law model is a special case of both the Carreau and MPL-Cross models. The modified power law was presented by Dunleavy and Middleman (1966) and referenced in other studies (Lee and Park 2001).

The Carreau model is expressed as follows:

$$\mu = \frac{(\mu_o - \mu_\infty)}{[1+(t\dot{\gamma})^2]^N} + \mu_\infty \tag{4.1}$$

$$N = \frac{1-n}{2}$$

where, μ_o = zero-shear rate viscosity; μ_∞ = viscosity at infinite shear; t = time constant; n = flow behavior index. Usually, μ_∞ can be neglected because $\mu_\infty << \mu_o$.

The MPL-Cross model is derived by considering two models—the modified power law and Cross models. The Cross (1965) model is expressed as follows:

$$\mu = \frac{(\mu_o - \mu_\infty)}{[1+(t\dot{\gamma})^{1-n}]} + \mu_\infty \tag{4.2}$$

The MPL-Cross (Lee and Park 2001) is expressed as follows:

$$\mu = \frac{\mu_o}{\left[1+\left(\frac{\mu_o}{K_{MPL}}\right)\dot{\gamma}^{1-n}\right]} + \mu_\infty \tag{4.3}$$

Equation (4.3) represents an improvement to the existing MPL; it has a term to account for viscosity at high shear rates. Thus, Eq. (4.3) is termed the “extended power law model,” or more conveniently “EPL.”

Neglecting the μ_∞, the EPL model can be recast in the form of the Cross model as follows:

$$\mu = \frac{\mu_o}{\left[1+\left(\left\{\frac{\mu_o}{k_{MPL}}\right\}^{\frac{1}{c}}\dot{\gamma}\right)^{c}\right]} \tag{4.4}$$

where, c = 1-n

Non-linear regression was used to fit Eqs. (4.1) and (4.4) to steady shear data. Figures 4.5 and 4.6 show the fit for 4% APA-T and 5% APA-TW. The fit parameters for the Carreau model are summarized in Table 4.1 for other concentrations. Average errors of less than 10% were calculated. It can be seen from Figs. 4.5 and 4.6 that both models satisfactorily describe the steady shear character of both surfactant samples. The Carreau model, however, gave the lowest average error. The time constant increases with concentration, whereas the flow behavior index (n) decreases with concentration (the degree of shear thinning increases with surfactant concentration).

Table 4.1: Carreau Model Parameters

	Concentration (%)	**μ_o (cP)**	**t (s)**	**N**
APA-T	4	1659	0.676	0.322
	3	1030	0.543	0.298
	2	115	0.695	0.149
	1.5	58	0.050	0.133
APA-TW	6	156	0.047	0.239
	5	109	0.040	0.227
	4	53	0.030	0.189
	3	20	0.014	0.120
	2	15	0.010	0.105

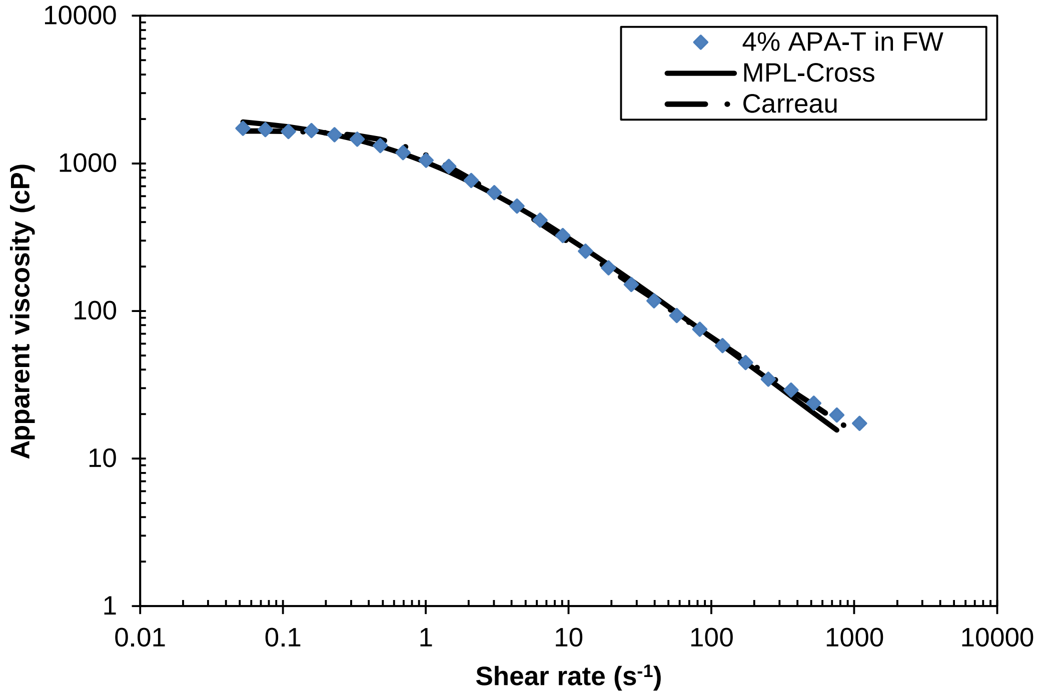

Figure 4.5: Model Prediction of Apparent Viscosity for 4% APA-T

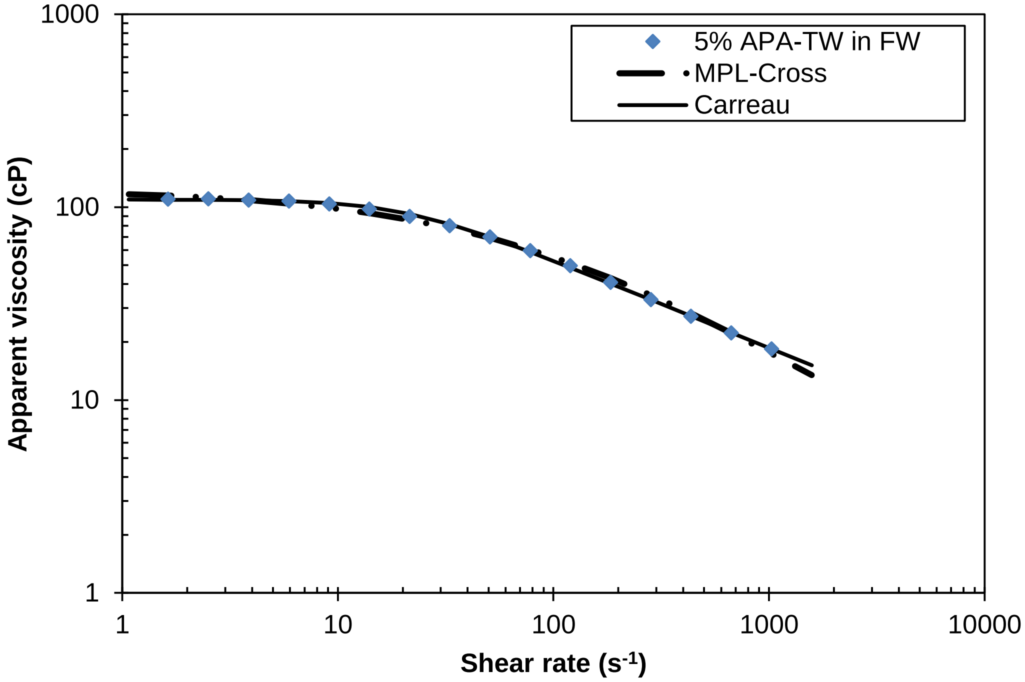

Figure 4.6: Model Prediction of Apparent Viscosity for 5% APA-TW

4.2.3 Temperature Dependence

Temperature has a significant effect on the rheological properties of surfactant solutions. Figures 4.7 and 4.8 show a comparison of apparent viscosity-shear rate curves at 100 °F, 125 °F, and 150 °F for 4% APA-T and 5% APA-TW. The effect of temperature is visible in both regions of the apparent viscosity-shear rate plot. The dependence of μ_o on temperature is shown in Fig. 4.9. It is evident that μ_o increases at 100 °F ($T_{\mu omax}$) and subsequently decreases at higher temperatures. The shear thinning region at 100 °F begins at lower shear rates. This implies an improved solution structure as indicated by an increase in μ_o. In the shear thinning region, the flow behavior index decreases with temperature between 75 °F and 100 °F. Conversely, at higher temperatures (> 100 °F), the apparent viscosity decreases with temperature, shear thinning begins at higher shear rates, and the flow behavior index increases with temperature.

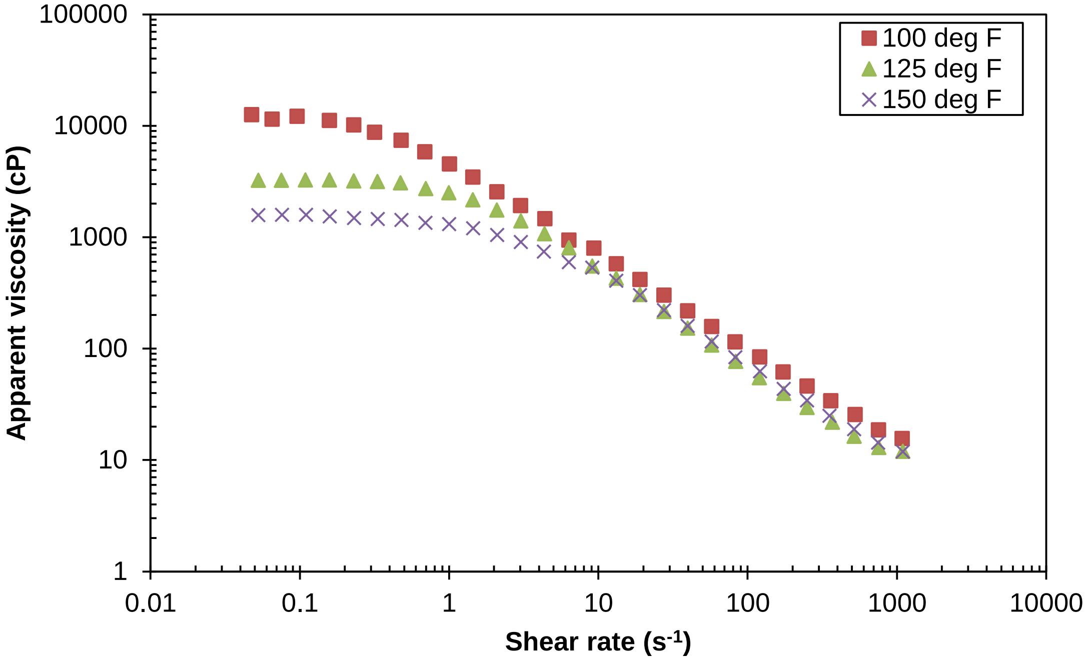

Figure 4.7: Temperature Dependence of Apparent Viscosity of 4% APA-T

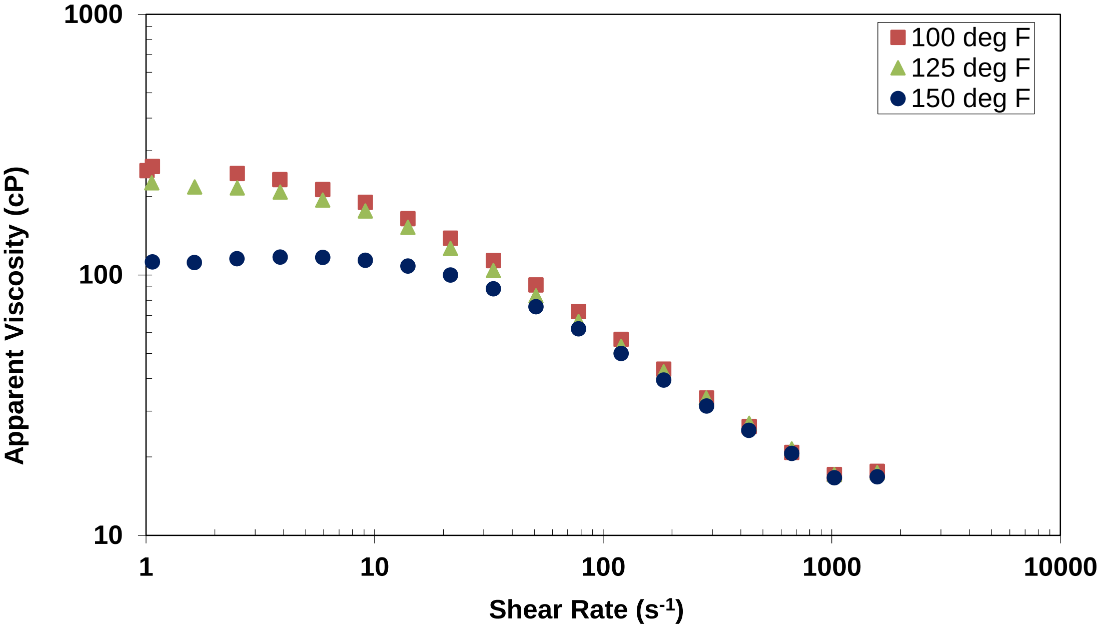

Figure 4.8: Temperature Dependence of Apparent Viscosity of 5% APA-TW

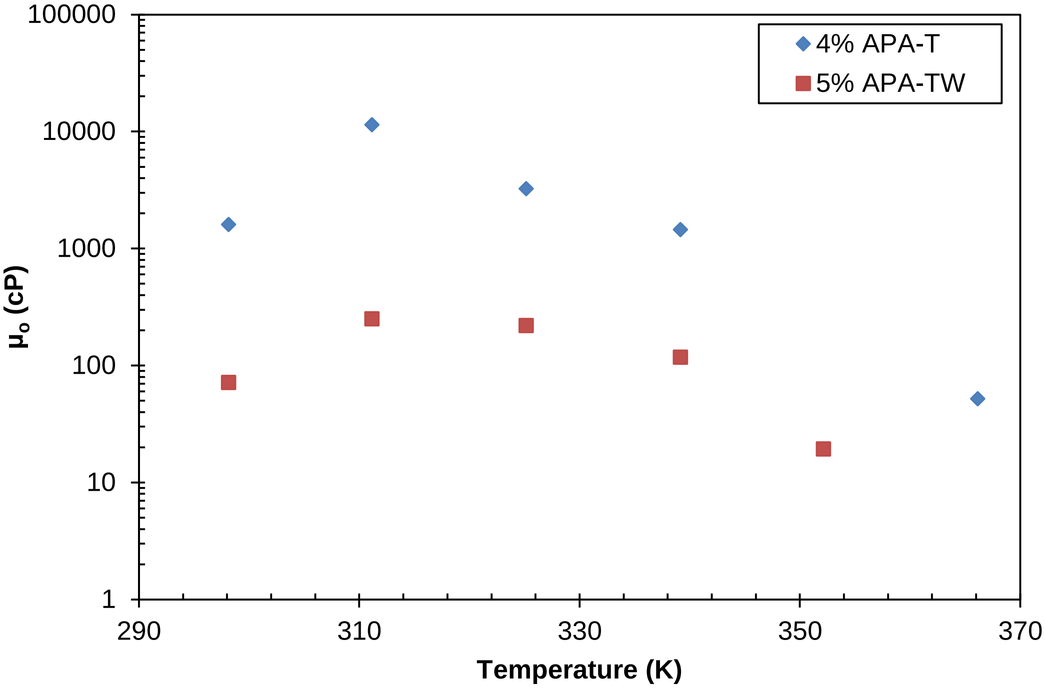

Figure 4.9: Temperature Dependence of Zero Shear Rate Viscosity of SB Fluids

The temperature dependence of viscosity can be qualitatively evaluated in terms of the area of head group and interfacial curvature of micellar aggregates. In the range of 75-100 °F, one-dimensional growth and entanglement occurs as the formation of end caps is unfavorable. Thus, an increase in μ_o is observed. At higher temperatures, the decrease in μ_o (> 100 °F) might be due to shorter micelles or dehydration of the tail group. First, increasing temperatures can result in a decrease in average micellar length. Shorter micelles imply lower entanglement density and lower μ_o values. As a consequence, higher shear rates are required to orient micelles in the direction of flow (Makhloufi and Cressely 1992). This is evident by a shift of the critical shear rate to higher values. Second, the dehydration of hydrophobic chains due to higher temperatures can lead to lower μ_o values.

This promotes a decrease in the average area of head groups (Acharya et al. 2006). It is possible that above $T_{\mu omax}$, micellar joints (intermicellar connections or branching) are formed, resulting in lower μ_o values.

An attempt was made in generating master curves for the 4% APA-T and 5% APA-TW solutions at various temperatures using the method of reduced variables. The concept behind this technique is to superimpose experimental data at different temperatures (or concentrations) onto a reference temperature (or concentration) using calculated vertical and horizontal shift factors. Master curves compare polydispersity and molecular weight using rheological data (Venkataiah and Mahadevan 1982). Both shift factors have physical meanings that are important from a steady shear characterization point of view. The horizontal shift factor is indicative of the shear intensity on the fluid, while the vertical shift factor correlates with the structural changes that occur under flow conditions (Venkataiah and Mahadevan 1982).

The vertical and horizontal shift factors for apparent viscosity and wall shear rate at the different temperatures are expressed as follows:

$$a_T = \frac{(\mu_o - \mu_s)_T}{(\mu_o - \mu_s)_{Tr}} \frac{Tr}{T} \tag{4.5a}$$

$$b_T = \frac{(\mu_o)_{Tr}}{(\mu_o)_T} \tag{4.5b}$$

where, T_r is the reference temperature, T is the temperature, μ_o is the zero shear viscosity, and μ_s is the solvent viscosity.

The resulting master curve (Figs. 4.10 and 4.11) is of the form of the Carreau model, expressed as:

$$\frac{\mu}{\mu_o} = [1 + (\alpha\dot{\gamma})^2]^{-N} \tag{4.6}$$

Fitting the above equation yields α = 0.532 s and N = 0.406 for 4% APA-T, while α = 0.0168 s and N = 0.693 for 5% APA-TW. The master curve covers five decades of shear rate.

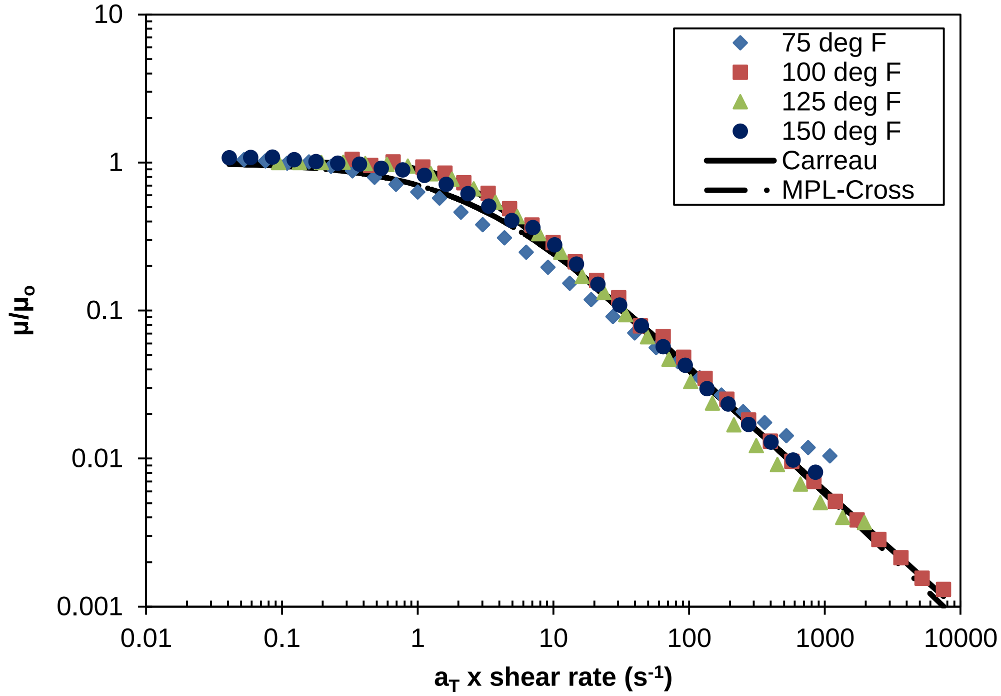

Figure 4.10: Reduced Apparent Viscosity Plot for 4% APA-T Solution at Various Temperatures

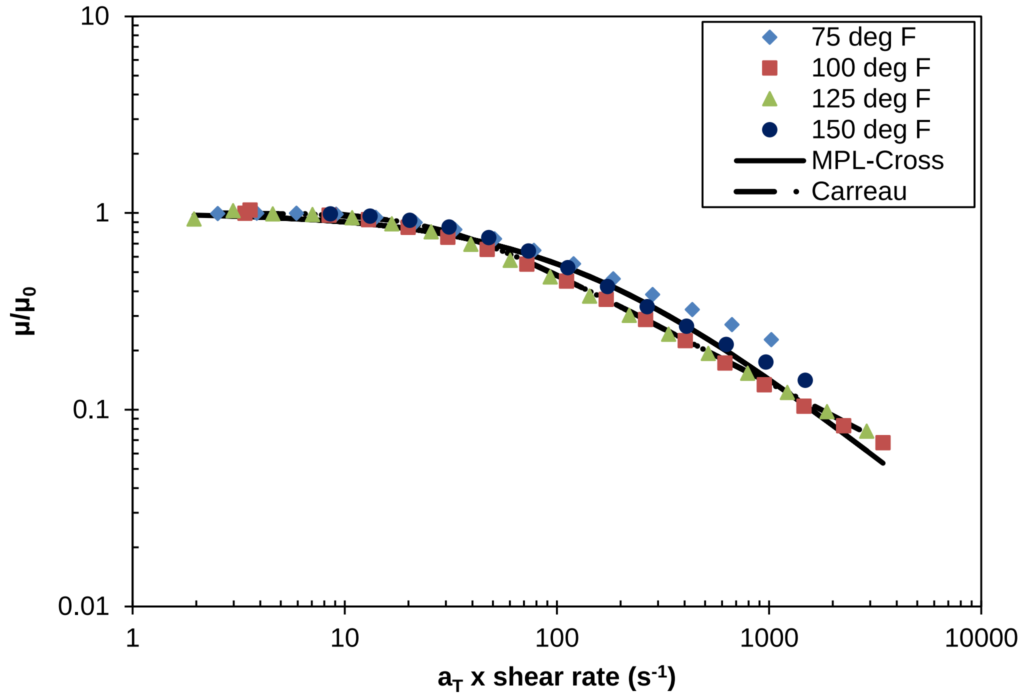

Figure 4.11: Reduced Apparent Viscosity Plot for 5% APA-TW Solution at Various Temperatures

4.2.4 Master Curves for Viscosity Data

Preceding sections presented and discussed the effects of concentration and temperature on the steady shear rheological behavior of test samples. It is evident that micellar interactions occur due to changes in both factors. As stated in Sect. 4.2.3, a convenient method of evaluating concentration and temperature effects on fluid structure is through the use of reduced variables. Here, a molecular approach is used. This molecular technique has been successfully applied to polymers as shown by Graessley (1974) and involves scaling the shear rate axis with the characteristic relaxation time (λ).

$$\lambda = \frac{(\mu_o - \mu_s)}{cRT} \tag{4.7}$$

The apparent viscosity–shear rate relationship can be expressed as follows:

$$\frac{\mu}{\mu_o} = f(\lambda, \dot{\gamma}) \tag{4.8}$$

Figures 4.12 and 4.13 show the reduced variables scaling approach on APA-T and APA-TW samples at 75 °F. The values of λ are reported in Table 4.2. Obvious concentration dependence is observed from these figures. Apart from the 1.5% APA-T sample, all other data points collapse to a single master curve, especially in the low shear rate region. Scaling of the APA-TW samples results in a single master curve for concentrations greater than 3%. At lower concentrations (1.5–3%), deviations can be observed. This suggests that the non-Newtonian character of surfactant samples is concentration dependent, as shown by an inability to generate suitable master curves. Thus, the molecular scaling approach using the characteristic time is not applicable at low surfactant concentrations.

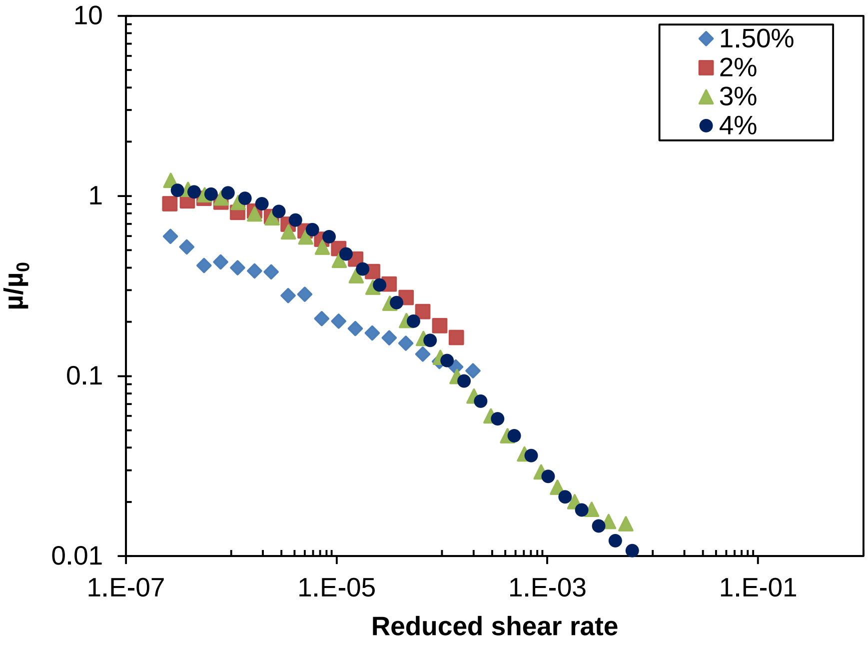

Figure 4.12: Master Plot of Apparent Viscosity for APA-T

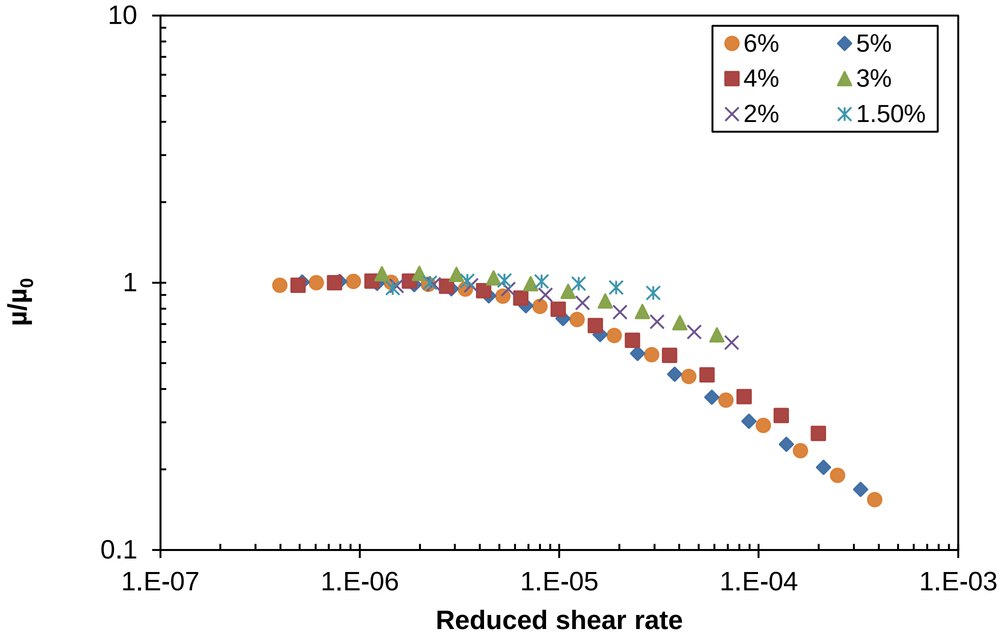

Figure 4.13: Master Plot of Apparent Viscosity for APA-TW

Table 4.2: Summary of Reduced Variable λ

	Concentration (%)	λ (s)
APA-T	4	5.88×10^{-6}
	3	5.07×10^{-6}
	2	7.96×10^{-7}
	1.5	5.49×10^{-7}
APA-TW	6	3.72×10^{-7}
	5	3.16×10^{-7}
	4	1.94×10^{-7}
	3	9.23×10^{-8}
	2	1.09×10^{-7}
	1.5	6.08×10^{-8}

4.3 Oscillatory Shear Properties

4.3.1 Concentration Dependence

Dynamic shear data at 75 °F are shown in Figs. 4.14 and 4.15. There is an increased frequency dependence of both moduli at lower surfactant concentration. From the data, there is an increase in $G'(\omega)$ and $G''(\omega)$, with concentration. This increase is attributed to greater network entanglements. Higher $G'(\omega)$ data reflect a more elastic response with better structure of micellar networks. Maxwell-type behavior is evident in the low frequency region. The solutions exhibit viscoelastic behavior, with $G'(\omega) > G''(\omega)$ at high frequencies and $G''(\omega) > G'(\omega)$ at lower frequencies. The appearance of a crossover point (ω_c), which depends on concentration, is indicative of structural changes. The inverse of the crossover frequency ($1/\omega_c$) is the relaxation time (τ_R) for the samples. The crossover point is a function of the degree of network entanglements within the solution. Higher crossover frequencies and lower relaxation times are indicative of less structure. It is evident that an increase in concentration shifts the crossover point to lower frequencies. With increasing concentration, the number density of micellar entanglements is increased. The greater number of entanglements requires longer relaxation times for stress relaxation to occur (Kamel 2008).

The Maxwell parameters for both surfactants are reported in Table 4.3. From this table, the scaling relationships for APA-T fluid follow a power-law expression with exponents different from theoretical values ($\tau_R \sim c^{1.25}$ and $G_o \sim c^{2.25}$). Lower exponent values for τ_R suggest the formation of micellar joints common to branched micelle networks (Acharya et al. 2006; Oelschlaeger and Willenbacher 2011). Higher values indicate the presence of long micelles. For APA-T fluid, an exponent of 2.85 (i.e., $\tau_R \sim c^{2.85}$) is determined, which implies the presence of long micelles in solution. Due to measurable viscoelasticity displayed by APA-TW at only two concentrations (5% and 6% v/v) in fresh water, the scaling relationship is based on the steady shear data.

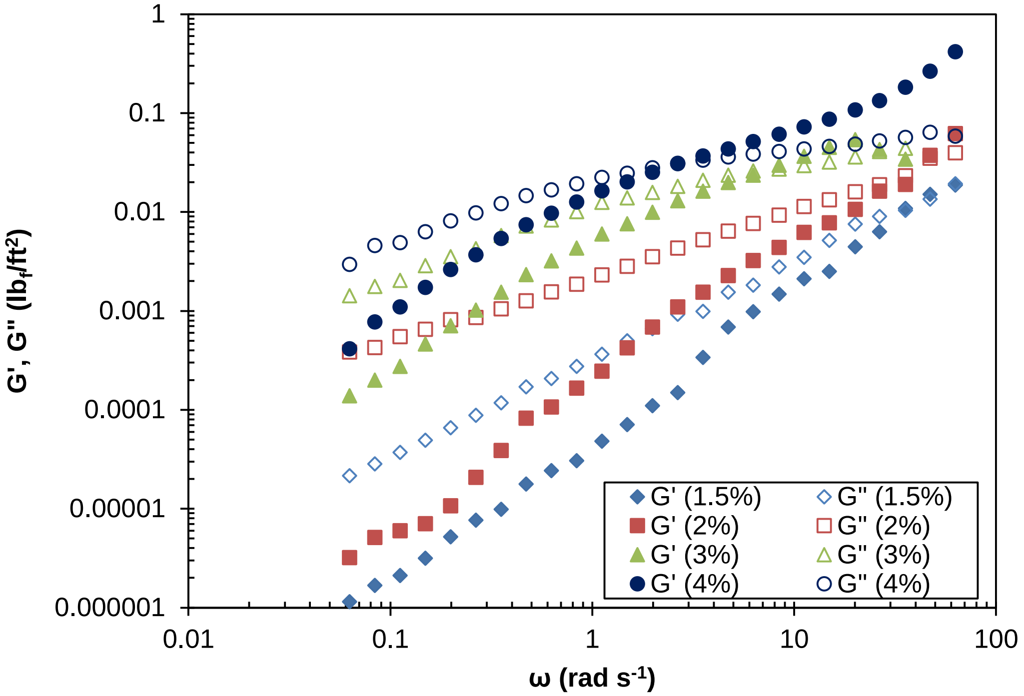

Figure 4.14: Storage and Loss Moduli vs. Frequency for APA-T

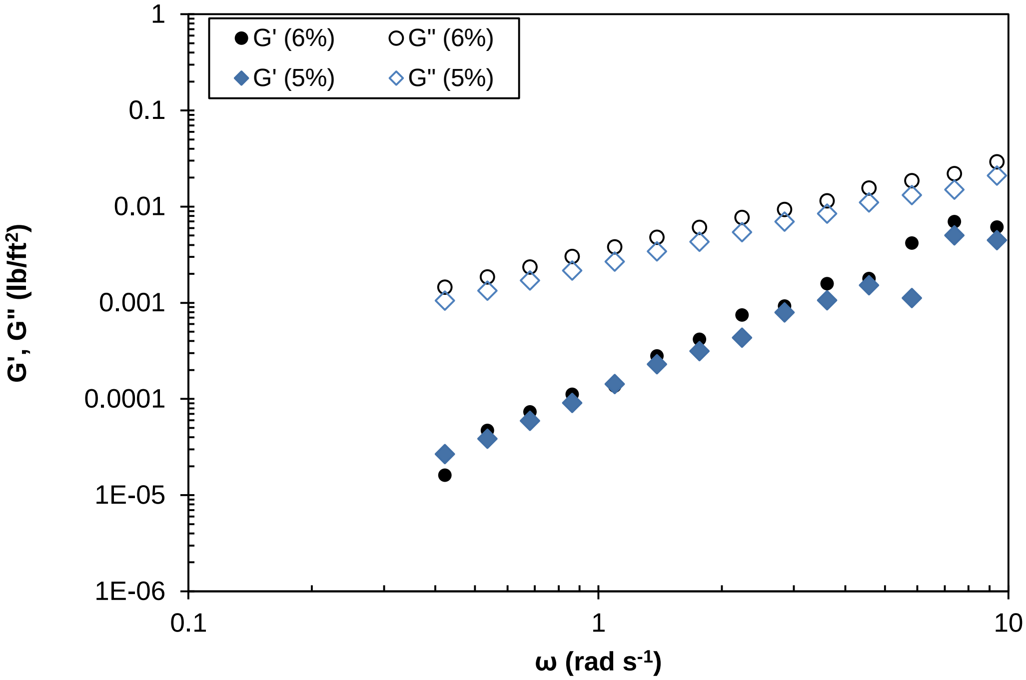

Figure 4.15: Storage and Loss Moduli vs. Frequency for APA-TW

Table 4.3: Maxwell Parameters for Test Solutions in Freshwater

	Concentration (%)	τ_R (s)	G_o (lb_f/ft^2)
APA-T	4	0.37	0.062
	3	0.133	0.054
	2	0.033	0.04
	1.5	0.025	0.03
APA-TW	6	0.035	0.135
	5	0.03	0.111

4.3.2 Temperature Dependence

Temperature effect on a 4% APA-T surfactant solution is shown in Fig. 4.16. Figure 4.16 shows data at 75 °F, 100 °F, and 125 °F; it is evident that the crossover point decreases from 2.7 rad/s at 75 °F to 0.65 rad/s at 100 °F. This implies an improved structural arrangement (more elasticity), which corresponds to an increase in μ_o from the steady shear data. Such a behavior is odd because it is expected that with temperature rise, there should be a reduction in viscosity (Rosen 2004). A valid explanation for the better structure is the growth of cylindrical micelles (Kalur et al. 2005; Raghavan and Kaler 2000) which are known to impart the viscoelastic characteristic displayed by surfactant solutions. Thus, a temperature of 100 °F is favorable for organized intermicellar interactions. Progressive loss of structure is visible at temperatures between 125 °F and 200 °F as marked by higher crossover frequencies (Fig. 4.17). In this temperature range, the disruption and hindrance of intermicellar interactions are dominant. Under high temperatures, it is possible that the lower moduli values are due to the formation of spherical micelles, manifested by a loss in viscoelasticity.

Figure 4.18 shows the variation of rheological parameters (τ_R, G_o) with temperature for the 4% APA-T solution. The τ_R exhibits a similar trend as μ_o with an initial increase between 75 °F and 100 °F followed by a decline at temperatures greater than 100 °F. The G_o remains constant with temperature between 75 °F and 100 °F. Above 100 °F, it increases with temperature. The implication of Fig. 4.18 is that there is a decrease in the disentanglement time (τ_R) as well as an increase in the volume fraction of entanglements (G_o). Hashizaki et al. (2009) attributed this to greater hydrophibicity of surfactant solutions. Higher temperatures decrease the interfacial curvature of the micelle assembly and cause dehydration of micelle chains. Dehydration tends to favor a more hydrophobic character and hence an increase in the volume fraction of entanglements.

To properly isolate the effect of temperature from other possible mechanisms affecting structural changes, the time (or frequency)-temperature superposition principle is used. The time-temperature superposition (TTS) is primarily used to examine the equivalency between frequency and temperature. This principle simply assumes equal temperature dependence on relaxation mechanisms (Povolo and Fontelos 1987) and assesses the similarity of responses at several temperatures (Raghavan and Kaler 2000). Three approaches were tested for reducing the 4% solution to a single master curve for $G'(\omega)$. The first approach uses the method of reduced variables with the horizontal shift factor from Eq. (4.5a). The second approach involves scaling the angular frequency with the relaxation time, which has been successfully applied to surfactant solutions (Arora 2004).

The third approach (Figs. 4.19 and 4.20) scales the moduli axis with the plateau modulus and the frequency axis with the relaxation time (Macias et al. 2011).

The result of the TTS shows an inability to reduce the data to a single curve. As a result, it may be stated that there are possible structural changes within the sample that are not solely due to temperature. Fluids displaying this sort of behavior are called "thermorheologically" complex fluids.

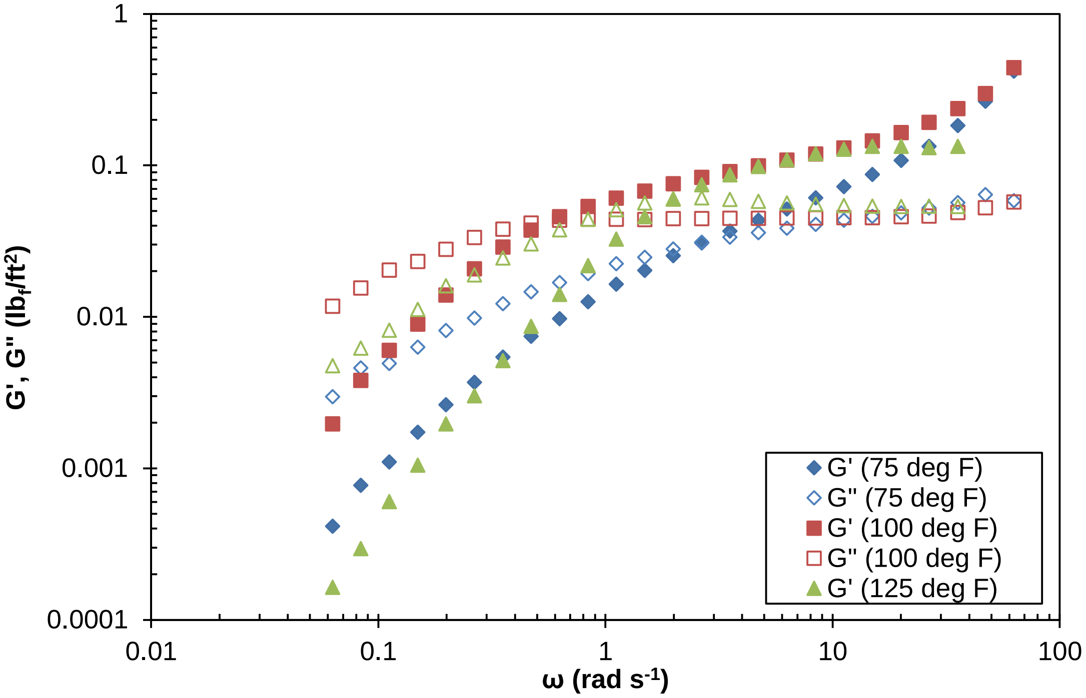

Figure 4.16: Temperature Dependence of Storage and Loss Moduli for 4% APA-T (75–125 °F)

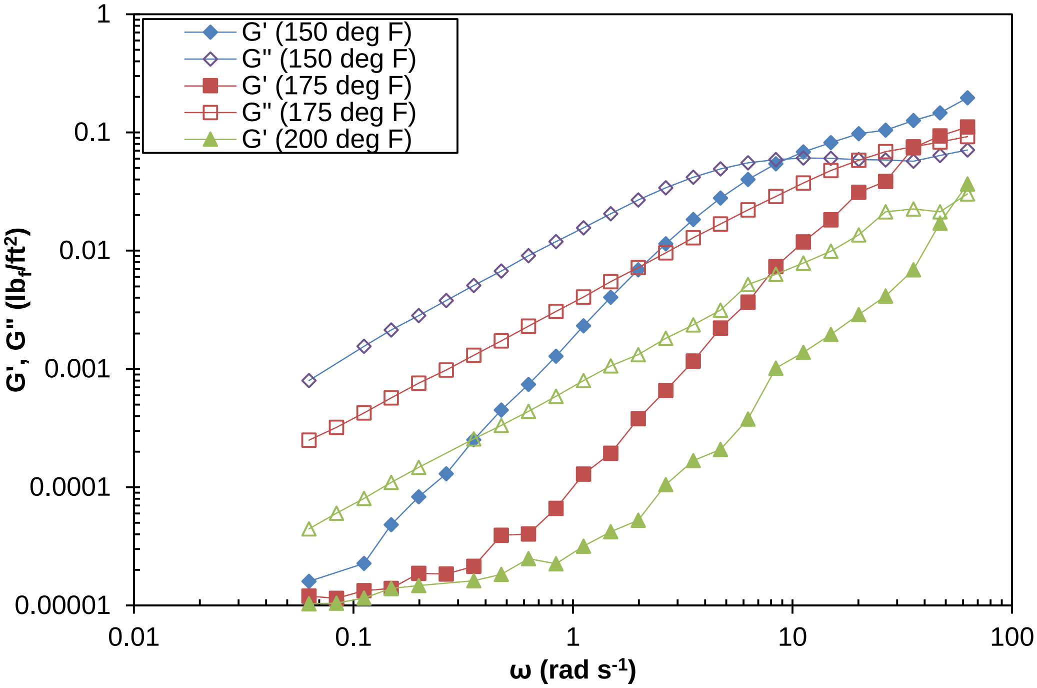

Figure 4.17: Temperature Dependence of Storage and Loss Moduli for 4% APA-T (150–200 °F)

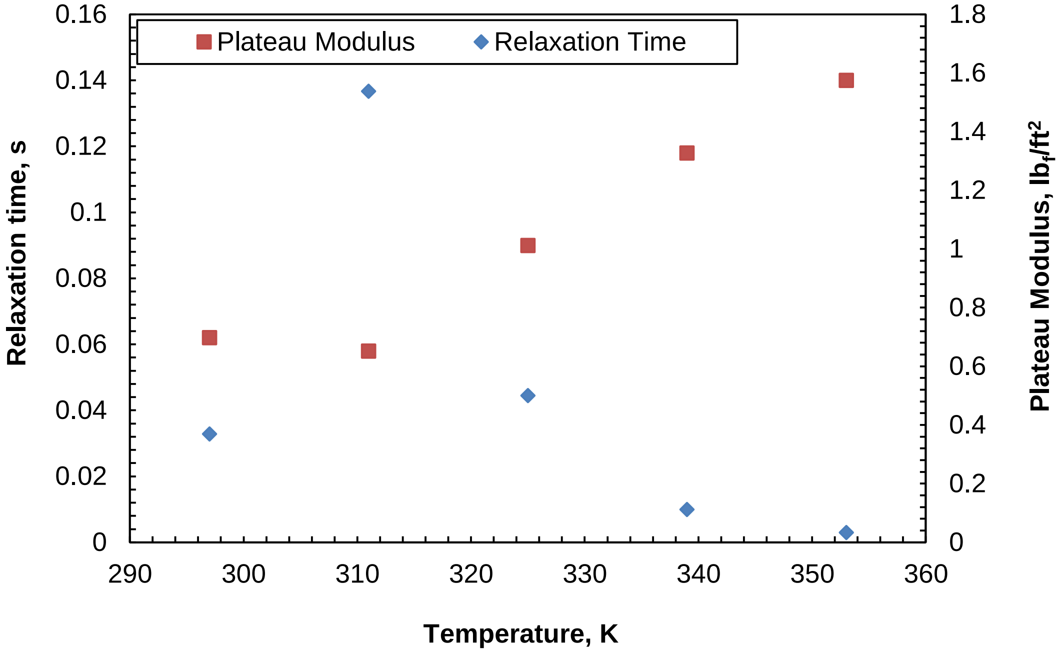

Figure 4.18: Maxwell Parameters vs. Temperature for 4% APA-T

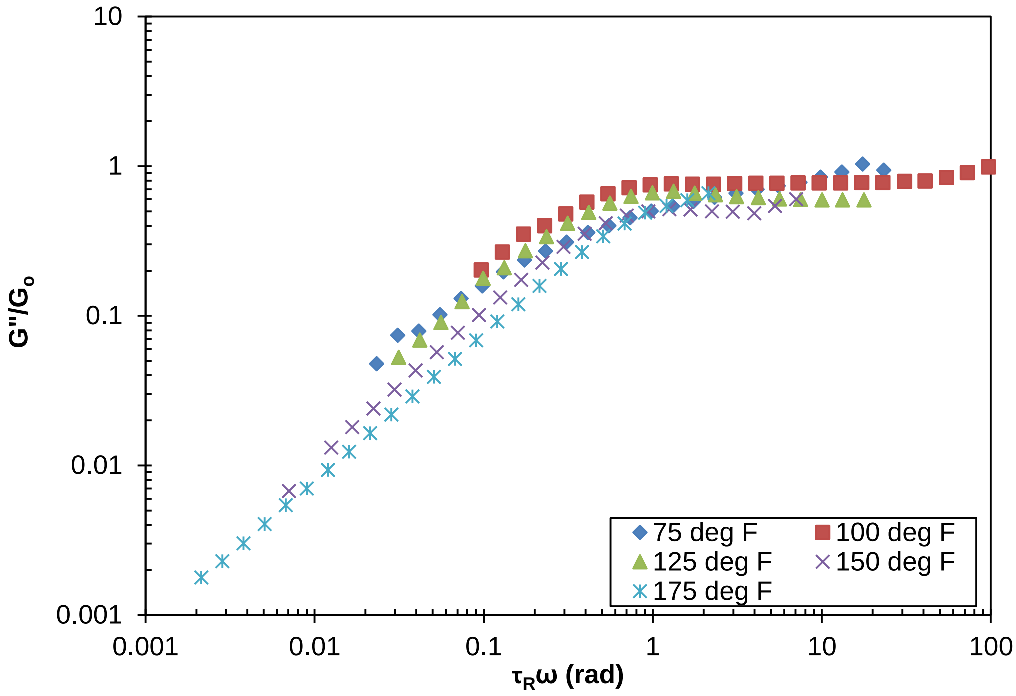

Figure 4.19: Reduced Loss Modulus at Various Temperatures

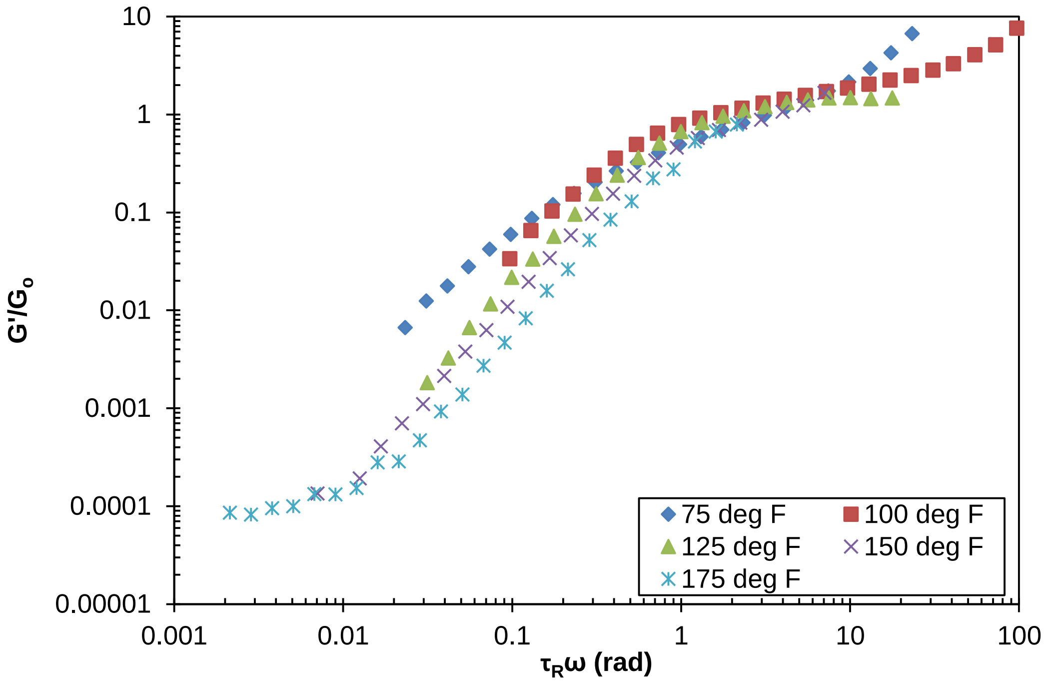

Figure 4.20: Reduced Storage Modulus at Various Temperatures

With these findings, it obvious that structural changes in WLMs occur with increasing temperature. The largest value of τ_R at 100 °F suggests the presence of long micelles as stress relaxation is reduced. At higher temperatures (> 100 °F), the presence of shorter micelle length (Sect. 4.2.3) is unlikely because the mesh and entanglement network density increases with temperature. This is confirmed by an increase in G_o with temperature. An explanation for this observation can be attributed to branching or formation of joints in micellar network. These joints slide along the micelle length, resulting in faster stress relaxation (Acharya et al. 2006).

4.4 Summary

The rheological behavior of surfactant solutions (Aromox® APA-T and APA-TW) at different concentrations was investigated using steady shear and dynamic oscillatory testing. The influence of concentration and temperature on rheological properties is reported. The zero shear rate viscosity increased with concentration, as expected. An increase in concentration promotes formation and growth of rod-like micelles. Temperature had a significant effect on the rheological character of test solutions. The zero shear rate viscosity increased with temperature between 75 °F and 100 °F. Correspondingly, the relaxation time increased with temperature within the same range. This observation can be attributed to the growth and entangling of worm-like micelles. At higher temperatures, the zero shear rate viscosity and relaxation time decreased with temperature. The plateau modulus increased with temperature.

Scaling relationships with concentration are compared to theoretical values. For APA-T solutions, the higher exponents for zero shear rate and relaxation time with concentration indicate the presence of long micelles. These longer micelles are responsible for higher zero shear rate viscosity and greater viscoelastic response. APA-TW solutions, on the other hand, contained branched micelles because scaling exponents are lower than theoretical values.

Master curves are generated for 4% APA-T and 5% APA-TW steady shear data at different temperatures. However, all attempts to generate master curves for viscoelastic data failed due to the thermorheologically complex nature of these fluids. Molecular scaling using the characteristic time for data at different concentrations proved unsuccessful because the non-Newtonian character of surfactant solutions prevented the collapse of data to a single curve.

Chapter 5

EFFECT OF IONIC STRENGTH ON THE RHEOLOGICAL BEHAVIOR OF SURFACTANT SOLUTIONS

5.1 Introduction

Several factors are known to influence the rheological properties of surfactant solutions. Some of these factors are concentration, temperature, and electrolytes. Electrolytes are known to alter the physicochemical properties of surfactants (Myers 2005; Wang 1993). Organic and inorganic salts act as thickening agents that promote formation of wormlike micelles (Oelschlaeger and Willenbacher 2011; Wang 1993). Favorable interactions can be the result of screening of electrostatic repulsions or the formation of hydrogen bonds with water, as in the case of water structure promoters. It is well documented that salts can reduce the CMC, thereby inducing structural changes in surfactant solutions. In some instances, depending on the nature and type of counterion, salts can induce and regulate viscoelasticity in surfactants solutions (Lu et al. 2011).

This chapter studies the rheological behavior of surfactant solutions, at concentrations used in oilfield operations, in the presence of inorganic monovalent and divalent salts. The salts used here are 2% KCl and 2% $CaCl_2$. Comparisons are made between salt and freshwater solutions in terms of micellar growth and degree of entanglements. Microstructural changes are investigated and analyzed using steady shear as well as dynamic oscillatory measurements.

5.2 Steady Shear Behavior

The apparent viscosity–shear rate curves are shown in Figs. 5.1 and 5.2 for several concentrations of the two surfactant solutions containing 2% KCl. The steady shear behavior of solutions containing 2% KCl is qualitatively similar to solutions in freshwater. However, the addition of salt alters the magnitude of viscosity. At low shear rates, a clear Newtonian plateau is observed. Above a particular shear rate, transition to shear thinning behavior can be seen in both figures. The apparent viscosity–shear rate data can be represented by the Carreau (1972) and MPL-Cross models (Figs. 5.3 and 5.4). Parameters (μ_o, t, and N) for the Carreau model are reported in Table 5.1.

Marked differences in the magnitude of rheological parameters suggest changes in micellar structure with salt addition. The μ_o at all concentrations is greater in magnitude than at equivalent concentrations in freshwater (see Tables 4.1 and 5.1). For example, μ_o for the 4% APA-T solution is three times greater in 2% KCl than in freshwater. Similarly, μ_o for the 5% APA-TW sample is two times greater in 2% KCl than in freshwater. Similar trends were observed at all other concentrations. The increased flow resistance at low shear rates can be attributed to electrostatic screening among head groups. Electrostatic screening promotes growth, aggregation, and entanglement of micelles.

Another effect of salts is the faster transition from the lower Newtonian plateau to the shear thinning region (i.e., lower critical shear rate). The critical shear rate is a function of salt and polymer concentrations. For the 4% APA-T solution, the critical shear rate is reduced from 0.676 s^{-1} in freshwater to 0.476 s^{-1} in 2% KCl. This effect is more pronounced with the APA-TW samples. For a concentration of 5% APA-TW, the critical shear rate is 21.3 s^{-1} in freshwater but 8.41 s^{-1} in 2% KCl. From Tables 4.1 and 5.1, it is obvious that salts induce greater shear thinning (increase slope of apparent viscosity–shear rate curve) than surfactant solutions do in freshwater.

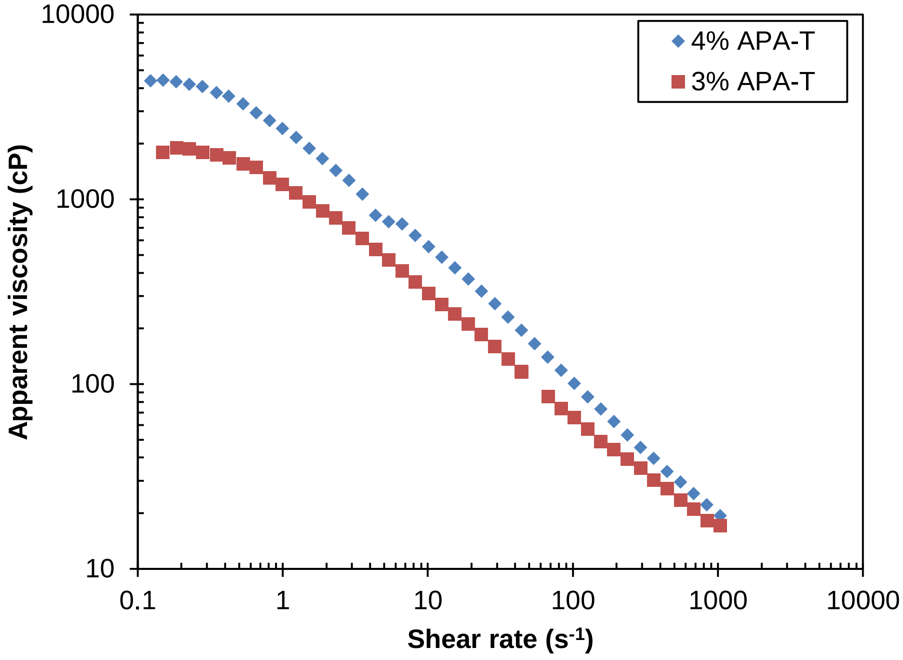

Figure 5.1: Apparent Viscosity of 3 and 4% APA-T in 2% KCl

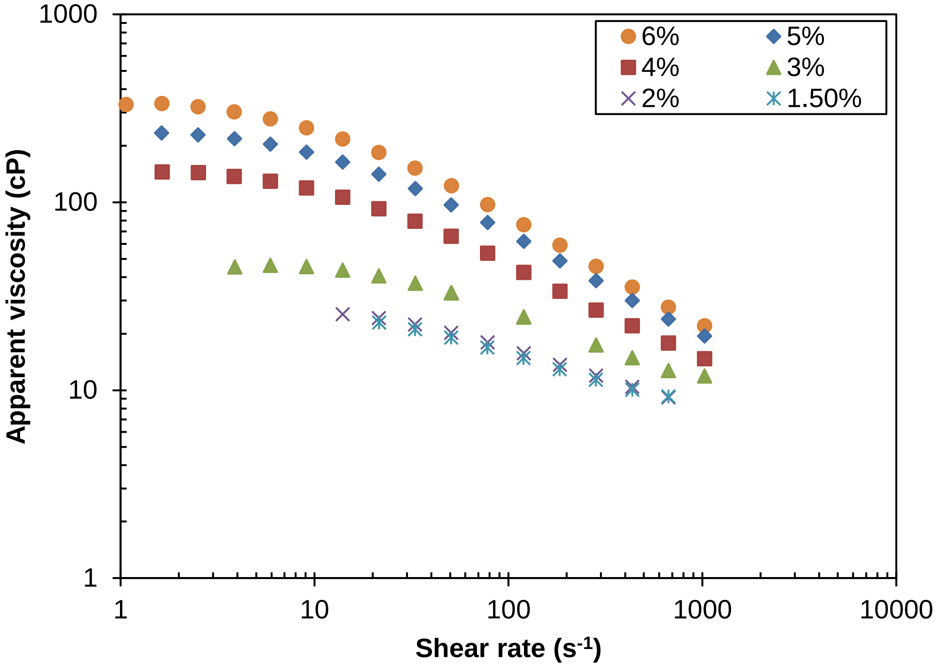

Figure 5.2: Apparent Viscosity of APA-TW in 2% KCl

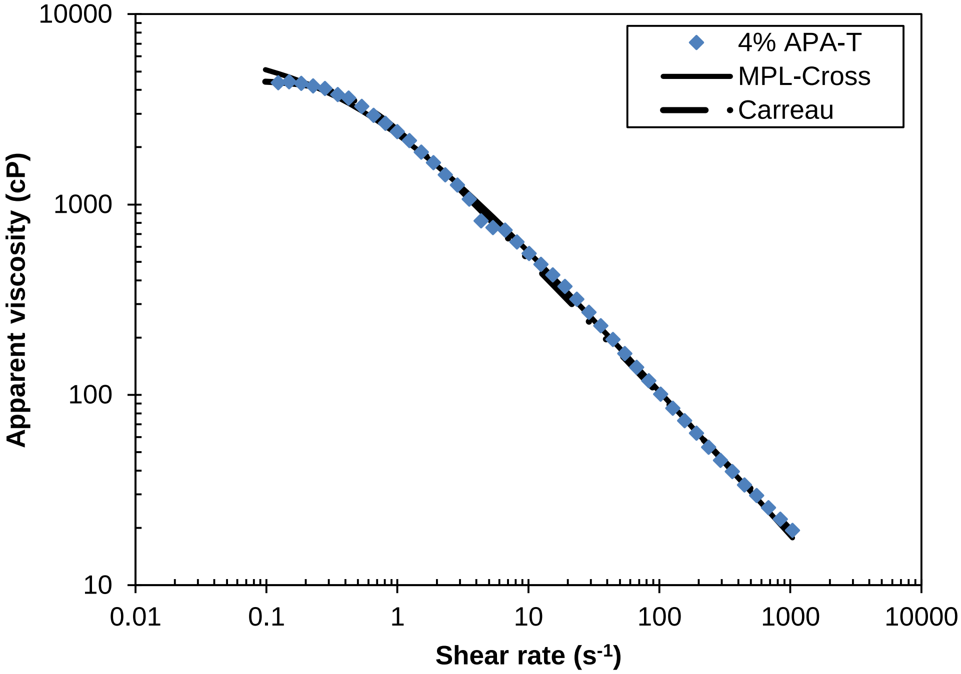

Figure 5.3: Model Predictions for 4% APA-T in 2% KCl

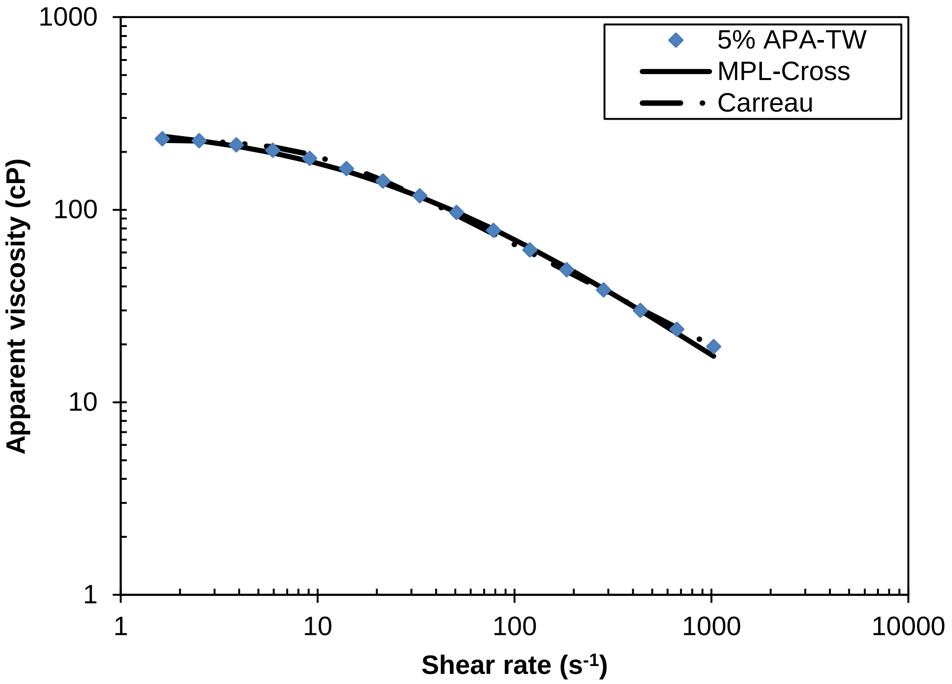

Figure 5.4: Model Predictions for 5% APA-TW in 2% KCl

Table 5.1: Carreau Model Parameters for Test Solutions in 2% KCl

	Concentration (%)	**μ_o (cP)**	**t (s)**	**N**
APA-T	4	4482	0.475	0.36
	3	1755	0.704	0.32
APA-TW	6	330	0.119	0.281
	5	232	0.109	0.262
	4	142	0.101	0.246
	3	46	0.044	0.191
	2	26	0.0411	0.162
	1.5	25	0.049	0.152

5.3 Dynamic Oscillatory Shear Behavior

The mechanical spectra data [G'(ω) and G"(ω)] are important for the complete characterization of surfactant solutions. Generally, the G'(ω) obtained from small strain oscillatory experiments is used to make inferences on the structure of fluids (Rochefort 1986; Rochefort and Middleman 1987). Dynamic oscillatory experiments were performed with the Bohlin CS-50 rheometer to measure the G'(ω) and G"(ω). The same concentrations to those of the steady shear characterization study are considered. Furthermore, the influence of salt (2% KCl) on the micellar structure is studied and compared with solutions in freshwater (FW). Salts induce viscoelasticity at lower surfactant concentrations. For instance, strong viscoelastic character is exhibited by APA-TW samples at a concentration of 4% in salt as opposed to 5% in freshwater.

The dynamic oscillatory properties of APA-T and APA-TW samples are shown in Figs. 5.5 through 5.10. The data in 2% KCl are qualitatively similar to those of freshwater samples. However, differences in the magnitude of G' and G" are observed. Addition of salt increases the magnitude of the storage and loss moduli. Figure 5.5 shows the moduli data for 4% APA-T solution as a function of angular frequency. In the presence of salt, there is an increase in G'(ω) (~ 400%) over the frequency range studied. This suggests that in solutions containing 2% KCl, the surfactant micellar structure is improved. Similarly, an increase is recorded in G"(ω) (~ 200%) over the entire frequency range studied. A trend similar to that of 4% APA-T is observed for the 3% solution (Fig. 5.6). At low frequencies, G"(ω) > G'(ω) in FW and 2% KCl. Both moduli are also found to be dependent on frequency. With the addition of 2% KCl, higher G'(ω) (~280%) and G"(ω) (~200%) are recorded.

The data for 2% and 1.5% APA-T solutions indicate less structure and an increased frequency dependence of G'(ω) and G"(ω) with G'(ω) < G"(ω) at low frequencies (Figs. 5.7 and 5.8). Crossover points at high angular frequencies indicate structure loss as faster stress relaxation processes are dominant. In other words, an increase in the magnitude of the crossover frequency leads to greater frequency dependence and structure loss (Rochefort and Middleman 1987). An addition of 2% KCl increases the magnitude of G'(ω) as compared to the equivalent concentrations in freshwater.

Similar observations are made for 5% APA-TW in terms of higher G"(ω) and G'(ω) in the presence of 2% KCl (see Figs. 5.9 and 5.10). Important inferences can be drawn from the foregoing discussion. At higher concentrations, there is less frequency dependence and overall better fluid structure as the crossover frequency is shifted to lower frequencies. At lower concentrations in the frequency regime studied, greater frequency dependence and crossover points at higher frequencies indicate decreased structure. Irrespective of concentration, solutions displayed greater viscoelasticity (higher magnitude of moduli data) and improved structure with a decrease in the crossover frequency with 2% KCl in solution.

The relaxation times are determined from oscillatory measurements as the inverse of ω_c for APA-T samples and from a fit of mechanical spectra data using Maxwell relations for APA-TW samples. Table 5.2 shows the variation of τ_R and G_o at different concentrations for APA-T and APA-TW. Comparatively, the magnitude of τ_R is higher in salt than in freshwater solutions (see Tables 4.3 and 5.2). The dependence of τ_R on concentration corresponds to trends observed with μ_o. An increasing trend of τ_R with concentration suggests micellar growth (Oelschlaeger and Willenbacher 2011).

For APA-T samples, G_o is determined from oscillatory measurements as 2 times G* (the modulus at which G' = G''). Whereas, G_o for APA-TW samples is determined from fitting Maxwell relations to viscoelastic data. The plateau modulus increased with concentration corresponding to observed trends with μ_o and τ_R. This can be interpreted as greater micellar interactions, which result in an increased number of entanglements, attributed to linear micellar growth (Oelschlaeger and Willenbacher 2011).

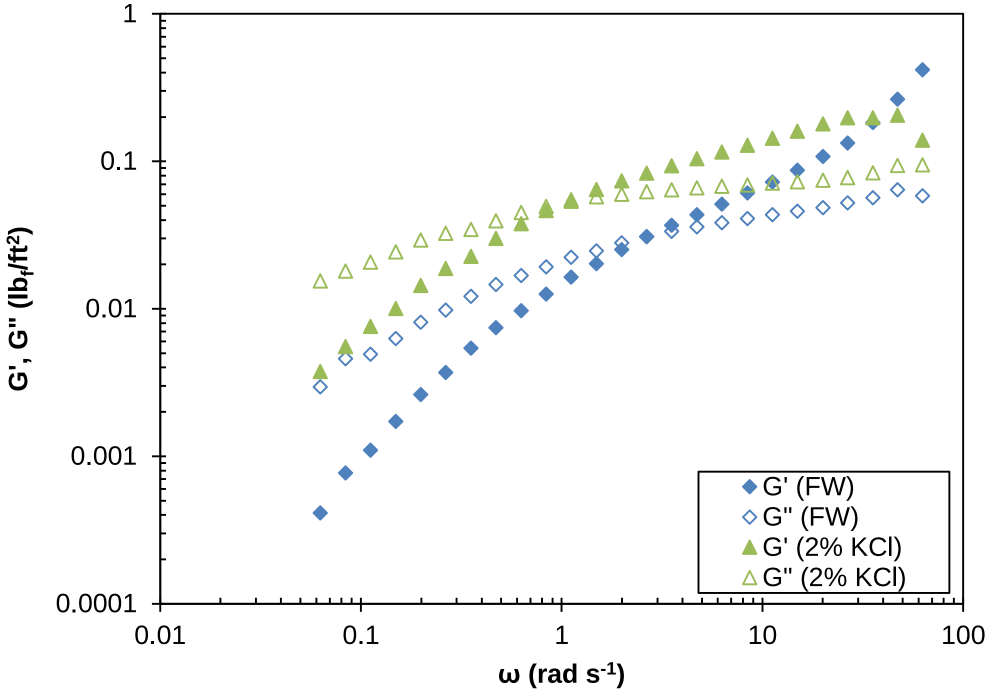

Figure 5.5: Storage and Loss Moduli for 4% APA-T in Freshwater and 2% KCl

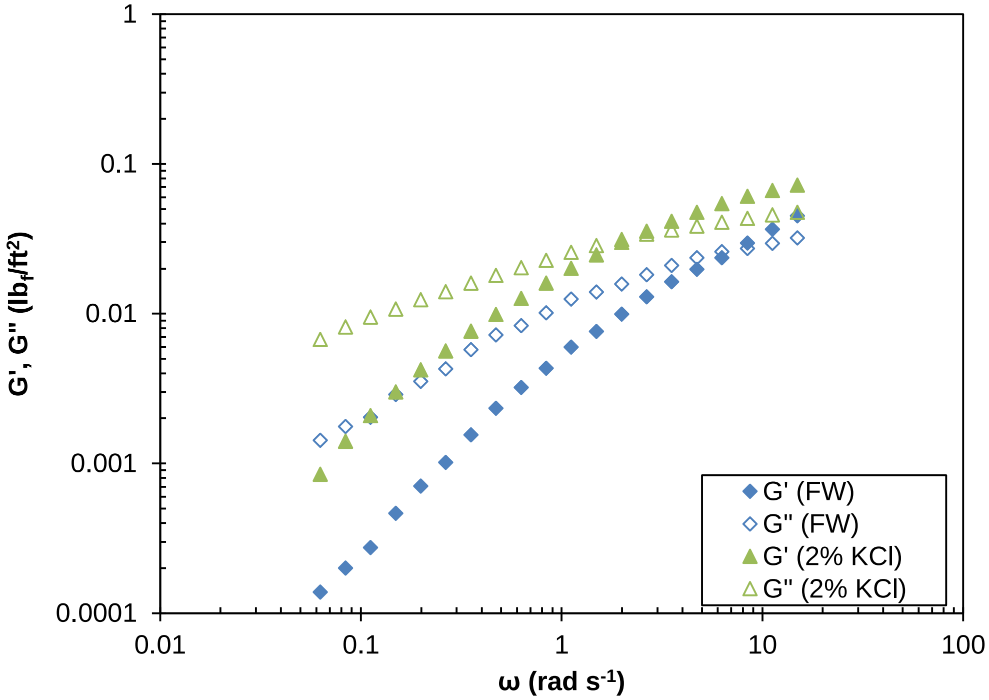

Figure 5.6: Storage and Loss Moduli for 3% APA-T in Freshwater and 2% KCl

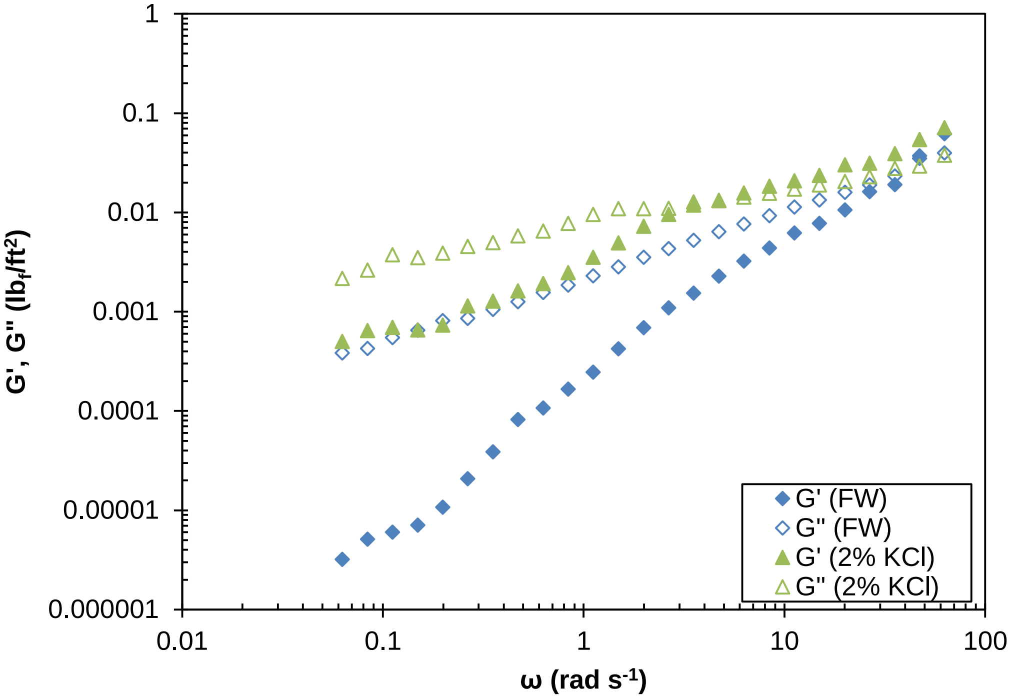

Figure 5.7: Storage and Loss Moduli for 2% APA-T in Freshwater and 2% KCl

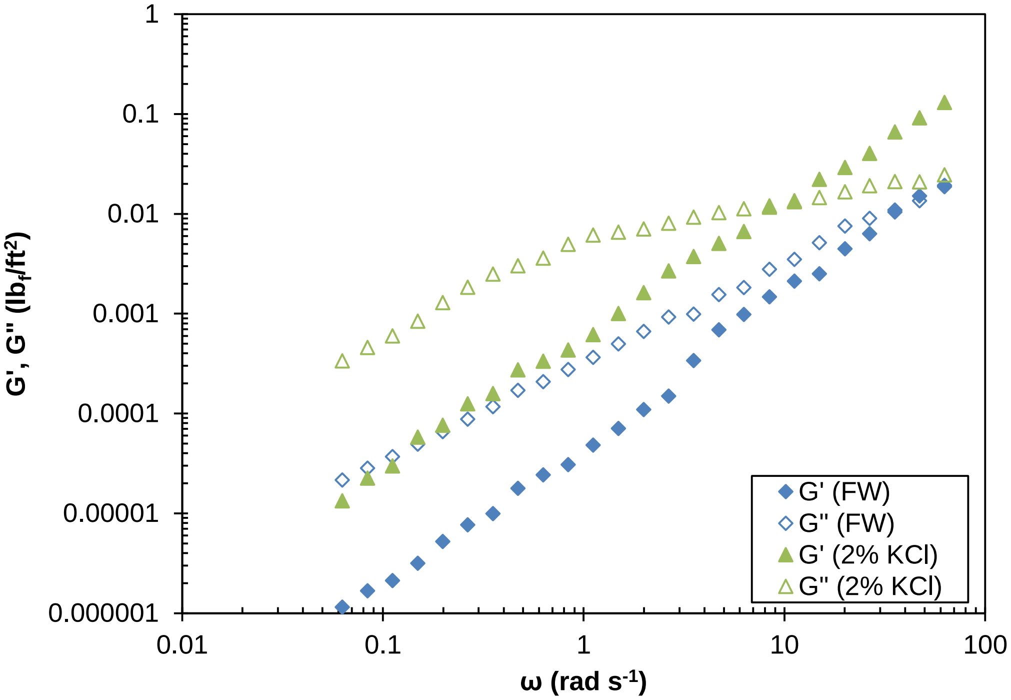

Figure 5.8: Storage and Loss Moduli for 1.5% APA-T in Freshwater and 2% KCl

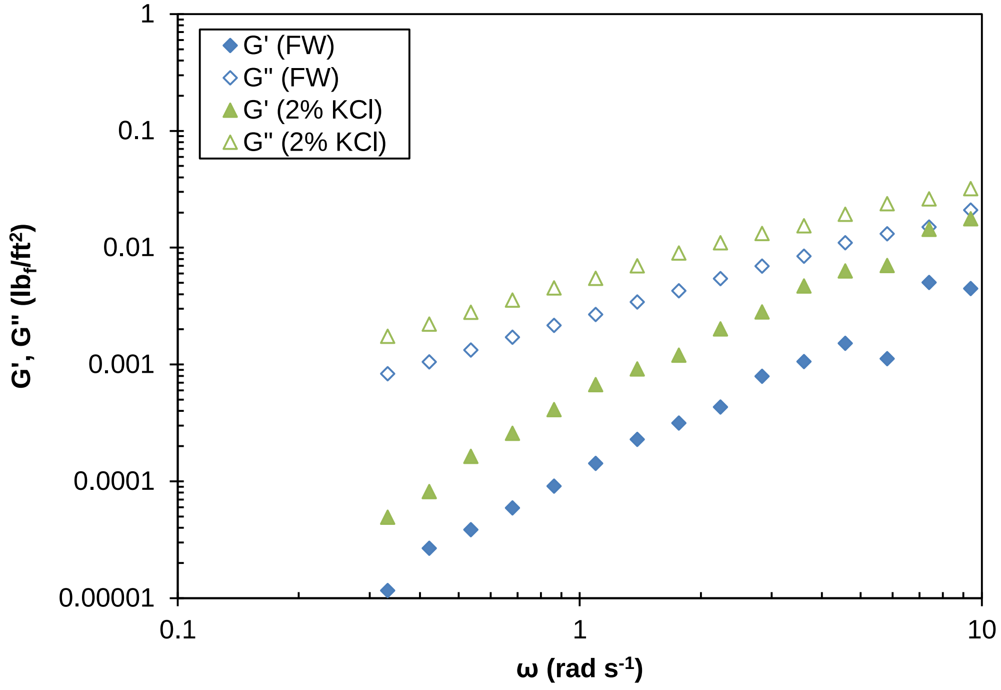

Figure 5.9: Storage and Loss Moduli for 5% APA-TW in Freshwater and 2% KCl

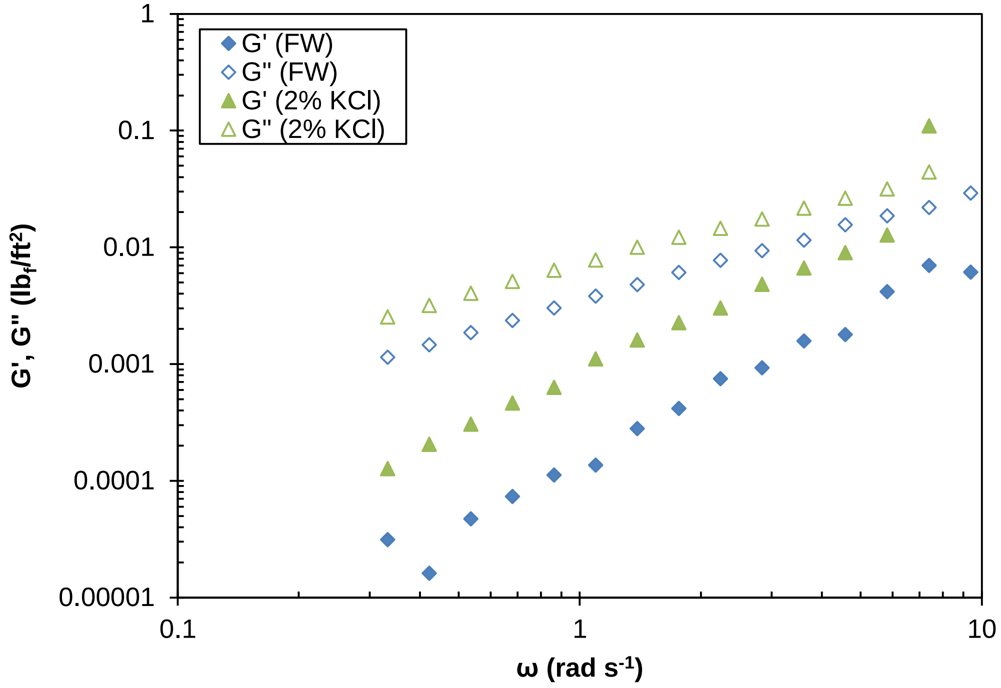

Figure 5.10: Storage and Loss Moduli for 6% APA-TW in Freshwater and 2% KCl

Table 5.2: Maxwell Parameters for Test Solutions in 2% KCl

	Concentration (%)	τ_R (s)	$G_o(lb_f/ft^2)$
APA-T	4	0.8	0.09
	3	0.6	0.066
	2	0.175	0.05
	1.5	0.133	0.041
APA-TW	6	0.103	0.068
	5	0.084	0.058
	4	0.082	0.038

5.4 Effect of Divalent Salt

In the preceding section, the effect of a monovalent salt (2% KCl) was shown to drastically alter the rheological properties of surfactant solutions. The zero shear rate viscosity, relaxation time, and plateau modulus were higher in 2% KCl than in freshwater. Next, the effect of a divalent salt (2% $CaCl_2$) is tested. The steady shear curve (Fig. 5.11) is qualitatively similar to solutions in freshwater and 2% KCl. A Newtonian plateau is observed at low shear rates, while shear thinning is evident at higher shear rates. Figure 5.12 shows μ_o as a function of concentration in 2% $CaCl_2$. The magnitude of the zero shear rate viscosity is in the following order; μ_o (2% KCl) > μ_o (2% $CaCl_2$) > μ_o (freshwater). In comparison to solutions in 2% KCl, the transition from low Newtonian plateau to the shear thinning region is shifted to higher shear rates (delayed shear thinning) with 2% $CaCl_2$ in solution.

Normalized zero shear rate viscosity ($\mu_n = \mu_{o(salt)} / \mu_{o(freshwater)}$) provides a means of comparing solutions in salt to those in fresh water. KCl (K^+ radius) which has an ion hydration radius of 2.32 Å promotes a viscosity increase greater than $CaCl_2$ (Ca^{2+}) with an ion hydration radius of 3.21 Å. This claim is supported by comparing the normalized viscosity of 5% APA-TW solution in KCl ($\mu_n = 2.1$) and $CaCl_2$ ($\mu_n = 1.1$). Thus, it can be stated that a greater concentration of an inorganic divalent salt is required to give the same μ_o as a monovalent salt. The critical shear rate is higher in $CaCl_2$ than in KCl (see Table 5.3). These observations imply that the smaller the hydration radius, the more effective the salt in promoting micelle growth (Wang, 1993). Micelle growth is favored by screening electrostatic repulsions or interference with water structure (Myers 2005; Wang 1993). The ability to interfere with water molecules has led to the characterization of salts/electrolytes as either water structure enhancers or water structure breakers. Charge screening is common to ionic surfactant solutions. In nonionic and zwitterionic solutions, a combination of electrostatic charge screening and water structure alteration (especially above a certain salt concentration) is responsible for micellar structural changes (Myers 2005).

The dynamic properties for all three base fluids are shown in Fig. 5.13. The fitted Maxwell parameters (relaxation time and plateau modulus) for the test solution in 2% $CaCl_2$ are 0.044 s and 0.058 lb_f/ft^2 for 5% APA-TW. Similarly, the relaxation time and plateau modulus are 0.049 s and 0.074 lb_f/ft^2 for 6% APA-TW in 2% $CaCl_2$. The magnitudes of G' and G'' are greater in 2% $CaCl_2$ than in freshwater. On the other hand, both moduli are lower in 2% $CaCl_2$ than in 2% KCl. The values of relaxation time and plateau modulus for 2% $CaCl_2$ lie between those of freshwater and 2% KCl. This implies a slight improvement in structure in 2% $CaCl_2$ over that of freshwater. All samples have better structure in 2% KCl than in any other base fluid.

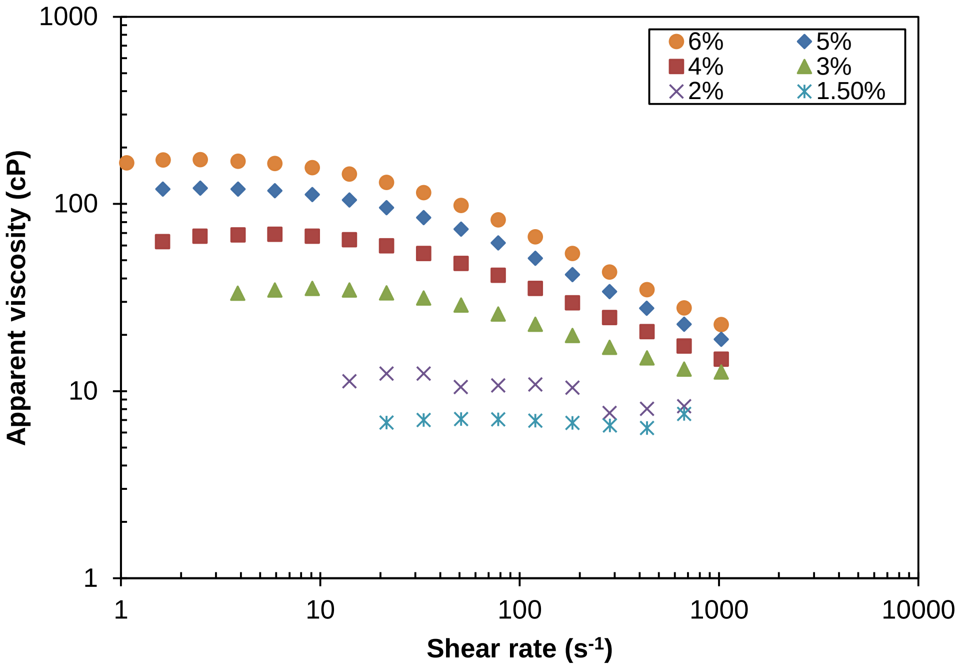

Figure 5.11: Apparent Viscosity for APA-TW in 2% $CaCl_2$

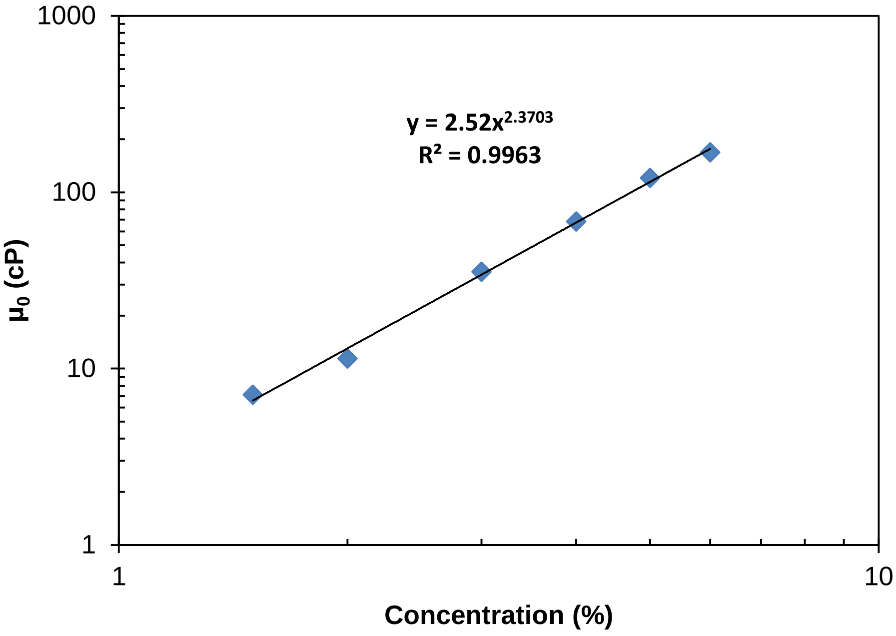

Figure 5.12: Concentration Dependence of Zero Shear Rate Viscosity

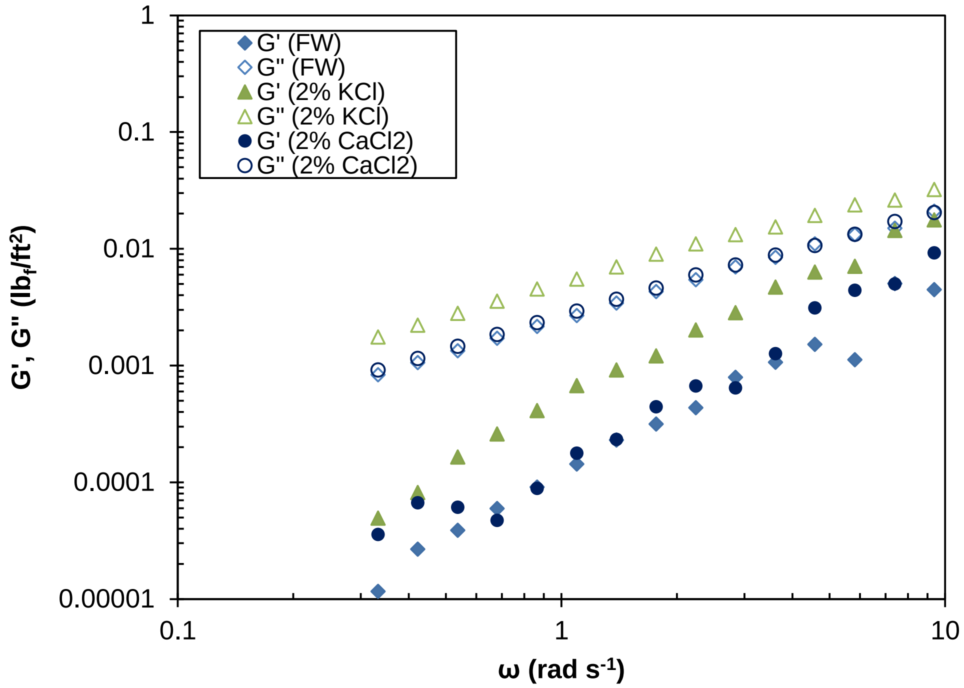

Figure 5.13: Storage and Loss Moduli for 5% APA-TW in Freshwater, 2% KCl and 2% $CaCl_2$

Table 5.3: Comparison of Critical Shear Rate in Different Base Fluids

	Concentration (%)	Critical shear rate (s^{-1})		
		Freshwater	2% $CaCl_2$	2% KCl
APA-TW	6	21.3	18.3	8.4
	5	20.5	17.6	9.2
	4	33.1	23.8	9.9
	3	71.4	32.5	22.9

5.5 Summary

This chapter investigated the effect of added salts on the steady and dynamic properties. Salts are shown to increase the zero shear rate viscosity. Solutions of APA-T and APA-TW are observed to be more viscoelastic in salts than in freshwater. The crossover frequency is observed to decrease with salts in solution, indicating better fluid structure. The formation and growth of rod-like micelles as well as greater intermicellar interactions are favored in the presence of salts.

The valency and size of salt counterion on rheological properties are reported. A monovalent salt, 2% KCl, is observed to be more effective at promoting favorable micellar interactions than a divalent salt (2% $CaCl_2$). The increase in rheological parameters with the addition of both salts depends on the size of salt counterion, with potassium (smallest ion) producing the highest increase in viscosity.

Chapter 6

THEORETICAL STUDY OF LAMINAR PIPE FLOW OF NON-NEWTONIAN FLUIDS

6.1 Introduction

Equations for flow characteristics of Newtonian fluids are widely available and accepted for accurate prediction of pressure loss across a pipe section in all flow regimes. Analytical equations for Newtonian fluid hydraulics can be found in literature. The same cannot be stated for non-Newtonian fluids in terms of a unique set of flow equations. This is due to the complex nature of non-Newtonian fluids as well as non-Newtonian flows.

The linear relationship between shear stress and shear rate for Newtonian fluids cannot generally be applied to non-Newtonian fluids. As a consequence, several time-independent and time-dependent constitutive (rheological) models have been developed. Some of these equations are based on analytical methods while others are strictly empirical. Any study on the flow behavior of non-Newtonian fluids begins with the selection of the rheological model that best describes the steady shear behavior. Depending on the nature of this equation, analytical or numerical solutions can be obtained.

Many oilfield non-Newtonian fluids of the time-independent type typically have a low shear rate viscosity region preceding the shear thinning region. At even higher shear rates, a second Newtonian region is encountered. Rheological models such as the power law model are routinely employed because of their simplicity and ease of application. It is worth noting that the power law model takes into account only the shear thinning interval of the shear stress—shear rate flow curve. The lower and upper Newtonian regions are ignored. This might affect the accuracy of friction pressure predictions made using the power law model.

This chapter presents a review of mathematical models for laminar pipe flow. Specifically, it discusses the flow behavior of power law, Carreau, and MPL-Cross fluids. It also presents a new easily adaptable pressure drop – flow rate equation for laminar flow of Carreau and MPL-Cross fluids and compares predictions, using this new equation, with experimental data found in literature.

6.2 Fundamental Equations for Laminar Pipe Flow

Figure 6.1 illustrates flow through a straight pipe of length l and diameter d. The resulting pressure loss, Δp, across the pipe length is measured as a function of flow rate, q.

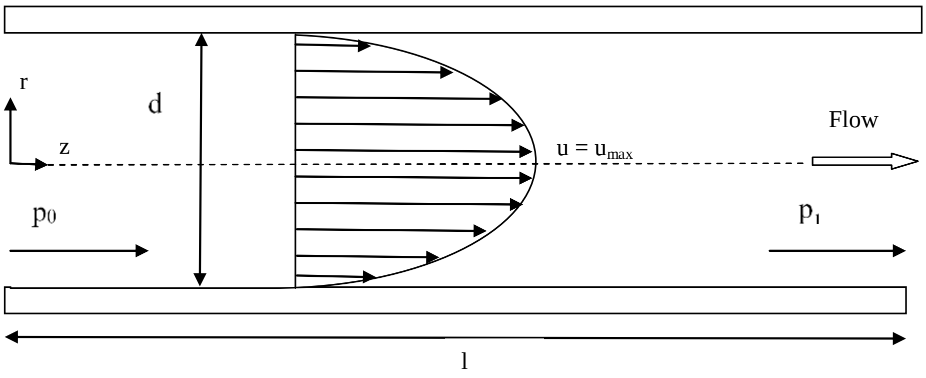

Figure 6.1: Laminar Flow in a Pipe

For horizontal flow, the shear stress can be related to the pressure gradient by the expression.

$$\tau = \frac{r}{2}\frac{\Delta p}{l} \tag{6.1}$$

The maximum (wall) shear stress (τ_w) occurs at the pipe wall, while the zero shear stress occurs at the pipe center. The relationship between wall shear stress and pipe radius is expressed as follows:

$$\tau_w = \frac{R}{2}\frac{\Delta p}{l} \tag{6.2}$$

The forms of Eqs. (6.1) and (6.2) indicate a linear relationship between shear stress and pipe radius. Combining these equations gives the expression below:

$$\frac{\tau}{\tau_w} = \frac{r}{R} \tag{6.3}$$

Equation (6.3) is independent of fluid rheology and applies to both Newtonian and non-Newtonian fluids.

6.3 Average Velocity

The Rabinowitsch-Mooney equation (Rabinowitsch 1929; Mooney 1931) provides a relationship between average velocity and wall shear stress. The closed form of the integral is expressed in Eq. (6.4).

$$\frac{8u}{d} = \frac{4}{\tau_w^3}\int_0^{\tau_w} \tau^2 \dot{\gamma}(\tau) d\tau \tag{6.4}$$

Equation (6.4) is valid for laminar flow of any time-independent fluid with non-slip at the pipe wall. Direct numerical integration of Eq. (6.4) is dependent on the nature of the rheological model. Analytical expressions for Newtonian, Bingham plastic, power law, and Herschel-Bulkley models are expressed in Eqs. (6.5) – (6.8), respectively.

$$\frac{8u}{d} = \frac{\tau_w}{\mu} \tag{6.5}$$

$$\frac{8u}{d} = \frac{\tau_w}{\mu_p}\left[1 - \frac{4}{3}\left(\frac{\tau_y}{\tau_w}\right) + \frac{1}{3}\left(\frac{\tau_y}{\tau_w}\right)^4\right] \tag{6.6}$$

$$\tau_w = K\left(\frac{3n+1}{4n}\right)^n \left(\frac{8u}{d}\right)^n \tag{6.7}$$

$$\frac{8u}{d} = \frac{4n}{3n+1}\left(\frac{\tau_w - \tau_y}{K}\right)^{\frac{1}{n}}\left[1 - \frac{1}{2n+1}\frac{\tau_y}{\tau_w}\left[1 + \frac{2n}{n+1}\frac{\tau_y}{\tau_w}\left(1 + n\frac{\tau_y}{\tau_w}\right)\right]\right] \tag{6.8}$$

For n = 1, Eq. (6.8) is reduced to Eq. (6.6), which is the Buckingham equation for Bingham plastic fluid. The preceding equations can be expressed in terms of either average velocity or frictional pressure loss (Δp). This implies that the average velocity can be determined if Δp is known, and vice versa.

6.4 Velocity Distribution

This section presents results for computation of velocity profiles using the power law, Carreau, and MPL-Cross models. Rheological parameters are determined by fitting fluid models to experimental data for 4% APA-T solution. The shear rate profile is calculated using the Newton-Raphson method for root extraction.

$$\dot{\gamma}_{(r)i+1} = \dot{\gamma}_{(r)i} - \frac{\left[\dot{\gamma}_{(r)i} + \frac{\mu_o \dot{\gamma}_{(r)i}}{\left(1+\left(t\dot{\gamma}_{(r)i}\right)^2\right)^m} - \tau_w \frac{r}{R}\right]}{1-2\mu_o m\left(t\dot{\gamma}_{(r)i}\right)^2\left(1+\left(t\dot{\gamma}_{(r)i}\right)^2\right)^{-(1+m)} + \mu_o\left(1+\left(t\dot{\gamma}_{(r)i}\right)^2\right)^{-m}} \tag{6.9}$$

where, $m = \frac{1-n}{2}$

The velocity profile is determined using the finite difference method, as expressed below. At the wall (R = 1), the velocity is zero ($u_N = 0$), while the velocity is greatest at the pipe center.

$$\dot{\gamma}_{(r)} = \frac{du}{dr} = -\frac{(u_{N-i+1} - u_{N-i})}{\Delta r} \tag{6.10}$$

Equation (6.10) can be solved for each i from 1 to N at a specified value of ΔP. The same procedure was performed for the MPL-Cross model to generate a velocity distribution plot.

Figure 6.2 shows the measured apparent viscosity as a function of shear rate for 4% APA-T. In addition, the rheological parameters obtained from fitting both fluid models are reported in Table 6.1. Using these parameters, velocity profiles through 2 ⅞-in. pipe are determined. Simulated profiles are determined for a flow rate of 30 gpm in the laminar flow regime. Further, the velocity at each radius was normalized using the numerically obtained average velocities for Carreau and MPL-Cross models, while analytically determined average velocity is used for the power law model.

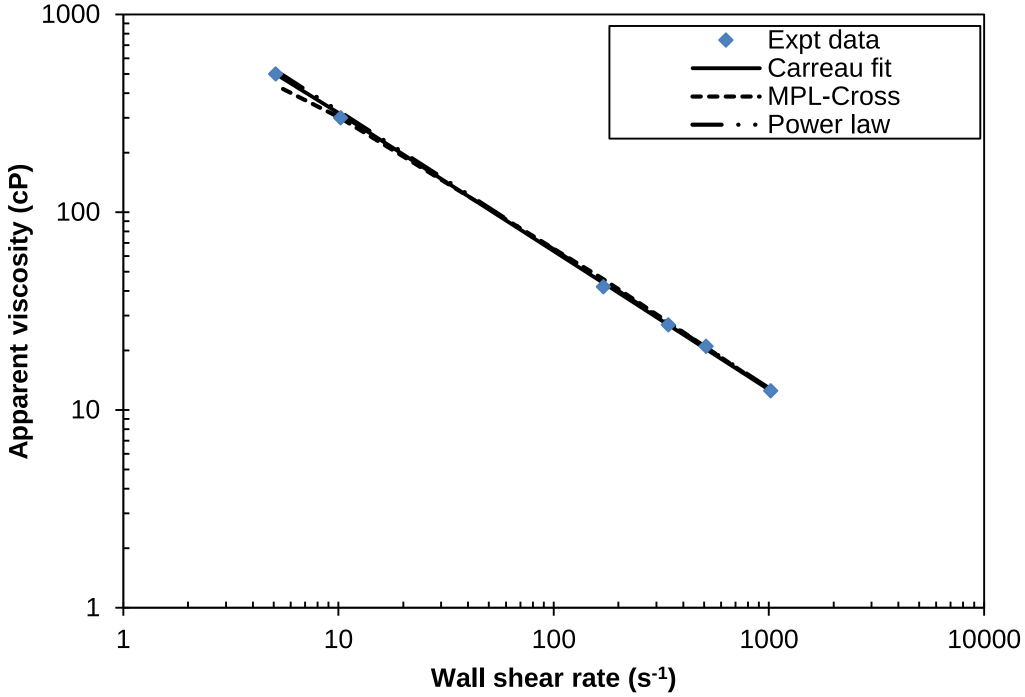

Figure 6.2: Apparent Viscosity for 4% APA-T

Table 6.1: Rheological Model Parameters

Model	Parameters	
Power law	n	0.31
	K_v ($lb_f\, s^n/ft^2$)	0.034
Carreau	μ_o (cP)	1276
	n	0.3
	t (s)	0.721
MPL-Cross	μ_o (cP)	1417
	n	0.25
	t (s)	0.57

Velocity and normalized distributions for the laminar flow of 4% APA-T are shown in Figs. 6.3 and 6.4. As expected, the shapes of velocity profiles for all models are qualitatively similar. The highest velocity at the pipe center is predicted by the Carreau model, while the power law predicted the lowest. This can be attributed to apparent viscosity variation with shear rate. At higher shear rates, the power law model underpredicts the apparent viscosity. Conversely, at lower shear rates, the power law model overpredicts the apparent viscosity; hence, the lower magnitude of velocity at the pipe center. Normalized velocity profiles show a trend reversal with respect to the power law model because this model had the lowest average velocity prediction of the models examined.

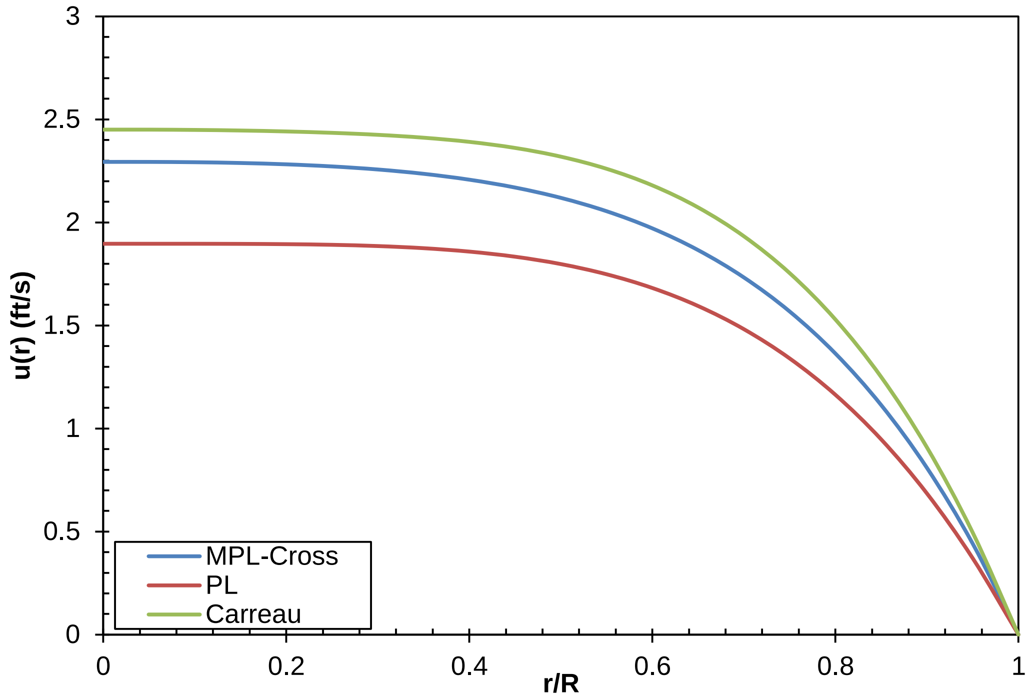

Figure 6.3: Laminar Flow Velocity Profiles

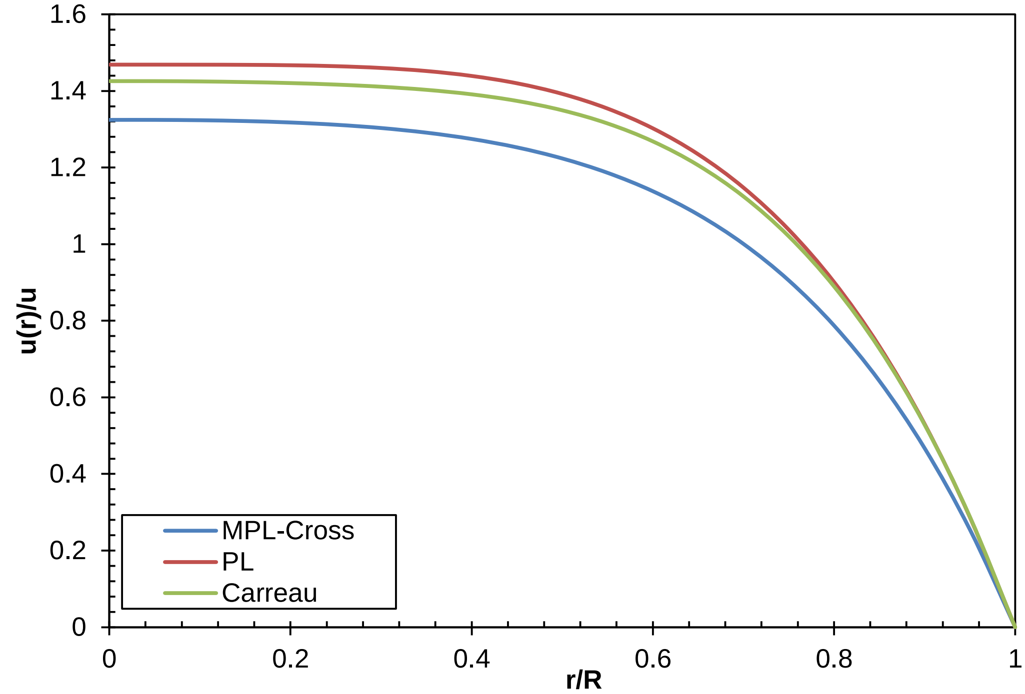

Figure 6.4: Normalized Velocity Profiles for Laminar Flow

6.5 Frictional Pressure Loss

As earlier stated, the Rabinowitsch-Mooney equation can be solved for either average velocity or frictional pressure loss. In most cases, however, the flow rate or average velocity is the control variable while pressure loss is the measured (or estimated) parameter. Simply rewriting Eqs. (6.5) – (6.8), the friction pressure can be calculated for Newtonian as well as non-Newtonian fluids. These flow equations can be conveniently expressed in terms of dimensionless quantities. Such relationships are useful in formulating empirical and graphical relationships for Newtonian and non-Newtonian fluids. For complex models (Carreau and MPL-Cross models), analytical equations cannot be derived. In this section, simple expressions are developed for both the Carreau and MPL-Cross models.

6.5.1 Dimensionless Expressions

Frictional pressure loss can be expressed using the Darcy-Weisbach equation (in consistent units) as:

$$\frac{\Delta p}{l} = \frac{2\rho f u^2}{d} \tag{6.11}$$

where, f is the Fanning friction factor; u is the average velocity; ρ is the fluid density; and d is pipe diameter.

The Fanning friction factor is the ratio between frictional to inertia forces. It can be defined using the Hagen-Poiseulle and Darcy-Weisbach equations as follows:

$$f = \frac{2\tau_w}{\rho u^2} \tag{6.12}$$

$$f = \frac{16}{\frac{\rho u d}{\mu}} \tag{6.13}$$

The denominator from Eq. (6.13) is the Reynolds number definition for Newtonian fluids. This represents the ratio of viscous to inertia forces.

$$N_{Re} = \frac{\rho u d}{\mu} \tag{6.14}$$

The Reynolds number provides a way to distinguish different flow regimes. For $N_{Re} \leq 2100$, laminar flow prevails, while $N_{Re} > 4000$ represents turbulent flow. The values between these two points represent transitional flow.

Metzner and Reed (1955) proposed a generalized Reynolds number equation for time-independent fluids, which is expressed as follows:

$$N_{Reg} = \frac{\rho u d}{K'\left(\frac{8u}{d}\right)^{n'-1}} \tag{6.15}$$

where, $n' = \frac{d\ln(\sigma_w)}{d\ln\left(\frac{8u}{d}\right)}$

The generalized approach by Metzner and Reed (1955) extends well-established procedures for determining friction factors for Newtonian fluids to non-Newtonian time-independent fluids. Applying the same reasoning for the formulation of Eq. (6.15), Madlener et al. (2009) proposed a generalized Reynolds number expression for the extended Herschel-Bulkley model. In this study, generalized Reynolds number expressions are derived by adopting the Metzner and Reed (1955) and Madlener et al. (2009) approach for Carreau and MPL-Cross models.

$$N_{Reg,Ca} = \frac{\rho u d}{\left[\frac{(\mu_O - \mu_\infty)\left(\frac{3n'+1}{4n'}\right)}{\left(1+\left(t\left(\frac{3n'+1}{4n'}\right)\frac{8u}{d}\right)^2\right)^{\frac{1-n}{2}}} + \mu_\infty\left(\frac{3n'+1}{n'}\right)\right]} \tag{6.16}$$

where, $n' = \frac{\frac{8u}{d}\left[\mu_\infty - 2t^2(\mu_O - \mu_\infty)\left(\frac{n-1}{2}\right)\left(\frac{8u}{d}\right)^2\left(1+t^2\left(\frac{8u}{d}\right)^2\right)^{-\left(1+\frac{1-n}{2}\right)} + (\mu_0 - \mu_\infty)\left(1+t^2\left(\frac{8u}{d}\right)^2\right)^{-\left(\frac{1-n}{2}\right)}\right]}{\mu_\infty\frac{8u}{d} + (\mu_O - \mu_\infty)\frac{8u}{d}\left(1+t^2\left(\frac{8u}{d}\right)^2\right)^{-\left(\frac{1-n}{2}\right)}}$

$$N_{Reg,MPL} = \frac{\rho u d}{\left[\frac{\mu_O\left(\frac{3n'+1}{4n'}\right)}{\left(1+t\left(\frac{8u}{d}\right)^{1-n}\right)} + \mu_\infty\left(\frac{3n'+1}{4n'}\right)\right]} \tag{6.17}$$

where, $n' = \frac{\frac{8u}{d}\left[\mu_\infty - \frac{(1-n)\mu_O^2\left(\frac{8u}{d}\right)^{1-n}}{K_{MPL}\left(1+t\dot{\gamma}_W^{1-n}\right)^2} + \frac{\mu_0}{1+t\left(\frac{8u}{d}\right)^{1-n}}\right]}{\mu_\infty\frac{8u}{d} + \frac{\mu_O\dot{\gamma}_W}{1+t\left(\frac{8u}{d}\right)^{1-n}}}$

Full derivations of Eqs. (6.16) and (6.17) can be found in Appendix III.

6.5.2 Evaluation of Reynolds Number Definitions

Experimental friction pressure loss data for 4% APA-T in a 2 ⅞-in. pipe are used to validate the various Reynolds number definitions (Eqs. 6.16 and 6.17). The friction pressure data are converted to Fanning friction factor as shown in Fig. 6.5. The solid black line corresponds to the 16/N_{Reg} line for laminar flow. The new Reynolds number definitions are compared with the generalized Reynolds number for power law. Table 6.2 is a summary of the percent error deviation for each definition.

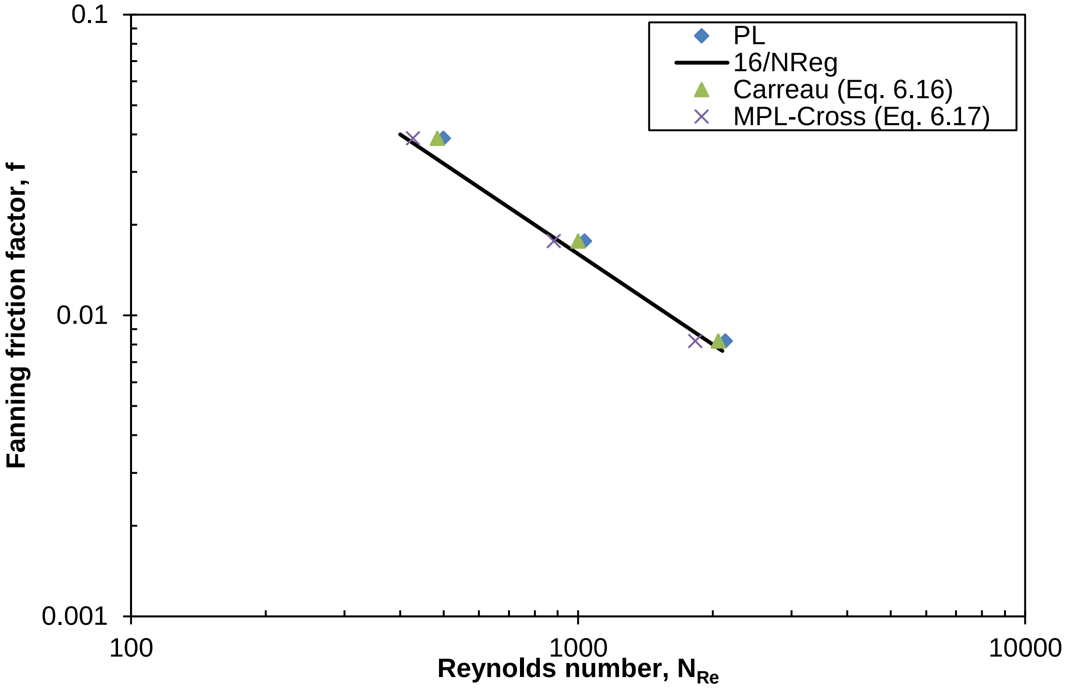

Figure 6.5: Evaluation of Reynolds and Generalized Reynolds Number Definitions

Table 6.2: Percent Deviation Comparison of Reynolds Number Definitions

	Reynolds number		
q (gpm)	**Power law**	**Carreau (Eq. 6.16)**	**MPL-Cross (Eq. 6.17)**
30	17.29	14.65	3.38
50	12.41	9.44	2.25
75	8.80	5.37	6.10
Ave. Dev	12.83	9.82	3.91

From Fig. 6.5 and Table 6.2, it is evident that all Reynolds number definitions compare favorably with experimental data. Individual data points have deviations of less than 20%. Average deviation values are less than 15% with all definitions. For the data set, the Carreau and MPL-Cross definitions compare favorably with the generalized Reynolds number for power-law fluids on both an individual data-point basis and average-deviation basis. At flow rates of 50 and 75 gpm, the Carreau and MPL-Cross models offer improved estimates of friction pressure.

6.5.3 Generalized Shear Stress–Shear Rate Expression

The form of the Rabinowitsch-Mooney equation can be transformed into Eq. (6.18) for substitution of both the Carreau and MPL-Cross models.

$$\frac{8u}{d} = \frac{4}{3}\left[\dot{\gamma}_R - \frac{1}{\tau_w^3}\int_0^{\dot{\gamma}_R} \tau^3 d\dot{\gamma}\right] \tag{6.18}$$

Dimensional analysis is performed generating dimensionless parameters as defined below:

$$\dot{\gamma}' = t\dot{\gamma} \tag{6.19a}$$

$$\tau' = \frac{t\tau}{\mu_o}$$

$$\tau_w' = \frac{t\tau_w}{\mu_o}$$

$$\left(\frac{8u}{D}\right)' = t\ \frac{8u}{D} \tag{6.19d}$$

The Carreau and MPL-Cross models can now be written in dimensionless form as follows:

$$\tau' = \dot{\gamma}'[1 + (\dot{\gamma}')^2]^{\frac{n-1}{2}} \tag{6.20}$$

$$\tau' = \dot{\gamma}'[1 + (\dot{\gamma}')^{1-n}]^{-1} \tag{6.21}$$

Using dimensionless forms of the Carreau and MPL-Cross models, the following expressions for the generalized flow exponent (local gradient) are derived.

$$n' = \left(1 + \left(\left(\frac{8u}{d}\right)'\right)^2\right)^{\frac{1-n}{2}} \left[\frac{1}{2}(n-1)\left(\left(\frac{8u}{d}\right)'\right)^2 \left(1 + \left(\left(\frac{8u}{d}\right)'\right)^2\right)^{-1+\frac{1-n}{2}} + \left(1 + \left(\left(\frac{8u}{d}\right)'\right)^2\right)^{\frac{1}{2}(n-1)}\right]$$

$$n' = \left(1 + \left(\left(\frac{8u}{d}\right)'\right)^{1-n}\right) \left[\frac{1}{1+\left(\left(\frac{8u}{d}\right)'\right)^{1-n}} - \frac{(1-n)\left(\left(\frac{8u}{d}\right)'\right)^{1-n}}{\left(1+\left(\left(\frac{8u}{d}\right)'\right)^{1-n}\right)^2}\right]$$

The generalized flow exponent for the power law model is the same as the global flow exponent and remains constant irrespective of flow rate variations. The same cannot be stated for the other models. The next step is to assess the effect of variations in flow rate with corresponding changes in the magnitude of the generalized flow exponent.

For illustrative purposes, Table 6.3 presents a summary of percent changes in n' caused by flow rate variations from 0.1% to the maximum variation studied, 10%. It is evident from this table that apart from the power law model, the MPL-Cross model is least sensitive to flow rate variations than the Carreau model. The percent changes in n' are lower with increasing n for the MPL-Cross model. As an example, at 10% flow rate variation, percent changes in n' of 1.33% and 0.086% are calculated for n of 0.1 and 0.8, respectively.

The Carreau model, on the other hand, is the most sensitive with respect to variations in flow rate. With the Carreau model, percent changes in n' at 10% flow rate variation are -2.3% and 3.6% for n of 0.1 and 0.8, respectively. It is clear that some models are more sensitive to flow rate variations than others. Thus, for fluids sensitive to flow rate changes, proper attention should be given to the choice of rheological model that best describes the fluid while accounting for local flow exponent changes. Failure to consider local flow exponent changes might result in inaccurate pressure loss predictions.

Table 6.3: Percentage change in n' with variations in flow rate

Flow exponent	Model	Change in n' (%)				
		ε (0.1%)	ε (1%)	ε (2%)	ε (5%)	ε (10%)
n = 0.1	Carreau	-0.024	-0.239	-0.475	-1.17	-2.272
	MPL-Cross	0.014	0.14	0.276	0.681	1.33
	Power law	-	-	-	-	-
n = 0.5	Carreau	0.015	0.153	0.308	0.784	1.61
	MPL-Cross	0.005	0.05	0.1	0.244	0.48
	Power law	-	-	-	-	-
n = 0.8	Carreau	0.035	0.348	0.698	1.757	3.554
	MPL-Cross	0.001	0.01	0.018	0.044	0.086
	Power law	-	-	-	-	-

As mentioned earlier, one of the objectives of this study is to develop flow rate - pressure drop relationships for the Carreau and MPL-Cross fluids. The Rabinowitsch-Mooney equation can be expressed in dimensionless form.

$$\left(\frac{8u}{d}\right)' = \frac{4}{3}\left[\dot{\gamma}_R' - \frac{1}{(\tau_w')^3}\int_0^{\dot{\gamma}_R'} (\tau^3)' d\dot{\gamma}'\right] \tag{6.22}$$

Equation (6.22) is numerically integrated to obtain dimensionless wall shear stress–apparent wall shear rate profiles for flow indices in the range 0.1–1. These profiles are shown in Figs. 6.6 and 6.7.

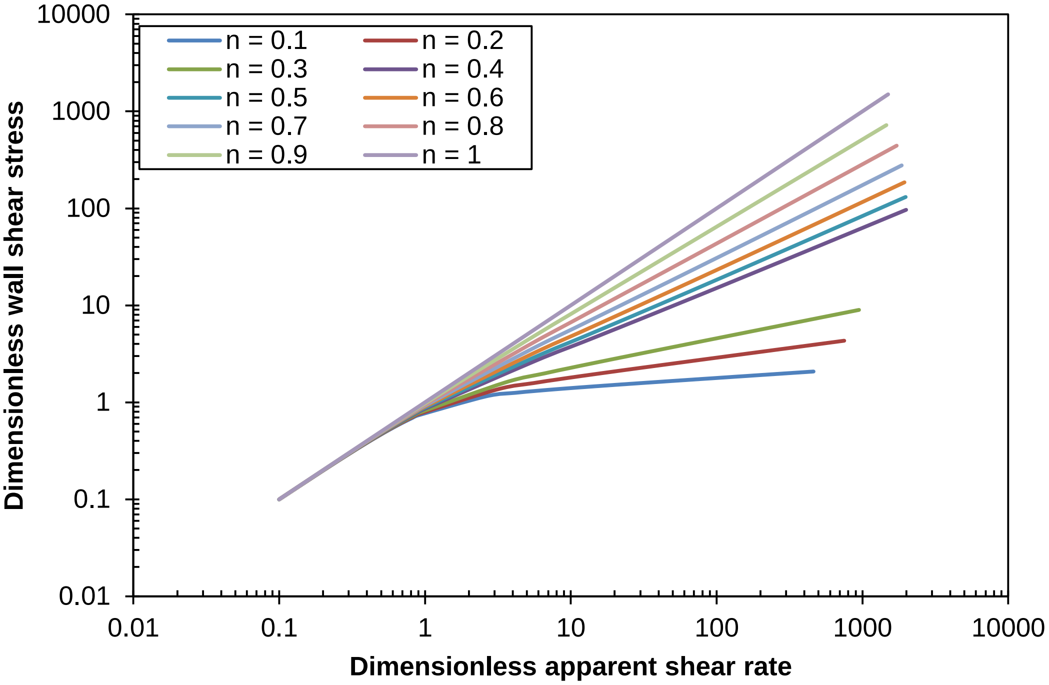

Figure 6.6: Dimensionless Wall Shear Stress vs. Dimensionless Apparent Wall Shear Rate for Carreau Fluid

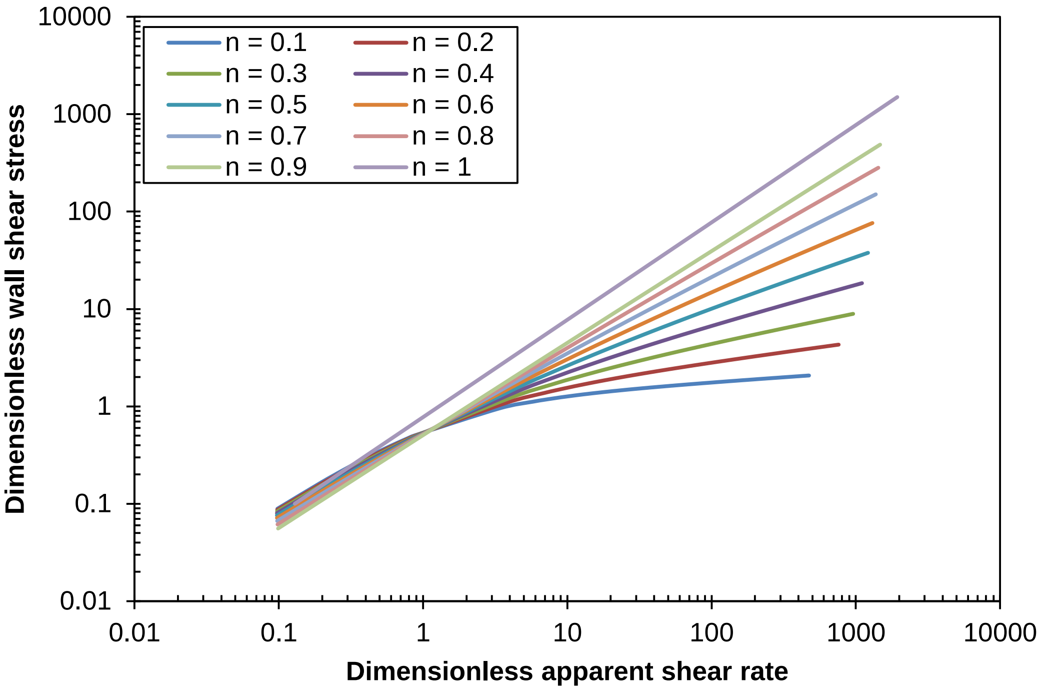

Figure 6.7: Dimensionless Wall Shear Stress vs. Dimensionless Apparent Wall Shear Stress for MPL-Cross Fluid

The profiles can be approximated by the equation below (Derezinski 1990):

$$\tau_w' = a(\dot{\gamma}_w' - b)^c - (d\dot{\gamma}_w') \tag{6.23}$$

where, a, b, c, and d are constants for a given flow behavior index value in Carreau and MPL-Cross models.

The values of a, b, c, and d are determined by least square regression. It was discovered that Eq. (6.23) was deemed satisfactory in describing both models. The parameters in this equation are reported in Tables 6.4 and 6.5. The constants in both tables are valid for dimensionless wall shear rates in the range 0–1500. Simple interpolation can be used to determine the parameters for exponent values between those reported.

Table 6.4: Equation Constants for Carreau Model

n	a	b	c	d
0.1	0.577	0.00103	0.296	0.00365
0.2	0.648	0.00103	0.354	0.0037
0.3	0.687	0.00105	0.436	0.00556
0.4	0.787	0.00109	0.649	0.00644
0.5	0.813	0.00121	0.685	0.00902
0.6	0.849	0.00144	0.731	0.0162
0.7	0.905	0.00178	0.789	0.0383
0.8	1.004	0.0511	0.829	0.0231
0.9	1.043	0.0352	0.904	0.0228
1	1.022	0	1	0.0222

Table 6.5: Equation Constants for MPL-Cross Model

n	a	b	c	d
0.1	0.576	0.247	0.283	0.00295
0.2	0.558	0.156	0.381	0.00396
0.3	0.573	0.153	0.469	0.00628
0.4	0.585	0.13	0.561	0.0111
0.5	0.565	0.0475	0.672	0.0251
0.6	0.638	0.0289	0.797	0.1022
0.7	0.639	0.0176	0.853	0.112
0.8	0.792	0.0047	0.929	0.277
0.9	0.857	0.00301	0.968	0.345
1	0.873	0	1	0.099

The validity of Eq. (6.23) is tested for a flow index of 0.4. An average deviation of 3% is calculated between Eq. (6.23) and the numerical solution of Eq. (6.18) for both models (Fig. 6.8). For practical purposes, a 10% deviation is deemed adequate for pressure loss calculations. If higher accuracy to cover a wider range of dimensionless apparent wall shear rate is desired, a more complex approximation than Eq. (6.23) can be derived. The pressure loss (in consistent units) can be determined for a specified flow rate and pipe size by substituting the definitions given in Eqs. (6.19a) to (6.19d) into Eq. (6.23).

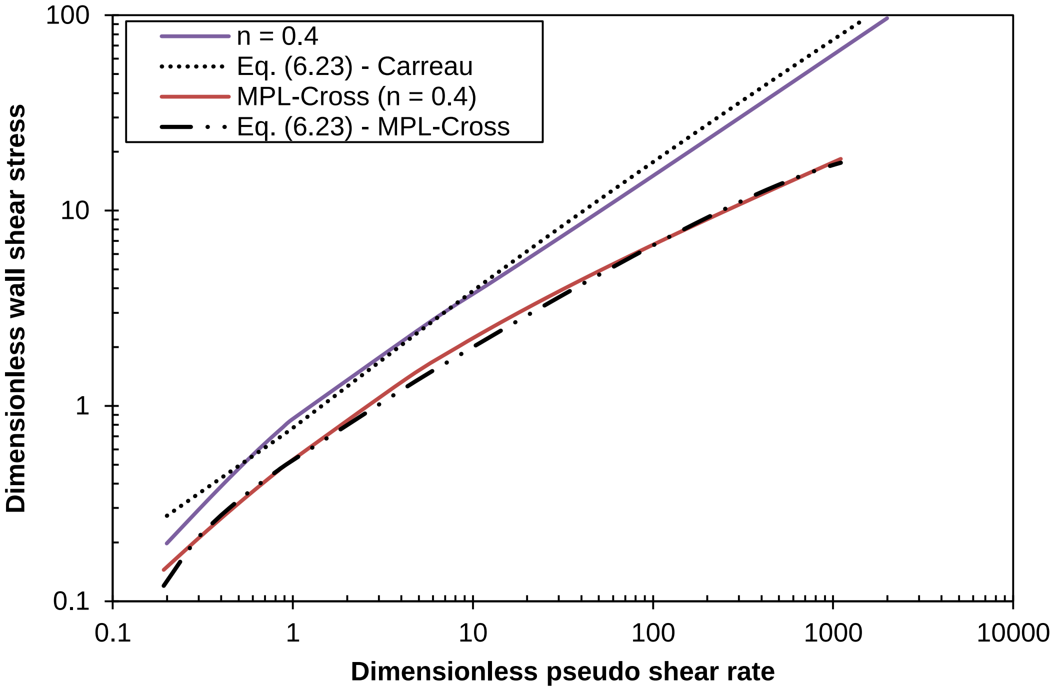

Figure 6.8: Comparison of Eq. (6.23) with Numerical Solution

$$\frac{\Delta p}{l} = \frac{2\mu_o}{tR}\left[a\left(t\frac{8u}{d} - b\right)^c - \left(d\,t\frac{8u}{d}\right)\right] \qquad (6.24)$$

Equation (6.24) is valid for laminar flow only.

The applicability of Eq. (6.24) is demonstrated using experimental data for 4% APA-T solution and laminar flow data from the study of Pereira and Pinho (1994) for 0.4, 0.5, and 0.6% tylose solutions. Rheological model parameters for 4% APA-T are given in Table 6.1. The results of calculations are presented in Tables 6.6 and 6.7. In Table 6.7, the comparison of predictions with experimental flow data of Pereira and Pinho (1994) is presented. Data by Pereira and Pinho (1994) were gathered for flow in a 26 mm inside diameter vertical pipe. A complete experimental setup description can be found in their paper. The rheological parameters were obtained by fitting the Carreau model to steady shear data. Rheological parameters for 0.4% tylose solution are: μ_o = 0.0208 Pa s, n = 0.725, t = 0.0047 s. Rheological parameters for 0.5% tylose solution are: μ_o = 0.0344 Pa s, n = 0.660, t = 0.005 s. Similarly, rheological parameters for 0.6% tylose solution are: μ_o = 0.0705 Pa s, n = 0.637, t = 0.0112 s.

It can be seen from these tables that the new flow rate-pressure drop equation compares favorably with experimental data especially for fluids described by the Carreau model. However, from Table 6.7, a higher percentage deviation is calculated for 0.4% tylose at a velocity of 1.77 ft/s. All other points are within 10% deviation.

Table 6.6: Percentage Deviations for Laminar Pressure Gradient Prediction and Measured Data for 4% Aromox® APA-T

	Pressure loss (psi)		
Flow rate (gpm)	**Experimental**	**Carreau**	**MPL-Cross**
32.5	3.11	3.12	3.49
50.0	3.35	3.67	4.09
76.6	3.67	4.28	4.77
Ave. Dev. (%)		8.8	21.5

Table 6.7: Percentage Deviations for Laminar Pressure Gradient Prediction and Measured Data for 4, 5, and 6% Tylose

Fluid	Velocity (m/s)	Exp. pressure gradient (Pa/m)	Cal. pressure gradient (Pa/m)	Dev. (%)
0.4% Tylose	0.54	371	515	38.9
	1.13	853	931	9.1
0.5% Tylose	0.56	826	839	1.6
	1.41	1674	1690	0.9
0.6% Tylose	1.14	2402	2359	1.8
	2.8	5038	4596	8.8

6.6 Summary

The laminar flow behavior of non-Newtonian fluids is investigated using the Carreau and MPL-Cross rheological models. These models are considered because they provide better fit to experimental data while covering a wider range of shear rates not afforded by the widely used power law model. Reynolds number definitions based on both models are proposed; they are equivalent to the Metzner-Reed generalized Reynolds number. Evaluations of these definitions show satisfactory prediction accuracy.

A new pressure drop – flow rate equation is derived for non-Newtonian fluids. This equation can easily be adapted for either the Carreau or MPL-Cross model. This equation provides satisfactory accuracy for laminar flow of non-Newtonian fluids described by both rheological models.

Chapter 7

TURBULENT PIPE FLOW OF NON-NEWTONIAN FLUIDS

7.1 Introduction

The preceding chapter presented laminar flow equations for Carreau and MPL-Cross type fluids. As discussed in Chapter 6, a considerable amount of work based on established principles for laminar flow of Newtonian and non-Newtonian is readily available in the literature. Turbulent flow of Newtonian fluids is given by several theoretical equations as well as empirical correlations. These approaches are well-established and can be applied to hydraulic calculations with a high degree of accuracy. The same cannot be stated for turbulent flow of non-Newtonian fluids.

Most fluids used in the oil and gas industry are non-Newtonian. In the case of drilling and hydraulic fracturing applications, these fluids display drag reducing characteristics. As such, solutions to turbulent flow equations of non-Newtonian fluids can be intractable because of a greater level of complexity. The presence of drag reducing agents adds a dimension of complexity to flow hydrodynamics. Unfortunately, no universal set of flow equations has been reported for non-Newtonian drag reducing fluids. The intractability of solutions has not deterred research into drag reducing flows. Several approaches are available for predicting friction pressure. In deriving equations or correlations, limiting assumptions are imposed to arrive at friction pressure relationships.

In this chapter, the turbulent flow behavior of non-Newtonian fluids through pipes is studied. The first part of this chapter deals with drag reduction behavior of test solutions with respect to the effects of various factors (concentration, pipe diameter, and salinity). The second part presents a Fanning friction factor relationship for purely viscous non-Newtonian fluids.

7.2 Flow Data Calibration and Analysis

Figure 7.1 is an example of recorded signals after elimination of transient data points. On this plot are measured data, including flow rate, fluid density, temperature, and pressure drop. The pressure loss and flow rate are converted to dimensionless quantities. The pressure loss is converted to Fanning friction factor, while the flow rate is converted to the generalized Reynolds number. The equations used for conversion can be found in Chapter 3.

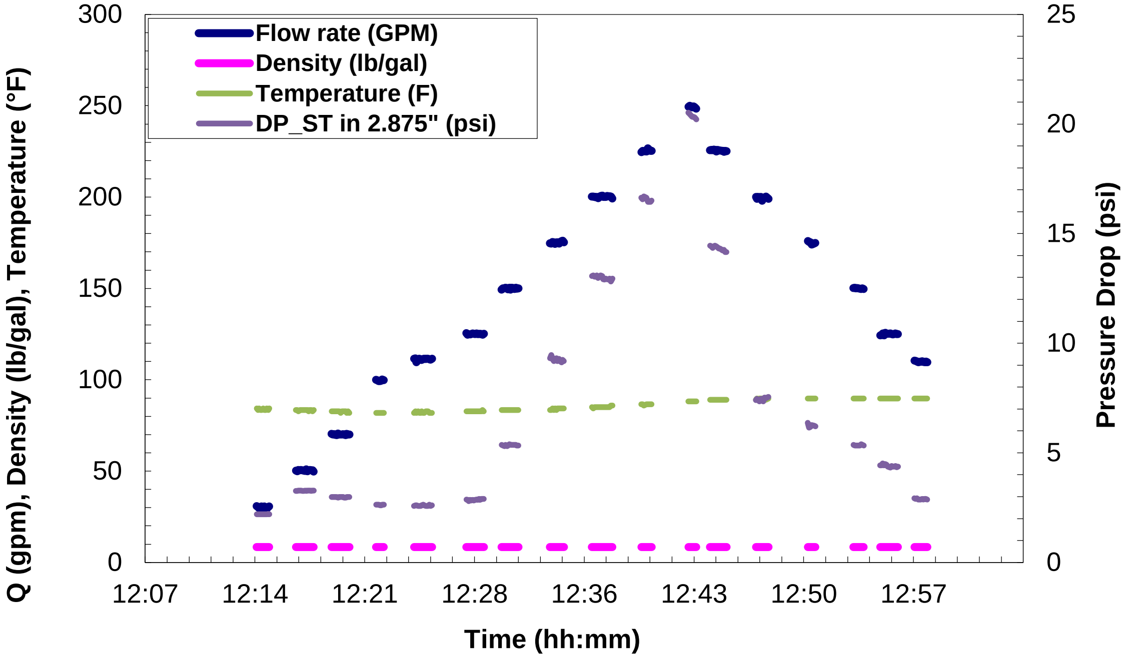

Figure 7.1: Recorded Data for 5% APA-TW through 2 ⅞-in. Pipe

7.2.1 Water Calibration Test

System calibration was performed with water to validate pressure drop–flow rate measurements. This serves as a reference for data comparison with test solutions. Under turbulent flow, two correlations are considered: the Drew correlation (Drew et al. 1932) for smooth pipes and Chen correlation (Chen 1979) for rough pipes. Pipe roughness affects pressure loss measurements and should be considered in any analysis. As such, the height of roughness projections is determined using the Chen correlation (Chen 1978).

The Drew correlation is expressed as follows:

$$f = 0.0014 + \frac{0.125}{N_{Re}^{0.32}} \tag{7.1}$$

where, f is the Fanning friction factor and N_{Re} is the solvent Reynolds number.

The Chen correlation is expressed as:

$$\frac{1}{\sqrt{f}} = -4\log\left[\frac{h}{3.7065d} - \frac{5.0452}{N_{Re}}\log\left\{\frac{1}{2.8257}\left(\frac{h}{d}\right)^{1.1098} + \frac{5.8506}{N_{Re}^{0.8981}}\right\}\right] \quad (7.2)$$

where, h/d = relative roughness (dimensionless).

The explicit form of the Chen correlation makes it appealing for data analysis. Figures 7.2 and 7.3 show calibration plots for 1½-in. and 2⅞-in. pipes. The roughness projection height was determined by curve fitting (Eq. 7.2) to experimental turbulent data. Projection height in inches can be seen in the legends of both plots.

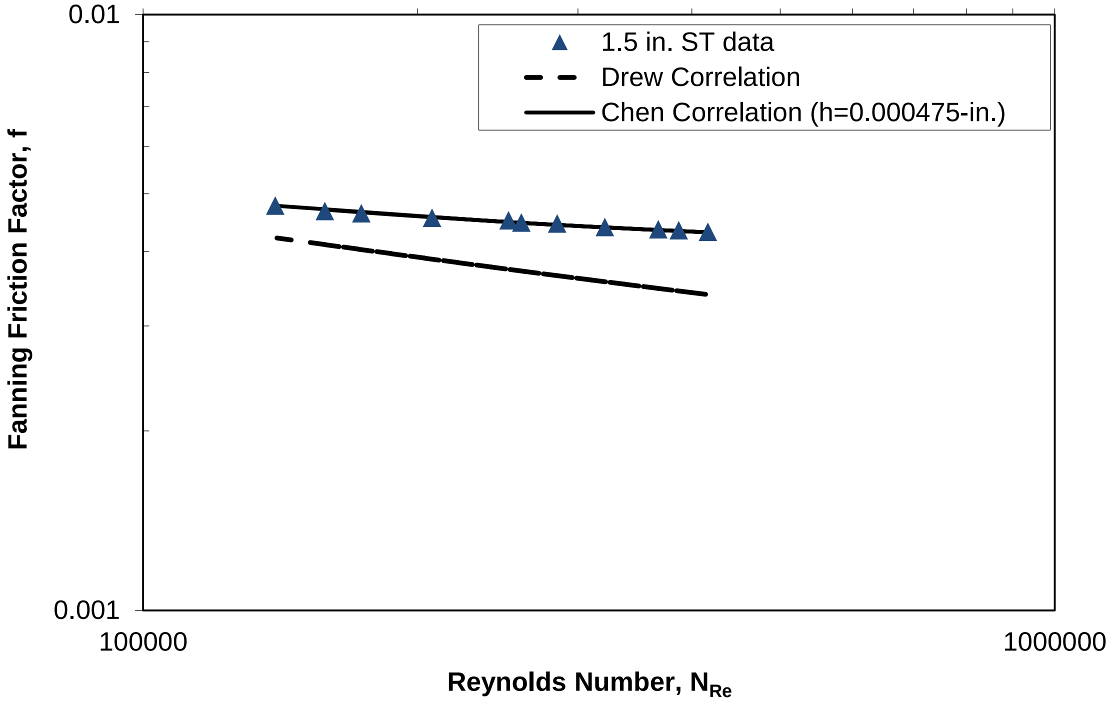

Figure 7.2: Water Data for 1½-in. Pipe

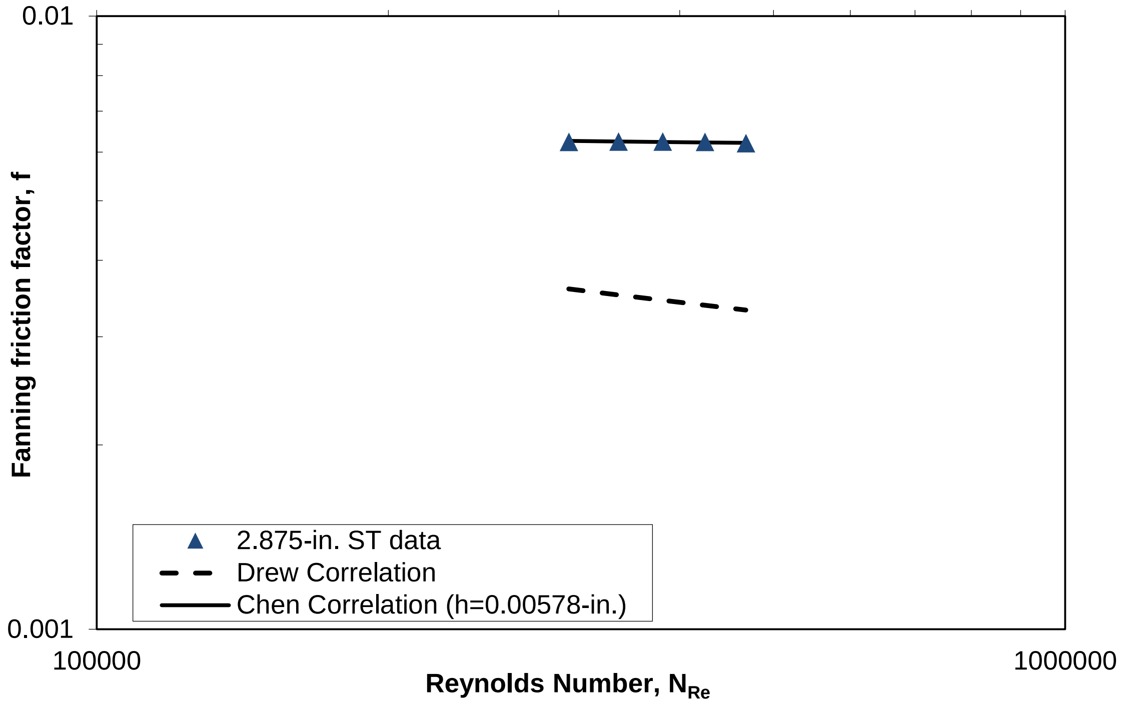

Figure 7.3: Water Data for 2⅞-in. Pipe

7.3 Flow Behavior and Drag Reduction Characteristics

As stated in Chapter 2, surfactant drag reduction is a function of concentration, temperature, pipe size, and the presence of salts. This section presents results of the flow behavior of surfactant solutions in straight pipes. The focus here is on turbulent flow data and drag reduction phenomena associated with the test fluid. This work elucidates the effects of surfactant concentration, pipe size and roughness, and solvent type on drag reduction characteristics of Aromox® APA-T and APA-TW.

7.3.1 Concentration Effect

Figure 7.4 shows Fanning friction factor dependence on the generalized Reynolds number at ambient temperature for two surfactant concentrations (1.5% and 4% v/v Aromox®

APA-T) in ½-in. straight pipe. From this figure, it is obvious that Aromox® APA-T can be classified as a Type-B drag reducer; there is no clear transition as the data points lie close to the extended laminar line in the flow regime transition region (in the generalized Reynolds number range of 2100 to 4000). Figure 7.5 is an alternative form of Fig. 7.4 expressed in terms of percent drag reduction vs. generalized Reynolds number. The maximum drag reduction for 1.5% solution is 55% at a generalized Reynolds number of 5524, whereas for the 4% solution, it is 63% at a generalized Reynolds number of 10202. Evidently at lower concentrations, the maximum drag reduction occurs at lower generalized Reynolds numbers than it does at higher concentrations.

The higher drag reduction with concentration is because of the formation/growth of rod-like micelles and favorable intermicellar associations altering turbulence structures. Drag reduction is influenced by the amount of energy drag reduction additives can extract from flow (Rochefort 1986). Long flexible micellar structures aid in further dampening of eddies at higher N_{Reg}. Concentration increase thickens the elastic sublayer, which results in higher drag reduction.

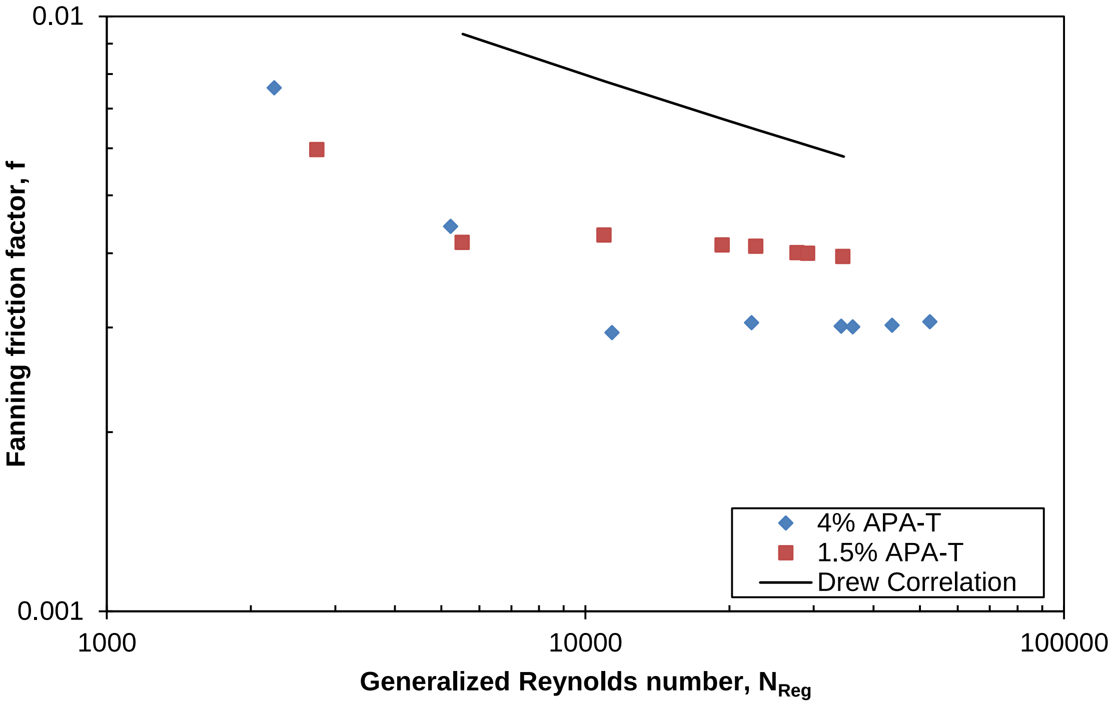

Figure 7.4: Fanning Friction Factor Plot for 1.5% and 4% APA-T in ½-in. Pipe

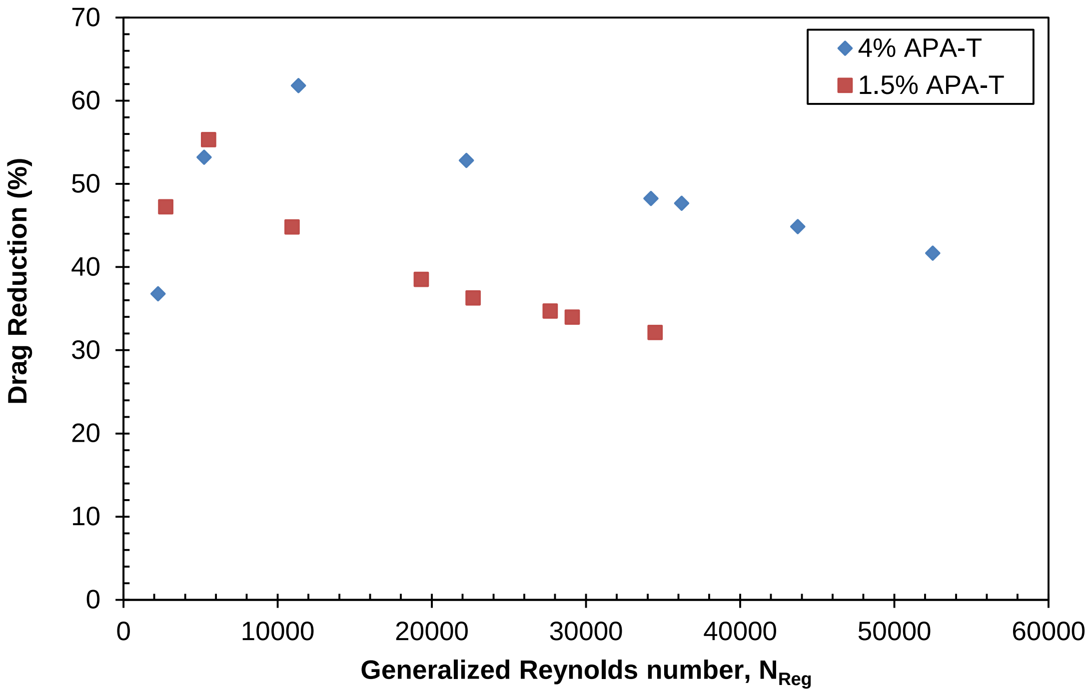

Figure 7.5: Effect of Concentration of Drag Reduction

7.3.2 Pipe Diameter and Roughness Effect

The pipe diameter effect is shown in Figs. 7.6 and 7.7 for 4% APA-T and 5% APA-TW solutions. Figure 7.6 shows a decrease in Fanning friction factor with diameter for 4% APA-T solution. A corresponding drag reduction increase can be seen in Fig. 7.7 with a maximum of 55% for 1½-in. pipe as compared to 62% for the 2⅞-in. pipe. This is in agreement with observations by Berman et al. (1978), Mansour et al. (1988), and Salem (1996). Drag reduction is attributed to the interaction between molecules in solution and turbulence structures. Berman et al. (1978) explained this observation in terms of rate of strain and persistence time of turbulence eddies.

The persistence time is the length of time molecules are elongated under high-strain without the effects of rotation (Mansour et al. 1988). Under high-strain rate and time scale conditions, molecules are continuously stretched and aligned in the direction of flow. This continues until an equilibrium rate is reached for a fluid and pipe size. Changes to any of these factors results in a change in equilibrium. The equilibrium level is increased proportionally with pipe diameter as micelles have more time to be stretched. A consequence of this is greater interaction and interference with eddies and an increase in drag reduction, provided that no limitations to molecule stretching exist.

For the APA-TW solution, two effects can be seen—pipe diameter and pipe roughness. Roughness values in the 1½-in. and 2⅞-in. are 0.000475-in. and 0.00578-in., respectively. Maximum percent drag reduction are 68% and 69% for the 1½-in. and 2⅞-in. pipes. It is evident that the diameter effect is nullified by roughness. Roughness is less important in laminar flow but can be significant under turbulent conditions. This is because in laminar flow, the viscous sublayer is thicker, thereby containing the roughness projections. Under turbulent flow, the viscous sublayer is thin; thus, roughness projections interfere with flow, resulting in higher friction pressures (Shah 1990).

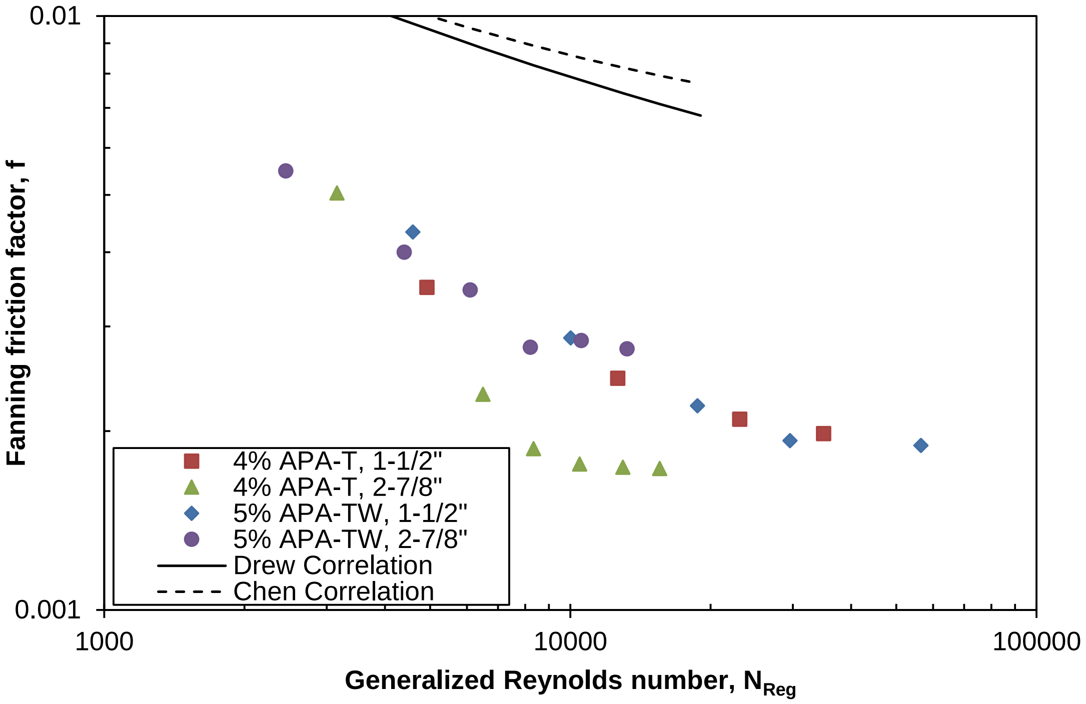

Figure 7.6: Fanning Friction Factor Plot for 4% APA-T and 5% APA-TW in 1½- and 2⅞-in. Pipes

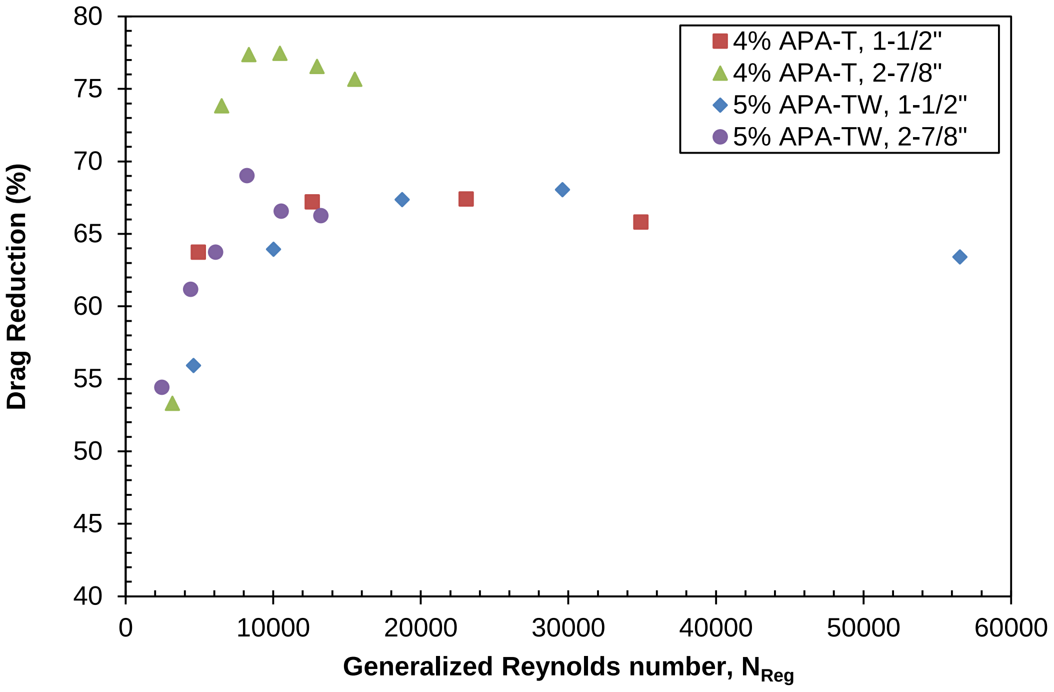

Figure 7.7: Effect of Pipe Diameter and Surface Roughness on Drag Reduction

7.3.3 Solvent Type Effect

Figures 7.8 and 7.9 show the effect of 2% KCl and 2% $CaCl_2$ on the flow behavior of 5% APA-TW in 2⅞-in. pipe. On these plots, freshwater data are shown for comparison. From these plots, it is obvious that drag reduction is improved with salts in the solution. Maximum drag reduction values for freshwater, 2% KCl, and 2% $CaCl_2$ are 70%, 84%, and 82%, respectively. Salts have a dramatic effect on micellar solutions, as discussed in Chapter 5. Macroscopic changes were recorded under steady shear as well as oscillatory tests. With salts in solution, micelle restructuring is evident. Salts promote aggregation and growth of worm-like micelles. Micelle growth leads to greater flexibility and intermicellar interactions. These longer micelles have the potential to interact more with turbulence structures. Elongation of micelles causes an enhancement in drag reduction (Kulicke et al. 1989).

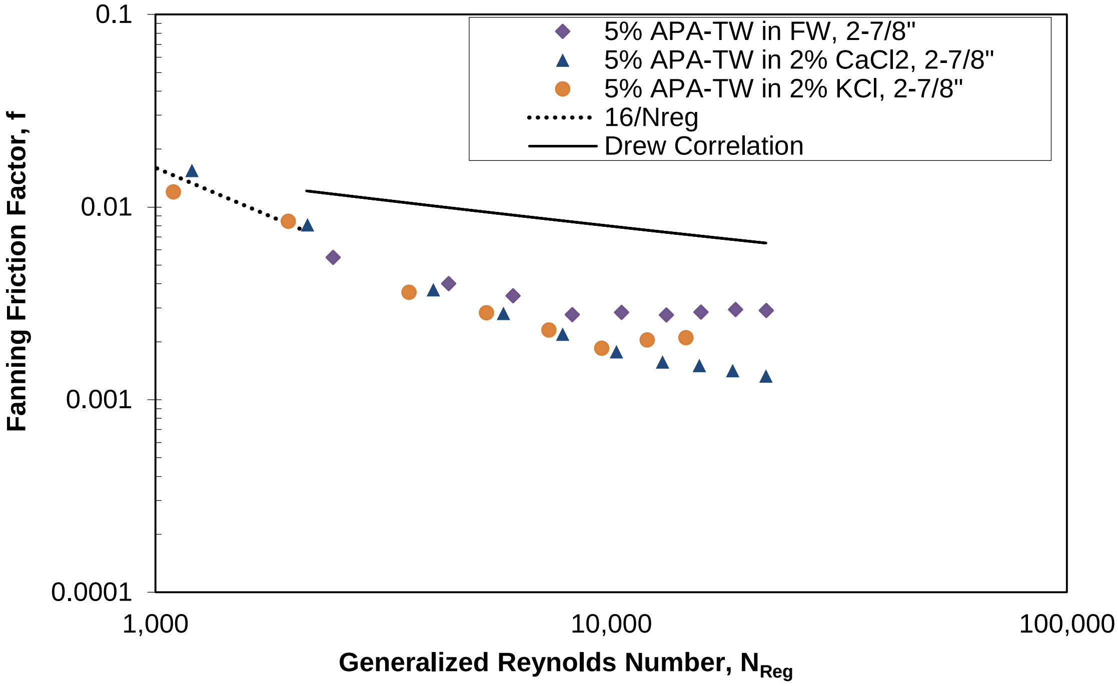

Figure 7.8: Fanning Friction Factor Plot for 5% APA-TW in Different Solvents

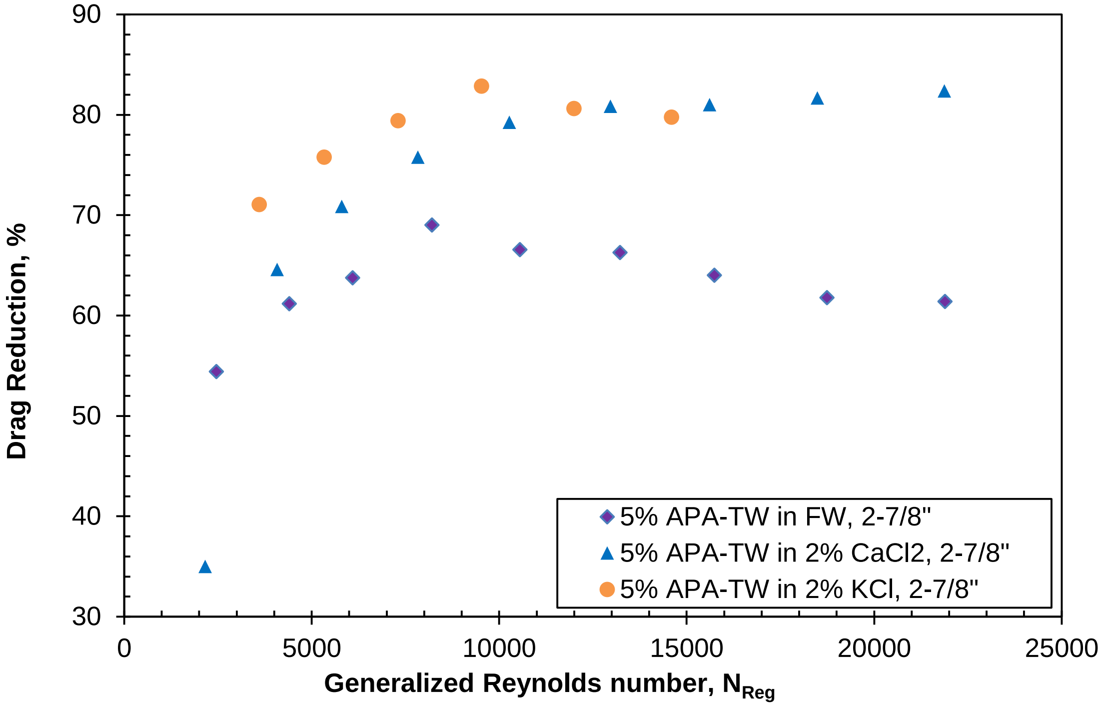

Figure 7.9: Effect of Solvent Type on Drag Reduction

7.4 Purely Viscous Non-Newtonian Fluids

An analytical expression relating the Fanning friction factor to the generalized Reynolds number for a purely viscous pseudoplastic fluid is derived. In deriving this relationship, the following assumptions apply:

1. Steady state conditions
2. Constant density of fluid (incompressible fluid)
3. Prevalent isothermal conditions
4. Fully developed flow

The implicit relation of Dodge and Metzner (1959) is widely accepted for friction factor determination. The Dodge and Metzner (1959) equation, which is based on the mixing length approach, requires numerical techniques to obtain the Fanning friction factor.

$$\frac{1}{\sqrt{f}} = \frac{4}{(n')^{0.75}} \log\left[N_{Reg} f^{1-\frac{n'}{2}}\right] - \frac{0.395}{(n')^{1.2}} \tag{7.3}$$

In this work, a simple equation that relates the Fanning friction factor to the generalized Reynolds number is sought. To achieve this aim, the dimensionless velocity and distance from the wall are used. A relationship between the dimensionless distance (y_w^+) and the apparent viscosity for the viscous sublayer was presented by Edwards and Smith (1980).

$$y_w^+ = \frac{y(u^*)^{\frac{2-n}{n}}}{\left(\frac{K}{\rho}\right)^{\frac{1}{n}}} \tag{7.4}$$

For a Newtonian fluid, the dimensionless turbulent velocity profile can be expressed as:

$$u^+ = 8.57(y^+)^{\frac{1}{7}} \tag{7.5a}$$

Similarly, the dimensionless turbulent velocity profile for a non-Newtonian fluid can be written as (Edwards and Smith 1980):

$$u^+ = 8.57(y_w^+)^{\frac{1}{7}} \tag{7.5b}$$

Wilson and Thomas (1985) suggested that the viscous sublayer near the wall is thicker for the case of turbulent pipe flow of a non-Newtonian fluid. This increase in thickness can be accounted for by comparing the area under the rheogram of the non-Newtonian fluid to that of a Newtonian one between zero shear rate and the wall shear rate. With respect to dissipative energy, they assumed that the non-Newtonian fluid behaves Newtonian with the viscosity multiplied by the area ratio, α.

Adopting this assumption, the dimensionless turbulent velocity profile can be expressed as:

$$u^+ = \frac{\bar{u}_z}{u^*} = 8.57\left(\frac{y_w^+}{\alpha}\right)^{\frac{1}{7}} \tag{7.6}$$

$$\alpha = \frac{A_{NN}}{A_N}$$

where, A_{NN} is the area under the rheogram of a non-Newtonian fluid and A_N is the area under the rheogram of a Newtonian fluid.

For a yield-pseudoplastic fluid, α is expressed as:

$$\alpha = \frac{2}{n+1}\left(1 + n\frac{\tau_o}{\tau_w}\right) \tag{7.7}$$

Upon simplification, Eq. (7.7) reduces to the following expression for power law fluids.

$$\alpha = \frac{2}{n+1}$$

Thus, Eq. (7.5a) can be rewritten as:

$$u^+ = \frac{\bar{u}_z}{u^*} = 8.57\left((n+1)\frac{y_w^+}{2}\right)^{\frac{1}{7}}$$

An expression for the average velocity can be obtained by integrating the dimensionless turbulent velocity profile over the pipe cross section.

$$u = \frac{2}{R^2}\int_0^R \bar{u}_z r dr$$

$$u = \frac{2}{R^2}\int_0^R u^* \left(8.57\left(\frac{y_w^+}{\alpha}\right)^{\frac{1}{7}}\right) r dr \tag{7.8a}$$

By letting r = R – y and substituting Eq. (7.4) into (7.8a).

$$u = 2u^* \int_0^1 \left(8.57\left(\frac{y(u^*)^{\frac{2-n}{n}}}{\alpha}\right)^{\frac{1}{7}}\right)\left(1-\frac{y}{R}\right) d\,\frac{y}{R} \tag{7.8b}$$

To obtain a Fanning friction – generalized Reynolds number relationship, the following definitions are used.

$$\frac{u^*}{u} = \sqrt{\frac{f}{2}} \tag{a}$$

$$N_{Reg} = \frac{\rho d^n u^{2-n}}{K} \tag{b}$$

Substituting the relations (a) and (b) into Eq. (7.8b) and integrating, the Fanning friction factor equation is derived.

$$f = \frac{2\left(\frac{2^n}{7^{7n}}\right)^{\frac{1}{(3n+1)}}}{\left[(n+1)\frac{N_{Reg}}{2}\right]^{\frac{1}{(3n+1)}}} \tag{7.9}$$

Equation (7.9) represents a modification of the relationship presented by Irvine (1988).

7.4.1 Evaluation of Equation

The accuracy of Eq. (7.9) is assessed using experimental data of Yoo (1974) for 0.3 < n < 0.892. Figures 7.10 and 7.11 show comparisons between predictions and experimental data for n = 0.892 and 0.675, respectively. On the same plot, predictions using the Dodge and Metzner (1959) correlation are shown. In addition, a cross plot between measured Fanning friction factor and predicted Fanning friction factor is shown in Fig. 7.12. The cross plot shows that most data points lie within the ±10% tolerance band. Furthermore, an average percent deviation of 6.6% was calculated. This compares favorably with predictions by the implicit Dodge and Metzner (1959) correlation.

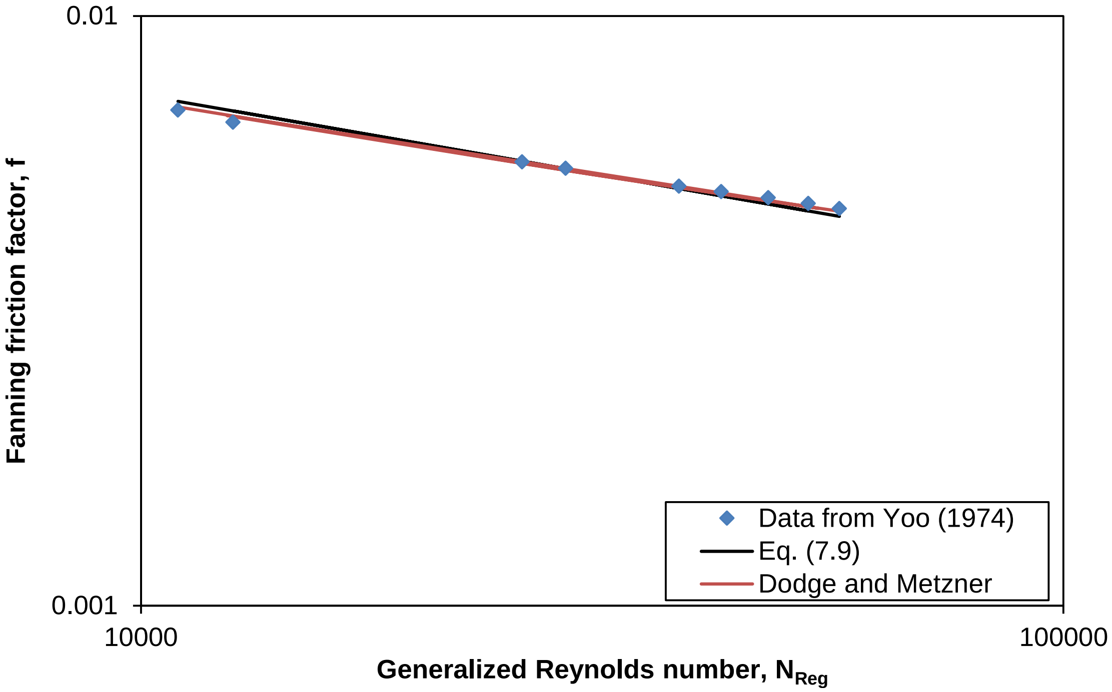

Figure 7.10: Fanning Friction Factor vs. Generalized Reynolds Number for Experimental Data of Yoo (1974) with n = 0.892

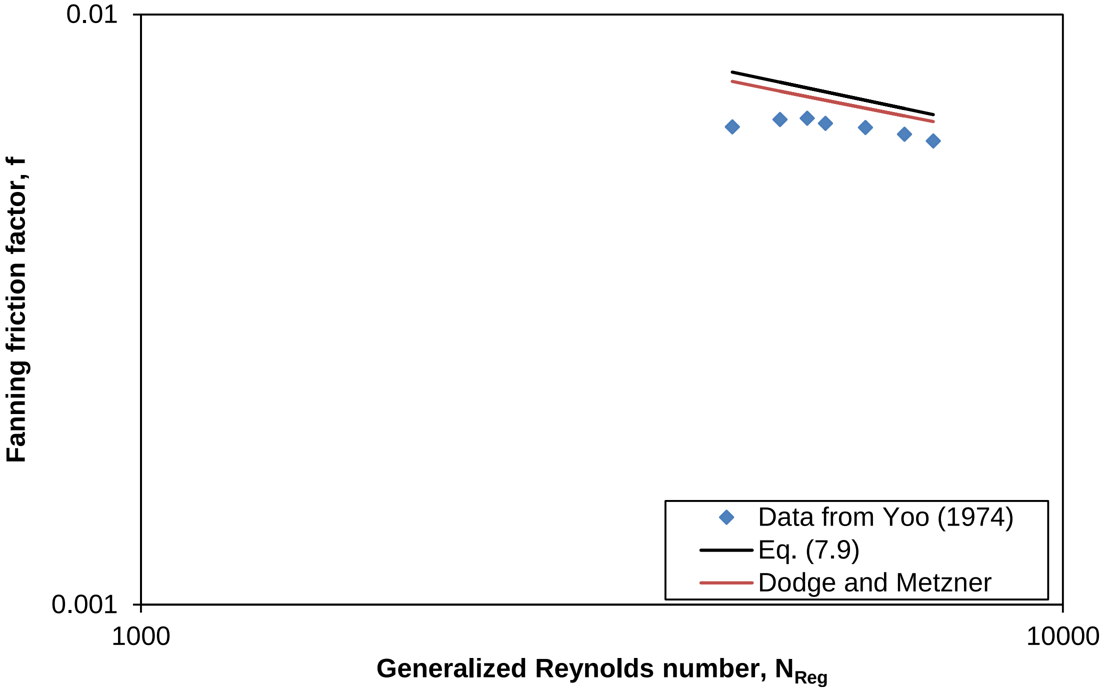

Figure 7.11: Fanning Friction Factor vs. Generalized Reynolds Number for Experimental Data of Yoo (1974) with n = 0.675

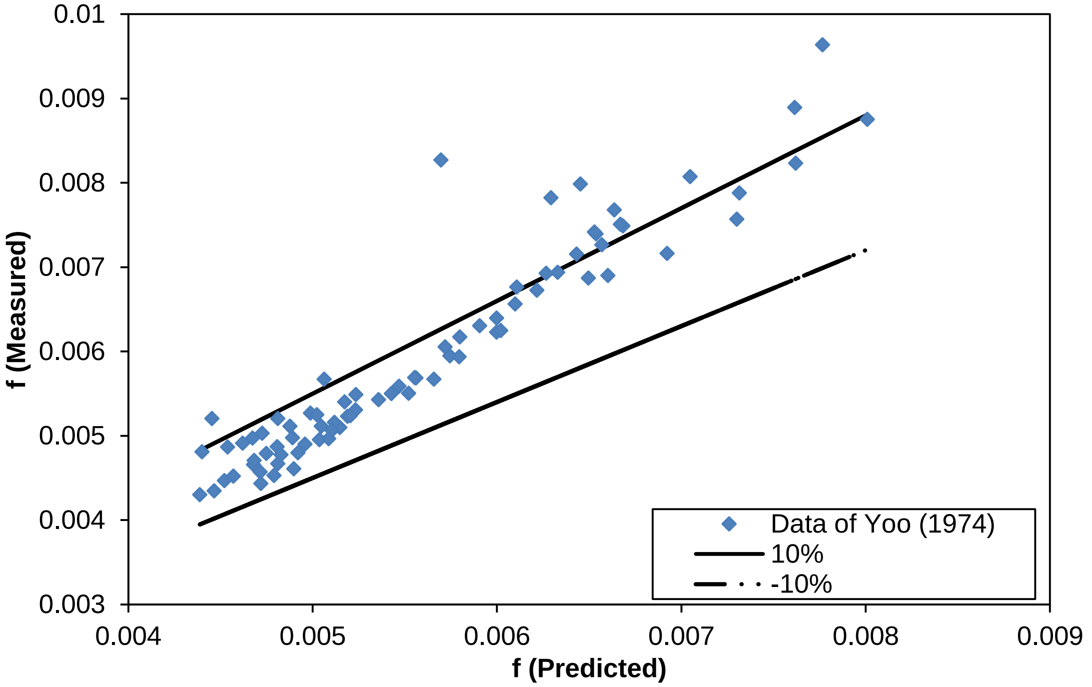

Figure 7.12: Cross Plot of Measured Fanning Friction Factor vs. Predicted Fanning Friction Factor

7.5 Summary

In this chapter, the turbulent flow behavior of surfactant-based fluids was investigated. Flow data were measured using field scale flow-loop to study the effect of various factors on drag reduction characteristics of test solutions. The drag reduction character of surfactant fluids is observed to be strongly affected by concentration, pipe diameter, pipe surface roughness, and solvent type. Favorable drag reduction is recorded with increases in concentration, pipe diameter, and presence of salts. However, pipe roughness is shown to have a negative effect on drag reduction.

A new turbulent friction factor equation is developed for purely viscous fluids in smooth pipes. This equation is shown to predict friction factor with reasonable accuracy for non-drag reducing solutions. Satisfactory agreement is obtained between predicted and measured data with the new equation

Chapter 8

LAMINAR AND TURBULENT ANNULAR FLOW OF NON-NEWTONIAN FLUIDS

8.1 Introduction

The preceding chapters (Chapters 6 and 7) presented information on laminar and turbulent pipe flow behavior of purely viscous and drag reducing fluids (surfactant solutions). Flow of Newtonian and non-Newtonian fluids in annular geometries is typically encountered in many industrial applications, with those in the petroleum and chemical industries as notable examples. In the petroleum industry, annular flow situations arise in oil well drilling, well completion operations, and hydraulic fracturing jobs. Annular flow modeling presents a greater level of complexity as compared with flow through cylindrical ducts. As a result, flow field modeling can be described as nontrivial and has been the subject of many studies.

Generally, fluids are broadly classified as Newtonian or non-Newtonian depending on the shear rate dependence (or not) of viscosity. Analytical solutions to annular flow of Newtonian fluids can be found in many standard chemical or petroleum engineering texts. Non-Newtonian fluids, however, represent a greater challenge because solutions to flow equations can be intractable. This challenge can be attributed to a wide range of rheological character exhibited by many industrial fluids. Industrial fluid systems are often described by complex rheological models that have up to five or six unknown parameters.

In the literature, analytical (exact and approximate) and numerical solutions to annular flow problems have been derived and reported. The nature of these solutions is related to the form of the chosen rheological model. Axial laminar flow of Bingham plastic and power law fluids has been reported by Fredrickson and Bird (1958) as well as by Hanks and Larsen (1979). Analytical solutions to laminar flow of yield-pseudoplastic fluids have been presented by Hanks (1979) and Gucuyener and Mehmetoglu (1992). Concentric annular flow of Eyring and Powell-Eyring fluids was investigated by Nebrensky and Ulbrecht (1968) and Russell and Christiansen (1974), respectively. Analytical and numerical solutions to eccentric annular flow have been reported by Haciislamoglu and Langlinais (1990) for power law and yield-pseudoplastic fluids. Similarly, a solution to flow of a Bingham plastic fluid in an eccentric annulus was presented by Walton and Bittleston (1991).

Many of the studies in the literature deal with laminar flow of non-Newtonian fluids. For turbulent flow of non-Newtonian fluids, a comprehensive theoretical solution to the equation of motion is not possible. In other words, universal solutions to turbulent non-Newtonian fluid flow are unavailable. Consequently, empirical and semi-theoretical approaches have been proposed by several researchers for the purpose of pressure loss estimation.

Turbulent flow is encountered in many industrial processes. For example, in drilling and hydraulic fracturing operations, fluid systems are routinely pumped under turbulent conditions through pipes and annular ducts. Thus, there is a need to understand flow hydrodynamics in such situations (especially in annular ducts) as well as to develop a relationship for friction pressure estimation.

This chapter examines the axial annular flow of pseudoplastic fluids and has three motivations. The first motivation is driven by the objective to develop an approach for determining friction pressure loss suitable for field-wide applications. Here, the power law model is selected because of its simplicity and ease of use for fluid characterization and flow modeling. In achieving this aim, a modified-slot flow approximation is used to derive Fanning friction factor–generalized Reynolds number expressions. Prediction comparisons are made between the current approach and the narrow slot approximation. The second motivation seeks to model the flow of a Carreau fluid (Carreau 1972) through a concentric annulus. The Carreau model is selected because it encompasses a wider range of shear rates, which can be encountered in many industrial processes. With the Carreau model, the flow equation is solved numerically to determine the location of zero shear stress as well as to present design charts in the form of dimensionless pressure drop–flow rate plots for diameter ratios (κ) of 0.1, 0.5, and 0.9 as a function of the flow behavior index. The third motivation of this chapter is to investigate the turbulent annular flow behavior of non-Newtonian drag reducing fluids as well as to develop a simple relationship for determining friction pressure without resorting to complicated numerical computations.

8.2 Review of Previous Work on Annular Flow

The hydrodynamics of annular flow present additional complexities when compared to flow in straight pipes. Studies on annular flow (Heyda 1959; Fredrickson and Bird 1958; Redberger and Charles 1962; Haciislamoglu and Langlianis 1990; Cummings 1993) have been reported in the literature. Laminar and turbulent flow of Newtonian fluids (Heyda 1959; Redberger and Charles 1962) and non-Newtonian fluids (Fredrickson and Bird 1958; McEachern 1966; Ballal and Rivlin 1975 and 1979; Kazakia and Rivlin 1979; Haciislamoglu and Langlianis 1990; Ogugbue and Shah 2010) have been studied experimentally, analytically, and numerically.

Fredrickson and Bird (1958) derived flow rate expressions for both Bingham plastic and power law fluids in cylindrical annuli. McEachern (1966) solved the governing momentum equation to derive flow rate expressions for generalized Newtonian and Ellis fluids. Although important, these earlier efforts focused on flow between two concentric cylinders and represent only an idealized description of wellbore annular flow. In wellbores, an eccentric annular geometry is expected (Fig. 8.1). Eccentricity is defined by the following expression:

$$\varepsilon = \frac{\delta}{(r_2 - r_1)}$$

For concentric annuli, $\varepsilon = 0$, while for a fully eccentric annuli, $\varepsilon = 1$.

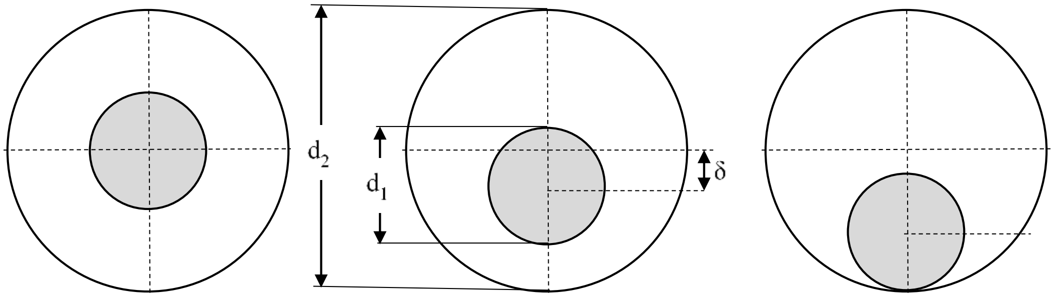

Figure 8.1: Concentric, Partially Eccentric, and Fully Eccentric Annular Geometries

Pressure losses in an eccentric annulus can be as low as 40 to 50% that of a concentric annulus (Haciislamoglu and Langlinais 1990; Cartalos et al. 1996). Eccentricity is a parameter that is impossible to control (Cartalos et al. 1996) in field operations. For horizontal wells however, a fully eccentric annulus is assumed as gravitational forces cause the inner pipe to rest on the bottom of the outer pipe or the wellbore.

Heyda (1959) presented an analytical solution for the velocity profile of steady-state laminar flow of Newtonian fluids in between eccentric cylinders (see Redberger and Charles 1962). Redberger and Charles (1962) extended the work of Heyda (1959) by using bipolar coordinates to numerically obtain a relationship between flow rate and pressure drop. Ballal and Rivlin (1975, 1979) considered the flow of a viscoelastic fluid, characterized by the Rivlin-Ericksen constitutive equation, in between two eccentric cylinders. They studied how the motion of one cylinder affects the eccentric annular flow field. Similarly, Kazakia and Rivlin (1976) expanded on the work of Ballal and Rivlin

(1975) by calculating the forces that occur due to the rotational motion of the inner cylinder about the axis of the outer one.

In 1975, Guckes (1975) presented an approach to predict flow rate and velocity distribution for laminar flow of incompressible non-Newtonian fluids (Bingham plastic and power law). Haccislamoglu (1989) stated that the Guckes' approach is susceptible to numerical instabilities at high eccentricities (see Azouz et al. 1992).

Approximate analytical solutions to eccentric annular flow using the "slot model" have been reported by Tao and Donovan (1955), Vaughn (1965), Iyoho and Azar (1981), Uner et al. (1988), and Luo and Peden (1990). As Haciislamoglu (1989) has pointed out, the mathematical analyses used in some of these studies were erroneous because of the use of inaccurate governing equations (see Azouz et al. 1992; Cummings 1993).

Feldman et al. (1981) presented numerical solutions using bipolar coordinates for developing fully eccentric annular flow. Velusamy et al. (1994) highlighted the shortcomings of the work of Feldman et al. (1981), stating that it applies to a limited range of eccentricities ($\varepsilon > 0.5$) and radius ratios (> 0.5). They provided a complete set of solutions by considering a wider range of eccentricities and diameter ratios.

Using transformations to bipolar coordinates, Haciislamoglu and Langlinais (1990) studied the eccentric annular flow of yield-pseudoplastic fluids. They presented velocity and viscosity profiles at different eccentricities. Haciislamoglu and co-workers (Haciislamoglu and Langlinais 1990; Haciislamoglu and Cartalos 1994), furthermore, developed widely accepted frictional pressure loss correlations for both laminar and turbulent flow of power law fluids. They presented the ratio of pressure loss in an eccentric annulus to that in a corresponding concentric one as a function of the power law flow behavior index, diameter ratio, and eccentricity. Silva and Shah (2000), and later Ogugbue and Shah (2010), developed empirical correlations to determine laminar and turbulent Fanning friction factors for polymeric fluid flow in concentric and fully eccentric annuli. These correlations are valid for conditions under which the experiments were conducted.

8.3 Theoretical Development of Annular Flow

The assumptions used in this work are as follows: 1) steady state and laminar conditions prevail, 2) fluid is incompressible under isothermal conditions, 3) flow is fully developed, and 4) no-slip boundary condition exists at the wall. For one-dimensional flow, the momentum equation in cylindrical coordinates can be expressed as:

$$\frac{1}{r}\frac{\partial}{\partial r}(r\tau_{rz}) = -\frac{\partial p}{\partial z} + \rho g_z = \frac{dp}{dz} \qquad (8.1)$$

where, r is the radial distance, ρ is the fluid density, dp/dz is the pressure gradient, and τ_{rz} is the shear stress.

With Eq. (8.1), the shear stress distribution in an annulus is obtained as:

$$\tau_{rz} = \frac{\Delta p}{2l}\left(r' - \frac{\lambda^2}{r'}\right), \qquad (8.2)$$

where, $r' = \frac{r}{r_2}$, λ is the dimensionless distance of zero shear stress, and l is the length.

8.4 Laminar Flow in an Eccentric Annulus

Fredrickson and Bird (1958) studied the axial flow of non-Newtonian fluids in concentric annuli. They presented an expression to determine the volumetric flow rate or pressure drop. This expression, however, required numerical techniques to obtain solutions, rendering their approach cumbersome. To overcome the difficulties with the Fredrickson and Bird (1958) approach, Hanks and Larsen (1979) presented a simple explicit relationship between pressure drop (Δp) and flow rate (q) that took geometry effects into consideration. Prasanth and Shenoy (1992) also derived the same relationship:

$$q = \frac{\pi n d_2^3}{8(3n+1)}\left(\frac{d_2}{4K}\frac{\Delta p}{l}\right)^{\frac{1}{n}}\left[(1-\lambda^2)^{\frac{n+1}{n}} - \kappa^{\frac{n-1}{n}}(\lambda^2-\kappa^2)^{\frac{n+1}{n}}\right] \tag{8.3}$$

where, n is the flow behavior index, l is pipe length, κ is the diameter ratio (d_1/d_2), and K is the consistency index. The parameter, λ, is the location of maximum velocity. It can be determined by solving the following condition reported by Fredrickson and Bird (1958):

$$\int_\kappa^\lambda \left(\frac{\lambda^2}{\xi} - \xi\right)^{\frac{1}{n}} d\xi - \int_\lambda^1 \left(\xi - \frac{\lambda^2}{\xi}\right)^{\frac{1}{n}} d\xi = 0 \tag{8.4}$$

The solution to Eq. (8.3) involves satisfying the condition in Eq. (8.4). This requires an iterative procedure that limits its applicability.

David and Filip (1995) proposed an alternative technique. They used a quasisimilarity approach between flow through parallel plates (q_{pl}) and concentric annular flow to obtain a simple, approximate, and explicit expression for determining the volumetric flow rate. Their approach eliminates the difficulties with calculating λ in Eq. (8.4), as this parameter is not required. With the David and Filip (1995) approach, the flow rate is:

$$q = q_{pl}\left[1 - \frac{1}{93}n^{-\frac{5}{9}}\left(\frac{1}{\kappa} - 1\right)^{\frac{9}{10}}\right]^{-1} \tag{8.5}$$

where, $q_{pl} = \frac{\pi n R^3}{2(2n+1)}(1+\kappa)(1-\kappa)^{2+\frac{1}{n}}\left(\frac{\Delta p}{l}\frac{R}{2K}\right)^{\frac{1}{n}}$ (8.6)

In the region of $\kappa \geq 0.4$ and $n \geq 0.1$, percent deviations were less than 1%.

Equation (8.5) can be expressed in dimensionless form using the Fanning friction factor and generalized Reynolds number:

$$q = u\frac{\pi}{4}(d_2^2 - d_1^2) \tag{8.7}$$

$$\frac{\Delta p}{l} = \frac{2f\rho u^2}{g_c(d_2 - d_1)} \tag{8.8}$$

where, f is the Fanning friction factor, ρ is the fluid density, u is the fluid velocity, g_c is the conversion factor, d_1 is the outer diameter of the inner pipe, and d_2 is the inner diameter of the outer pipe.

By substituting Eqs. (8.7) and (8.8) into Eq. (8.5) and making algebraic manipulations, the following form of the Fanning friction factor–generalized Reynolds number expression is obtained:

$$f\left[\frac{\beta d_2^{\frac{3n+1}{n}}}{(d_1+d_2)(d_2-d_1)^{\frac{n+1}{n}}}\right]^n \frac{\rho u^{2-n}}{12^{n-1}g_c K\left(\frac{2n+1}{3n}\right)^n} = 24 \tag{8.9}$$

where, $\beta = (1+\kappa)(1-\kappa)^{2+\frac{1}{n}}\left[1-\frac{1}{93}n^{-\frac{5}{9}}\left(\frac{1}{\kappa}-1\right)^{\frac{9}{10}}\right]^{-1}$ (8.10)

From Eq. (8.9), it is obvious that the effective diameter for concentric annuli can be expressed as:

$$d_{eff} = \frac{\beta d_2^{\frac{3n+1}{n}}}{(d_1+d_2)(d_2-d_1)^{\frac{n+1}{n}}} \tag{8.11}$$

Pilehvari and Serth (2009) derived a similar expression for effective diameter. The term β, however, is expressed as an explicit relationship (Eq. 8.10), which eliminates the iterative calculation procedure Pilehvari and Serth (2009) suggested. The effective diameter can be recast in a generalized form using n' and K$_a$':

$$n' = \frac{d\ln(\tau_w)}{d\ln(\dot{\gamma}_w)} \tag{8.12}$$

$$\tau_w = K'(\dot{\gamma}_w)^{n'} \tag{8.13}$$

$$N_{Reg} = \frac{\rho u^{2-n'}\ (d_{eff})^{n'}}{12^{n'-1}K_a'} \tag{8.14}$$

$$\beta = (1+\kappa)(1-\kappa)^{2+\frac{1}{n'}}\left[1-\frac{1}{93}n'^{-\frac{5}{9}}\left(\frac{1}{\kappa}-1\right)^{\frac{9}{10}}\right]^{-1} \tag{8.15}$$

$$d_{eff} = \frac{\beta d_2^{\frac{3n'+1}{n'}}}{(d_1+d_2)(d_2-d_1)^{\frac{n'+1}{n'}}} \tag{8.16}$$

The foregoing equations are applicable to laminar axial flow in a concentric annulus. The effective diameter can be corrected for eccentric annular flow using a conversion term.

8.4.1 Eccentric Annular Flow Correlations

Haciislamoglu and Langlinais (1990) numerically investigated laminar flow through eccentric annuli. They presented an expression (by regression), relating pressure drop in an eccentric annulus to pressure drop in a concentric annulus:

$$\frac{\Delta p_{ecc}}{\Delta p_{conc}} = R_c = 1 - 0.072\frac{\varepsilon}{n}\kappa^{0.8454} - 1.5\varepsilon^2\sqrt{n}\,\kappa^{0.1852} + 0.96\varepsilon^3\sqrt{n}\,\kappa^{0.2527} \qquad (8.17)$$

where, ε is pipe eccentricity. In the region 0.3 ≤ κ ≤ 0.9, 0 ≤ ε ≤ 0.9, and 0.4 ≤ n ≤ 1, a relative deviation of less than 5% was obtained with Eq. (8.17).

Similarly, Pilehvari and Serth (2009) presented a conversion correlation using numerical data by Fang et al. (1999) and Escudier et al. (2002). Their correlation is expressed as follows:

$$\frac{\Delta p_{ecc}}{\Delta p_{conc}} = R_c = 1 - 0.1019\varepsilon n\,\kappa^{0.8454} - 1.6152\varepsilon^2 n^{0.085}\,\kappa^{0.7875} + 1.1434\varepsilon^3 n^{0.0547}\,\kappa^{1.1655} \qquad (8.18)$$

Equation (8.18) is valid for 0.2 ≤ n ≤ 1.0, 0.2 ≤ κ ≤ 0.8, and 0 ≤ ε ≤ 0.98.

In this study, the form of Eq. (8.17) is adopted. It was deemed necessary to develop a correction term by using experimental data (with realistic field annular geometries) for widely used oilfield fluids. Thus, regression is performed on experimental flow data for guar fluid (at concentrations of 20, 30, 40, and 60 lb/Mgal) and a surfactant solution [5% (v/v) Aromox® APA-TW] through fully eccentric annuli. The rheological properties and flow data (with tubing configurations) for the fluids used are given in Table 8.1 and Fig. 8.2, respectively. The resulting correlation for $\frac{\Delta p_{ecc}}{\Delta p_{conc}}$ is given as:

$$\frac{\Delta p_{ecc}}{\Delta p_{conc}} = R_c = 1 - \frac{0.0456}{n} \kappa^{0.7786} - 1.437\sqrt{n}\,\kappa^{0.03672} + 0.965\sqrt{n}\,\kappa^{0.4288} \tag{8.19}$$

Equation (8.19) is valid for $0.25 \leq n \leq 0.65$ and $0.64 \leq \kappa \leq 0.82$.

Using these conversion correlations, the effective diameter for laminar flow in an eccentric annulus can be calculated using Eq. (8.20).

$$d_{eff} = \frac{\beta d_2^{\frac{3n'+1}{n'}}}{(d_1+d_2)(d_2-d_1)^{\frac{n'+1}{n'}}(R_c)^{\frac{1}{n}}} \tag{8.20}$$

The accuracy of Eq. (8.19) is evaluated by comparing predictions with experimental data for welan gum solutions at two concentrations: 1.75 and 2.25 lb/bbl. Specifically, laminar flow data in fully eccentric annuli are used for comparative analysis. The flow loop consists of 3.5-in. x 1.75-in., and 5.5-in. x 4-in. fully eccentric annuli. For the purpose of analysis, the friction pressure and flow rate were converted to the generalized Reynolds number and Fanning friction factor using Eqs. (8.14) and (8.21), respectively.

$$f = 154.65\,\frac{(d_2-d_1)\left(d_2^2-d_1^2\right)^2 \Delta p}{l\rho q^2} \tag{8.21}$$

The parameters in Eq. (8.20) are in oilfield units.

Figures 8.3 and 8.4 show comparisons of the predicted and measured data using 1.75 and 2.25 lb/bbl welan solutions using Eq. (8.19) and the effective diameter definition for eccentric annular flow. It can be seen from both figures that reasonably good matches were obtained between the measured data and predictions with Eq. (8.19). Average percent deviations of 6.0% and 13.7% are calculated for 1.75 lb/bbl welan solution in 3.5-in. x 1.75-in., and 5.5-in. x 4-in. eccentric annuli, respectively. Similarly, average percent deviations of 4.9% and 12.2% are calculated for 2.25 lb/bbl welan solution in 3.5-in. x 1.75-in., and 5.5-in. x 4-in. eccentric annuli, respectively. Thus, the satisfactory matches confirm the accuracy and reliability of Eq. (8.19) in predicting pressure losses for the laminar flow of non-Newtonian fluids in fully eccentric annuli.

Table 8.1: Rheological Properties of Test Fluids

Fluid	Concentration	Flow Geometry (in.)	n	K_v ($lb_f\ s^n/ft^2$)
Guar*	20 lbm/Mgal	3.5 x 1.75	0.618	2.93E-03
		5.5 x 4 and 5 x 3.5	0.651	1.86E-03
	30 lbm/Mgal	3.5 x 1.75	0.546	8.85E-03
		5.5 x 4 and 5 x 3.5	0.536	6.94E-03
	40 lbm/Mgal	3.5 x 1.75	0.436	2.51E-02
		5.5 x 4 and 5 x 3.5	0.471	1.67E-02
	60 lbm/Mgal	3.5 x 1.75	0.36	8.27E-02
		5.5 x 4 and 5 x 3.5	0.341	7.79E-02
Aromox® APA-TW	5%	3.5 x 1.75, 5.5 x 4, 5 x 3.5	0.387	1.78E-02

* Adapted from Ogugbue and Shah (2010)

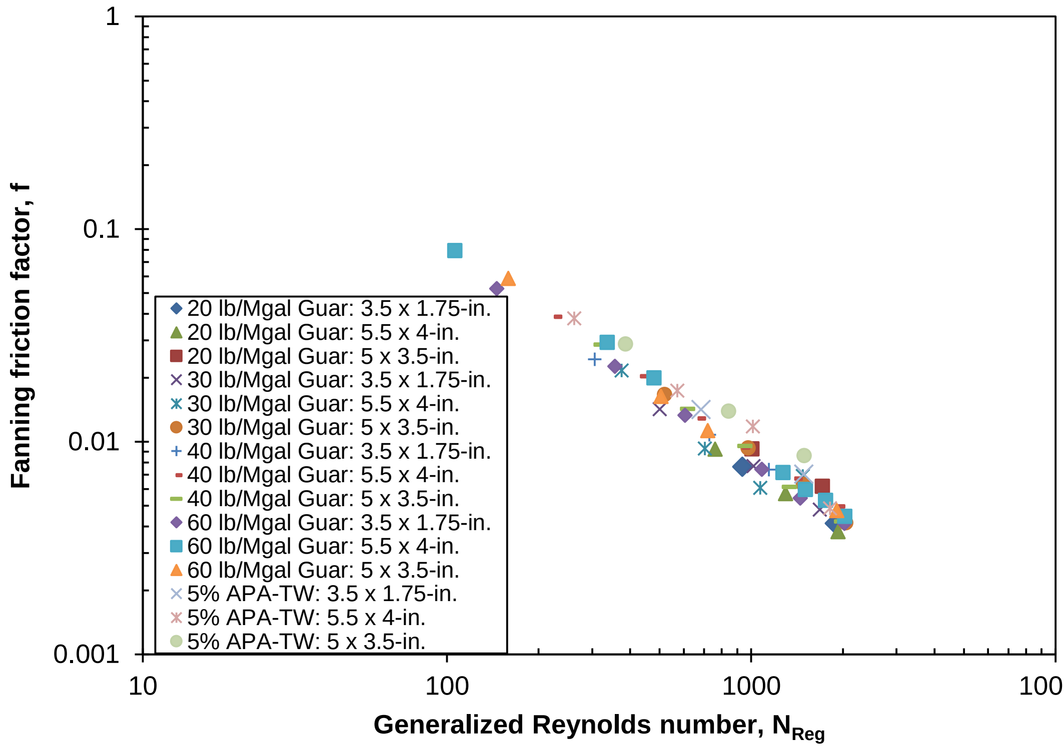

Figure 8.2: Composite Plot of Fanning Friction Factor vs. Generalized Reynolds Number for Laminar Flow of Guar and Aromox® APA-T Solutions

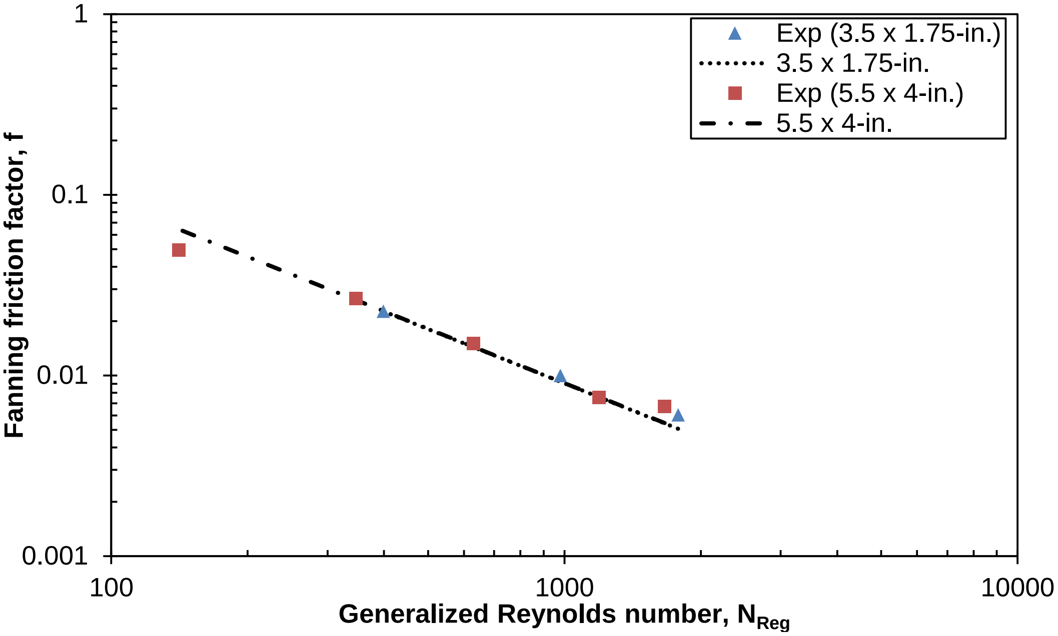

Figure 8.3: Fanning Friction Factor vs. Generalized Reynolds Number for Laminar Flow of 1.75 lb/bbl Welan Solution. Fluid Data: n = 0.206, K_v = 0.084 $lb_f\ s^n/ft^2$

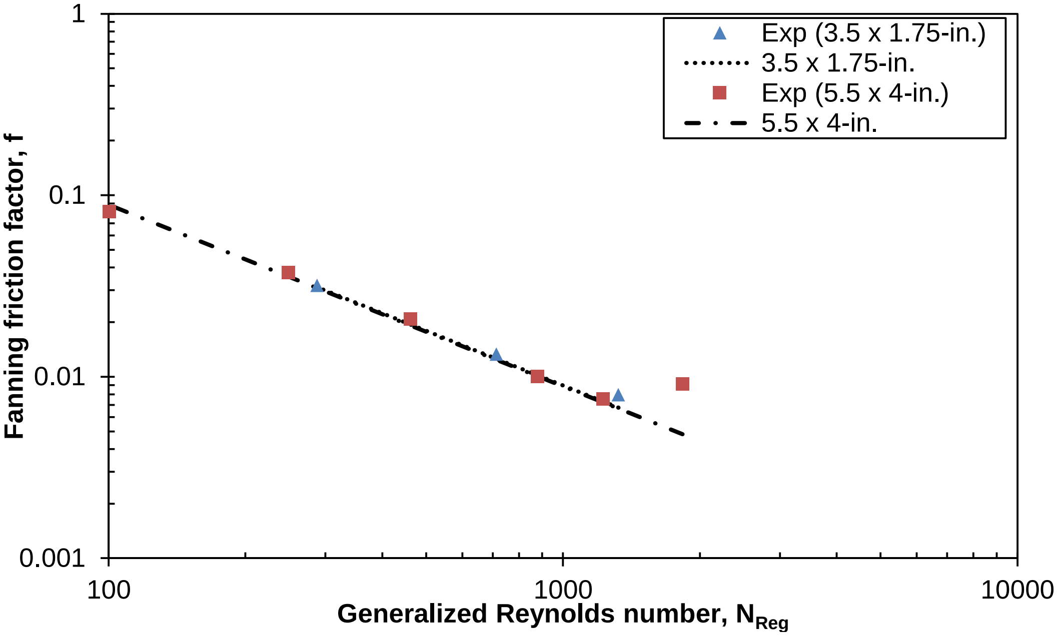

Figure 8.4: Fanning Friction Factor vs. Generalized Reynolds Number for Laminar Flow of 2.25 lb/bbl Welan Solution. Fluid Data: n = 0.177, K_v = 0.137 $lb_f\ s^n/ft^2$

The correlations above (Eqs. 8.17 - 8.19) are valid for laminar flow of non-Newtonian fluids. For turbulent flow of non-drag reducing non-Newtonian fluids, the Dodge and Metzner correlation (Dodge and Metzner 1959) is used in combination with the effective diameter definition given in Eq. (8.16). The Dodge and Metzner correlation is expressed as:

$$\frac{1}{\sqrt{f}} = \frac{4}{(n')^{0.75}} \log\left[N_{Reg} f^{1-\frac{n'}{2}}\right] - \frac{0.395}{(n')^{1.2}} \tag{8.22}$$

8.4.2 Comparison with Experimental Data

The accuracy of friction pressure predictions using the proposed approach for concentric and eccentric annular flow is evaluated. In addition, prediction comparisons are made between the current approach and the narrow slot approximation. The power law laminar flow equation using the narrow slot approximation is given in Appendix IV. Experimental flow data for concentric annuli from studies of Okafor and Evers (1992) and Langlinais et al. (1983) are considered for comparative purposes. Flow data from Okafor and Evers (1992) were gathered in the laminar regime, whereas data by Langlinais et al. (1983) covered both laminar and turbulent regimes. For eccentric annular flow, experimental data (for three fluids -1, 2, and 3) are obtained from the study of Subramanian (1995), as reported by Pilehvari and Serth (2009) and the study of Ahmed (2005). Experimental data (XCD-PAC2 and XCD-PAC3) from the study of Ahmed (2005) were gathered in the laminar flow regime.

Figures 8.5 and 8.6 show predictions with the present approach, slot flow approximation results, and experimental results of Okafor and Evers (1992) for two fluids (A and B). Fluid A has the following properties: $\rho = 8.9$ lb/gal, $n = 0.581$, and $K_v = 0.00775$ lb_f s^n/ft^2. Similarly, the properties of Fluid B are: $\rho = 8.65$ lb/gal, $n = 0.163$, and $K_v = 0.157$ lb_f s^n/ft^2. Both figures show excellent agreement between the predicted and measured data. Average percent deviations of 9.7% and 6.6% were calculated for fluids A and B, respectively. Good agreement can be seen between the slot flow approximation and experimental data with average percent deviations of 14% and 3.5% for fluids A and B, respectively.

In Fig. 8.7, comparisons between pressure loss predictions for concentric annular flow with experimental results of Langlinais et al. (1983) are shown. Slot flow approximation results are presented in this figure. The fluid properties are: $\rho = 8.8$ lb/gal, $n = 0.784$, and $K_v = 0.00144$ lb_f s^n/ft^2. Excellent agreement can be observed between predictions and experimental data, with an average percent deviation of 5.9%. A good match is obtained between the slot flow approximation and experimental data with an average percent deviation of 8%.

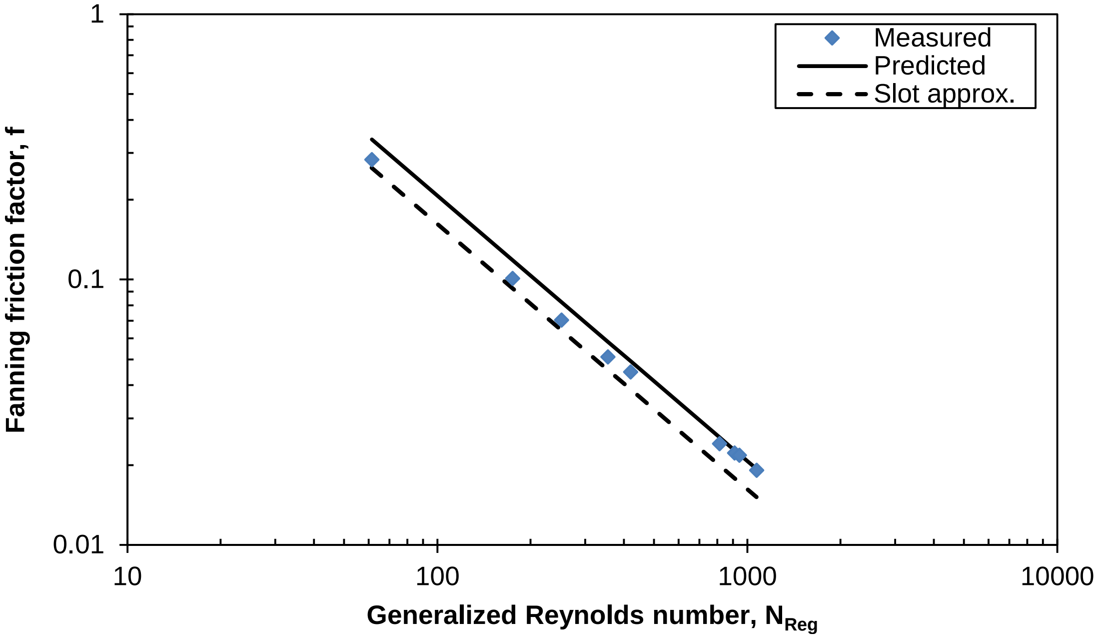

Figure 8.5: Comparison of Predictions with Measured Data of Okafor and Evers (1992) for Fluid A. Annulus Dimension: 3.0469 x 1.8984-in.

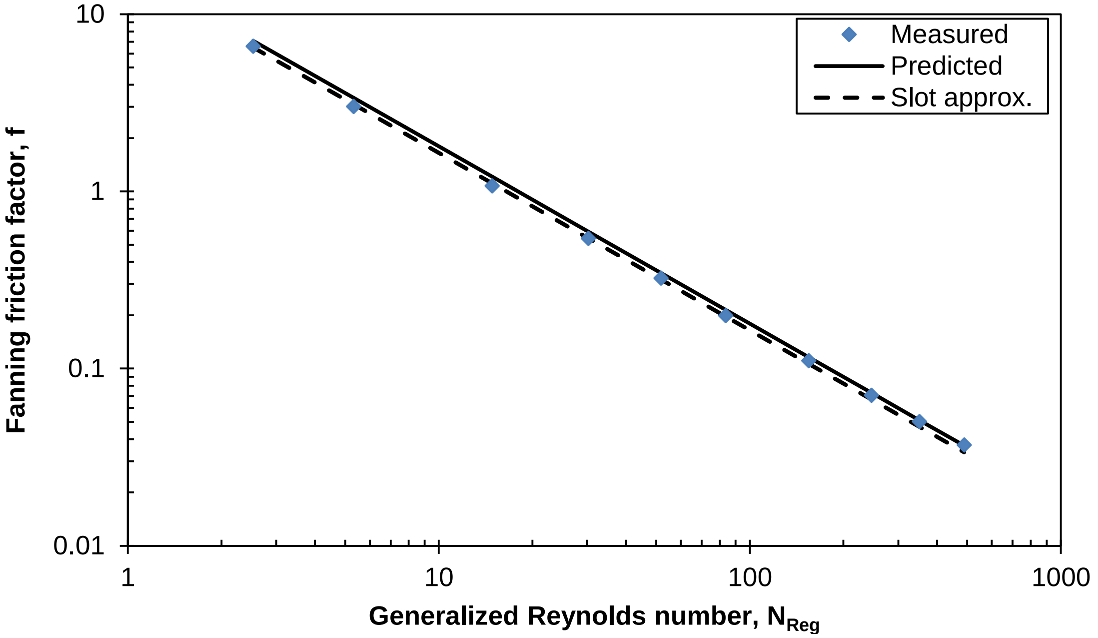

Figure 8.6: Comparison of Predictions with Measured Data of Okafor and Evers (1992) for Fluid B. Annulus Dimension: 3.0469 x 1.8984-in.

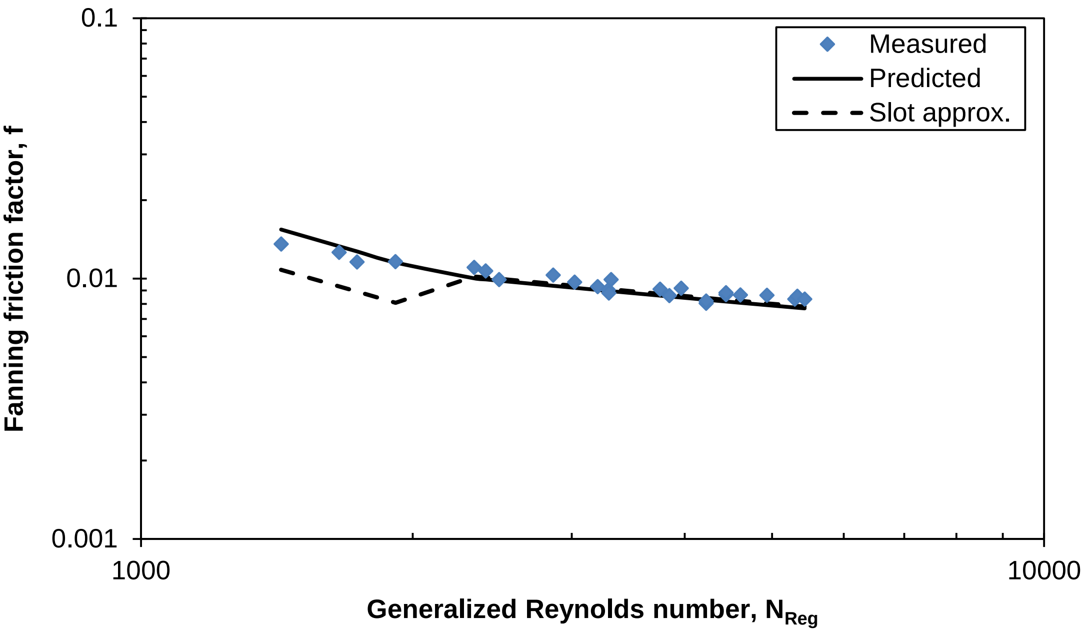

Figure 8.7: Comparison of Predictions with Measured Data of Langlinais et al. (1983), Annulus Dimension: 2.441 x 1.315-in.

Figures 8.8 through 8.10 show experimental data from the study of Subramanian (1995), model predictions and slot flow approximation results using the effective diameter definition for fully eccentric annular flow of three fluids – 1, 2, and 3. Fluid 1 has the following properties: ρ = 8.53 lb/gal, n = 0.602, K_v = 0.00199 lb_f s^n/ft^2. Fluid 2 has the following properties: ρ = 8.68 lb/gal, n = 0.488, K_v = 0.0197 lb_f s^n/ft^2. The properties of Fluid 3 are: ρ = 8.72 lb/gal, n = 0.397, K_v = 0.0848 lb_f s^n/ft^2. Also evident from these plots are comparisons among the various conversion correlations given in Eqs. (8.17) – (8.19). Satisfactory agreement is observed between model predictions (irrespective of the correlation) and experimental data. Table 8.2 reports the average percent deviation between the predicted and measured data. In addition, the mean percent deviations using the iterative approach by Pilehvari and Serth (2009) are reported in Table 8.2. It is evident that the present approach compares favorably and eliminates the need to adopt the Pilehvari and Serth (2009) iterative scheme. For subsequent eccentric annular flow analysis, the Haciislamoglu and Langlinais correlation is used. With the slot flow approximation, average percent deviations of 20.6%, 17.3%, and 8.2% are calculated between predictions and flow data for fluids 1, 2, and 3, respectively.

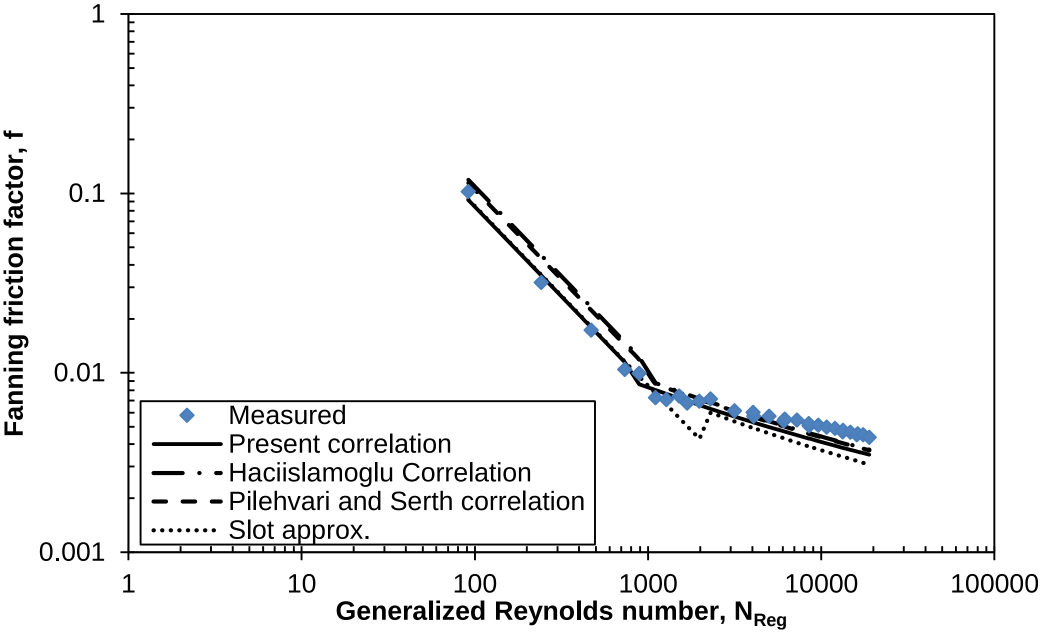

Figure 8.8: Comparison of Predictions with Measured Data of Subramanian (1995) for Fluid 1. Annulus Dimension: 5.023 x 2.375-in.

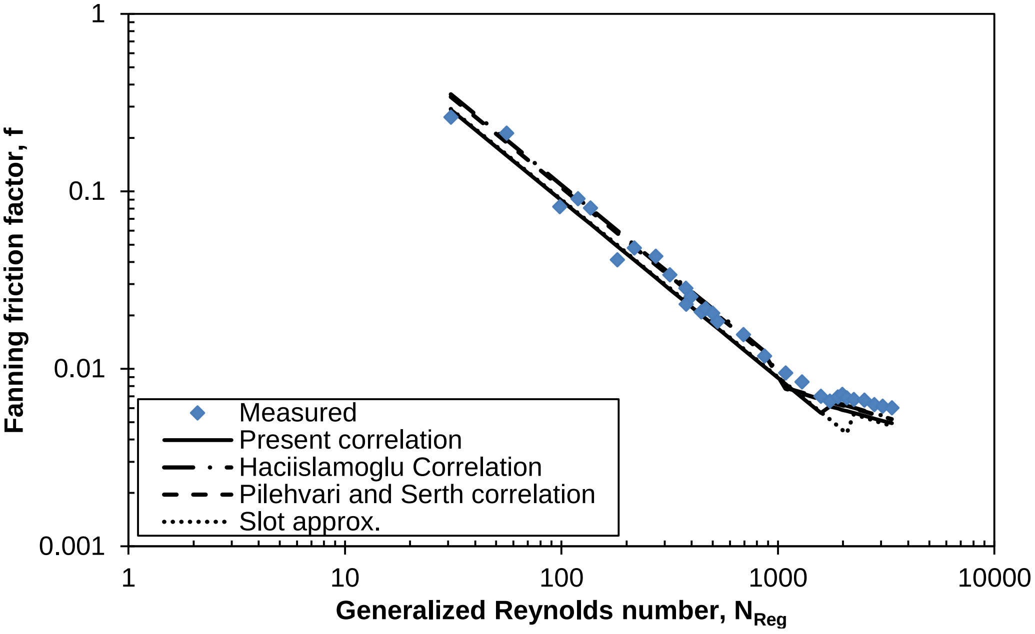

Figure 8.9: Comparison of Predictions with Measured Data of Subramanian (1995) for Fluid 2. Annulus Dimension: 5.023 x 2.375-in.

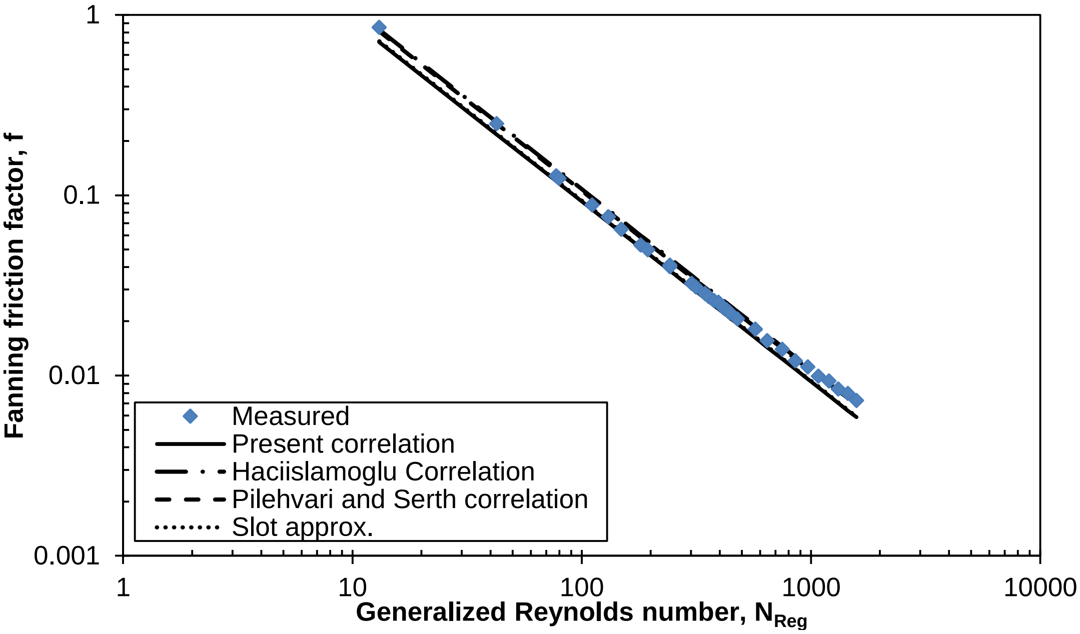

Figure 8.10: Comparison of Predictions with Measured Data of Subramanian (1995) for Fluid 3. Annulus Dimension: 5.023 x 2.375-in.

Table 8.2: Comparison of Mean Average Percent Deviation between Predictions and Experimental data of Subramanian (1995)

Fluid	**Eq. (8.19)**	**Haciislamoglu and Langlinais correlation**	**Pilehvari and Serth correlation**	**Pilehvari and Serth approach***
1	15.6	11.2	13.5	14.9
2	15.0	11.4	10.9	10.3
3	9.0	7.7	6.2	5.6

* Reported by Pilehvari and Serth (2009)

Predictions with the current approach, slot flow approximation results, and experimental data from the study of Ahmed (2005) are presented in Figs. 8.11 and 8.12. XCD-PAC2 has the following properties: ρ = 8.33 lb/gal, n = 0.305, K_v = 0.148 lb_f s^n/ft^2. XCD-PAC3 has the following properties: ρ = 8.33 lb/gal, n = 0.489, K_v = 0.0231 lb_f s^n/ft^2. From both figures, the current approach and experimental data are in good agreement. Average percent deviations of 16.2% and 12.8% are calculated for XCD-PAC2 and XCD-PAC3 between model predictions and experimental data. On the other hand, higher percent average deviations are calculated between the slot flow approximation and experimental data; percent average deviations of 25% and 20.4% for XCD-PAC2 and XCD-PAC3 are calculated, respectively.

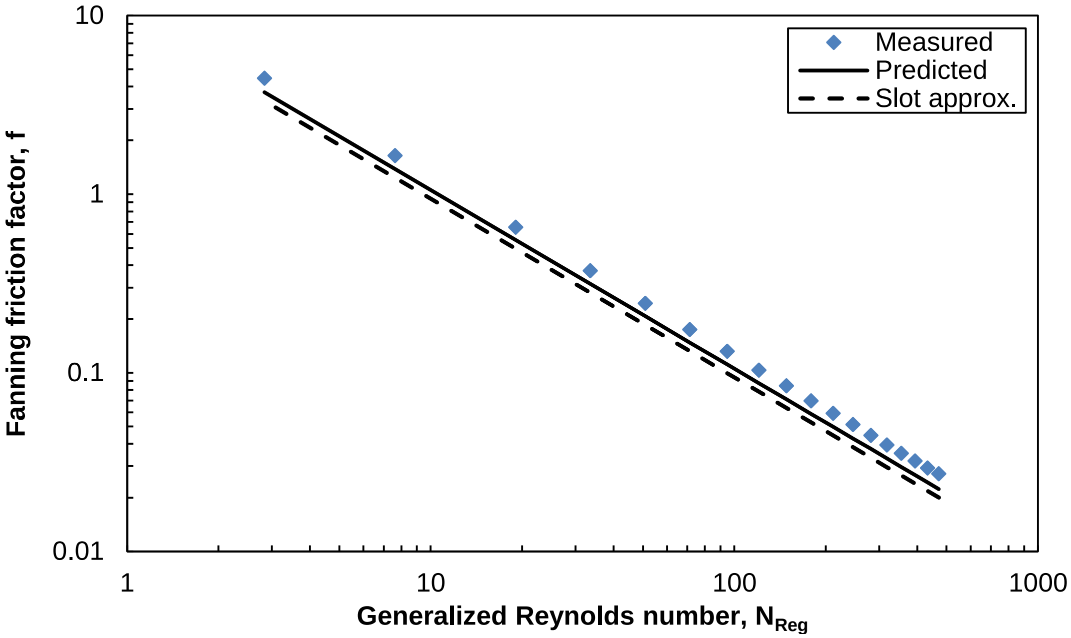

Figure 8.11: Comparison of Predictions with Measured Data of Ahmed (2005) for XCD-PAC2. Annulus Dimension: 1.38 x 0.68-in.

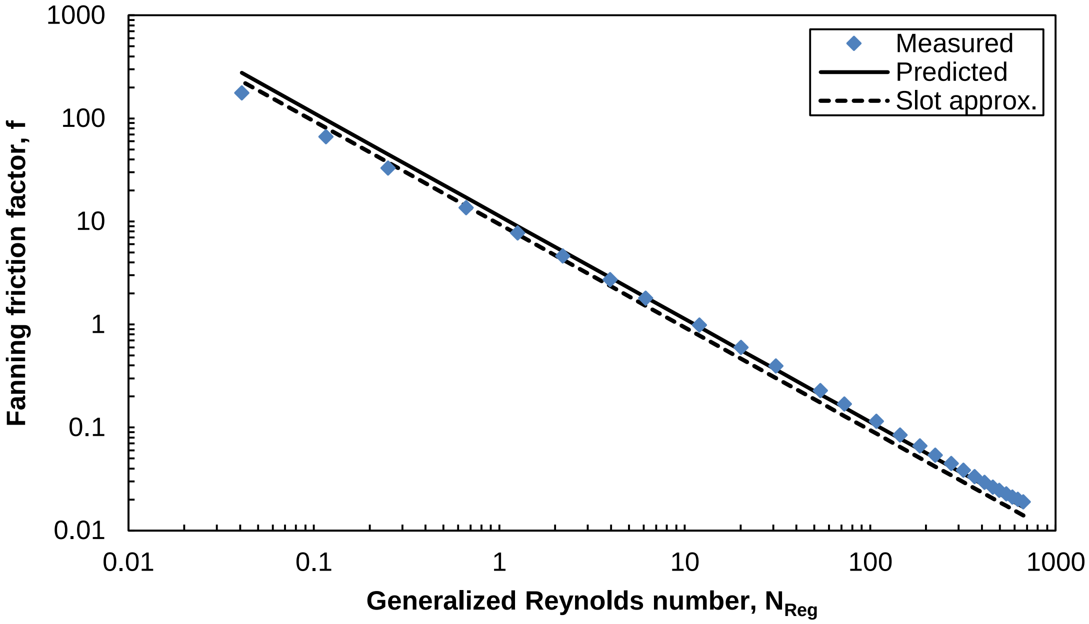

Figure 8.12: Comparison of Predictions with Measured Data of Ahmed (2005) for XCD-PAC3. Annulus Dimension: 1.38 x 0.5-in.

8.5 Annular Flow of Power Law Fluid

As earlier stated, Fredrickson and Bird (1958) and Hanks and Larsen (1979) derived relationships between flow rate and pressure drop for power law fluids. The rheological model for the power law fluid is expressed in Eq. (8.23).

$$\tau_{rz} = K\left(-\frac{du}{dr}\right)^{n} \tag{8.23}$$

In this study, the approach by Mishra and Mishra (1976) with improvements is adopted. The normalized velocity distribution is of the form:

$$\frac{u_r}{u_m} = \left(1 - Z^{\frac{n+1}{n}}\right), \tag{8.24}$$

where, Z is the dimensionless distance from zero shear stress, n is the flow behavior index, u_r is the velocity distribution, and u_m is the maximum velocity. The velocity profiles for the two regions in the annulus are expressed as (Mishra and Mishra 1976):

Inner Region ($r_1 \leq r \leq r_m$)

$$\frac{u_1}{u_m} = 1 - \left(\frac{r_m - r}{r_m - r_1}\right)^{\frac{n+1}{n}} \tag{8.25}$$

Outer Region ($r_m \leq r \leq r_2$)

$$\frac{u_2}{u_m} = 1 - \left(\frac{r - r_m}{r_2 - r_m}\right)^{\frac{n+1}{n}}, \tag{8.26}$$

where, r_m is the radius of maximum velocity, r_1 is the outer radius of the inner pipe, and r_2 is the inner radius of the outer pipe.

With Eqs. (8.25) and (8.26), the average velocity can be expressed as:

$$\frac{u}{u_m} = \left[\frac{(n+1)}{(1+\kappa)}\right]\left[\frac{(2n+1)(1+\kappa)+2n\lambda}{(3n+1)(2n+1)}\right] \tag{8.27}$$

In conventional drilling, the diameter ratios tend to be greater than 0.5. For coiled tubing operations, higher diameter ratios (> 0.8) are encountered. Thus, the slot approach is deemed suitable for the present study. By combining the slot approximation with the quasisimilarity factor presented by David and Filip (1995), the maximum velocity (u_m) expression can be written as:

$$u_m = \left(\frac{\Delta p}{Kl}\right)^{\frac{1}{n}}\left(\frac{n}{n+1}\right)\left(\frac{h}{2}\right)^{\frac{n+1}{n}}\left(1-\frac{1}{93}n^{-\frac{5}{9}}\left(\frac{1}{\kappa}-1\right)^{\frac{9}{10}}\right)^{-1}, \tag{8.28}$$

where, h is the height of the slot, K is the consistency index, and κ is the diameter ratio.

An expression for h (for an eccentric annulus) was derived by Vaughn (1965) and subsequently modified by Iyoho and Azar (1981).

$$h = (r_2^2 - \varepsilon^2 c^2 \sin^2\theta)^{\frac{1}{2}} - r_1 + \varepsilon c \cos\theta \tag{8.29a}$$

As a basis for derivation, Eq. (8.29a) is reduced to Eq. (8.29b) for a concentric annulus:

$$h = r_2 - r_1 \tag{8.29b}$$

A Fanning friction factor–generalized Reynolds number relationship is derived by substituting Eqs. (8.28) and (8.29b) into Eq. (8.27) as well as by using the following pressure loss equation:

$$f = \frac{\Delta p(d_2-d_1)g_c}{2l\rho u^2} \tag{8.30}$$

$$f\left(wd_h\frac{(n+1)}{(1+\kappa)}\left[\frac{(2n+1)(1+\kappa)+2n\lambda}{(3n+1)(2n+1)}\right]\right)^n\frac{u^{2-n}\rho}{k\left(\frac{n}{n+1}\right)^n g_c 8^{n-1}}=16 \tag{8.31}$$

$$w=\left(1-\frac{1}{93}n^{-\frac{5}{9}}\left(\frac{1}{\kappa}-1\right)^{\frac{9}{10}}\right)^{-1}$$

For slot flow, λ = 1. Eq. (8.31) represents an expression for determining the Fanning friction factor. By comparison with the relationship f N_{Reg} = 16, the following generalized Reynolds number and effective diameter (d_{eff}) expressions can be obtained:

$$N_{Reg}=\frac{u^{2-n}d_{eff}^n\rho}{k\left(\frac{n}{n+1}\right)^n g_c 8^{n-1}} \tag{8.32}$$

$$d_{eff}=\left(wd_h\frac{(n+1)}{(1+\kappa)}\left[\frac{(2n+1)(1+\kappa)+2n}{(3n+1)(2n+1)}\right]\right) \tag{8.33}$$

The effective diameter can be modified to account for eccentric annular flow with the conversion factor developed by Haciislamoglu and Langlinais (1990). Thus, the effective diameter for eccentric annular flow is expressed as:

$$d_{eff}=\left(wd_h\frac{(n+1)}{(1+\kappa)}\left[\frac{(2n+1)(1+\kappa)+2n}{(3n+1)(2n+1)}\right]\frac{1}{(R_c)^{\frac{1}{n}}}\right) \tag{8.34}$$

8.5.1 Evaluation of Fanning Friction Factor Relationship

The accuracy of predictions using the proposed approach is compared with experimental data from various sources in literature. For concentric annular flow, pressure drop data from the studies of Okafor and Evers (1992) and Langlinais et al. (1983) are used for comparative purposes. For fully eccentric annular flow, flow data from the studies of

Subramanian (1995) and Ahmed (2005), are used. The fluid properties for experimental data used as well as annular dimensions are reported Sect. 8.4.2.

Figures 8.13 to 8.15 are Fanning friction factor–generalized Reynolds number plots for concentric annular data. Figures 8.13 and 8.14 show predictions with the current approach, slot flow approximation results, and experimental results of Okafor and Evers (1992) for two fluids—A and B. It is obvious that there is good agreement between the proposed method and experimental data. Average percentage deviations of 6.9% and 6.3% are calculated for fluids A and B, respectively. Figure 8.15 shows a comparison between the predictions and experimental results of Langlinais et al. (1983). There is a satisfactory match between the predictions and flow data, as an average deviation of 7.4% is calculated. In Figs. 8.13 to 8.15, good matches are obtained between slot flow approximation results and experimental data (see Sect. 8.4.2).

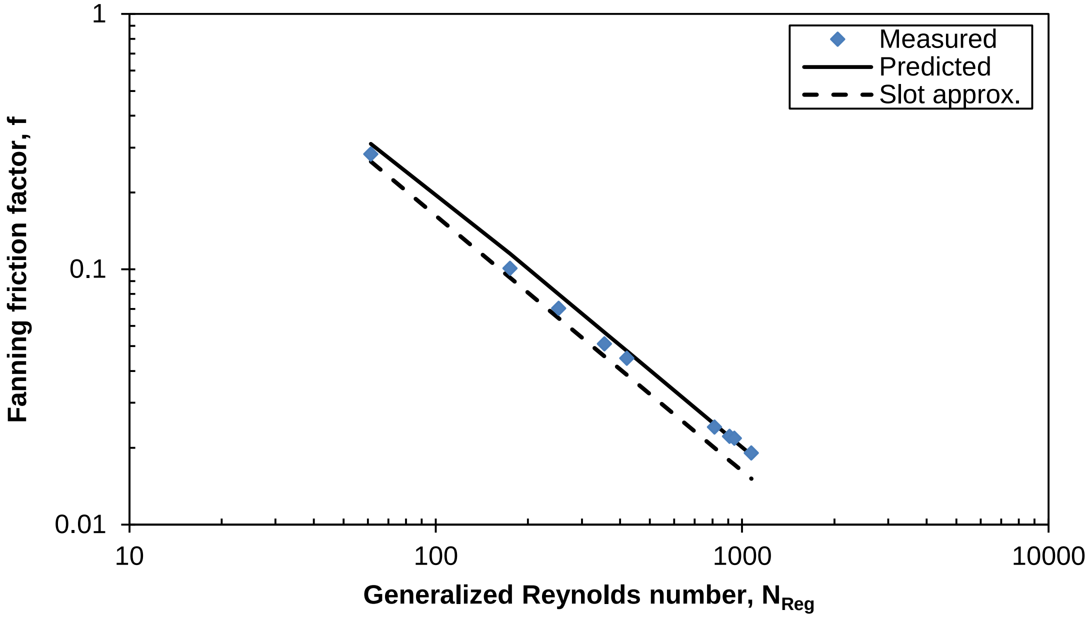

Figure 8.13: Comparison of Predictions with Experimental Results of Okafor and Evers (1992) – Fluid A. Annulus Dimension: 3.0469 x 1.8984-in.

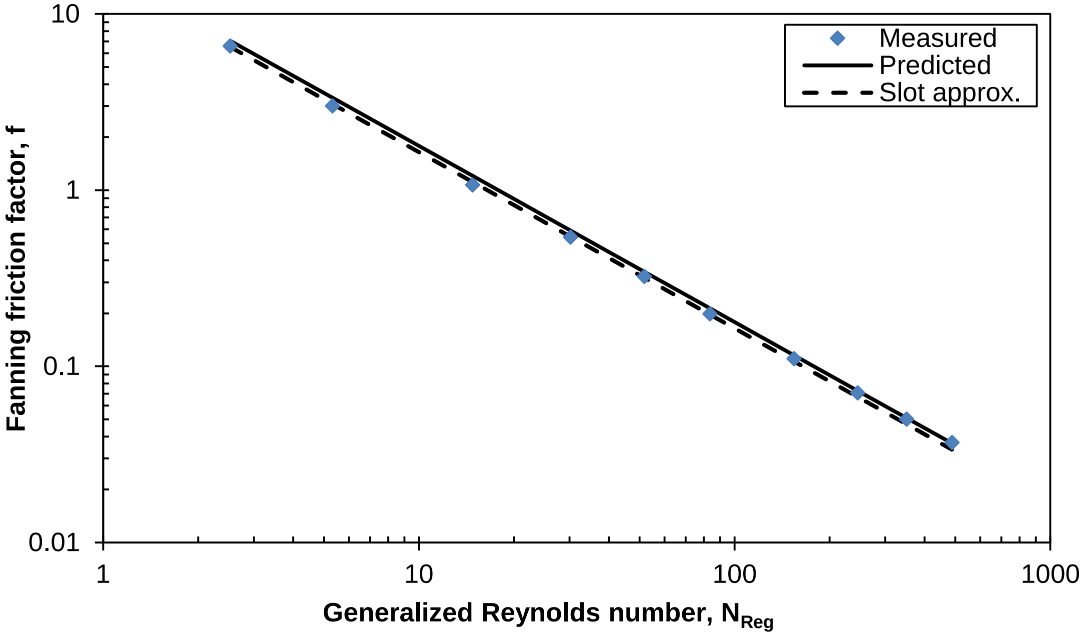

Figure 8.14: Comparison of Predictions with Experimental Results of Okafor and Evers (1992) – Fluid B. Annulus Dimension: 3.0469 x 1.8984-in.

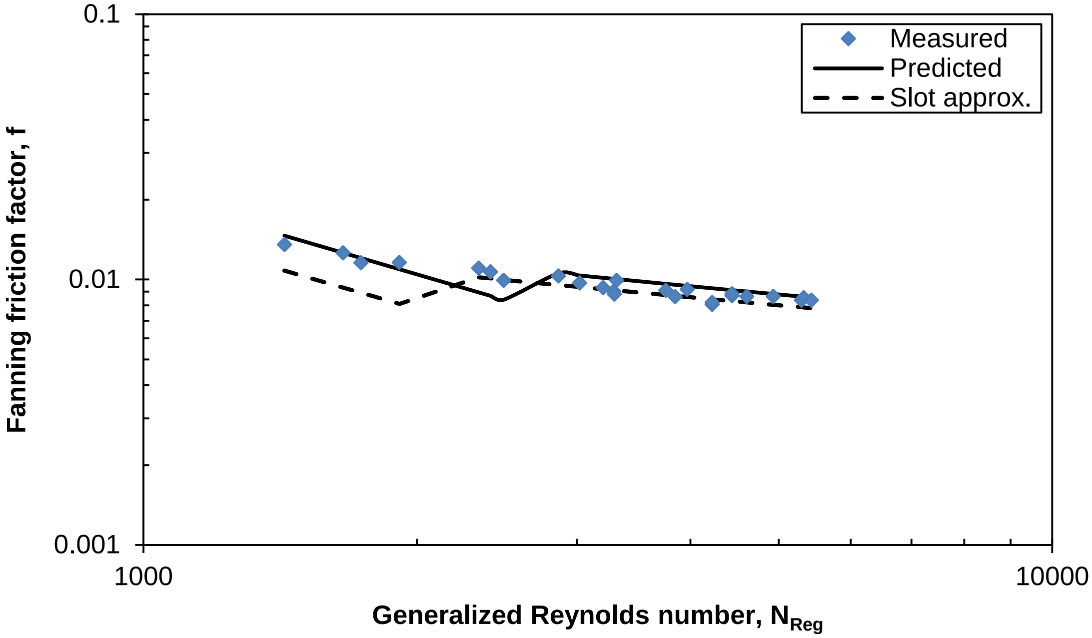

Figure 8.15: Comparison of Predictions with Experimental Results of Langlinais et al. (1983). Annulus Dimension: 2.441 x 1.315-in.

Figures 8.16 to 8.18 show comparisons between predictions and experimental data from Subramanian (1995) for flow in an eccentric annulus for fluids 1, 2, and 3. Slot flow approximation results can be seen in these figures. In all these figures, there is a reasonable match between predictions and experimental data. However, slightly higher average percentage deviations are calculated as compared with the concentric case described above. Average percentage deviations of 12.3%, 9.1%, and 8.7% are calculated for fluids 1, 2, and 3, respectively. With the slot approximation, average percent deviations of 20.6%, 17.3%, and 8.2% are calculated for fluids 1, 2, and 3, respectively.

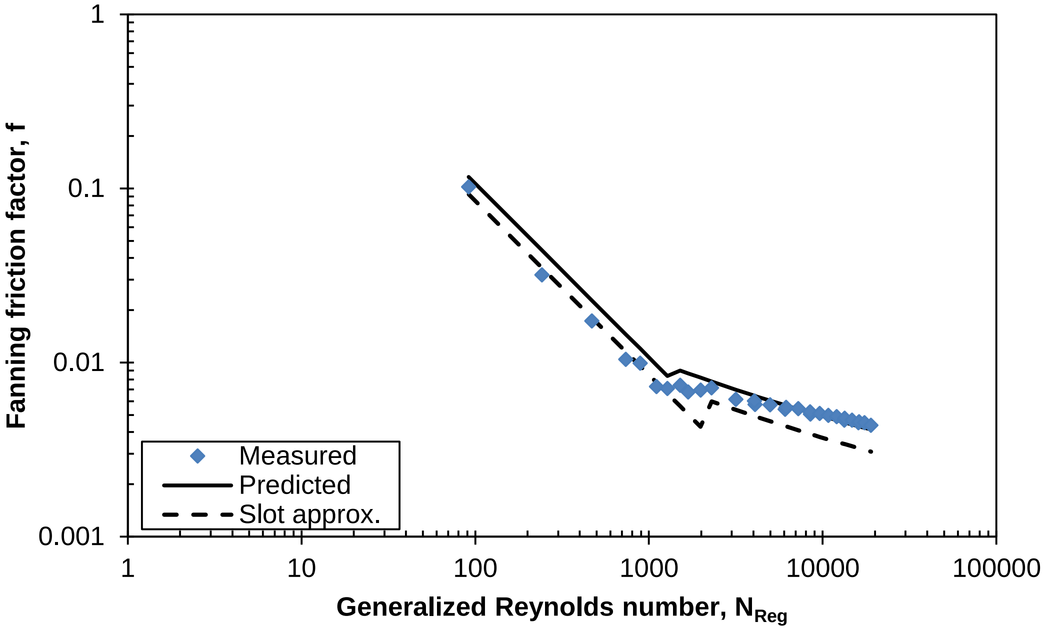

Figure 8.16: Comparison of Predictions with Experimental Results of Subramanian (1995) – Fluid 1. Annulus Dimension: 5.023 x 2.375-in.

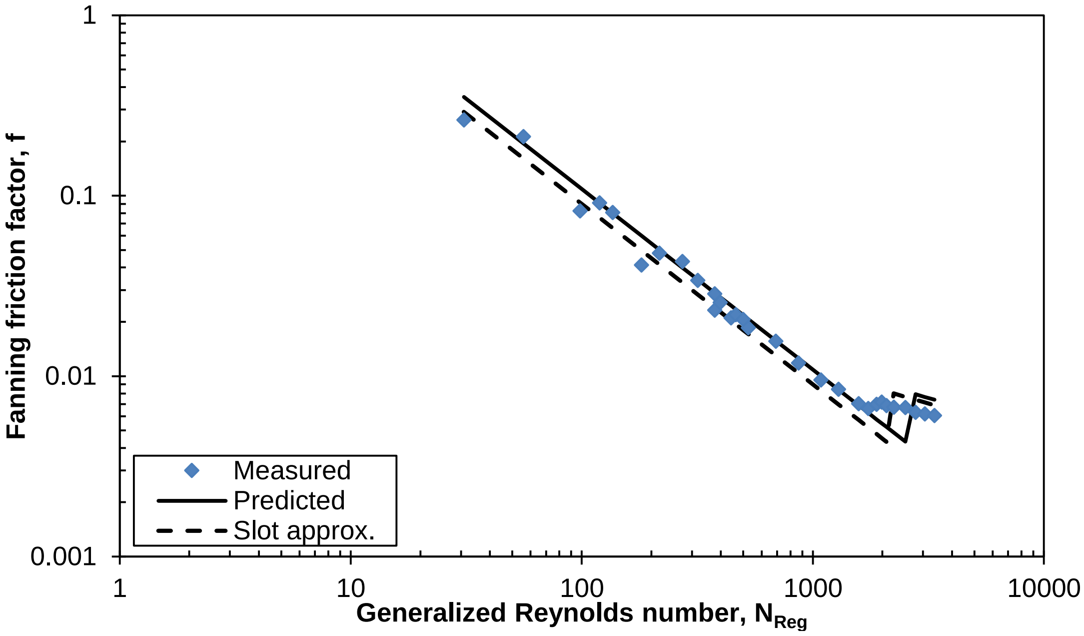

Figure 8.17: Comparison of Predictions with Experimental Results of Subramanian (1995) – Fluid 2. Annulus Dimension: 5.023 x 2.375-in.

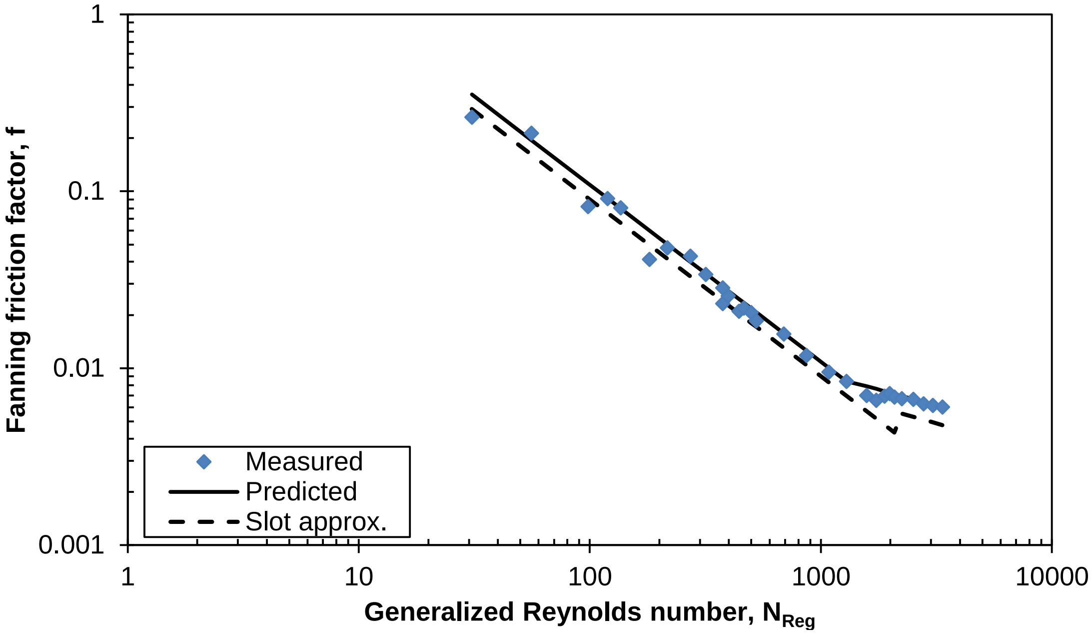

Figure 8.18: Comparison of Predictions with Experimental Results of Subramanian (1995) – Fluid 3. Annulus Dimension: 5.023 x 2.375-in.

Model predictions, slot flow approximation results, and flow data from the study of Ahmed (2005) are presented in Figs. 8.19 and 8.20. It is clear from both figures that model predictions accurately match experimental data; percent average deviations of 1.9% and 13.2% for XCD-PAC2 and XCD-PAC3 are calculated, respectively. However, higher percent deviations are calculated between slot flow approximation predictions and flow data; average percent deviations of 25% and 20.4% are calculated for XCD-PAC2 and XCD-PAC3, respectively.

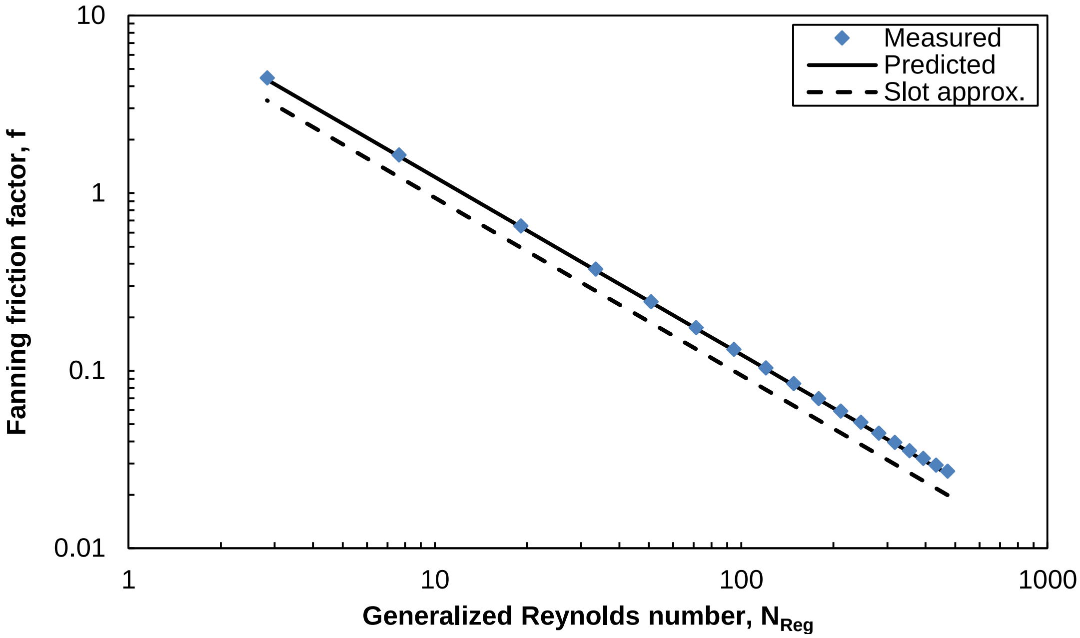

Figure 8.19: Comparison of Predictions with Experimental Results of Ahmed (2005) for XCD-PAC2. Annulus Dimension: 1.38 x 0.68-in.

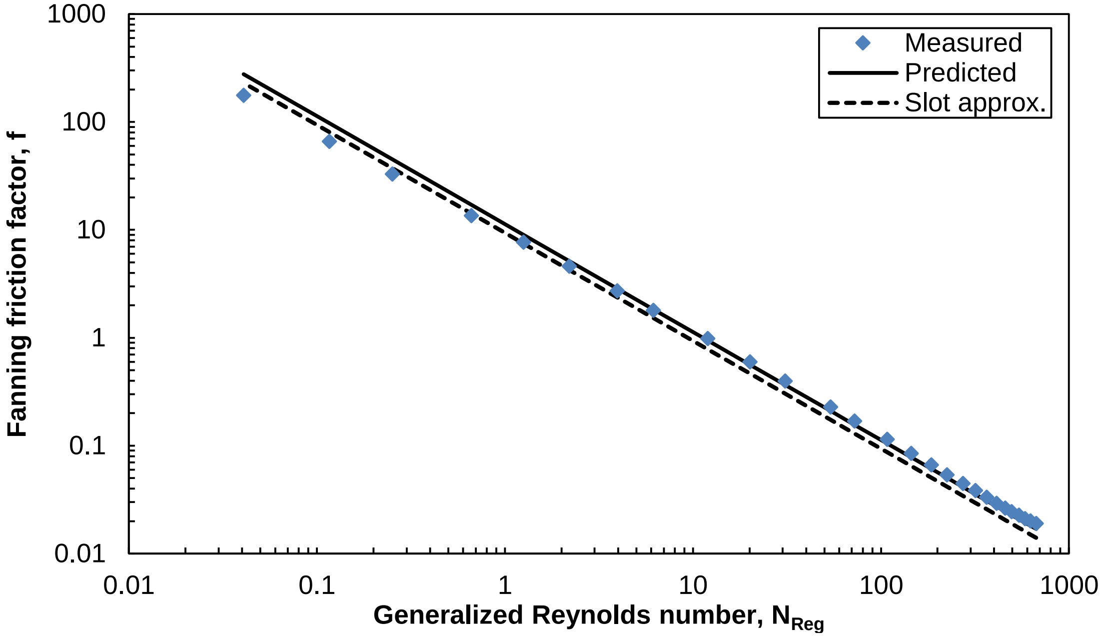

Figure 8.20: Comparison of Predictions with Experimental Results of Ahmed (2005) for XCD-PAC3. Annulus Dimension: 1.38 x 0.5-in.

8.6 Annular Flow of Carreau Fluid

The preceding sections focused on friction pressure estimation for annular flow of a power law fluid. In this section, the Carreau model is considered. The Carreau model has the advantage of having a broader range of shear rates spanning the low and high shear rate regions as compared with the power law model. The power law model represents the simplest constitutive equation that relates the apparent viscosity to the rate of shear of a generalized Newtonian fluid. The shortcomings of the power law model are well known.

The power law model yields infinite viscosity in the zero shear rate range which can be described as physically unrealistic. At high shear rates, the power law model predictions zero viscosity. As a rheological model, the Carreau model provides a way of describing many fluid systems from a fluid characterization standpoint. The Carreau model is suitable for structural fluids that display complex behavior. However, for flow field modeling, it is impossible to obtain simple analytical solutions useful for field applications. Dealing with the Carreau model requires utilizing numerical techniques to solve flow equations.

The Carreau model is expressed as:

$$\tau_{rz} = \frac{\mu_o}{\left[1+\left(t\left|\frac{du}{dr}\right|^2\right)\right]^{\frac{1-n}{2}}}\left(-\frac{du}{dr}\right) \tag{8.35}$$

where, μ_o is the zero shear rate viscosity, t is the time constant, and du/dr is the velocity gradient.

In solving the equation of motion, the following dimensionless parameters are used:

$$q' = \frac{q\,t}{2\pi r_2^3}$$

$$\Delta p' = \frac{\Delta p t r_2}{2 l \mu_o}$$

$$u' = \frac{u\,t}{r_2}$$

$$\tau' = \frac{\tau\,t}{\mu_o}$$

$$\dot{\gamma}' = t\,\dot{\gamma}$$

$$r' = \frac{r}{r_2}$$

Substituting these parameters into Eq. (8.35) gives the dimensionless expression for the Carreau model:

$$\tau' = \frac{\dot{\gamma}'}{[1+(\dot{\gamma}')^2]^{\frac{1-n}{2}}} \tag{8.36}$$

The momentum equation (Eq. 8.1) and the shear stress distribution expression (Eq. 8.2) can be rewritten as:

$$\frac{1}{r'}\frac{d}{dr'}(r'\tau') = 2\Delta p' \tag{8.37}$$

$$\tau' = \Delta p'\left(r' - \frac{\lambda^2}{r'}\right) \tag{8.38}$$

Combining Eqs. (8.36) and (8.37) results in the following expression:

$$\Delta p'\left(\frac{\lambda^2}{r'} - r'\right) = \frac{\frac{du'}{dr'}}{\left[1+\left|\frac{du'}{dr'}\right|^2\right]^{\frac{1-n}{2}}} \tag{8.39}$$

Equation (8.39) is solved numerically for the location of zero shear stress (λ) and dimensionless volumetric flow rate (q'). Parameters λ and q' were determined for $\Delta p'$, ranging from 0.1 to 10,000, and n varying from 0.2 to 0.8 in intervals of 0.2. The results are presented in Figs. 8.21 and 8.22 for λ as a function of $\Delta p'$ (for diameter ratios (κ) of 0.1 and 0.5). In both figures, λ is normalized with respect to the location of zero shear stress for a Newtonian fluid (λ_N). Dimensionless plots of pressure drop against flow rate are shown in Figs. 8.23 to 8.28 for the diameter ratios studied (0.1, 0.5, and 0.9).

The following observations can be made from annular flow of a Carreau fluid:

1. The location of zero shear stress is not constant for $\Delta p' < 10$. This is evident with a decrease in diameter ratio for each flow behavior index value. The magnitude of λ increases with $\Delta p'$ until a certain point above which it remains constant.
2. At high diameter ratios, λ remains constant.
3. Curves corresponding to various flow behavior indices collapse to a single line at low $\Delta p'$ values, which is more evident at high diameter ratios.
4. There is a decrease in the magnitude of q' with an increase in diameter ratio for the same $\Delta p'$.

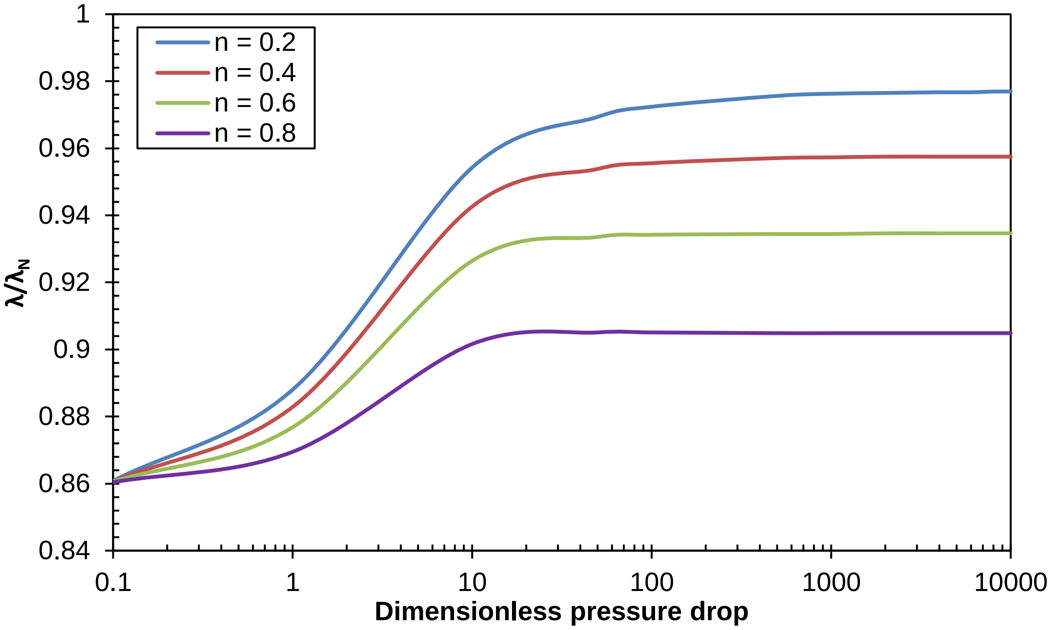

Figure 8.21: Computed Values of λ/λN against Dimensionless Pressure Drop for κ = 0.1

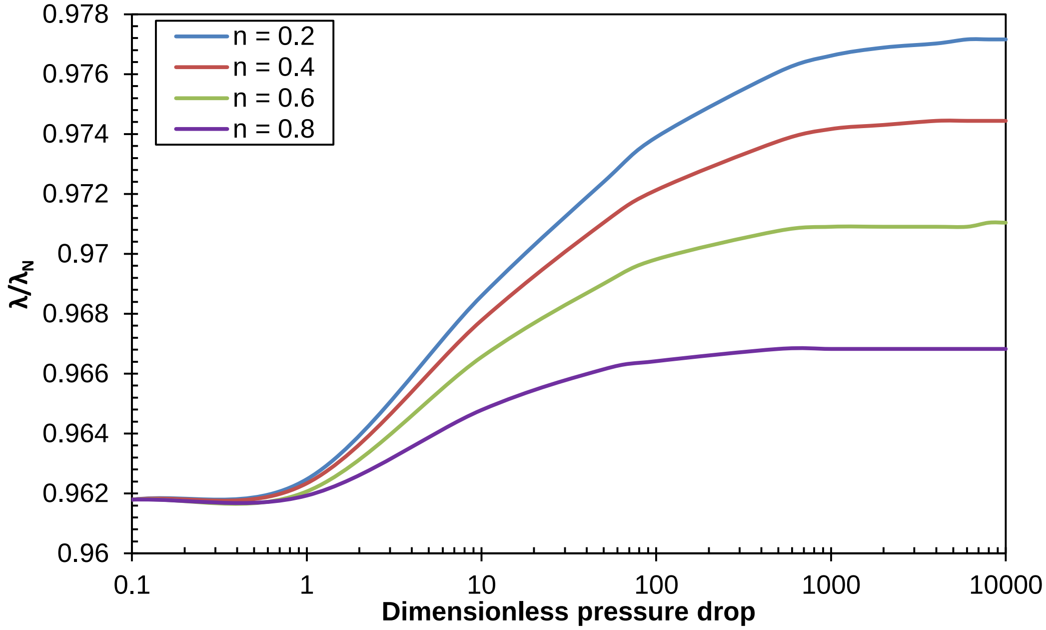

Figure 8.22: Computed Values of λ/λN against Dimensionless Pressure Drop for κ = 0.5

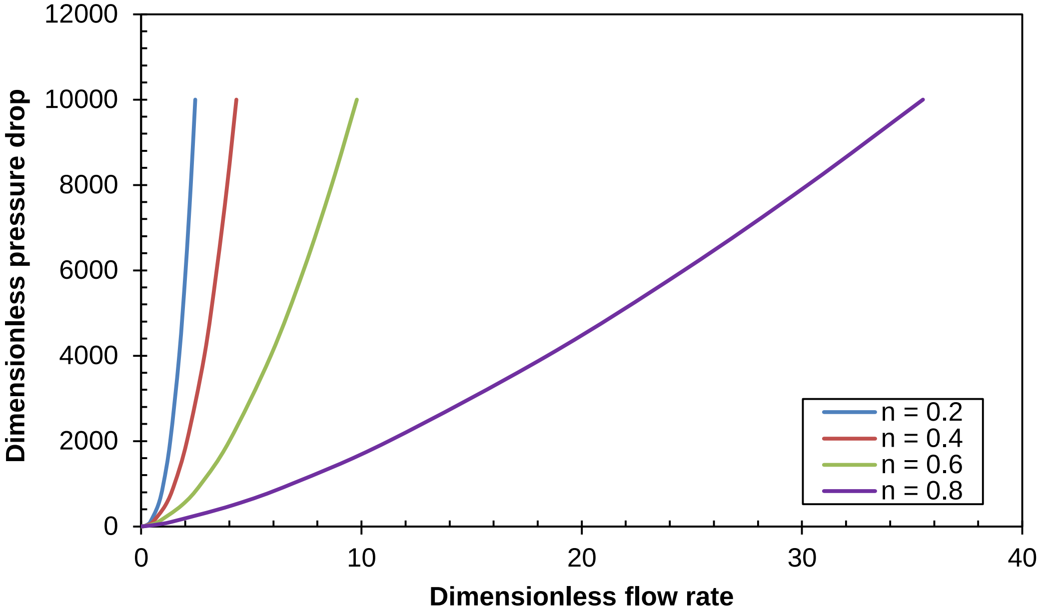

Figure 8.23: Dimensionless Plot of Pressure Drop vs. Flow Rate for Carreau Fluid in Annulus, κ = 0.1

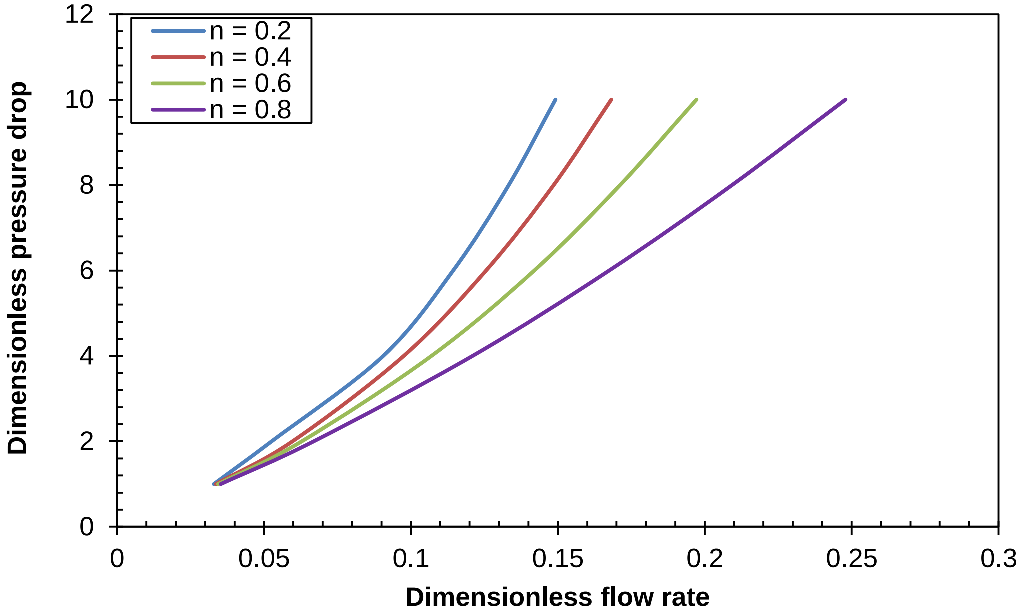

Figure 8.24: Dimensionless Plot of Pressure Drop vs. Flow Rate for Carreau Fluid in Annulus, κ = 0.1 (Δp' < 10)

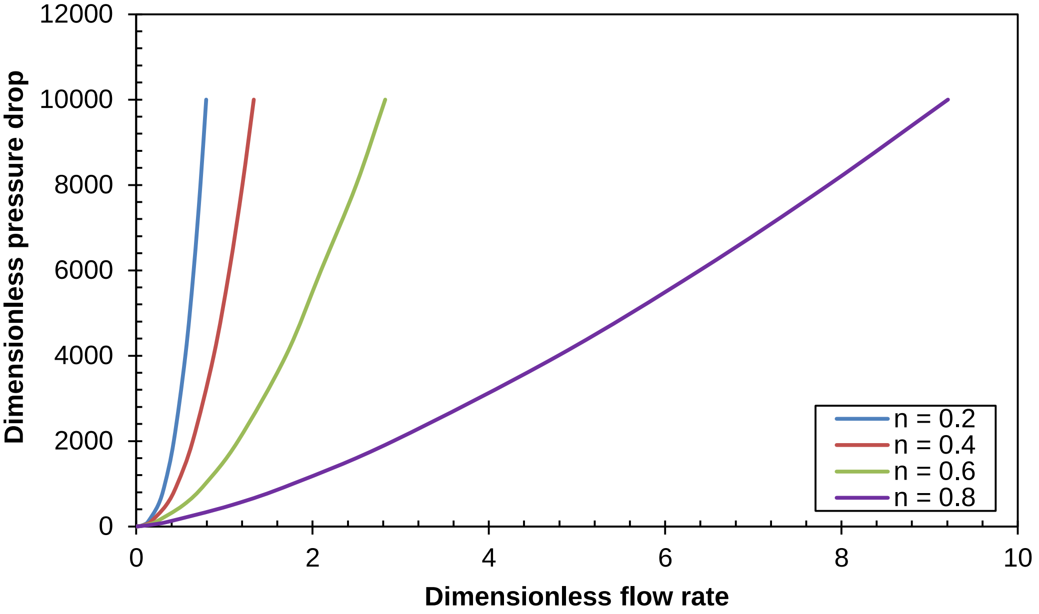

Figure 8.25: Dimensionless Plot of Pressure Drop vs. Flow Rate for Carreau Fluid in Annulus, κ = 0.5

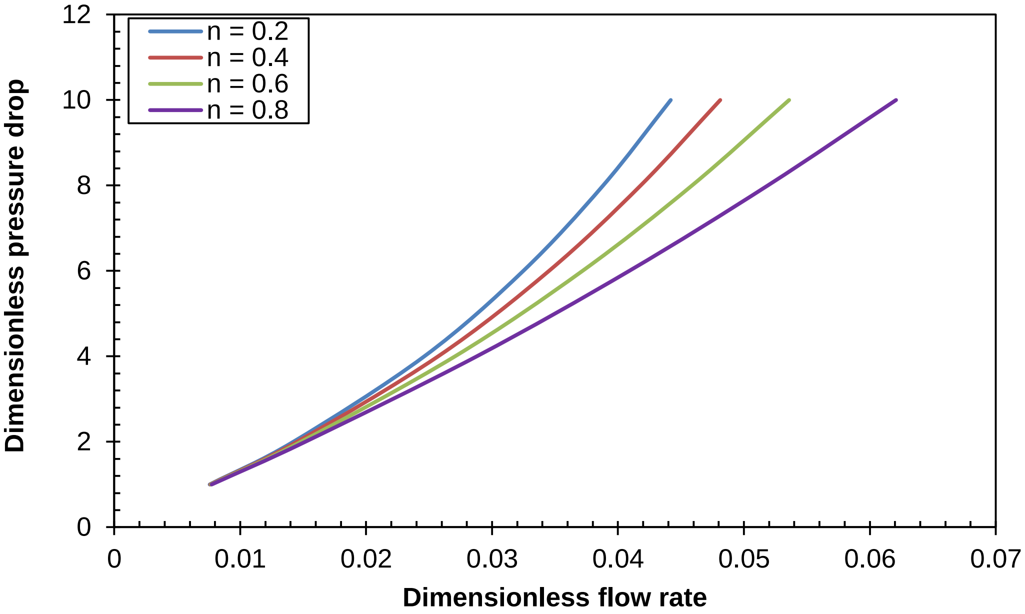

Figure 8.26: Dimensionless Plot of Pressure Drop vs. Flow Rate for Carreau Fluid in Annulus, κ = 0.5 (Δp' < 10)

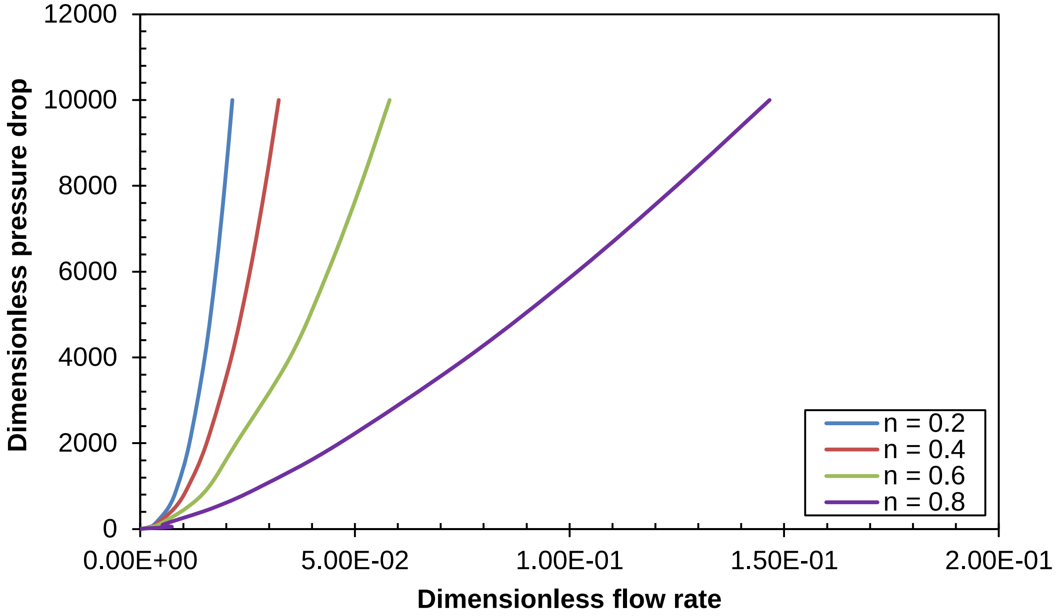

Figure 8.27: Dimensionless Plot of Pressure Drop vs. Flow Rate for Carreau Fluid in Annulus, κ = 0.9

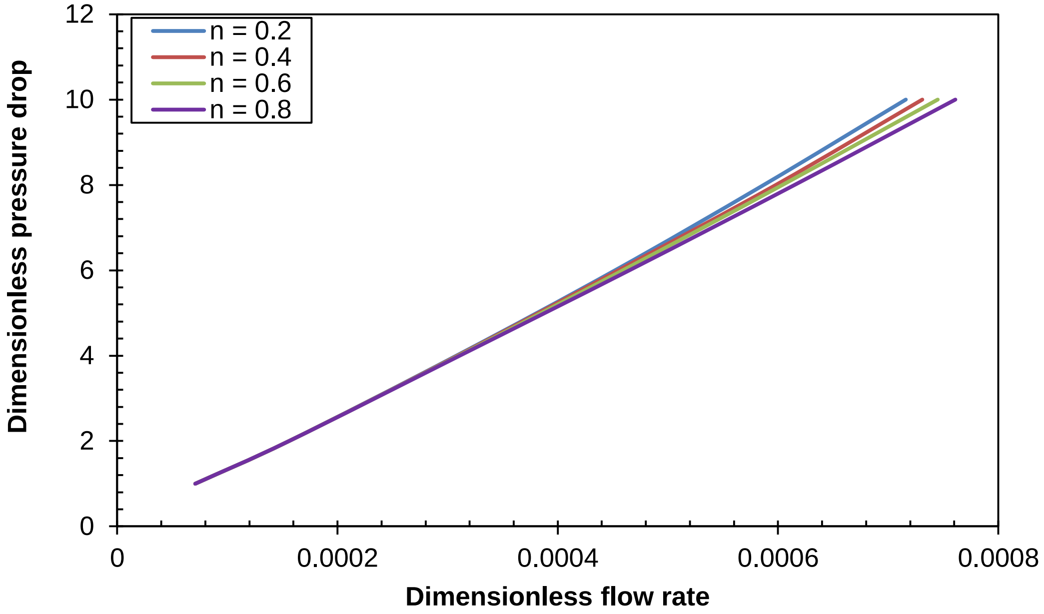

Figure 8.28: Dimensionless Plot of Pressure Drop vs. Flow Rate for Carreau Fluid in Annulus, κ = 0.9 ($\Delta p' < 10$)

8.7 Drag Reducing Turbulent Flow

Fluids used in the oilfield are known to display non-Newtonian character and to be effective drag reducers in the case of drilling and stimulation fluids. Drag reduction, associated with turbulent flow, implies a reduction in friction pressure by the interaction between molecules in the fluid and turbulence structures.

The complexity of drag reducing flows renders modeling difficult. Therefore, empirical correlations between the Fanning friction factor and generalized Reynolds number are common in the literature. In this study, an explicit Fanning friction factor correlation has been developed. The difference between the proposed correlation and attempts by other researchers is the inclusion of a relative roughness term. Experimental data for guar (20, 30, 40, and 60 lb/Mgal) and 5% Aromox® APA-TW solutions are used for correlation development. The choice of different fluids at several concentrations allows for a more robust correlation to cover a wider range of flow behavior indices.

8.7.1 Development of Turbulent Fanning Friction Correlation

The need to develop a friction factor correlation was stated in the previous section. In achieving this aim, a correlation is developed using only turbulent flow data (Fig. 8.29). The resulting correlation is expressed in terms of the generalized Reynolds number, diameter ratio (κ), and relative roughness (h/d_h) as:

$$f = 0.002527\frac{d_1}{d_2} + \frac{16.966}{N_{Reg}^{1.1106}} + 0.04102\left(\frac{h}{d_h}\right) - 0.000521 \tag{8.40}$$

The form of Eq. (8.40) was deemed satisfactory for describing the eccentric annular flow behavior of guar and 5% Aromox® APA-TW solutions. This correlation is valid for $0.213 \leq n \leq 0.651$, $0.636 \leq d_1/d_2 \leq 0.818$, $0.003 \leq h/d_h \leq 0.0867$, and $2{,}100 \leq N_{Reg} \leq 20{,}000$.

For turbulent flow of drag reducing fluids in straight pipes ($d_1/d_2 = 1$), Eq. (8.40) reduces to the following expression.

$$f = 0.002006 + \frac{16.966}{N_{Reg}^{1.1106}} + 0.04102\left(\frac{h}{d_h}\right) \tag{8.41}$$

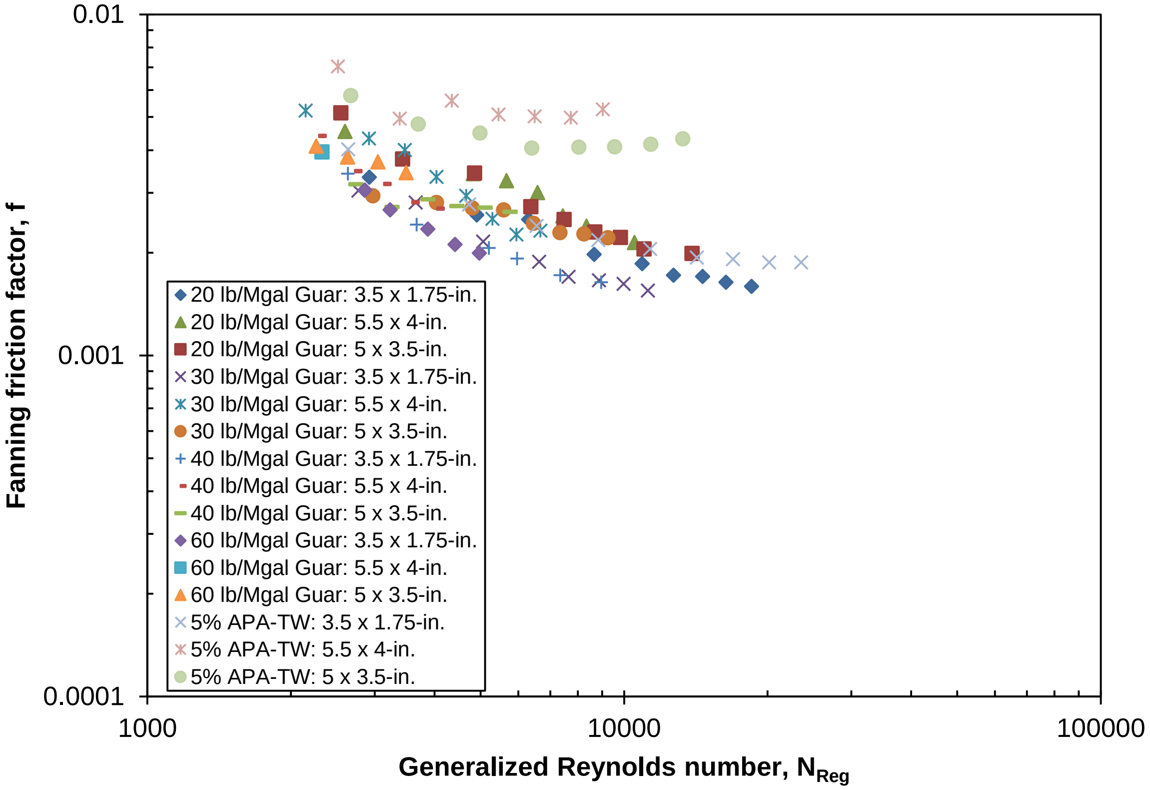

Figure 8.29: Composite Plot of Fanning Friction Factor vs. Generalized Reynolds Number for Turbulent Flow of Guar and Aromox® Solutions

8.7.2 Evaluation of Turbulent Fanning Friction Correlation

Comparisons between experimental data and correlation predictions are given in Figs. 8.30 and 8.31. The data shown are for turbulent flow of 1.75 and 2.25 lb/bbl welan solutions in 3.5-in. x 1.75-in. and 5.5-in. x 4-in. eccentric annuli. Fluid properties are reported in Sect. 8.4.1. In both figures, it is evident that the predicted values closely match the experimental data. An average percent deviation of 3.1% is determined for 1.75 lb/bbl welan in both 3.5-in. x 1.75-in. and 5.5-in. x 4-in. eccentric annuli. For 2.25 lb/bbl, average percent deviations of 4.9% and 11.2% are calculated for flow in 3.5-in. x 1.75-in. and 5.5-in. x 4-in. eccentric annuli, respectively.

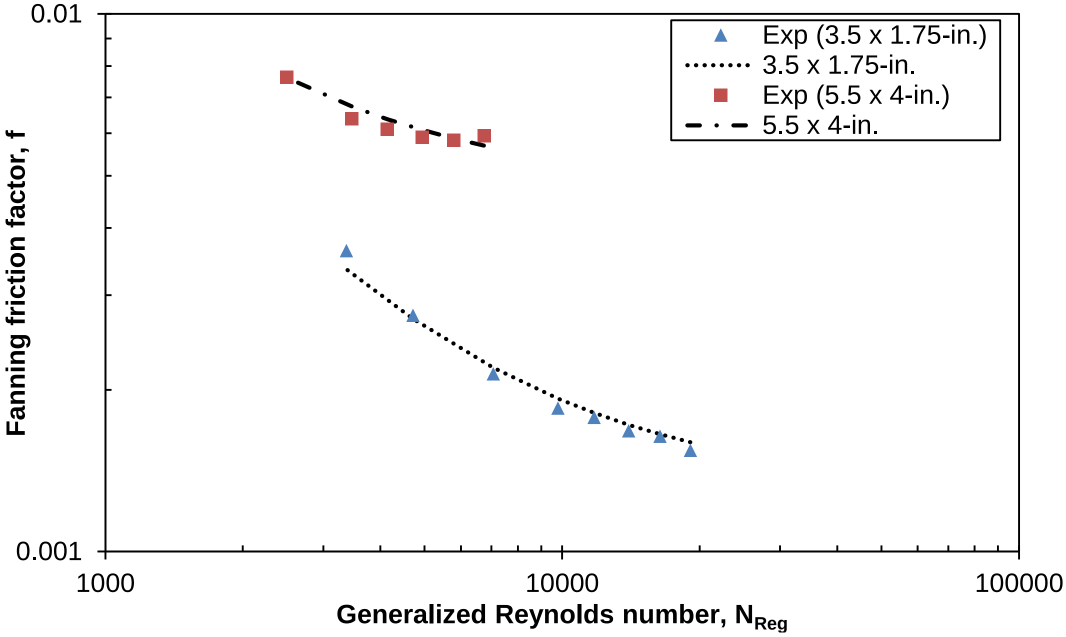

Figure 8.30: Fanning Friction Factor vs. Generalized Reynolds Number for Turbulent Flow of 1.75 lb/bbl Welan Solution

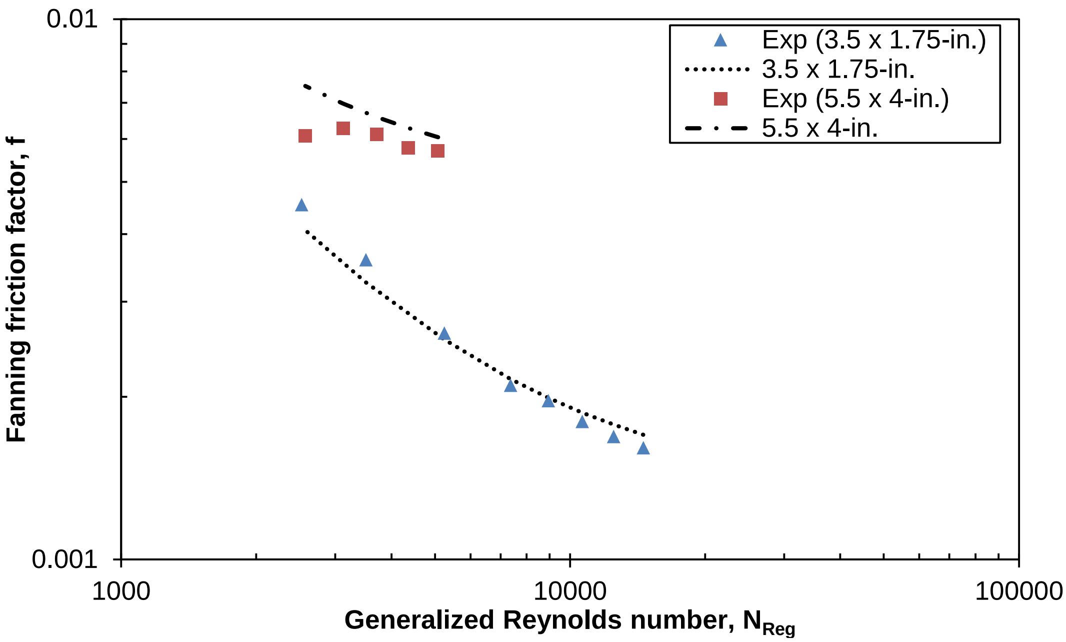

Figure 8.31: Fanning Friction Factor vs. Generalized Reynolds Number for Turbulent Flow of 2.25 lb/bbl Welan Solution

For completeness, Eq. (8.41) is evaluated for turbulent flow of drag reducing fluids in straight pipes. Correlation predictions and experimental data for 1.75 lb/bbl and 2.25 lb/bbl welan solutions in 2⅞-in. straight tubing are shown in Figs. 8.32 and 8.33, respectively. Reasonable accuracy can be seen from both figures; percent average deviations of 13.9% and 10.6% are calculated for 1.75 lb/bbl and 2.25 lb/bbl welan solutions, respectively.

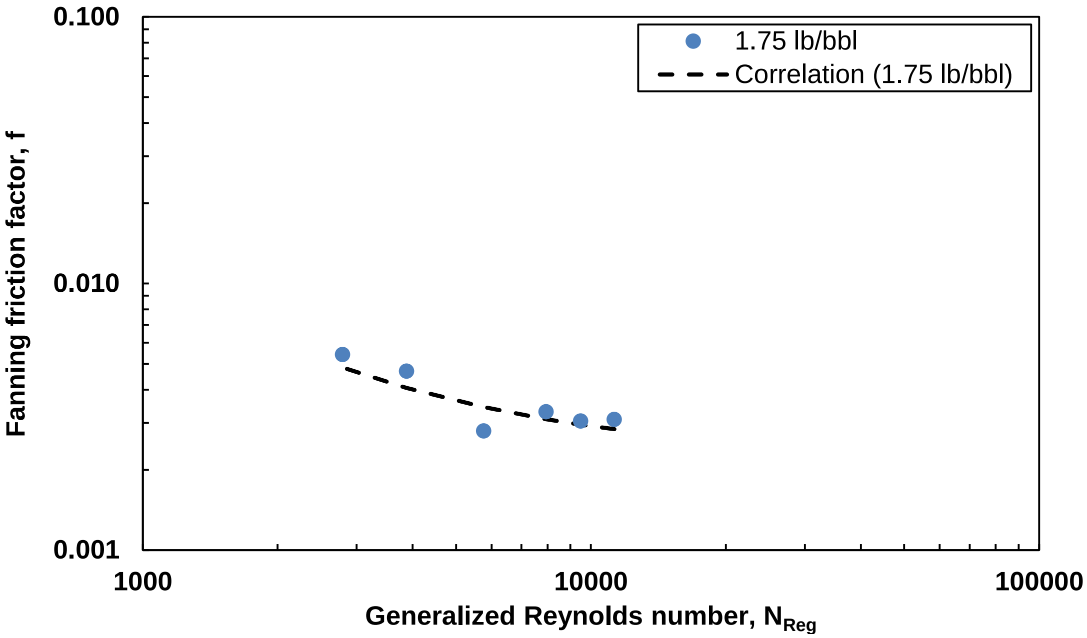

Figure 8.32: Fanning Friction Factor vs. Generalized Reynolds Number for Turbulent Flow of 1.75 lb/bbl Welan Solution in 2⅞-in. Straight Tubing

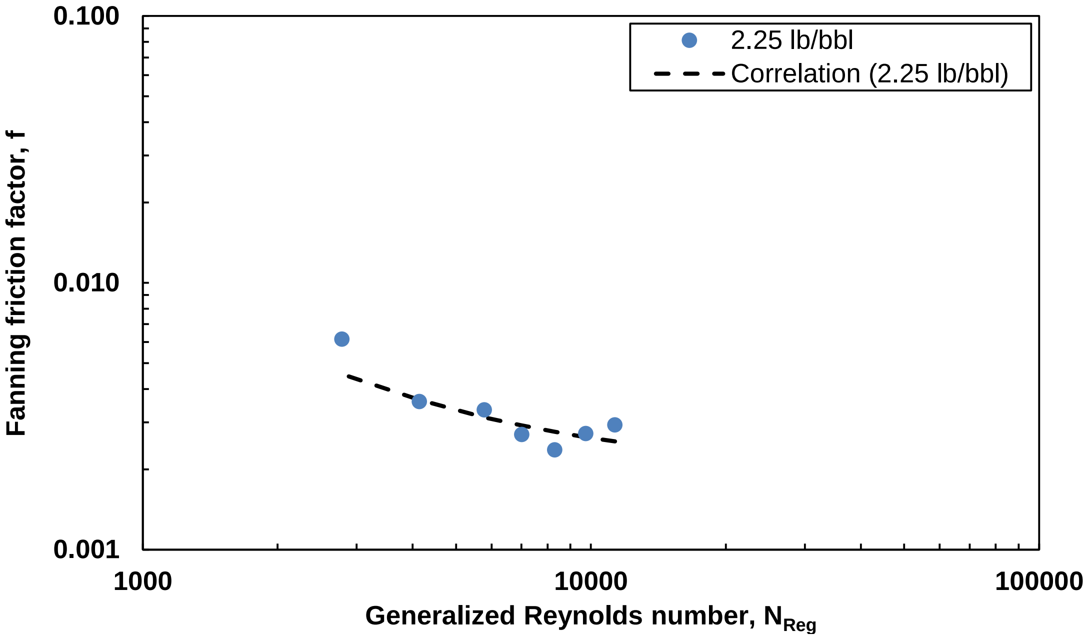

Figure 8.33: Fanning Friction Factor vs. Generalized Reynolds Number for Turbulent Flow of 2.25 lb/bbl Welan Solution in 2⅞-in. Straight Tubing

8.8 Summary

An effective diameter definition for the flow of non-Newtonian fluids in concentric and eccentric annuli, modeled as a modified-slot, has been presented. The use of this definition is compared with flow data in the literature. In all cases, satisfactory agreement is obtained between model predictions and measured data. In addition, a concentric-to-eccentric friction pressure conversion correlation is developed for fully eccentric annular laminar flow.

The annular axial flow of pseudoplastic fluid of the power law and Carreau type was studied. In this work, a Fanning friction factor–generalized Reynolds number relationship for a power law fluid is developed for both concentric and eccentric annular flow. Comparisons of predictions using the proposed approach with experimental data are shown to be satisfactory. The new relationship is shown to outperform the narrow slot approximation for fully eccentric annular flow. The main advantage of the new relationship is that it eliminates the need for determining the location of zero shear stress. With this approach, the need for heavy or complicated numerical techniques is not required, thus making the new method appealing for field applications. Design charts are developed for annular flow of Carreau fluid by virtue of numerical methods for several diameter ratios as a function of flow behavior index.

An empirical Fanning friction factor correlation for the turbulent flow of drag reducing fluids is presented. This correlation was developed using field scale experimental data in different annular geometries. Reasonably good agreement is obtained between correlation predictions and experimental data.

Potential applications of the developed equations include 1) drilling and hydraulic fracturing operations and 2) processes in the chemical industry that require flow through annular sections. It is anticipated that this work will find application in industries that handle flow of non-Newtonian fluids through concentric and eccentric ducts.

Chapter 9

CONCLUSIONS AND RECOMMENDATIONS

9.1 Conclusions

An extensive investigation of the rheological and drag reducing properties of two surfactant solutions (Aromox® APA-T and APA-TW) has been performed. The results from this study allow the following conclusions to be made:

- The temperature dependence of viscosity data can be analyzed using horizontal and vertical shift factors. Master curves in the form of the Carreau model are developed for steady shear data. The thermorheologically complex nature of surfactant solutions resulted in an inability to generate suitable master curves for the dynamic data.
- Salts are observed to have a profound effect on the rheological character of the surfactant solutions investigated. With 2% KCl (monovalent salt), a three-fold increase in the zero-shear rate viscosity is measured. A smaller increase is measured with 2% $CaCl_2$ (divalent salt). With salts in solution, the test fluids displayed improved structure as the crossover frequency is shifted to smaller frequencies.
- New Reynolds number and generalized Reynolds number expressions have been developed for non-Newtonian Carreau and MPL-Cross fluids. These expressions incorporate a wider range of shear rates than the power law model. These new

definitions are shown to provide satisfactory prediction accuracy for laminar flow conditions.

- An equation for estimating pipe flow friction pressure of Carreau and MPL-Cross fluids is presented. This equation yielded good prediction accuracy for laminar flow of non-Newtonian fluids. Accompanying dimensionless wall shear stress–wall shear rate curves for both fluid models were generated for flow indices in the range of 0.1 to 1.
- The drag reduction behavior of surfactant solutions is affected by concentration, pipe diameter, surface roughness, and salts. The drag reduction effectiveness of test fluids is improved at higher surfactant concentrations. This increase in drag reduction effectiveness is attributed to greater intermicellar associations. Drag reduction is higher in larger pipes provided that surface roughness is minimal. Salts added to test fluid resulted in higher drag reduction when compared to solutions in freshwater.
- An analytical Fanning friction factor equation as a function of the generalized Reynolds number for non-Newtonian pseudoplastic fluids in turbulent flow has been derived. Predictions with this equation reasonably agree with experimental data found in literature, with an average deviation of 10%.
- The annular flow behavior of pseudoplastic fluids is investigated. Analytical Fanning friction factor – generalized Reynolds number relationships are developed for concentric and eccentric annular flow. Good agreement is obtained between friction pressure predictions and experimental data. In addition, design

charts in the form of dimensionless pressure drop against dimensionless flow rate are presented for the annular flow of Carreau fluids.

- An empirical Fanning friction correlation has been developed for turbulent flow of drag reducing fluids in fully eccentric annuli. Satisfactory agreement was obtained between correlation predictions and experimental data.

9.2 Recommendations for Future Studies

- Employ sophisticated visual techniques (small-angle neutron scattering or Cyro-TEM) to investigate the interaction between surfactant molecules and salt ions. This will provide conclusive results on the role of salt counterion size on the rheological and drag reduction character of surfactant solutions.
- Investigate the effect of temperature on the rheological and drag reduction behavior of surfactants in different brines to provide a better understanding of surfactant drag reduction performance at higher temperatures.
- Studies on the effect of thixotropy, elongational viscosity, and viscoelasticity on the flow character of non-Newtonian fluids in straight pipes and annular ducts are recommended. This will be beneficial to industries that handle flow of rheologically-complex fluids.
- Further research into the transitional flow behavior of non-Newtonian fluids is recommended. Some studies have shown that the critical Reynolds number for flow regime transition is affected by the rheological model used.

- For an academic pursuit, a detailed and systematic study on the synergistic effect between surfactants and polymers in terms of rheological behavior and drag reducing flow characteristics for oilfield applications is recommended.
- Conduct studies on two-phase solid-liquid flow for a wider class of non-Newtonian fluids. The Reynolds number definitions derived in the present study can provide a basis for future work on wellbore cleanout and proppant transport.

REFERENCES

Acharya, D.P., Sharma, S.C., Rodriguez-Abreu, C., and Aramaki, K. 2006. Viscoelastic Micellar Solutions in Nonionic Fluorinated Surfactant Systems. *The Journal of Physical Chemistry B* **110** (41): 20224-20234.

Ahmed, R. 2005. Experimental Study and Modeling of Yield Power-Law Fluid Flow in Pipes and Annuli. Report for The University of Tulsa, Drilling Research Projects (TUDRP), Tulsa, Oklahoma.

Aït Ali, A., and Makhloufi, R. 1997. Linear and Nonlinear Rheology of an Aqueous Concentrated System of Cethyltrimethylammonium Chloride and Sodium Salicylate. *Physical Review E* **56** (4): 4474-4478.

Akzo Nobel USA. 2001. Aromox® APA T – Viscoelastic Surfactant (VES). Akzo Nobel Surface Chemistry Product Brochure.

Arora, K. 2004. Experimental and Theoretical Investigation of Flow Micro-Structure Coupling in Viscoelastic Solutions. PhD. Dissertation, Washington University, Saint Louis, Missouri.

Azouz, I., Shirazi, S.A., Pilehvari, A. and Azar, J.J. 1992. Numerical Simulation of Laminar Flow of Newtonian and Non-Newtonian Fluids in Conduits of Arbitrary Cross-Section. Proc.

Ballal, B.Y. and Rivlin, R.S. 1976. Flow of a Newtonian Fluid between Eccentric Rotating Cylinders: Inertial Effects. *Archive for Rational Mechanics and Analysis* **62** (3): 237–294.

Ballal, B.Y. and Rivlin, R.S. 1979. Flow of a Viscoelastic Fluid between Eccentric Cylinders. *Rheologica Acta* **18** (3): 311–322.

Berman, N.S., Griswold, S. T., Elihu, S., and Yuen, J. 1978. An Observation of the Effect of Integral Scale on Drag Reduction. *AIChE J.* **24** (1): 124-130.

Bewersdorff, H. 1996. Rheology of Drag Reducing Surfactant Solutions. Fluids Engineering Division Conference (FED-ASME) 237: 25 – 29.

Brostow, W. 2008. Drag reduction in flow: Review of Applications, Mechanism and Prediction. *Journal of Industrial and Engineering Chemistry* **14** (4), 409-416.

Burger, E.D., Munk, W.R. and Wahl, H.A. 1982. Flow Increase in the Trans-Alaska Pipeline through Use of a Polymeric Drag Reducing Additive. *Journal of Petroleum Technology* **34** (2): 377 – 386.

Carreau, P.J. 1972. Rheological Equations from Molecular Network Theories. *Transactions of the Society of Rheology* **16** (1): 99-127.

Cartalos, U., King, I., Dupuis, D. and Sagot, A. 1996. Field Validated Hydraulic Model Predictions Give Guidelines for Optimal Annular Flow in Slimhole Drilling. Proc., SPE/IADC Drilling Conference, New Orleans, Louisiana.

Castro, W., and Squire, W. 1968. The Effect of Polymer Additives on Transition in Pipe Flow. *Applied Scientific Research* **18** (1): 81-96.

Cates, M.E. and Candau, S.J. 1990. Static and Dynamics of Worm-like Surfactant Micelles. *J. Phys. Condensed Matter* **2**: 6869-6880.

Chen, N.H. 1979. An Explicit Equation for Friction Factor in Pipe. *Industrial & Engineering Chemistry Fundamentals* **18** (3): 296-297.

Chou, L.C. 1991. Drag Reducing Cationic Surfactant Solutions for District Heating and Cooling Systems. Ph.D. dissertation, The Ohio State University.

Cowan, M.E. 2000. Synthesis and Characterization of High Molecular Weight Water-Soluble Polymers to Study the Role of Extensional Viscosity in Polymeric Drag Reduction. Ph.D. Dissertation, The University of Southern Mississippi.

Cross, M. M. 1965. Rheology of Non-Newtonian Fluids: A New Flow Equation for Pseudoplastic Systems. *Journal of Colloid Science* **20** (5): 417-437.

Cummings, C.A. 1993. A Theoretical Study of the Flow of Slightly Compressible Non-Newtonian Fluids in Eccentric Annuli with Entrance Effects. Ph.D. Dissertation. The University of Oklahoma.

David, J. and Filip, P. 1995. Relationship of Annular and Parallel-Plate Poiseuille Flows for Power-Law Fluids. *Polymer-Plastics Technology and Engineering* **34** (6): 947–960.

Derezinski, S.J. 1990. Dimensionless Slot Flow Using the Carreau Viscosity Model. *Journal of Plastic Film and Sheeting* **6** (4): 276-291.

Dimitropoulos, C. D., Sureshkumar, R., and Beris, A. N. 1998. Direct Numerical Simulation of Viscoelastic Turbulent Channel Flow Exhibiting Drag Reduction: Effect of the Variation of Rheological Parameters. *Journal of Non-Newtonian Fluid Mechanics* **79** (2–3): 433-468.

Dodge, D.W., and Metzner, A.B. 1959. Turbulent Flow of Non-Newtonian Systems. *AIChE J.* **5** (2): 189-204.

Dreiss, C.A. 2007. Wormlike Micelles: Where do we stand? Recent Developments, Linear Rheology and Scattering Techniques. *Soft Matter* **3** (8): 956-970.

Drew, T.B., Koo, E.C., and McAdams, W. H. 1932. The Friction Factor for Clean Round Pipes. *Trans., AIChE J.* **28**: 56-72.

Dunleavy, J. E., and Middleman, S. 1966. Correlation of Shear Behavior of Solutions of Polyisobutylene. *Trans. Soc. Rheol.* **10**: 157-168.

Edwards, M.F. and Smith, R. 1980. The Turbulent Flow of Non-Newtonian Fluids in the Absence of Anomalous Wall Effects. *Journal of Non-Newtonian Fluid Mechanics* **7** (1): 77-90.

Escudier, M.P., Oliveira, P.J. and Pinho, F.T. 2002. Fully Developed Laminar Flow of Purely Viscous Non-Newtonian Liquids through Annuli, including the Effects of Eccentricity and Inner-cylinder Rotation. *International Journal of Heat and Fluid Flow* **23** (1): 52–73.

Fang, P., Manglik, R.M. and Jog, M.A. 1999. Characteristics of Laminar Viscous Shear-thinning Fluid Flows in Eccentric Annular Channels. *Journal of Non-Newtonian Fluid Mechanics* **84** (1): 1–17.

Feldman, E.E., Hornbeck, R.W. and Osterle, J.F. 1982. A Numerical Solution of Laminar Developing Flow in Eccentric Annular Ducts. *International Journal of Heat and Mass Transfer* **25** (2): 231–241.

Fredrickson, A.G. and Bird, R.B. 1958. Non-Newtonian Flow in Annuli. *Industrial & Engineering Chemistry* **50** (3): 347–352.

Gadd, G.E. 1968. Effects of Drag Reducing Additives on Vortex Stretching. *Nature* **217**: 1040-1042.

Gad-el-Hak, M. 2000. Flow Control: Passive, Active, and Reactive Flow Management. Cambridge University Press.

Gasljevic, K. 1995. An Experimental Investigation of Drag Reduction by Surfactant Solutions and of its Implementation in Hydronic Systems. Ph.D. Dissertation, University of California, Santa Barbara.

Gasljevic, K., Aguilar, G., and Matthys, E.F. 1999. An Improved Diameter Scaling Correlation for Turbulent Flow of Drag Reducing Polymer Solutions. *Journal of Non-Newtonian Fluid Mechanics* **84** (2): 131-148.

Gasljevic, K., Aguilar, G., and Matthys, E.F. 2001. On Two Distinct Types of Drag Reducing Fluids, Diameter Scaling, and Turbulent Profiles. *Journal of Non-Newtonian Fluid Mechanics* **96** (3): 405-425.

Ge, W. 2008. Studies on the Nanostructure, Rheology and Drag Reduction Characteristics of Drag Reducing Cationic Surfactant Solutions. Ph.D. Dissertation, The Ohio State University.

Giles, W.B., and Pettit, W.T. 1967. Stability of Dilute Viscoelastic Flows. [10.1038/216470a0]. *Nature* **216** (5114): 470-472.

Goel, N., Shah, S.N., Yuan, W.-L., and O'Rear, E.A. 2001. Suspension Characteristics of Borate-Crosslinked Gels: Rheology and Atomic Force Microscopy Measurements. *Journal of Applied Polymer Science* **82***:* 2978-2990.

Graessley, W. 1974. The Entanglement Concept in Polymer Rheology. Springer Berlin Heidelberg.

Guckes, T.L. 1975. Laminar Flow of Non-Newtonian Fluids in an Eccentric Annulus. *Journal of Engineering for Industry* **97** (2): 498–506.

Gücüyener, H.I. and Mehmetoglu, T. 1992. Flow of Yield Pseudoplastic Fluids through a Concentric Annulus. *AIChE J.* **38** (7): 1139–1143.

Haciislamoglu, M. 1989. Non-Newtonian Fluid Flow in Eccentric Annuli and Its Application to Petroleum Engineering Problems. Ph.D. Dissertation, Louisiana State University, Baton Rouge.

Haciislamoglu, M. and Cartalos, U. 1994. Practical Pressure Loss Predictions in Realistic Annular Geometries. Paper SPE 28304 presented at the SPE Annual Technical Conference and Exhibition, New Orleans, Louisiana.

Haciislamoglu, M. and Langlinais, J. 1990. Non-Newtonian Flow in Eccentric Annuli. *Journal of Energy Resources Technology* **112** (3): 163–169.

Hanks, R.W. 1979. The Axial Laminar Flow of Yield Pseudoplastic Fluids in a Concentric Annulus. *Industrial & Engineering Chemistry Process Design and Development* **18** (3): 488–493.

Hanks, R.W., and Larsen, K.M. 1979. The Flow of Power-Law Non-Newtonian Fluids in Concentric Annuli. *Industrial & Engineering Chemistry Fundamentals* **18** (1): 33–35.

Hashizaki, K., Taguchi, H., and Saito, Y. 2009. Effects of Temperature on the Rheological Behavior of Worm-like Micelles in a Mixed Nonionic Surfactant System. *J Oleo Sci* **58** (5): 255-260.

Heinz, H. 2003. Viscoelastic Surfactant Solutions Structure-Performance Relationships in Surfactants: CRC Press.

Heinz, R. 2005. Rheological Properties of Viscoelastic Surfactant Solutions Dynamics of Surfactant Self-Assemblies: CRC Press.

Heyda, J.F. 1959. A Green's Function Solution for the Case of Laminar Incompressible Flow between Non-Concentric Circular Cylinders. *Journal of the Franklin Institute* **267** (1): 25–34.

Hoffman, H. and Ulbricht, W. 2001. Rheology Effects in Surfactant Phases. In Handbook of Applied Surface and Colloid Chemistry, ed. K. Holmberg, Chap. 10, 189-124. John Wiley and Sons.

Hoyt, J.W. 1972. A Freeman Scholar Lecture: The Effect of Additives on Fluid Friction. *Journal of Basic Engineering* **94** (2): 258-285.

Hoyt, J.W. 2003. Scale-up from Laboratory Pipe-Flow Data to Large Flows. Proceedings of the ASME/JSME 4th Joint Fluids Summer Engineering Conference (FEDSM '03), vol. 1, pp. 745–749, Honolulu, Hawaii, USA.

Irvine, T.F. 1988. A Generalized Blasius Equation for Power Law Fluids. *Chemical Engineering Communications,* **65** (1): 39-47.

Iyoho, A.W., and Azar, J.J. 1981. An Accurate Slot-Flow Model for Non-Newtonian Fluid Flow Through Eccentric Annuli. *Society of Petroleum Engineers Journal* **21** (5): 565–572.

Jacques, Z., Wu, G., and Ying, Z. 2007. Drag Reduction by Surfactant Giant Micelles (pp. 473-492): CRC Press.

Kalur, G.C., Frounfelker, B.D., Cipriano, B.H., Norman, A.I., and Raghavan, S.R. 2005. Viscosity Increase with Temperature in Cationic Surfactant Solutions Due to the Growth of Wormlike Micelles. *Langmuir* **21** (24): 10998-11004.

Kamel, A.H.A., and Shah, S.N. 2010. Scale-Up Correlation for the Flow of Surfactant-Based Fluids in Circular Coiled Pipes. *Journal of Fluids Engineering* **132** (8): 081101.

Kamel, A.H.A. 2008. Flow Characteristics of Surfactant-based Fluids in Straight and Coiled Tubing. Ph.D. Dissertation. University of Oklahoma, Norman.

Kazakia, J.Y. and Rivlin, R.S. 1977. Flow of a Viscoelastic Fluid between Eccentric Rotating Cylinders and Related Problems. *Rheologica Acta* **16** (3): 229–239.

Kefi, S., Lee, J., Pope, T., Sullivan, P., Nelson, E., Hernandez, A., Olsen, T., Parlar, M., Powers, B., Roy, A., Wilson, A., and Twynam, A. 2004. Expanding Applications for Viscoelastic Surfactants. *Oilfield Rev. Serv.* **16**: 10–16.

Kohn, M.C. 1973. Energy Storage in Drag Reducing Polymer Solutions. *Journal of Polymer Science: Polymer Physics Edition* **11** (12): 2339-2356.

Kohn, M.C. 1974. Criteria for the Onset of Drag Reduction. *AIChE J.* **20** (1): 185-188.

Kostic, M. 1994. The Ultimate Asymptotes and Possible Causes of Friction Drag and Heat Transfer Reduction Phenomena. *Journal of Energy, Heat and Mass Transfer* **16**: 1-14.

Kulicke, W.M., Kötter, M., and Gräger, H. 1989. Drag Reduction Phenomenon with Special Emphasis on Homogeneous Polymer Solutions. *Advances in Polymer Science* **89**: 1-68.

Langlinais, J.P., Bourgoyne A.T. and Holden, W.R. 1983. Frictional Pressure Losses for the Flow of Drilling Mud and Mud/Gas Mixtures. Proc., SPE Annual Technical Conference and Exhibition, San Francisco, California.

Lee, D., and Park, S. 2001. Predictions of Heat Transfer and Pressure Drop for a Modified Power Law Fluid Flow in a Square Duct. *Korean Journal of Chemical Engineering* **18** (3): 277-284.

Lequeux, F. 1992. Reptation of Connected Wormlike Micelles. *EPL (Europhysics Letters)* **19** (8): 675-681.

Li, F., Yu, B., Wei, J., and Kawaguchi, Y. 2012. Turbulent Drag Reduction by Surfactant Additives. John Wiley and Sons, Singapore.

Lin, Z., Bin, L., Zakin, J.L., Talmon, Y., Zheng, Y., Davis, H.T., and Scriven, L.E. 2001. Influence of Surfactant Concentration and Counterion to Surfactant Ratio on Rheology of Wormlike Micelles. *Journal of Colloid and Interface Science* **239** (2): 543-554.

Lin, Z., Chou, L., Lu, B., Zheng, Y., Davis, H.T., Scriven, L.E., Zakin, J.L. 2000. Experimental Studies on Drag Reduction and Rheology of Mixed Cationic Surfactants with Different Alkyl Chain Lengths. *Rheologica Acta* **39** (4): 354-359.

Lin, Z., Mateo, A., Zheng, Y., Kesselman, E., Pancallo, E., Hart, D., and Zakin, J.L. 2002. Comparison of Drag Reduction, Rheology, Microstructure and Stress-Induced Precipitation of Dilute Cationic Surfactant Solutions with Odd and Even Alkyl Chains. *Rheologica Acta* **41** (6): 483-492.

Lu, T., Xia, L.G., Wang, X., Wang, A., and Zhang, T. 2011. A Dually Effective Inorganic Salt at Inducing Obvious Viscoelastic Behavior of both Cationic and Anionic Surfactant Solutions. *Langmuir* **27** (16): 9815-9822.

Lumley, J.L. 1969. Drag Reduction by Additives. *Annual Review of Fluid Mechanics* **1** (1): 367-384.

Luo, Y. and Peden, J.M. 1990. Flow of Non-Newtonian Fluids Through Eccentric Annuli. *SPE Production Engineering* **5** (1): 91-96.

Macias, E.R., Bautista, F., Perez-Lopez, J.H., Schulz, P.C., Gradzielski, M., Manero, O., Puig, J.O., and Escalante, J.I. 2011. Effect of Ionic Strength on Rheological Behavior of Polymer-like Cetyltrimethylammonium Tosylate Micellar Solutions. *Soft Matter* **7** (5): 2094-2102.

Macosko, C. W. 1994. Rheology: Principles, Measurements and Applications, Wiley/VCH, Poughkeepsie, New York.

Madlener, K., Frey, B., and Ciezki, H.K. 2009. Generalized Reynolds Number for Non-Newtonian Fluids. *Progress in Propulsion Physics* **1**: 237-250.

Makhloufi, R., and Cressely, R. 1992. Temperature Dependence of the Non-Newtonian Viscosity of Elongated Micellar Solutions. *Colloid and Polymer Science* **270** (10): 1035-1041.

Mansour, A.R., Swaiti, O., Aldoss, T., and Issa, M. 1988. Drag Reduction in Turbulent Crude Oil Pipelines using a New Chemical Solvent. *International Journal of Heat and Fluid Flow* **9** (3): 316-320.

Martin, I. 2007. Linear Rheology of Aqueous Solutions of Wormlike Micelles. Giant Micelles (pp. 249-287): CRC Press.

McEachern, D.W. 1966. Axial Laminar Flow of a Non-Newtonian Fluid in an Annulus. *AIChE J.* **12** (2): 328-332.

Metzner, A.B., and Reed, J.C. 1955. Flow of Non-Newtonian Fluids—Correlation of the Laminar, Transition, and Turbulent-Flow Regions. *AIChE J.* **1** (4): 434-440.

Mishra, P. and Mishra, I. 1976. Flow Behavior of Power Law Fluids in an Annulus. *AIChE J.* **22** (3): 617-619.

Mooney, M. 1931. Explicit Formulas for Slip and Fluidity. *Journal of Rheology* **2** (2): 210-222.

Morgan, S.E., and McCormick, C.L. 1990. Water-Soluble Copolymers XXXII: Macromolecular Drag Reduction. A Review of Predictive Theories and the Effects of Polymer Structure. *Progress in Polymer Science* **15** (3): 507-549.

Moroi, Y. 1992. Micelles: Theoretical and Applied Aspects. New York: Plenum Press.

Moussa, T., and Tiu, C. 1994. Factors affecting Polymer Degradation in Turbulent Pipe Flow. *Chem. Eng. Sci.* **49**: 1681-1692.

Myers, D. 2006. Surfactant Science and Technology (3rd ed.). Hoboken, N.J.: Wiley-Interscience.

Nebrensky, J. and Ulbrecht, J. 1968. Non-Newtonian Flow in Annular Ducts. *Collect. Czech. Chem. Commun.* **33**: 363-375.

Nelson, R.C. 1982. Application of Surfactants in the Petroleum Industry. *Journal of the American Oil Chemists Society* **59** (10): 823A-826A.

Oelschlaeger, C., and Willenbacher, N. 2011. Rheological Properties of Aqueous Solutions of Cetylpyridinium Chloride in the Presence of Sodium Chlorate. *Rheologica Acta* **50** (7-8): 655-660.

Ogugbue, C.C. and Shah, S.N. 2011. Laminar and Turbulent Friction Factors for Annular Flow of Drag Reducing Polymer Solutions in Coiled-Tubing Operations. *SPE Drilling & Completion* **26** (4): 506–518.

Okafor, M.N. and Evers, J.F. 1992. Experimental Comparison of Rheology Models for Drilling Fluids. Proc., SPE Western Regional Meeting, Bakersfield, California.

Pereira, A.S. and Pinho, F.T. 1994. Turbulent Pipe Flow Characteristics of Low Molecular Weight Polymers. *Journal of Non-Newtonian Fluid Mechanics* **55** (3): 321-344.

Pfenninger, W. 1967. A Hypothesis of the Reduction of the Turbulent Friction Drag in Fluid Flows by Means of Additives, Northrop Corp Norair Division Report BLC-179

Pilehvari, A. and Serth, R. 2009. Generalized Hydraulic Calculation Method for Axial Flow of Non-Newtonian Fluids in Eccentric Annuli. *SPE Drilling & Completion* **24** (4): 553–563.

Pollert, J., Komrzy, P., Svejkovsky, K., Pollert Jr., J., Lu, B., and Zakin, J.L. 1996. Drag Reduction and Heat Transfer of Cationic Surfactant Solutions. Proceedings of the ASME Fluids Engineering Division Summer Meeting, vol. 237, no. 2, pp. 31–36.

Povolo, F., and Fontelos, M. 1987. Time-Temperature Superposition Principle and Scaling Behaviour. *Journal of Materials Science* **22** (5): 1530-1534.

Prasanth, N. and Shenoy, U.V. 1992. Poiseuille Flow of a Power Law Fluid between Coaxial Cylinders. *Journal of Applied Polymer Science* **46** (7): 1189–1194.

Pyun, C.W. and Fixman, M. 1965. Intrinsic Viscosity of Polymer Chains. *The Journal of Chemical Physics* **42** (11): 3838-3844.

Rabinowitsch, Z. 1929. Ueber die viskositat and elastizitat von solen. *Z Physik Chem.* **145**: 1-26.

Raghavan, S.R., and Kaler, E.W. 2000. Highly Viscoelastic Wormlike Micellar Solutions Formed by Cationic Surfactants with Long Unsaturated Tails. *Langmuir* **17** (2), 300-306.

Raoul, Z. 2005. Introduction to Surfactants and Surfactant Self-Assemblies. Dynamics of Surfactant Self-Assemblies (pp. 1-35): CRC Press.

Redberger, P.J. and Charles, M.E. 1962. Axial Laminar Flow in a Circular Pipe containing a Fixed Eccentric Core. *The Canadian Journal of Chemical Engineering* **40** (4): 148–151.

Rochefort, W.E., and Middleman, S. 1987. Rheology of Xanthan Gum: Salt, Temperature, and Strain Effects in Oscillatory and Steady Shear Experiments. *Journal of Rheology* **31** (4): 337-369.

Rochefort, W.E. 1986. Xanthan Gum: Rheology and Drag Reduction Studies. Ph.D. Dissertation. University of California, San Diego, 1986.

Rosen, M.J. 2004. Surfactants and Interfacial Phenomena. 3rd Edition, Wiley, New York.

Russell, C.P. and Christiansen, E.B. 1974. Axial, Laminar, Non-Newtonian Flow in Annuli. *Industrial & Engineering Chemistry Process Design and Development* **13** (4): 391-396.

Salem, A.A. 1996. An Experimental Investigation of the Drag and Heat Transfer Reduction of Drag Reducing Surfactants. Ph.D. Dissertation, University of Akron.

Samuel, M., Polson, D., Graham, D., Kordziel, W., Waite, T., Waters, G., and Downey, R. 2000. Viscoelastic Surfactant Fracturing Fluids: Applications in Low Permeability Reservoirs. Paper SPE 60322 presented at the SPE Rocky Mountain Regional/Low-Permeability Reservoirs Symposium and Exhibition, Denver, Colorado.

Savins, J.G., and Seyer, F.A. 1977. Drag Reduction Scale-up Criteria. *Physics of Fluids* **20** (10): S78-S84.

Savins, J.G. 1967. A Stress Controlled Drag-reduction Phenomena. *Rheologica Acta* **6** (4): 323-330.

Savins. J.G. 1964. Drag Reduction Characteristics of Solutions of Macromolecules in Turbulent Pipe Flow. *SPEJ* **4** (3): 203-214.

Schramm, L.L. 2000. Surfactants: Fundamentals and Applications in the Petroleum Industry. Cambridge University Press, United Kingdom.

Sellin, R.H.J., and Ollis, M. 1983. Effect of Pipe Diameter on Polymer Drag Reduction. *Industrial & Engineering Chemistry Product Research and Development* **22** (3): 445-452.

Shah, S.N. 1984. Correlations Predict Friction Pressures of Fracturing Gels. *Oil Gas J.* **82** (3): 93-98.

Shah, S.N. 1990. Effects of Pipe Roughness on Friction Pressures of Fracturing Fluids. *SPE Production Engineering* **5** (2): 151-156.

Shashkina, J.A., Philippova, O.E., Zaroslov, Y.D., Khokhlov, A.R., Pryakhina, T.A., and Blagodatskikh, I.V. 2005. Rheology of Viscoelastic Solutions of Cationic Surfactant. Effect of Added Associating Polymer. *Langmuir* **21** (4): 1524-1530.

Shaver, R.G., and Merrill, E.W. 1959. Turbulent Flow of Pseudoplastic Polymer Solutions in Straight Cylindrical Tubes. *AIChE J.* **5** (2): 181-188.

Shenoy, A.V. 1984. A Review on Drag Reduction with Special Reference to Micellar Systems. *Colloid and Polymer Science* **262** (4): 319-337.

Silva, M.A. and Shah, S.N. 2000. Friction Pressure Correlations of Newtonian and Non-Newtonian Fluids through Concentric and Eccentric Annuli. Proc., SPE/ICoTA Coiled Tubing Roundtable, Houston, Texas.

Singh, R.P. 2002. Drag Reduction. In Encyclopedia of Polymer Science and Technology. John Wiley and Sons, Inc.

Singh, R.P. 2010. Drag Reduction. In Encyclopedia of Polymer Science and Technology. John Wiley and Sons, Inc.: 519 – 563.

Soltero, J.F.A., Fernando, B., Jorge, P., and Octavio, M. 2007. Nonlinear Rheology of Giant Micelles Giant Micelles (pp. 289-322): CRC Press.

Sood, A., and Rhodes, E. 1998. Pipeline Scale-up in Drag Reducing Turbulent Flow. *The Canadian Journal of Chemical Engineering* **76** (1): 11-18.

Sreenivasan, K.R., and White, C.M. 2000. The Onset of Drag Reduction by Dilute Polymer Additives, and the Maximum Drag Reduction Asymptote. *Journal of Fluid Mechanics* **409**: 149-164.

Subramanian, R. 1995. A Study of Pressure Loss Correlations of Drilling Fluids in Pipes and Annuli. MS Thesis. The University of Tulsa.

Sureshkumar, R., Beris, A.N., and Handler, R.A. 1997. Direct Numerical Simulation of the Turbulent Channel Flow of a Polymer Solution. *Physics of Fluids* **9** (3): 743-755.

Suzuki, H., Fuller, G., Nakayama, T., and Usui, H. 2004. Development Characteristics of Drag Reducing Surfactant Solution Flow in a Duct. *Rheologica Acta* **43** (3): 232-239.

Tabor, M. and de Gennes, P.G. 1986 A Cascade Theory of Drag Reduction. *Europhys. Lett.* **2**: 519–522.

Tao, L.N. and Donovan, W.F. 1955. Through Flow in Concentric and Eccentric Annuli of Fine Clearance with and without Relative Motion of the Boundaries. *Trans. ASME* **77**: 1291–1301.

Tiederman, W.G., Luchik, T.S., and Bogard, D.G. 1985. Wall-layer Structure and Drag Reduction. *Journal of Fluid Mechanics* **156**: 419-437.

Toms, B.A. 1948. Some Observation on the Flow of Linear Polymer Solutions Through Straight Tubes at Large Reynolds Numbers. Paper presented at the Proc. 1st Intl. Congr. on Rheology.

Toms, B.A. 1977. Early Experiments on Drag Reduction by Polymers. *Phys. Fluids* **20**.

Truong, V.T. 2001. Drag Reduction Technologies. Report for the Australian Dept. of Defense (DSTO-GD-0290).

Tulin, M.P. 1966 Hydrodynamic Aspects of Macromolecular Solutions. Proc. 6th Symp. on Naval Hydrodynamics (ed. R. D. Cooper & S. W. Doroff), pp. 3–18.

Uner, D., Ozgen, C. and Tosun, I. 1988. An Approximate Solution for Non-Newtonian Flow in Eccentric Annuli. *Industrial & Engineering Chemistry Research* **27** (4): 698–701.

Vaughn, R.D. 1965. Axial Laminar Flow of Non-Newtonian Fluids in Narrow Eccentric Annuli. *Trans. AIME* **234**: 277–280.

Velusamy, K., and Garg, V.K. 1994. Entrance Flow in Eccentric annular Ducts. *International Journal for Numerical Methods in Fluids* **19** (6): 493–512.

Venkataiah, S., and Mahadevan, E. G. 1982. Rheological Properties of Hydroxypropyl- and Sodium Carboxymethyl-substituted Guar Gums in Aqueous Solution. *Journal of Applied Polymer Science* **27** (5): 1533-1548.

Virk P.S. and Wagger, D.L. 1989. Aspects of Mechanism in Type B Drag Reduction. In Proceedings of the 2nd IUTAM Symposium on Structure of Turbulence and Drag Reduction, Zurich, Switzerland.

Virk, P.S., and Merrill, E.W. 1969. Onset of Dilute Polymer Solution Phenomena. Proceedings of the Symposium on Viscous Drag Reduction, pp. 107–130.

Virk, P.S. 1975. Drag Reduction Fundamentals. *AIChE J.* **21**: 625 – 656.

Walsh, M.A. 1967. On the Turbulent Flow of Dilute Polymer Solutions, Ph.D. Dissertation, California Institute of Technology, Pasadena.

Walton, I.C. and Bittleston, S.H. 1991. The Axial Flow of a Bingham Plastic in a Narrow Eccentric Annulus. *Journal of Fluid Mechanics* **222**: 39-60.

Wang, J. 1993. The Effect of Inorganic Salts on the Viscosity Behavior of Sodium Dodecylbenzene Sulfonate Solution with High Concentration. *Colloids and Surfaces A: Physicochemical and Engineering Aspects* **70** (1): 15-21.

Wang, Y., Yu, B., Zakin, J.L., and Shi, H. 2011. Review on Drag Reduction and Its Heat Transfer by Additives. *Advances in Mechanical Engineering: 1-17*.

Whitsitt, N.F., Harrington, L.G., H.R. Crawford, H.R. 1968. Effect of Wall Shear Stress on Drag Reduction of Viscoelastic Fluids. Western Co. Report No. DTMB-3.

Wilson, K.C. and Thomas, A.D. 1985. A New Analysis of the Turbulent Flow of Non-Newtonian fluids. *The Canadian Journal of Chemical Engineering* **63** (4): 539-546.

Yoo, S.S. 1974. Heat transfer and Friction Factors for Non-Newtonian Fluids in Turbulent Pipe Flow. Ph.D. Dissertation, University of Illinois at Chicago.

Zakin, J.L., and Ge, W. 2010. Polymer and Surfactant Drag Reduction in Turbulent Flows Polymer Physics (pp. 89-127): John Wiley & Sons, Inc.

Zakin, J.L., Myska, J. and Chara, Z. 1996. New Limiting Drag Reduction and Velocity Profile Asymptote for Nonpolymeric Additive Systems. *AIChE J.* **42**: 3544 – 3546.

Zhang, Y. 2005. Correlations among Surfactant Drag Reduction Additive Chemical Structures, Rheological Properties and Microstructures in Water and Water/Co-solvent Systems. Ph.D. Dissertation, The Ohio State University.

APPENDIX I

NOMENCLATURE

a, b, c, d	Constants in Eq. (6.23)
c	Concentration
c	Concentric radial clearance ($r_2 - r_1$), *in.*
conc	Concentric
d	Diameter, *in.*
d_1	Outer diameter of inner pipe, *in.*
d_2	Inner diameter of outer pipe, *in.*
D_e	Deborah number, dimensionless
d_{eff}	Effective diameter, *in.*
d_h	Hydraulic diameter ($d_2 - d_1$), *in.*
dp/dz, $\Delta p/l$	Pressure gradient, *psi/ft*
E_c	End cap energy
ecc	Eccentric
E_e	Energy component
f	Fanning friction factor
G'	Storage modulus, lb_f/ft^2
G"	Loss modulus, lb_f/ft^2
G*	Complex modulus, lb_f/ft^2
g_c	Conversion factor
G_o	Plateau modulus, lb_f/ft^2
h	Roughness projection, *in.*
h	Slot height in Eqs. (8.28) and (8.29)
k	Constant in deriving Eq. (7.13)
K	Consistency index, $lb_f\,s^n/ft^2$
K_a	Annular consistency index, $lb_f\,s^n/ft^2$
K_B	Boltzman constant

K_I	Rate constant for breakage
K_{MPL}	Consistency index for MPL-Cross model, $lb_f s^n/ft^2$
K_p	Pipe consistency index, $lb_f s^n/ft^2$
K_v	Viscometer consistency index, $lb_f s^n/ft^2$
l	Pipe length, *ft*
l_c	Contour length
l_e	Entanglement length
l_p	Persistence length
M	Molecular weight
n	Flow behavior index
n'	Local flow exponent, dimensionless
N, n	Flow exponent, dimensionless
N_{Re}	Solvent Reynolds number, dimensionless
N_{Reg}	Generalized Reynolds number, dimensionless
Q, q	Flow rate, *gal/min*
q_{pl}	Flow rate through parallel plate
R	Gas constant in Eqs. (2.20) and (4.7)
R	Radius of outer pipe
R_c	Concentric-to-eccentric conversion ratio
R_g	Radius of gyration
r_1	Outer radius of inner pipe, *in.*
r_2	Inner radius of outer pipe, *in.*
r_i	Outer radius of inner pipe, *in.*
r_m	Radius of maximum velocity, *in.*
r_o	Inner radius of outer pipe, *in.*
S	Spring constant
T	Temperature, *K or °F*
t	Time constant in Eqs. (3.1) and (3.2)
T_r	Reference temperature, *K or °F*

u	Average velocity, *ft/s*
u(r)	Velocity distribution
u^*, u_τ	Friction velocity
u_m	Maximum velocity
u_r	Velocity distribution
Z	Dimensionless distance
Δp	Pressure drop, *psi*
u^+	Dimensionless velocity
y	Distance from wall
y^+	Dimensionless distance from wall for Newtonian fluid
y_w^+	Dimensionless distance from wall for non-Newtonian fluid
$\bar{u}_z$	Time average velocity

GREEK SYMBOLS

$\dot{\gamma}'$	Dimensionless shear rate
$\dot{\gamma}_R$	Shear stress at the wall, s^{-1}
$\dot{\gamma}_w$	Wall/Pseudo shear rate, s^{-1}
$\dot{\gamma}'_w$	Dimensionless wall shear rate
$\dot{\gamma}$	Shear rate, s^{-1}
μ_∞	Viscosity at infinite shear, *cP*
τ'_w	Dimensionless wall shear stress
τ^*_w	Onset wall shear stress
Ø	Surfactant volume fraction
β	Ratio of bob to cup, dimensionless
γ	Shear strain
δ	Phase angle, boundary layer thickness
δ	Offset distance between the center of inner and outer pipes for eccentricity definition

ε	Eccentricity factor
ζ_c	Mesh size
η^*	Complex viscosity, *cP*
μ	Apparent viscosity, *cP*
μ_o	Zero shear rate viscosity, *cP*
θ	Eccentric angle
θ_i	Dial reading
λ	Characteristic rel. time (Eq. 4.7)
λ	Dimensionless radial location of zero shear stress for annular flow in Chapter 8
λ_N	Dimensionless radial location of zero shear stress for Newtonian fluid
μ_n	Normalized viscosity, dimensionless
μ_p	Plastic viscosity, *cP*
μ_s	Solvent viscosity, *cP*
ν	No. density of entanglements
ξ	Non-dimensional radial coordinate
ρ	Fluid density, *lb/gal (ppg)*
σ	Shear stress relaxation
τ	Shear stress, lb_f/ft^2
τ'	Dimensionless shear stress
τ_b	Breaking time, *s*
τ_R	Relaxation time, *s*
τ_{rep}	Reptation time, *s*
τ_{rz}, τ	Shear stress, lb_f/ft^2
τ_w	Wall shear stress, lb_f/ft^2
τ_{wc}	Critical shear stress, lb_f/ft^2
τ_y	Yield stress, lb_f/ft^2
ω	Angular frequency, $rad\ s^{-1}$

ω_c	Cross over frequency, *rad* s^{-1}
κ	Diameter ratio (d_1/d_2)

APPENDIX II

Water Test for Annular Flow

Acquired water data were used for system check and calibration as well as to establish a baseline for subsequent analysis. Turbulent flow water data were analyzed and compared with published correlations. Specifically, the Chen correlation (Eq. II.1) was used in combination with the Haciislamoglu et al. (Eq. II.2) correlation.

$$\frac{1}{\sqrt{f}} = -4\log\left[\frac{h}{3.7065d} - \frac{5.0452}{N_{Re}}\log\left\{\frac{1}{2.8257}\left(\frac{h}{d}\right)^{1.1098} + \frac{5.8506}{N_{Re}^{0.8981}}\right\}\right] \tag{II.1}$$

$$\frac{\Delta p_{ecc}}{\Delta p_{conc}} = R_c = 1 - 0.072\frac{\varepsilon}{n}\kappa^{0.8454} - 1.5\varepsilon^2\sqrt{n}\,\kappa^{0.1852} + 0.96\varepsilon^3\sqrt{n}\,\kappa^{0.2527} \tag{II.2}$$

For annular flow, the pipe diameter (d) is replaced with the hydraulic diameter ($d_2 - d_1$). where, d_2 is the inner diameter of outer pipe and d_1 is the outer diameter of inner pipe.

Figure II.1 shows a comparison between water test data and predictions with the combined Chen and Haciislamoglu et al. correlations for flow in 3.5 x 1.75-in., 5.5 x 4-in., and 5 x 3.5-in. eccentric annular sections. Good agreement is obtained between measured and predicted data with tubing roughness values of 0.00525-in., 0.0507-in., and 0.0359-in. calculated for 3.5 x 1.75-in., 5.5 x 4-in., and 5 x 3.5-in. eccentric annular sections, respectively.

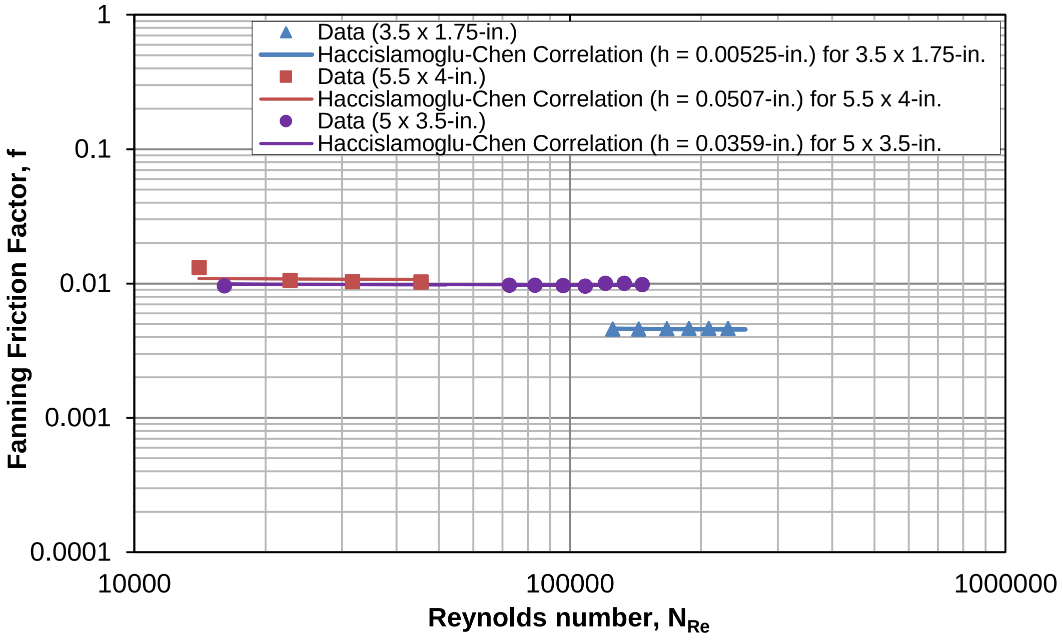

Figure II.1: Fanning Friction Factor vs. Reynolds Number for Water in Eccentric Annuli

APPENDIX III

DERIVATION OF GENERALIZED REYNOLDS NUMBER

The approach by Metzner and Reed (1955) is extended here to derive generalized Reynolds number expressions for the Carreau and MPL-Cross models. A similar approach was followed by Madlener et al. (2009) in deriving a generalized Reynolds number expression for the extended Herschel-Bulkley rheological model. For laminar, the Fanning friction factor is related to the Reynolds number by the expression below:

$$N_{Re} = \frac{16}{f} \tag{III.1}$$

The Fanning friction factor is expressed as:

$$f = \frac{2\tau_w}{\rho u^2} \tag{III.2}$$

The viscosity of non-Newtonian fluids is a function of shear rate and a constant viscosity value cannot be used.

An expression for the wall shear rate for non-Newtonian was derived by Mooney (1931) as:

$$\dot{\gamma}_w = \frac{3}{4}\left(\frac{8u}{d}\right) + \frac{1}{4}\left(\frac{8u}{d}\right)\frac{d\ln\left(\frac{8u}{d}\right)}{d\ln(\tau_w)} \tag{III.3}$$

The logarithmic differentiation term on the right hand side of Eq. (III.3) is the inverse of the local gradient n'.

$$\frac{1}{n'} = \frac{d\ln\left(\frac{8u}{d}\right)}{d\ln(\tau_w)} \tag{III.4}$$

Substituting Eq. (III.4) into (III.3) gives the expression below:

$$\dot{\gamma}_w = \frac{3n'+1}{4n'}\left(\frac{8u}{d}\right) \tag{III.5}$$

Using Eq. (4.1) for a Carreau fluid and Eq. (III.5), the generalized Reynolds number can be expressed as:

$$N_{Reg} = \frac{\rho u d}{\left[\frac{(\mu_o-\mu_w)\left(\frac{3n'+1}{4n'}\right)}{\left(1+\left(t\left(\frac{3n'+1}{4n'}\right)\frac{8u}{d}\right)^2\right)^{\frac{1-n}{2}}}+\mu_\infty\left(\frac{3n'+1}{4n'}\right)\right]} \tag{III.6}$$

With

$$n' = \frac{\frac{8u}{d}\left[\mu_\infty-2t^2(\mu_o-\mu_\infty)\frac{1-n}{2}\left\{\frac{8u}{d}\right\}^2\left(1+\left\{t\frac{8u}{d}\right\}^2\right)^{-\left(1-\frac{1-n}{2}\right)}+(\mu_o-\mu_\infty)\left(1+\left\{t\frac{8u}{d}\right\}^2\right)^{-\left(\frac{1-n}{2}\right)}\right]}{\mu_\infty\frac{8u}{d}+(\mu_o-\mu_\infty)\frac{8u}{d}\left(1+\left\{t\frac{8u}{d}\right\}^2\right)^{-\left(\frac{1-n}{2}\right)}} \tag{III.7}$$

Similarly, combining Eq. (4.4) for the MPL-Cross fluid and Eq. (III.5) gives the generalized Reynolds number expression below:

$$N_{Reg} = \frac{\rho u d}{\left[\frac{\mu_o\left(\frac{3n'+1}{4n'}\right)}{\left(1+t\left\{\frac{8u}{d}\right\}^{1-n}\right)}+\mu_\infty\left(\frac{3n'+1}{4n'}\right)\right]} \tag{III.8}$$

With

$$n' = \frac{\frac{8u}{d}\left[\mu_\infty-\frac{(1-n)(\mu_o)^2\left\{\frac{8u}{d}\right\}^{1-n}}{K_{MPL}\left(1+t\left\{\frac{8u}{d}\right\}^{1-n}\right)^2}+\frac{\mu_o}{\left(1+t\left\{\frac{8u}{d}\right\}^{1-n}\right)}\right]}{\mu_\infty\frac{8u}{d}+\frac{\mu_o\frac{8u}{d}}{\left(1+t\left\{\frac{8u}{d}\right\}^{1-n}\right)}} \tag{III.9}$$

APPENDIX IV

SLOT FLOW APPROXIMATION

The narrow slot approximation (Fig. IV.1) is widely used in practical applications for its simplicity. With this approximation, the Reynolds number is expressed as:

$$N_{Re} = \frac{928\rho u d_{eff}}{\mu_{eff}} \tag{IV.1}$$

where, ρ = fluid density (ppg); u = average velocity (ft/s); d_{eff} = effective diameter (in.); and μ_{eff} = effective viscosity (cP).

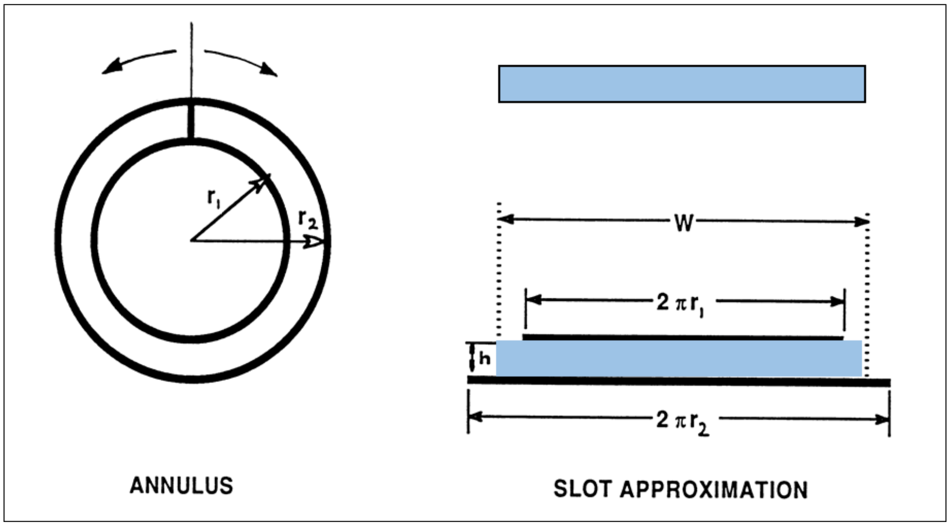

Figure IV.1: Slot Flow Approximation

The slot equation is used as the effective diameter to represent annular flow.

$$d_{eff} = 0.816(d_2 - d_1) \tag{IV.2}$$

The effective viscosity for power law fluids is expressed as:

$$\mu_{eff} = \left[\frac{K(d_2-d_1)^{1-n}}{144u^{1-n}}\right]\left[\frac{2+\frac{1}{n}}{0.028}\right]^n \qquad \text{(IV.3)}$$

For laminar flow, the Fanning friction factor is expressed as:

$$f = \frac{16}{N_{Re}} \qquad \text{(IV.4)}$$

For turbulent flow, the Dodge-Metzner equation is used.

$$\frac{1}{\sqrt{f}} = \frac{4}{(n')^{0.75}}\log\left[N_{Reg}f^{1-\frac{n'}{2}}\right] - \frac{0.395}{(n')^{1.2}} \qquad \text{(IV.5)}$$

The frictional pressure loss for eccentric annular flow can be calculated as:

$$f_{ecc} = R_c f_{conc} \qquad \text{(IV.6)}$$

where, R_c is a conversion (correction) term that is a function of the flow index, diameter ratio, and eccentricity. In this work, the Haciislamoglu and Langlinais (1990) function is used.

$$R_c = 1 - 0.072\frac{\varepsilon}{n}\kappa^{0.8454} - 1.5\varepsilon^2\sqrt{n}\,\kappa^{0.1852} + 0.96\varepsilon^3\sqrt{n}\,\kappa^{0.2527} \qquad \text{(IV.7)}$$

where, ε is pipe eccentricity; κ is the diameter ratio; and n is the flow behavior index.